



## Dissertation

# Description of Natural Surfaces by Laser Scanning

Ausgeführt zum Zwecke der Erlangung des akademischen Grades eines  
Doktors der technischen Wissenschaften (Dr.techn.)

Unter der Leitung von  
Univ.-Prof. Dipl.-Ing. Dr.techn. Norbert Pfeifer

E 120.7

Department für Geodäsie und Geoinformation  
Forschungsgruppe Photogrammetrie

Eingereicht an der Technischen Universität Wien  
Fakultät für Mathematik und Geoinformation

von

**Milutin Milenković**

Matrikelnummer: 01027638

Leopoldauer Straße 163/413

1210 Wien

Österreich

Wien, am 21. Dezember 2017

.....

Unterschrift



Dissertation

# Description of Natural Surfaces by Laser Scanning

A thesis submitted in fulfilment of the academic degree of  
„Doktor der technischen Wissenschaften (Dr.techn.)“<sup>\*)</sup>

under the supervision of  
Univ.-Prof. Dipl.-Ing. Dr.techn. Norbert Pfeifer

E 120.7  
Department of Geodesy and Geoinformation  
Research Group Photogrammetry

Research conducted at TU Wien  
Faculty of Mathematics and Geoinformation

by

**Milutin Milenković**

Matriculation number: 01027638  
Leopoldauer Straße 163/413  
1210 Vienna  
Austria

Vienna, December 21, 2017

\*) comparable to the Doctor of Engineering Sciences

.....  
Signature

Supervisor: Prof. Dr. Norbert Pfeifer  
Technische Universität Wien  
Department of Geodesy and Geoinformation  
Research Group Photogrammetry  
Gußhausstraße 27-29, 1040 Vienna, Austria .....  
E-Mail: Norbert.Pfeifer@geo.tuwien.ac.at

Referee: Prof. Dr. habil. Hans-Gerd Maas  
Technische Universität Dresden  
Institute of Photogrammetry and Remote Sensing  
Chair of Photogrammetry  
Helmholtzstraße 10, D-01069 Dresden, Germany .....  
E-Mail: hans-gerd.maas@tu-dresden.de

Referee: Prof. Dr. Bernhard Höfle  
Heidelberg University  
Institute of Geography  
GIScience Research Group  
Im Neuenheimer Feld 368, 69120 Heidelberg, Germany .....  
E-Mail: hoefle@uni-heidelberg.de

# Erklärung zur Verfassung der Arbeit

## Author's Statement

Hiermit erkläre ich, dass ich diese Arbeit selbstständig verfasst habe, dass ich die verwendeten Quellen und Hilfsmittel vollständig angegeben habe und dass ich die Stellen der Arbeit - einschließlich Tabellen, Karten und Abbildungen -, die anderen Werken oder dem Internet im Wortlaut oder dem Sinn nach entnommen sind, auf jeden Fall unter Angabe der Quelle als Entlehnung kenntlich gemacht habe.

I hereby declare, that I independently drafted this manuscript, that all sources and references used are correctly cited and that the respective parts of this manuscript including tables, maps and figures - which were included from other manuscripts or the internet, either semantically or syntactically -, are made clearly evident in the text and all respective sources are correctly cited.

Milutin Milenković  
Leopoldauer Straße 163/413  
A-1210 Wien  
Österreich

.....  
(Unterschrift / Signature)

# Table of Contents

<b>Table of Contents</b> .....	<b>i</b>
<b>Acknowledgments</b> .....	<b>ii</b>
<b>Abstract</b> .....	<b>iii</b>
<b>Kurzfassung</b> .....	<b>iv</b>
<b>Резиме</b> .....	<b>v</b>
<b>Abbreviations</b> .....	<b>vi</b>
<b>1 Introduction</b> .....	<b>1</b>
1.1 Laser Scanning .....	1
1.2 Motivation and Problem Statement.....	5
1.3 Objectives .....	7
1.4 List of Publications and the Author's Contribution .....	7
<b>2 Mapping and Modelling Natural Surfaces</b> .....	<b>10</b>
2.1 Ranging Techniques and Natural Surfaces .....	10
2.2 Surface Description Approaches.....	14
2.3 Problem Statement and Specific Objectives.....	18
<b>3 Overview of the Papers and their Contributions</b> .....	<b>19</b>
3.1 Paper I.....	22
3.2 Paper II .....	31
3.3 Paper III.....	71
3.4 Paper IV .....	80
3.5 Paper V.....	93
3.6 Paper VI.....	106
<b>4 Discussion</b> .....	<b>129</b>
4.1 Surface Roughness.....	129
4.2 3D Shoot Model.....	132
4.3 Canopy Transmittance .....	134
4.4 Surface Observations from Laser Scanning .....	137
<b>5 Conclusions</b> .....	<b>139</b>

# Acknowledgments

Many people made this dissertation possible. However, I would first like to thank Prof. Norbert Pfeifer for giving me the opportunity to work and learn about photogrammetry and remote sensing within the IPF/GEO group. In addition, I would like to thank Prof. Pfeifer for always having time for my questions, for being patient with my research, and for giving me the space to explore different ideas in detail. Without such support, this work would not have been possible. Dear Norbert, I feel privileged that I have had a chance to grow scientifically under your supervision!

Two other persons who strongly influenced my research and my view on photogrammetry are Prof. Josef Jansa and Dr. Camillo Ressler. Dear Jansa and Camillo, thank you very much for that – and more importantly, thank you for being such great friends and for making me feel at home here at the institute! I would also like to thank Dr. Markus Hollaus, who invested a lot of his time to work with me and from whom I learnt a lot about laser scanning of vegetation, for reviewing this dissertation. Then, I would like to thank Prof. Wolfgang Wagner for his support, for great discussions about physical aspects of waveform LiDAR, and for inspiring me to explore more about radar remote sensing. In addition, I would like to thank Dr. Andreas Roncat and Raphael Quast for their support during the work on physical aspects of waveform LiDAR. Then, I would like to thank Prof. Håkan Olsson, Dr. Sebastian Schnell, and Dr. Johan Holmgren for their support and cooperation on the biomass and space-borne LiDAR topic. Finally, I would like to thank all my co-authors for their help and support during this research.

Many of the calculations in this research were done by using the OPALS software. Therefore, I would like to thank the OPALS core team—Dr. Gottfried Mandlbauer, Dr. Johannes Otepka, Wilfried Karel and Bruno Wöhrer—for their permanent support and great discussions and, particularly, for dealing with a so-called “Milutin’s bug”! :)

The support from many of my colleagues was very important for me during this work. Therefore, I would like to thank Lothar Eysn, Wilfried Karel, Andreas Roncat, Martin Wieser, Wouter Dorigo, Eva Lindberg, Rok Vežočanik, Sajid Ghuffar, Eetu Puttonen, Ana Đuričić, Philipp Glira, Livia Piermattei, Elmar Sönser, and many others for being great friends, for many interesting discussions, for your support during the field measurements, or for just having fun together! Also, many thanks go to all colleagues from the SLU for being such great hosts and for helping me during my stay at SLU. Thank you all, it is a pleasure for me to know and be around such nice people!

Finally, I would like to thank my family. First, I would like to thank my wife Silvija for the support and understanding that she always had for my work. I would also like to thank my mother, my brother, and my nieces for their support, as well as my father, who is unfortunately not with us any more. Hvala vam puno—vi ćete uvek biti deo svakog mog uspeha!

Milutin Milenković

# Abstract

Laser scanning (also LiDAR – light detection and ranging) provides accurate and high-resolution geometric and radiometric measurements of natural surfaces at different spatial scales, which is relevant for many environmental and physical models. However, high-resolution laser scanning data are often not fully explored or are not used at all for surface description in such models. The aim of this research is to revisit current methods and to introduce new methods for the description of natural surfaces by exploring the full potential of novel high-resolution laser scanning data. The work comprises (a) natural surfaces such as soil, gravel, and vegetation; (b) a range of different laser scanning techniques, such as TLS (terrestrial laser scanning), ULS (unmanned aerial vehicle laser scanning), ALS (airborne laser scanning); and (c) ranging methods such as time-of-flight ranging, phase-shift ranging, and active and passive triangulation. The work is focused on three land-surface parametrisations such as surface roughness, a 3D model of a conifer shoot, and canopy transmittance, which are selected as representatives of geometric-stochastic, geometric-deterministic, and geometric-radiometric surface descriptions, respectively. As those parametrisations have also been the subject of several research projects, particular objectives are set and analysed in six separate studies. The research contributed by introducing new methods and by improving current methods for those parametrisations from contemporary high-resolution laser scanning data. Surface roughness is mainly analysed in the frequency domain by means of the roughness spectrum. A new method is introduced that optimizes the interpolation parameters so that a DTM (digital terrain model), derived from a laser scanning point cloud, has a unique stochastic property (the fractal dimension is maximized at high frequencies), which is important for an unbiased surface roughness assessment. Furthermore, multi-scale laser scanning point clouds are analysed to determine spatial scales over which corresponding roughness spectra can be used interchangeably. The 3D modelling of a conifer shoot is (to the author's best knowledge) modelled on the basis of point clouds up to individual needles for the first time. The modelling is based on a semiautomatic method developed here for micro-scale triangulating laser scanning data. Then, a new method is introduced to estimate canopy transmittance from small-footprint ALS waveform data, where assumptions on vegetation-ground scattering properties are not required. To enable upscaling of the canopy transmittance information to the space-borne LiDAR footprint scale, a waveform stacking method is developed in an additional study. The stacking method and the simulated space-borne LiDAR waveforms are then used, along with field measurements of forest inventory, to estimate aboveground biomass. The information and methods about surface roughness, 3D shoot geometry, and canopy transmittance that are derived here provide a basis for a better understanding and description of natural surfaces in environmental and physical models.

# Kurzfassung

Laserscanning stellt genaue, hoch aufgelöste geometrische und radiometrische Messungen von Oberflächen der natürlichen Umgebung auf verschiedenen räumlichen Skalen zur Verfügung. Diese werden für viele physikalische und andere Modelle, die die Umwelt beschreiben, benötigt. Ungeachtet dessen werden hoch-auflösende Laserscanning-Daten oft nur teilweise oder gar nicht für die Beschreibung der Oberflächen in diesen Modellen genutzt. Ziel der vorliegenden Forschung ist es, aktuelle Methoden zur Beschreibung natürlicher Oberflächen aufzugreifen und neue Methoden vorzuschlagen, sodass das volle Potential neuer hoch-auflösender Laserscanning-Daten ausgenutzt wird. Die Arbeit umfasst (a) beispielhaft die natürlichen Oberflächen(-Bedeckungen) Erde, Schotter und Vegetation, (b) eine Auswahl verschiedener Laserscanning-Techniken, nämlich TLS, ULS, und ALS, also terrestrisches, UAV-getragenes und luftgestütztes Laserscanning (wobei UAV für engl. unmanned airborne vehicle, zu dt. unbemanntes Luftfahrzeug, steht) und (c) die Entfernungsmessmethoden Pulslaufzeit, Phasenvergleichsverfahren, und aktive und passive Triangulation. Die Arbeit fokussiert auf drei Parametrisierungen der Landfläche, nämlich (Oberflächen-)Rauigkeit, das 3D-Modell eines Nadelbaum-Triebes und die Kronendurchdringung. Diese Parametrisierungen wurden als Repräsentanten von geometrisch-stochastischen, geometrisch-deterministischen und geometrisch-radiometrischen Oberflächenbeschreibungen ausgewählt. Da diese Parametrisierungen auch Untersuchungsgegenstand in unterschiedlichen Forschungsprojekten waren, werden in sechs verschiedenen Studien spezifische Ziele gesetzt und entsprechende Analysen durchgeführt. Der wissenschaftliche Beitrag dieser Arbeit umfasst neue Methoden zur Ableitung dieser Parametrisierung aus aktuellen hoch-auflösenden Laserscanning-Daten beziehungsweise die Verbesserung bestehender Methoden. Die Rauigkeit der Oberfläche wird hauptsächlich im Frequenzbereich des Spektrums der Rauheit analysiert. Es wird eine neue Methode zur Interpolation von Geländemodellen aus Laserscanning-Punktwolken vorgestellt, die eine besondere stochastische Eigenschaft hat, nämlich dass die fraktale Dimension für die hohen Frequenzen maximiert wird. Dies ist für eine unverzerrte Bestimmung der Oberflächenrauigkeit wichtig. Zusätzlich werden Laserscanning-Punktwolken, die auf unterschiedlichen räumlichen Skalen gewonnen wurden, verglichen, um zu bestimmen, auf welchen räumlichen Skalen die entsprechenden Rauigkeitsspektren untereinander auswechselbar sind. Das 3D-Modell eines Nadelbaum-Triebes wird, nach bestem Wissen und Gewissen des Autors, zum ersten Mal auf Basis von Punktwolken bis zu den einzelnen Nadeln hin modelliert. Die Modellierung basiert auf einer semi-automatischen Methode, die hier für die Daten eines triangulierenden Laserscanners entwickelt wurde. Schließlich wird eine neue Methode zur Schätzung der Kronendurchdringung vorgeschlagen, die auf ALS-Daten mit kleinem Abtastfleck und Aufzeichnung der vollen Wellenform beruht. Es müssen keine Annahmen über das Verhältnis der Streuung durch Boden und Vegetation getroffen werden. Um die Information über Kronendurchdringung auf den Maßstab der Abtastflecken von Weltraum-gestütztem LiDAR (Light Detection And Ranging) zu übertragen, wurde in einer weiteren Studie eine Methode für die Aufstapelung von Wellenformen entwickelt. Die Methode des Stapelns und simulierte, Weltraum-gestützte LiDAR-Wellenformen wurden dann gemeinsam mit Feldmessungen einer Forstinventur genutzt, um oberirdische Biomasse abzuschätzen. Die Information und die Methoden zur Oberflächenrauigkeit, zur Geometrie des Nadelbaum-Triebes und zur Kronendurchdringung, die hier abgeleitet wurden, führen zu einem besseren Verständnis der Beschreibung natürlicher Oberflächen, in physikalischen und empirischen Modellen, die unsere Umwelt beschreiben.

## Резиме

Ласерско скенирање обезбеђује прецизна геометријска и радиометријска опажања природних површи у високој резолуцији и на различитим мерним размерама. Ова мерења се могу користити за опис (параметризацију) природних површина у различитим физичким моделима и моделима животне средине. Међутим, врло често ласерски подаци нису у потпуности искоришћени или се уопште не користе у тим моделима. Циљ овог истраживања је да се размотре постојеће и представе нове методе за опис природних површи а да се при томе искористи потпуни потенцијал најсавременијих ласерских података. У оквиру овог рада анализирани су (а) природне површи као што су земљиште, шљунак и вегетација, (б) различите технике ласерског скенирања као што су ТАС, БАС и ААС (терестичко, БЛ-базирано и авионско ласерско скенирање, где је БЛ скраћеница за термин беспилотна летелица) и (ц) различити принципи мерења дужина као што су импулсно мерење, фазно мерење, активна и пасивна триангулација. Рад је усредсређен на три параметризације: површинску храпавост, 3Д модел четинарског изданка и трансмисију склопа шумских крошњи. Ове параметризације су изабране као представници геометријско-стохастичког, геометријско-детерминистичког и геометријско-радиометријског начина описивања природних површи. Оне су такође биле и предмет истраживања у неколико научних пројеката у оквиру којих су постављени појединачни циљеви за сваки од њих и анализирани у оквиру шест одвојених студија. Резултат овог истраживања су потпуно нове као и побољшане постојеће методе које су предложене за оцену сваког од три параметра на основу савремених ласерских података високе резолуције, што уједно представља и главни научни допринос овог истраживања. Површинска храпавост је већим делом анализирана у фреквентном домену и то користећи такозвани спектар храпавости (густина спектра снаге сигнала). Предложен је нови метод за интерполацију дигиталног модела терена (ДМТ) који је стохастички недвосмислено дефинисан (има највећу могућу фракталну димензију оцењену на основу високих фреквенција), што онда обезбеђује непомерену оцену површинске храпавости. Такође, упоређени су спектари храпавости оцењени из ласерских података прикупљених на различитим мерним размерама да би се одредиле просторне компоненте (фреквенције) на којима су ови спектри подједнако тачни. 3Д модел четинарског изданка је по први пут моделован из неког облака тачака и до детаља као што су појединачне иглице. Ово моделирање је засновано на једној полуаутоматској процедури која је предложена првенствено за ласерске податке прикупљене микро триангулацијом. Такође, предложена је нова метода за оцену трансмисије шумског склопа на основу анализе потпуних ААС сигнала прикупљених ласером мале дивергенције снопа. У поређењу са постојећим методама, ова нова метода не захтева претпоставке о оптичким својствима вегетације и земљишта испод ње. На крају је предложен још један метод где су на основу потпуних ААС сигнала симулирани сателитски ласерски сигнали који су потом калибрисани са теренским мерењима инвентара дрвећа да се извршила оцена надземне биомасе шуме. Информације и методе о површинској храпавости, 3Д моделирању вегетације и трансмисији шумског склопа које су резултат овог истраживања дају основ за боље разумевање проблема параметризације природних површина у физичким моделима и моделима животне средине.

# Abbreviations

2D	Two-Dimensional
3D	Three-Dimensional
2.5D	Two-and-Half Dimensional (planar coordinates that can contain only a single height information)
LiDAR	Light Detection And Ranging
DIM	Dense Image Matching
UAV	Unmanned Aerial Vehicle (also Drone)
TLS	Terrestrial Laser Scanning (laser scanning performed from geodetic tripods)
ULS	Laser Scanning from an UAV
ALS	Airborne Laser Scanning
GNSS	Global Navigation Satellite
GPS	System Global Positioning System
INS	Inertial Navigation System Earth
EO	Observation
LAI	Leaf Area Index
AGB	Above Ground Biomass
DTM	Digital Terrain Model
DSM	Digital Surface Model
DEM	Digital Elevation Model
nDSM	Normalized DSM (a DTM subtracted from a DSM)
DoD	DEM of Difference (height difference of two DEMs of the same area)
RMS <sub>h</sub>	Root Mean Square Height
GSD	Ground Sampling Distance (the pixel size in the object space)
IFOV	Instantaneous Field of View (e.g. a cone of the laser beam)
BBA	Bundle Block Adjustment

# 1 Introduction

A description of natural surfaces is required in environmental and physical models. In this research, geometric and radiometric observations collected by laser scanning for different natural surfaces are analysed and used for surface description. Laser scanning is the main focus of this work, although photogrammetry is also used for comparison.

## 1.1 Laser Scanning

Laser scanning is an active measurement technique that utilizes laser radiation and the LiDAR (light detection and ranging) principle to collect non-selectively 3D points  $P_i(x_i, y_i, z_i)$ . A set of such 3D points, which are (typically) irregularly distributed in Euclidian space, is also referred to as a *point cloud*. Additionally to the geometry, laser scanning can provide radiometric information that is a function of the laser radiation scattered back from the illuminated area of the object. This subsection presents briefly the background of laser scanning by following its basic processing steps shown in Figure 1. The presentation starts with raw LiDAR observations, such as ranges, angles and waveforms, and then continues with presenting different scanning approaches, and discussing point cloud georeferencing (orientation), and ends with presenting typical applications of laser scanning and point cloud modelling.

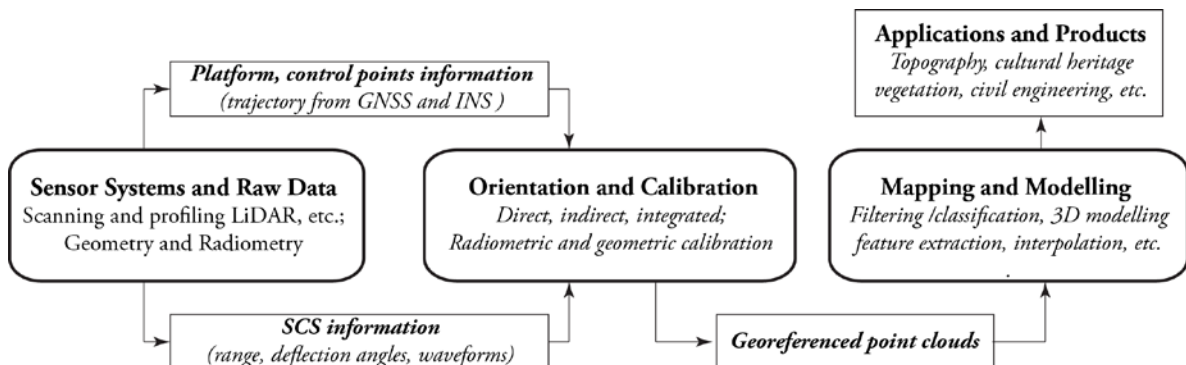


Figure 1: Basic steps in processing of laser scanning data from raw data until its products and particular applications.

### 1.1.1 Sensor Systems and Raw Data

In laser scanning, a range is observed by transmitting the laser radiation (a laser pulse) towards an object of interest and recording the laser radiation scattered back from the object. Most of the laser radiation is transmitted within the laser beam that is commonly considered to be a cone which opening angle (diffraction angle) depends on the laser wavelength and the aperture size of the laser sensor. In contrast to classical tachymeters or rangefinders, laser scanning provides a non-selective, systematic sampling, i.e. scanning. The ranges are collected systematically, by firing lasers pulses repeatedly and introducing a deflection unit (e.g. an oscillating mirror) to steer laser beams at predefined angular increments (laser-beam directions) and within a scanning plane. It is noted that an oscillating mirror is just one of many possible laser beam deflection approaches. The deflection is also done by using a rotating polygon, a fiber-optic array or a

rotation mirror in case of the Palmer scanner (Beraldin et al. 2010; Pfeifer et al. 2017; Wehr 2008). Nevertheless, in this introduction, a scanner with the oscillating mirror is assumed.

The output of scanning (with a oscillating mirror) includes the following observations: (a) range  $r_i$ , (b) deflection angle  $\varphi_i$  and (c) intensity. This means that laser scanning provides regularly-sampled points ( $r_i$  and  $\varphi_i$ ) in a polar coordinate system of the scanning plane, that is also called sensor coordinate system (SCS). In object space, these points are located along the intersection of the scanning plane and the object scanned, which will be referred here to as *a profile*. More information on laser scanning fundamentals can be found in, e.g. Baltsavias (1999), Petrie and Toth (2008), Beraldin et al. (2010), Jutzi et al. (2017), Heipke (2017) and Pfeifer et al. (2017).

To cover the whole object, or a wider area, it is however necessary to acquire points from many scanning planes. This problem is addressed by particular scanner architectures that consider additionally a platform on which the scanner is going to be mounted during the scanning. Here, the following scanning approaches are distinguished. The first approach is scanning from a static platform with a scanner that has a moving (typically rotating) scanning plane. An example is terrestrial laser scanning (TLS) performed from geodetic tripods. TLS collects a series of profiles by rotating the scanning plane for regular angular increments  $\alpha_i$ , while keeping the origin of the SCS fixed. Points corresponding to the profiles collected under the same position and orientation of the platform during TLS are commonly referred to as *a scan*. The second approach is scanning with a scanner which scanning plane is fixed relative to the body of a moving platform. An example here is airborne laser scanning (ALS) performed from an aeroplane. In ALS, aeroplanes typically try to follow a straight line during data acquisition, whereas the scanner is mounted so that a series of across-track profiles is collected. Points that correspond to the profiles collected along a single flight line are commonly referred to as *a strip*.

It should be noted that there are also laser profiles and laser altimeters, which collect a single profile. Laser profilers are mounted on a fixed platform (or permanently at a certain location) and acquire points repeatedly from one (or few) fixed scanning plane(s). They are used mostly for industrial applications (e.g. traffic control, process monitoring, etc.). There are also laser profiles with one (of few) fixed scanning planes mounted on vehicles (mobile platforms), which are mainly used for street mapping. Finally, laser altimeters typically do not have a deflection unit and measure the range at single (or a few) direction(s), but use a moving platform to acquire a profile of points. This scanning method is applied on space-borne LiDAR systems, where the global coverage and regular revisit times makes this data relevant for Earth observation (EO).

Raw radiometric data can be either intensity or waveforms, which introduce a further classification on *discrete-* and *waveform-LiDAR*, respectively. The waveform LiDAR scanners record the complete backscattered signal over a short time, i.e. a *waveform*, caused by the interaction of the transmitted laser pulse with objects placed within its laser beam. There are several methods how such waveforms can be further processed to extract individual *echoes* or (bio-)physical quantities such as the differential cross-section of an object (e.g., Jutzi and Stilla 2006; Roncat et al. 2011; Wagner et al. 2006). The extracted echoes are associated with their ranges (geometry) and radiometric features such as *echo amplitude* and *echo width*. Furthermore, the echoes are typically classified, according to their range, to *first*, *second*, etc. and *last*. In contrast, the discrete LiDAR scanners provide directly the ranges and a single intensity values for so-called *returns*, which also can be *first*, *last*, etc. The returns are recorded when the backscattered signal (typically additionally amplified by the scanner) exceeds a certain threshold imposed by the scanner

manufacturer. As the discrete scanners are primarily designed for range measurements, the physical meaning of the assigned intensity values is often unclear. More information on waveform and discrete LiDAR can be found in, e.g. Roncat et al. (2014), Mallet and Bretar (2009), Stilla and Jutzi (2008) and Harding (2008).

### 1.1.2 Orientation and Calibration

The SCS observations (ranges and beam directions) are transformed in the object space (typically a Cartesian coordinate system) for further analysis, providing a collection of 3D points, i.e. a point cloud. To this end, it is necessary to know the position and orientation (the exterior orientation) of each scanning plane in object space (Kraus 2007). The exterior orientation can be directly observed (measured) or indirectly derived from ground control points (GCPs) with known (measured) coordinates in the object space, which is known as direct and indirect georeferencing (El-Sheimy 2008; Kraus 2007, p.181). *The direct georeferencing* is typical for scanning from moving platforms where the position and orientation of the platform is observed with a global navigation system (GNSS) and an inertial measurement unit (IMU), respectively. This information is then synchronized (according to the recording times) with the SCS observations and directly transformed into the object coordinate system, providing a point cloud in a global coordinate system (e.g. WGS84), or a national projection system (e.g. the Gauß-Krüger projection based on the Bessel ellipsoid). The transformations for direct georeferencing of ALS and TLS is, e.g., given in Kraus (2007), equations 8.1-1 and 8.2-1, respectively. *The indirect georeferencing* is typically used in TLS, where specially designed targets are introduced inside the scanning area and used as GCPs. These targets can be automatically measured with a scanner and are additionally surveyed with a total station from a local geodetic network, or measured with static GNSS. The georeferencing is then performed in two steps: (a) transformation of SCS observations into Cartesian coordinates (e.g. Kraus 2007, equation 8.2-2) and (b) a similarity transformation from the Cartesian coordinates into final, global or national, coordinates. The latter requires at least three 3D GCPs. In case of several overlapping strips (or scans), georeferencing often leads to planar and height discrepancies in the overlapping areas (Huising and Gomes Pereira 1998). These discrepancies may occur, e.g., due to errors in the GNSS and IMU measurements. As a solution, different strip adjustment techniques are introduced to minimize these discrepancies (Maas 2000; Skaloud and Lichti 2006). The minimisation of the discrepancies is also done by using the Iterative Closest Point (ICP) algorithm (Besl and McKay 1992; Glira et al. 2016). The georeferencing that uses GNSS and IMU information together with strip adjustment (with GCPs and tie features) is also referred to as *integrated georeferencing* (Kraus, p.276). Finally, it is noted that the exterior orientation of the scanning plane can also be given in a local, or an arbitrarily defined coordinate system, providing the point clouds in the *local* or the *model* coordinate system, respectively. For example, an arbitrary definition of the TLS's exterior orientation would typically assume that the scanning plane is vertical, and that the SCS's origin is set to the point  $O_i(0,0,0)$ .

There are two types of calibration of laser scanning systems: geometric and radiometric. *The geometric calibration* has the aim of eliminating systematic errors from the resulting georeferenced points, i.e. leaving only random measurement errors. This requires, first, to introduce an error model of the raw LiDAR observations, and then, to estimate them within an adjustment procedure based on the observed points (Schenk 2001). Typical systematic errors of a LiDAR system includes range and scan angle errors, scan plane errors, mounting and synchronization

errors, etc. An example of observed errors is the mentioned discrepancies between the overlapping ALS strips. Therefore, in ALS, calibration is often a part of an integrated georeferencing, i.e. strip adjustment (e.g., Glira et al. 2016). Other examples of the observed errors are the discrepancies at control points, point cloud features (such as break lines) and/or regular 3D shapes (such as planes, spheres, cylinders, etc.). Such 3D shapes are typically used in the geometric calibration of TLS data (Chan et al. 2015; Dorninger et al. 2008; Lichti 2010). *The radiometric calibration* has the aim to derive well-defined physical quantities, such as reflectance, from the reordered waveforms or the intensity value of the object illuminated by laser radiation. Generally, waveforms and intensity values of an object are not necessarily identical when observed from different sensors or flight heights, whereas a physical quantity is inherent to the object. The radiometric calibration involves the lidar equation and a reference information such as artificial or natural targets with known reflectivity (Kaasalainen et al. 2005; Wagner 2010). However, the radiometric calibration can also be based purely on data, which is referred to as intensity correction methods (Höfle and Pfeifer 2007). More detail on the geometric and radiometric calibration can be found in, e.g., Lichti and Skaloud (2010) and Roncat et al. (2014).

### 1.1.3 Modelling and Mapping

Further processing of georeferenced point clouds involves modelling and/or mapping of information that is of interest for a particular application. This involves certain methods such as filtering, segmentation, feature extraction, pattern recognition, model fitting, parameter estimation, etc. The methods usually assume that the orientation and calibration of raw laser scanning data is resolved. Thus, typical input for this step is a georeferenced point cloud that is accurate up to random measurement errors. Ideally, the introduced methods should be robust (e.g. to handle datasets with different quality) and automatic (e.g. to allow for a rapid production). Here, only some of classical applications of lasers scanning will be mentioned to illustrate manifold methods and products available.

One of the first applications of laser scanning was in *topography*, aiming at the description of terrain, i.e. a bare-ground surface (Krabill 1984). This involves methods for *point cloud filtering* (a calcification to ground and non-ground points), and derivation of product such as *digital terrain models*, DTMs (Axelsson 1999; Kilian et al. 1996; Kraus and Pfeifer 1998). More information about point cloud filtering and DTM interpolation can be found in, e.g., Kraus (2000), Pfeifer and Mandlburger (2008) and Briese (2010). Another classical application of laser scanning is *forestry* and *ecology*. There, different methods are introduced to derive biophysical parameters, such as vegetation height, vegetation cover, gap fraction and (horizontal and vertical) structure, which are then used to model forest site parameters, estimate biomass and derive leaf area index (Lefsky et al. 1999; Nelson et al. 1984; Nilsson 1996). More information about laser scanning application in forestry and ecology can be found in, e.g., Maltamo et al. (2014), Maas (2010) and Hyypä et al. (2008). Then, laser scanning is also used in urban mapping, where different methods for extracting building footprint and roof facets from point clouds are introduced to derive automatically 3D building models (Bretar 2008; Maas and Vosselman 1999; Shan and Sampath 2008; Sohn et al. 2008; Zhang et al. 2008). Laser scanning is also used in archaeology, where e.g. filtering algorithms supported by waveform information are used to map different archaeological features under the vegetation (Doneus et al. 2008). A more detailed overview of the mapping and modelling methods in environmental and engineering applications is given in, e.g., (Heritage and Large 2009) and Lindenbergh (2010), respectively.

## 1.2 Motivation and Problem Statement

The aim of this thesis is to describe different natural surfaces with laser scanning observations. Natural surfaces are considered here as a boundary between land and atmosphere that is composed of a collection of natural elements aggregated purely naturally or with the least possible human activities. The aggregation of individual elements forms a boundary associated with certain thickness and spatial structure, which is here referred to as a layer. A gravel surface, for example, composed mainly of elements such as individual pebbles and sand particles. Soil surface is an aggregation of the elements such as individual clods. In addition, vegetation is a boundary layer formed of elements such as trees stems, branches, shoots, needles and leaves. Due to their high complexity, these natural surfaces can be described at different scales, e.g. describing the layer on the whole, or describing particular elements of the layer. Furthermore, there can be several possible surfaces that describe a complex layer structure. For example, the outer most surface, the bottom surface (e.g. digital surface and terrain models of a vegetation layer, respectively), or a surface understood as the outcome of a probabilistic process. The selection of these approaches depends on the data type and resolution, but also on the application.

A description of natural surfaces is required for environmental modelling. The surface, as a boundary between land and atmosphere, is an agent in climate simulation models. A natural surface is the memory of geomorphic processes that shaped their structure and features over long periods in the past. Natural surfaces are also one of the primary subjects in Earth observation. *Land-surface parameters* (also *geophysical*-, *biogeophysical*-, *biophysical-parameters*) derived from surface geometry and radiometry (such as slope, roughness, vegetation cover, surface albedo, soil moisture, vegetation optical depth, leaf area index – LAI, etc.) are variables in environmental modelling and monitoring of, e.g., water and carbon cycles, terrestrial ecosystems, etc. Land-surface parameters are also important for understanding and modelling signals observed by space-borne remote sensing sensors. Therefore, geometric and radiometric descriptions of natural surfaces are a relevant topic in the fields such as Earth observation, geomorphology and hydrology.

Laser scanning, on the other hand, is a measurement technique that provides highly accurate samples of surface geometry and radiometry at very high point density. The techniques such as ALS or TLS can readily collect tens to hundreds of points per  $\text{m}^2$  or  $\text{cm}^2$ , providing *high-resolution topographic data* at the patch- or landscape-scale, respectively. Furthermore, in the last decades, laser scanning software and algorithms matured, offering a high degree of automation in data processing. However, many of current methods for derivation of the mentioned land-surface parameters still do not take full advantage of the advancements in laser scanning. This discrepancy opens a possibility to develop new (and reconsider current) ways of describing natural surfaces with high-resolution laser scanning data.

In this dissertation, natural surfaces, such as soil, gravel and vegetation, are described using different approaches applied at different scales and on contemporary high-resolution laser scanning data. The natural surfaces are described using geometric and radiometric LiDAR observations. Furthermore, the geometric LiDAR observations are treated stochastically and deterministically in the description of natural surfaces. These descriptions are categorised here in the following three categories: (a) geometric-stochastic, (b) geometric-deterministic and (c)

geometric-radiometric. The results of the three descriptions are: (a) estimated parameters of a stochastic model applied, (b) a 3D model of a surface element and (c) estimated values of a (bio-)physical quantity. Each surface description is performed at a different scale: (a) at field plot scale, (b) at the needle-shoot-branch scale, and (c) at the landscape scale. The purpose of exercising such diverse surface descriptions and scales is to understand better advantages and drawbacks of each particular approach in the light of contemporary, high-resolution laser scanning data.

One additional variable in the experimentation is the natural surface itself. Soil, gravel and vegetation were selected because they are important for many environmental applications. Furthermore, these surfaces are differently “seen” by a laser scanning system. Laser radiation transmitted within a laser beam can “penetrate”, e.g., vegetation. This penetration is not due to a laser ability to penetrate into canopy materials (leaves, twigs, branches, etc.), but rather due to canopy gaps that allow a portion of the laser radiation to travel deeper into the canopy. The natural surfaces such as soil and gravel are non-penetrable for laser radiation, but they may cause certain artefacts in range determination. These and other sensing characteristics, such as measurement noise, may lead to an incorrect surface description if they are not appropriately considered during the data processing.

It should be noted that the coverage of laser scanning data is rather local or regional. For example, the accuracy of terrestrial laser scanning allows going to very small surface details such as soil clods and gravel pebbles, but the coverage of such a high-resolution data is typically at the patch scale (a field plot). For airborne laser scanning, the coverage is typically at the landscape scale. From, e.g., a geomorphological perspective, this means that surface descriptions by such data do not refer to global landform structures, but rather to elementary landform units such as patches of soil, gravel and forest. The derived land-surface parameters are valid for these landform scales. Therefore, the experiments presented here are primarily relevant to environmental processes that take place at these scales. Nevertheless, such patch-scale information is also required for the validation of many global-scale, land-surface parameters derived from Earth observation.

In the field of laser scanning, this work contributes to the modelling task as introduced in Figure 1 and Section 1.1. The aim was to reconsider current surface descriptions while addressing appropriately the LiDAR sensing properties and application needs. The term *description* that is used in this dissertation includes input data, modelling and a result. This term is used to emphasize that a description result (e.g. a biophysical parameter, a function or a digital map) is further used as input (that describes a natural surface) in environmental and physical models. The term *description* is also used to emphasize that this work considers surface descriptions (e.g. radiometric and stochastic) that are beyond the classical surface modelling that provides 3D object models and 2.5D digital terrain models. The experimentation involved (a) different laser scanning techniques (TLS, ULS and ALS), (b) the processing of both geometric and radiometric information (discrete returns and waveform LiDAR), (c) different ranging methods (time-of-flight, phase-shift, active and passive triangulation) and (d) the processing of data acquired at different spatial scales.

## 1.3 Objectives

The aim of this dissertation is to develop appropriate methods for surface descriptions required in environmental applications that are based on high-resolution laser scanning data. To this end, general and specific objectives are set.

This dissertation has the following general objectives:

- to consider different surface description approaches, such as (a) geometric-stochastic, (b) geometric-deterministic and (c) geometric-radiometric,
- to identify a particular land-surface parametrisation for each of the three description approaches and focus the research on them,
- to introduce new or improve current methods for the selected land-surface parametrisations,
- to consider both geometric and radiometric information for the description of natural surfaces,
- to analyse and compare different: measurement setups, laser scanning sensors and multi-scale data.

The specific objectives refer to the selected land-surface parametrisation, and these objectives are presented later, in Section 2.3.

## 1.4 List of Publications and the Author's Contribution

This thesis is based on the work contained in six papers: four journal papers and two conference papers. All papers are peer reviewed, including the two conference papers, as well. The papers are listed below according to their publication date:

- Paper I Milenković, M., Eysn, L., Hollaus, M., Karel, W. and N. Pfeifer (2012). "Modeling the tree branch structure at very high resolution." in: *SilviLaser 2012 - Conference Proceedings*, Paper ID SL2012-099, 8 pages. (peer reviewed conference paper)  
Online available at: [https://publik.tuwien.ac.at/files/PubDat\\_211339.pdf](https://publik.tuwien.ac.at/files/PubDat_211339.pdf)
- Paper II Milenković, M., Pfeifer, N. and Glira, P. (2015). "Applying Terrestrial Laser Scanning for Soil Surface Roughness Assessment." *Remote Sensing* 7(2): 2007-2045. (peer reviewed journal paper)  
Online available at: <http://www.mdpi.com/2072-4292/7/2/2007>
- Paper III Milenković, M., Karel, W., Ressel, C. and Pfeifer, N. (2016). "A comparison of UAV and TLS data for soil roughness assessment." *ISPRS Ann. Photogramm. Remote Sens. Spatial Inf. Sci.* III-5: 145-152. (peer reviewed conference paper)  
Online available at: <http://www.isprs-ann-photogramm-remote-sens-spatial-inf-sci.net/III-5/145/2016/>
- Paper IV Milenković, M., Wagner, W., Quast, R., Hollaus, M., Ressel, C., Pfeifer, N. (2017). "Total canopy transmittance estimated from small-footprint, full-waveform airborne

LiDAR." ISPRS Journal of Photogrammetry and Remote Sensing 128: 61-72. (peer reviewed journal paper)

Online available at: <https://doi.org/10.1016/j.isprsjprs.2017.03.008>

Paper V Milenković, M., Schnell, S., Holmgren, J. Ressler, C., Lindberg, E., Hollaus, M., Pfeifer, N. and Olsson, H (2017). "Influence of Footprint Size and Geolocation Error on the Precision of Forest Biomass Estimates from Space-Borne Waveform LiDAR." Remote Sensing of Environment, (peer reviewed journal paper)

Online available at: <https://doi.org/10.1016/j.rse.2017.08.014>

Paper VI Milenković, M., Ressler, C., Karel, W., Mandlbürger, G. and Pfeifer, N. (2017). "Roughness Spectra Derived from Multi-Scale LiDAR Point Clouds: A Comparison and Sensitivity Analysis", ISPRS International Journal of Geo-Information (manuscript under review)

The contribution of Milutin Milenković to the above papers was as follows:

- Paper I Planned the study and interpreted the results with the co-authors, planned and carried out the measurements, performed the data processing and analysis, wrote the major part of the manuscript and coordinated the review process.
- Paper II Planned the study and carried out the measurements, performed most of the data pre-processing, carried out the data analysis, interpreted the results with the co-authors, wrote the manuscript and coordinated the review process.
- Paper III Planned the study and interpreted the results with the co-authors, planned and carried out the measurements, performed most of the data pre-processing, carried out the data analysis, wrote the major part of the manuscript and coordinated the review process.
- Paper IV Planned the study and interpreted the results with the co-authors, developed the method, performed the data processing and analysis, wrote the manuscript and coordinated the review process.
- Paper V Planned the study and interpreted the results with the co-authors, developed the waveform stacking method, performed LiDAR-related processing, wrote the major part of the manuscript and coordinated the review process.
- Paper VI Planned the study interpreted the results with the co-authors, planned and carried out the terrestrial measurements (TLS and close-range image acquisition), performed the data pre-processing, carried out analysis, wrote the manuscript and coordinated the review process.

The above papers will be referred to by Roman numerals in the following text (e.g. Paper I, Paper II, etc.).

The research presented in the above papers was carried out under funding from several scientific projects:

- the 3DVegLab project funded by ESA (European Space Agency), ID: ESA STSE AO/1-6529/10/I-NB,
- the NEWFOR project funded by the European Regional Development Fund in the framework of the Alpine Space Program, ID: 2-3-2-FR,

- the Advanced\_SAR project funded by the European Community's Seventh Framework Programme ([FP7 / 2007 - 2013 ]) under grant agreement no. 606971,
- the Innovative Ideas project “MMRough” funded by TU Wien.

## 2 Mapping and Modelling Natural Surfaces

### 2.1 Ranging Techniques and Natural Surfaces

Determination of the range (sensor-to-object distance) is one of the fundamental tasks in deriving photogrammetric point clouds. There are many ranging techniques in use and the quality of the derived range may be considerably different when ranging over different natural surfaces. This subsection presents ranging techniques that are used in this dissertation, auxiliary information retrieved by such ranging, and then discusses briefly ranging properties for scanning over soil, gravel or vegetation.

Figure 2 shows an overview of the ranging techniques, where those used in the dissertation are coloured in red. The figure shows that laser scanning data were acquired with the three different ranging techniques: (a) time-of-flight, (b) phase-shift and (c) active triangulation. The passive triangulation is also used within this dissertation (the most upper branch in Figure 2), mostly as an independent (non-LiDAR) measurement technique for the comparison with laser scanning results. At the end of this subsection, there is Table 1 that summarizes ranging techniques, platforms, sensors and the data properties used in this dissertation.

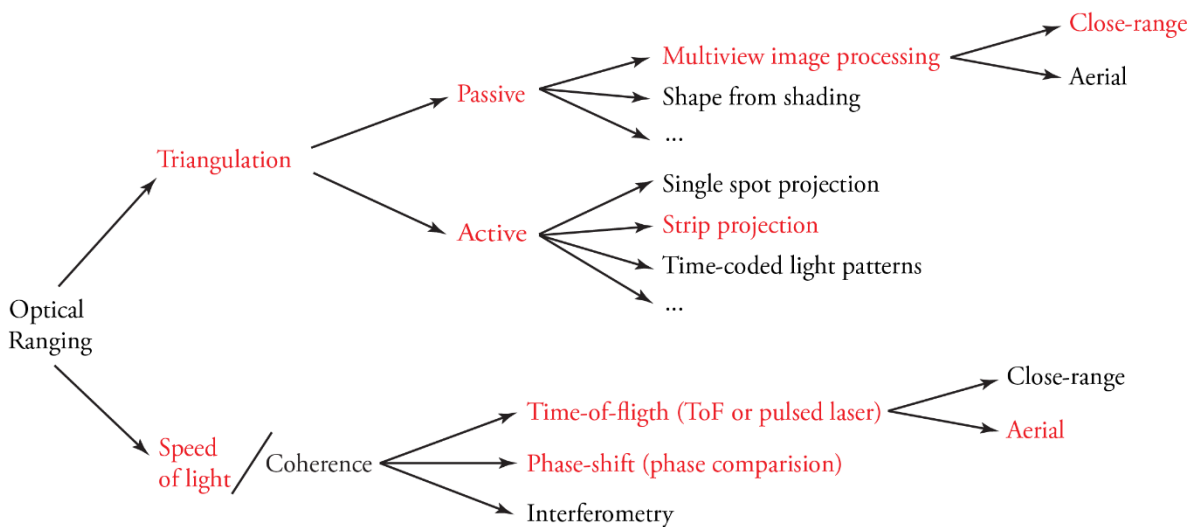


**Figure 2: Taxonomy of optical ranging techniques in photogrammetry and computer vision. This figure is an adaptation of Figure 1.1 from Beraldin et al. (2010).**

The *time-of-flight (ToF)* ranging sensors transmit laser pulses (that travel at the speed of light) towards an object and measure their round trip times to derive the corresponding ranges. In case of the discrete LiDAR, the time counting stops when the returned pulse energy (the waveform) exceeds a certain amplitude threshold. The output of the discrete LiDAR is a georeferenced point cloud (consisting of individual returns) with additional point attributes such as intensity and return number (e.g. first, second, ..., last). In case of the waveform LiDAR the whole waveform is recorded together with the recording time for each instantaneous amplitude of the waveform. The ranges of individual returns are then extracted using the signal processing techniques, such as Gaussian decomposition. The output of the waveform LiDAR is a

georeferenced point cloud (consisting of individual returns) with additional point attributes such as echo amplitude, echo width (EW) and echo number.

The ToF ranging has different properties when applied over a smooth (e.g. asphalt), rough surface (e.g. soil, gravel, etc.), or a porous surface (e.g. vegetation). For a perfectly smooth surface perpendicular to the laser beam direction, the waveform is a scaled replica of the transmitted pulse, i.e. a *unimodal waveform*. In case of soil, gravel, or an inclined but smooth terrain, the return waveform is also unimodal but broadened due to the rough surface or the slope. In case of vegetation, the returned waveform can be *multimodal* as a fraction of the pulse energy reflects from the canopy top, but also from canopy elements placed at longer ranges, inside the canopy. This penetration is due to the canopy gaps within the laser beam. For multimodal waveforms, the discrete- and waveform-LiDARs will detect several ranges, providing points at the top of the canopy (typically first return), within the canopy (intermediate or last returns) and from the terrain (last returns). The number of returns depends on the pulse length and the amplitude threshold value. One half of the pulse length is the range resolution and represent the smallest distance between two canopy elements that can be resolved by scanning. However, in case of very oblique laser beams, TLS of soil or gravel surfaces can lead to multiple returns and even to erroneous ranges. For example, an oblique laser beam can illuminate both the top of a soil clod (or a pebble) and terrain in the background. If the distance between these two object is larger than the half of the laser pulse, then they will lead to two separate returns. However, in the opposite case, scanning will provide an erroneous range measurement, which is known as *mixed pixel*. Such and other ranging artefacts should be excluded from data before the surface description.

The *phase-shift ranging* sensors do not transmit pulses, but several amplitude-modulated continuous waves (AM-CW) with different wavelengths. The fraction of the range is derived by comparing the phase of the transmitted and recorded wave at the smallest wavelength. The range ambiguity is then derived from the phase differences from the other wavelengths. Therefore, the longest wavelength used defines the maximum measurement range of the scanner (typically, < 200 m). The phase-shift scanner provides only a single range (no multiple returns). This is because a range of a phase-shift scanner corresponds to a single complex phasor, i.e. a vector associated with the phase angle and the intensity as the vector magnitude. This phasor is the superimposition of individual phasors corresponding to individual object elements that are illuminated by laser radiation and located at different ranges within the laser beam. TLS over soil, gravel and vegetation with this sensor causes erroneous ranges when the laser beam illuminates the edges of a pebble, soil clod, branch or leaf, etc. Therefore these scanners are designed to have a small beam divergence (leading to a small footprint size, i.e. high resolution scanning) to minimize the mentioned edge effects. The output of these scanners is a georeferenced point cloud with the intensity given as additional attribute per each point.

*Active triangulation ranging* sensors project a laser stripe on objects and capture its image with an additional imaging sensor (e.g. a CCD sensor). The range is derived by triangulation where the laser-stripe plane is intersected with the perspective projection rays of the line pixels. The relative orientation between the laser-strip plane and the imaging sensor centre of the imaging sensor is known in advance. As the imaging sensor comes typically with a fixed focus, commercial sensors based on the active triangulation ranging are limited to very short ranges (< 2 m). Another reason for having short range design is that the base and the principal distance of the system are fixed, and thus, the accuracy in the range direction is the square function of the range itself. In this

dissertation, two active triangulation scanners are used: (a) measurement arm and (b) a close-range triangulating scanner. *The measurement arm* is a fixed system that has a handheld head mounted on a mechanical arm with a fixed base. The head is actually an active triangulation ranging sensor, whereas the mechanical arm provides the exterior orientation. The scanning is performed by moving manually the head around the object. The measurement arm is a very precise instrument with a sub-mm accuracy and a sub-mm point sampling. The output of this scanner is a locally referenced point cloud with additional information about the pointing vector (the direction at which the head was pointing during the scanning). *The close-range triangulating scanner* sweeps with a laser stripe over an object and continuously captures images with a new stripe position. The sweeping is typically performed by rotating the stripe-plane by a deflection unit. This ensures that the relative orientation between each instantaneous laser-stripe plane and the imaging sensor is known in advance. The exterior orientation is then resolved as in TLS, using direct, indirect or integrated approaches. The accuracy and point sampling of the close-range triangulating scanner is typically at mm to sub-mm level. The output of this scanner is a georeferenced point cloud with intensity values in the red, green and blue channels.

**Table 1: An overview of the ranging techniques, sensors and their information used in this dissertation. The table also shows papers, scales and natural surfaces on which a particular technique was applied.**

Technique	Platform	Sensor	Radiometry	Aux. Info	Scales	Surfaces	Study
ToF, Waveform	Aeroplane (ALS)	Riegl LMS-Q680i LMS-Q1560	Waveform	Amp., EW Return Number	Landscape	Vegetation, Gravel	Paper IV Paper V Paper VI
ToF, Discrete	Drone/UAV (ULS)	Riegl VUX-1	Reflectance <sup>1</sup>	Pulse Deviation, Return Number	Patch	Gravel	Paper VI
Phase-Shift, Discrete	Geod.Tripod (TLS)	Zoller+Fröhlich IMAGER 5006i IMAGER 5010c	Intensity	-	Patch	Soil, Gravel	Paper II Paper III Paper VI
Active Triangulation	Measuring Arm/ Handheld	METRIS Model Maker D	-	Pointing Vector	Branch	Vegetation	Paper I
Active Triangulation	Triangulating scanner (OTS)	Minolta VIVID 9i	R, G, B	-	Sub-Patch	Soil	Paper II
Passive Triangulation	Handheld Images	Nikon D800	R, G, B	-	Patch	Gravel	Paper VI
Passive Triangulation	Drone/UAV Images	Sony $\alpha$	R, G, B	-	Patch	Soil	Paper III

<sup>1</sup>range corrected intensity

*Passive triangulation* is classical, close-range photogrammetry, also referred to as, structure-from-motion (SfM). This ranging technique was used in the dissertation for the comparison with the laser scanning results. The close-range photogrammetry uses multi-view stereo images of a natural surface as the input and provides a georeferenced point cloud and an orthophoto as the output. To this end, the images have to be oriented and homologous points have to be matched and triangulated. In this dissertation, the image orientation was done based on an automatic feature detection and the bundle block adjustment (BBA) implemented in a commercial software solution and in an in-house software solution. Furthermore, manual image measurements of GCPs and their object coordinates observed with the total station were included into BBA to fix the datum. The orientation is then imported into a commercial software package for image matching where a version of the semi-global matching algorithm was used to derive an automatically generated DSM. It is noted that the matching software does a pair-wise matching and triangulation, providing additionally a densely-matched point clouds. However, this point

cloud is usually very noisy and requires additional median based filtering. Therefore, the DSM filtered automatically by the software was used for the comparison.

## 2.2 Surface Description Approaches

Surface description is a broader term compared to a surface (biophysical) parameter and includes input data, modelling and a result. The latter can be, for example, a parameter, a function or a digital map (e.g. a grid structure) that is further used as input in environmental and physical models. Therefore, a surface (biophysical) parameter is just one possible result of a surface description.

As laser scanning provides geometric and radiometric data, surface descriptions are categorized here accordingly, i.e. in geometric and radiometric description approaches. The geometric descriptions consider only geometric information that can be treated in two ways during the modelling – stochastically and deterministically. Therefore, surface descriptions are categorised here in the following three categories: (a) geometric-stochastic descriptions, (b) geometric-deterministic descriptions and (c) geometric-radiometric descriptions. It is noted that the latter category also has the term “geometric” in its name. This is because radiometric observations are the function of the scanning (sensor-object) geometry and geolocation. Therefore, radiometric observations should be combined with geometric observations to provide an appropriate radiometric description of the surface. It is also noted that stochastic and deterministic approaches for the radiometric data are not separately analysed in this dissertation.

### 2.2.1 Geometric-Stochastic: Surface Roughness

The geometric-stochastic surface description considers only geometric information of the laser scanning data (3D points) and treats it stochastically. This means that each height, profile or an entire surface are considered as a realisation of a random experiment driven by an assumed stochastic model. The results of a geometric-stochastic description are the parameters of a stochastic process applied. In this dissertation, a geometric-stochastic description based on laser scanning data is applied for *Surface roughness* assessment. It is noted that geometric-stochastic descriptions are particularly studied in disciplines such as geostatistics and stochastic signal processing.

Surface roughness is a dynamic physical property that describes the complexity of the surface geometry. The indices that describe this surface complexity are referred to as *surface roughness indices*. In many physical processes, surface roughness figures as a variable that is typically understood as a complement to a general description of the surface topography. For example, directional backscattering pattern of a radar signal depends on both local slope and surface roughness (Ulaby et al. 1982). Then, the volume rate of a water flow in a river depends on the slope, lateral height profile and from surface (hydraulic) roughness (Manning 1891). In a roughness analysis, these general descriptions of topography, such as slope and other low-frequency terrain components are referred to as *trend*. The task of roughness analysis is then to describe the geometry of *the residual heights*, i.e. the heights calculated by subtracting the heights of a local trend surface from the original surface heights. Thus, the surface equation in roughness analysis is:

$$\text{Surface} = \text{Trend} + \text{Roughness} \quad (1)$$

Surface roughness is selected because of several reasons. First, it is hypothesized that novel high-resolution TLS data will allow describing fine surface details such as soil clods and gravel pebbles, which will then improve the surface roughness assessment. Then, in several environmental and

physical models, surface roughness is already described stochastically. For example, in the radar scattering problem, it is known that high-frequency (random) surface components (with a spatial wavelength smaller than the radar wavelength) cause incoherent scattering, (Woodhouse 2005, p.124-128). This random rough surface is usually treated as a single-scale, zero-mean stationary process with a Gaussian probability density function assigned to the surface heights (Tsang et al. 2000; Ulaby et al. 1982). Such a stochastic process is also known as a zero-mean Gaussian process and is completely described once the surface autocorrelation function is known (Ogilvy 1987; Ulaby et al. 1982). Another reason to consider surface roughness is the way that it has been measured. Roughness measurements were mainly acquired with destructive mechanical profiles (pin meters, wooden mesh boards or metal chains) or a non-destructive measurements, such as laser profiles or close-range photogrammetry (Álvarez-Mozos et al. 2009; Jester and Klik 2005; Mattia et al. 2003; Vidal Vázquez et al. 2010). In contrast, there are just a few studies, at the time, on the application of laser scanning for roughness measurement (Hollaus et al. 2011; Perez-Gutierrez et al. 2007).

The roughness parameters that are typically reported for the zero-mean Gaussian process are: (a) *the standard deviation of surface heights*, and *the correlation length*. The latter is given when a *exponential* or *Gaussian function* is used to parametrize an autocorrelation function empirically derived from the surface measurements, i.e. surface heights. The parametrisation can also be done, in the frequency domain, by analysing the power spectrum density, i.e. roughness spectrum, of the acquired surface heights. The roughness spectrum shows the variances distribution over a range of spatial frequencies, i.e. sinusoidal surface components. These variances can be linearly approximated when plotted in the logarithmic scale, whereas the slope of this linear trend is known as *spectral slope*. The latter roughness parameter is directly related to the *fractal dimension* of the surface. In this dissertation, surface roughness is analysed primarily using roughness spectra and spectral slope derived from the laser scanning height measurements.

The above roughness parameters are derived in this work for a predefined roughness plot. Such a plot is typically delineated beforehand in the field, taking care that it represents a patch of a natural surface with homogenous and distinctive characteristics, i.e. an elementary landform. Therefore, the roughness analysis in this work is focused on the description and NOT on the classification of elementary landforms. The classification of landforms is beyond the scope of this study.

### **2.2.2 Geometric-Deterministic: 3D Shoot Model**

The geometric-deterministic surface description considers only geometric information of the laser scanning data (3D points) and treats it deterministically. A geometric-deterministic description models (exactly or approximately) a point cloud using geometrical primitives and higher order surfaces (lines, planes, cylinders, splines etc.) to reconstruct the object. The result is a CAD (computer-aided design) model, or an ensemble of geometric primitives with resolved (or unresolved) topology. In this dissertation, a geometric-deterministic description is applied to derive a 3D CAD geometry of branches and foliage of a coniferous shoot. It is noted that 3D modelling is a task that is also studied within the visual computing discipline.

3D geometry models, as an ensemble of geometrical primitives, is a representation of real objects that, ideally, should be as close as possible to reality. A simplification of the reality with geometrical objects is used, for example, to parametrize 3D radiative transfer models such as

Librat and DART (Disney et al. 2010; Jean-Philippe Gastellu-Etchegorry et al. 2012). These models performs forward simulation of Earth observation data (i.e. predicts radiance, or even a complete LiDAR waveform) and different 3D models allows then to understand better the impact of particular object elements on the simulated and observed signal. For example, simulations with and without tree foliage in 3D models should explain leaf area index and its impact on the EO signal. Such analysis is also useful in resolving between the vegetation and background portions of a vegetation pixel value observed by an EO sensor.

3D geometrical modelling of vegetation with geometrical primitives and with laser scanning data has been in focus for many years. Thies et al. (2004) derived 3D stem models by fitting cylinders to TLS point cloud. The stems and branches are also approximated by fitting closed free-form curves to TLS points at different vertical slices (Pfeifer and Winterhalder 2004). Also, Bucksch and Lindenbergh (2008) introduced an skeletonization algorithm for a TLS point cloud of a tree to derive a graph that represents the stem-branch structure of the tree. Recent studies also focused on extraction of more comprehensive 3D stem-branch models from TLS data (Raumonen et al. 2013). However, there is still a lack of 3D information about shoot-needle structure, even though it is known that needle geometry affects the signal predictions based on radiative transfer models (Disney et al. 2006; Smolander and Stenberg 2003). Furthermore, some studies already used a generic conifer shoot model to account for the foliage in radiative transfer modelling (Côté et al. 2009; Disney et al. 2010). Therefore, the focus in this dissertation was to derive a 3D geometrical model of a coniferous shoot. To accomplish this task, in-door, micro-scale laser scanning is performed with the measurement arm instrument (Section 2.1). This scanner uses the active triangulation, and thus, is able to sample 3D points of sub-mm spacing and accuracy, which is necessary to model individual needles. Finally, it is noted that the focus here is only on geometr information, whereas the radiometric properties of the 3D shoot model are beyond the scope of this work.

### **2.2.3 Geometric-Radiometric: Canopy Transmittance**

The geometric-radiometric surface description considers both geometric and radiometric information of the laser scanning data. This means, 3D points with radiometric attributes such as echo width and amplitude, or observation directions and the associated full waveforms. The latter is a time-resolved signal proportional to the laser radiation incident to the aperture. A geometric-radiometric description models the recorded radiometric information to derive (bio-)physical parameters that are inherent to objects illuminated by the laser radiation, and thus, independent of sensor and scanning campaign parameters. Therefore, the result of a geometric-radiometric description is a well-defined (bio-)physical parameter such as reflectance and backscattering cross-section. It should be noted that these physical parameters have their directional properties, which means that both radiometric and geometric observations have to be considered to model them appropriately. In this dissertation, a geometric-radiometric description is applied on airborne waveform laser scanning data to derive a directional physical parameter referred to as canopy transmittance. It is noted that geometric-radiometric descriptions that provide biophysical parameters are particularly studied within the Earth observation discipline.

Canopy transmittance is a directional and spectral-specific physical parameter that shows how much of radiation is attenuated by passing through a vegetation canopy. For ALS data, this means that it refers to the used laser wavelength and the scanning direction of the laser beams.

The canopy transmittance is related to biophysical parameters such as leaf area index and the gap fraction (Armston et al. 2013; Bréda 2003). Therefore, the canopy transmittance is important canopy structural parameter for forestry and forest ecosystems (e.g., Maltamo et al. 2014; Musselman et al. 2013). Furthermore, canopy transmittance can help in resolving the vegetation and ground portions in space-borne waveform LiDAR signals recorded e.g. within IceSAT or the incoming GEDI missions.

Derivation of the gap fraction and leaf area index from ALS has been in focus for many years. The first methods are based on the discrete returns (echoes) where the ration of the vegetation and ground return was explored (Morsdorf et al. 2006; Solberg et al. 2009). Other methods focused more on the radiometric information such as raw intensity values and their corrections using the Beer-Lambert law (Hopkinson and Chasmer 2009; Lindberg et al. 2012). The newest methods explored more waveform information from small-footprint ALS data (Armston et al. 2013; Fieber et al. 2015). However, the above methods are either not physically rigorous (e.g. return-based), or require assumptions on vegetation physical properties (e.g. vegetation-ground reflectance and extinction coefficient). Therefore, the focus in this dissertation is on introducing a geometric-radiometric description of canopy gaps with a clearly defined physical parameter and a method that does not require knowledge about vegetation physical properties. To accomplish this task, a method for estimating canopy transmittance from the waveform ALS data is introduced.

## 2.3 Problem Statement and Specific Objectives

### 2.3.1 Surface Roughness

The roughness analysis is currently shifting from manual profile measurements to digital measurements such as digital elevation models (DEMs) interpolated from georeferenced point clouds. This means that basic processing steps are still missing or not standardized for roughness assessment with laser scanning data. For example, DEMs may contain measurement noise that can introduce bias in geometric-stochastic roughness parameters. In contrast, if the data are oversmoothed during interpolation of the DEM, some of the local surface features may be lost, which will again lead to biased parameters. Thus, there is a need to optimize the interpolation of DEMs for roughness assessment. Furthermore, there is a practical question on how to optimally measure a roughness plot (number of scans, scanning angle, etc.).

The following specific objectives for surface roughness study are set:

- to analyse a geometric-stochastic description of surface roughness at the patch scale with high-resolution laser scanning
- to develop a new method for interpolating stochastically appropriate DEM
- to compare different laser scanning techniques for roughness assessment

### 2.3.2 3D Shoot Model

The modelling of trees with geometric primitives fitted to laser scanning data is currently more focused on tree elements such as stems, branches and crown shape. Modelling individual needles on the basis of TLS data is, however, not possible because the contemporary TLS instruments have a footprint ( $>3$  mm) larger than the needle itself. In contrast, high-resolution active-triangulation laser scanning offers sub-mm point sampling and accuracy, which was not previously used for vegetation measurement. Therefore, more research on modelling of individual shoots at the single leaf- or needle-level is required.

The overall objective for the geometric-deterministic description is to develop a transferable, robust and objective method for 3D shoot model reconstructions from micro-scale (high-resolution) laser scanning data. The reconstructed 3D model should represent reality (a conifer shoot) as closely as possible. Furthermore, the conifer shoot should be modelled up to the position, orientation and length of its individual needles.

### 2.3.3 Canopy Transmittance

In contrast to surface roughness, canopy transmittance is a well-studied problem as it is closely related to key vegetation biophysical parameters such as the leaf area index and canopy gaps. Therefore, the overall objective here is to introduce a physically strict method for deriving the canopy transmittance from ALS waveform data. Furthermore, this method should not require knowledge about vegetation physical properties, which is the case in the current canopy gap models. Finally, the transmittance method should work on the laser beam level, but different aggregation strategies should be suggested, as well.

### 3 Overview of the Papers and their Contributions

Figure 3 groups the papers published within this dissertation within the three description approaches. The *geometric-stochastic description of surface roughness* is analysed in Paper II, Paper III and Paper VI. In Paper II, soil surface roughness is analysed with TLS and triangulating laser scanning data. This paper presents a method where the interpolation parameters are optimized to derive a DEM with stochastically unique properties. In Paper III, soil roughness is analysed with TLS and point clouds derived from UAV images. This paper focuses on the comparison of TLS- and UAV-derived roughness spectra. In Paper VI, gravel roughness is analysed with TLS, ALS, ULS data and a point cloud derived from handheld images. This study mainly concentrates on roughness spectra comparison and the optimisation of the TLS setup. The *geometric-deterministic description of a coniferous shoot* using micro-scale triangulating laser scanning data is presented in Paper I. The *geometric-radiometric description of canopy transmittance* from airborne waveform data is analysed in Paper IV and Paper V. Paper IV introduces a new physically-rigors model for deriving total canopy transmittance per single LiDAR beam or an aggregation cell. Paper V presents a method for simulating large-footprint space-borne waveforms, which is relevant for upscaling the canopy transmittance for space borne LiDAR observing geometry. Furthermore, Paper V presents an approach where the simulated space-borne waveforms are used together with the field measurements of the forest inventory to estimate the above ground biomass.

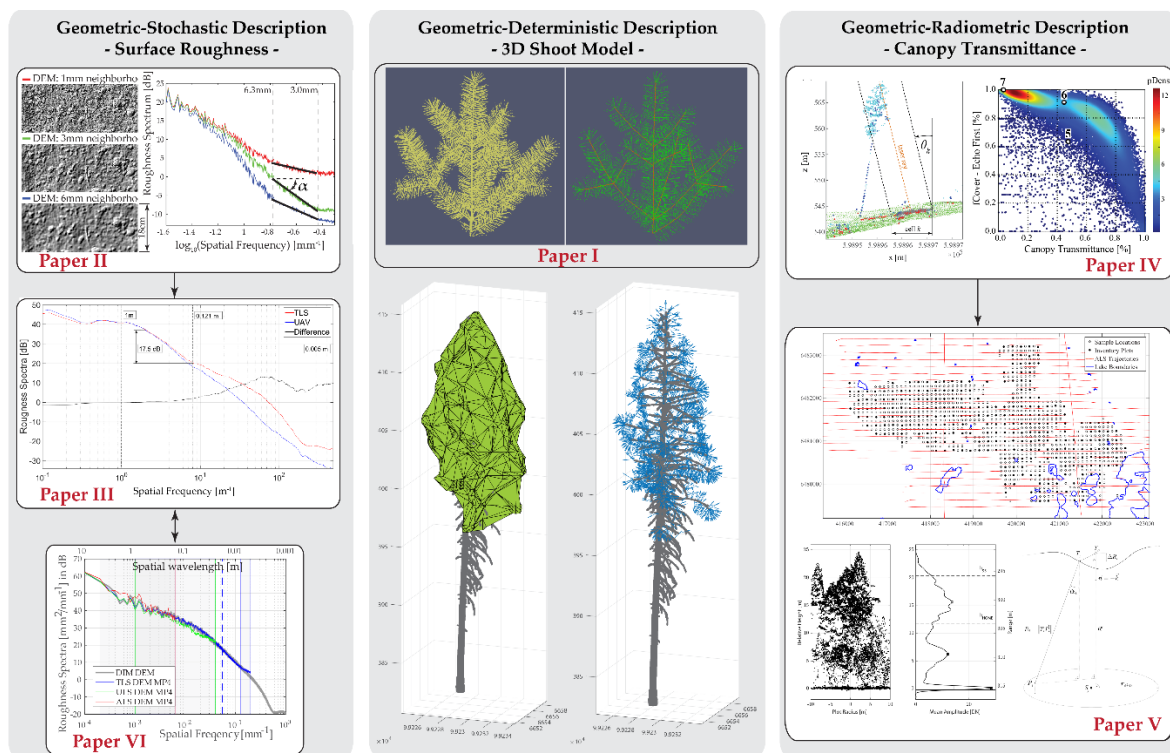


Figure 3: Graphical abstract of the published papers and the three description approaches.

Paper I has the following main contributions:

- a micro-resolution laser scanner is applied for the first time for 3D vegetation modelling,
- a new method for 3D model of a conifer shoot up to the single needle level is introduced

- a 3D shoot model on the basis of a real data is for the first time (to the author's best knowledge) derived.

Paper II has the following main contributions:

- a new method is suggested to interpolate gridded DEMs (from TLS point clouds) while preserving the surface's stochastic properties at high frequencies and additionally providing an estimate of the spatial resolution,
- scanning conditions on the TLS's incidence angle and number of scans are introduced for applying TLS in soil roughness assessment,
- the study compares TLS- and triangulating laser scanning- based roughness spectra and other roughness index values
- the cm-mm scale directional blurring of TLS DEMs along the laser beam direction is discussed for the first time (to the author's best knowledge) in this study.

Paper III has the following main contributions:

- the study analyses whether the roughness spectra derived from UAV images can replace the TLS-based roughness spectra for soil roughness assessment task,
- systematic residuals in the image-based DEM are observed, which was explained by weakly tied sub-blocks in the bundle block adjustment of this particular image set,
- the systematic errors caused deformation of the UAV roughness spectrum at low frequencies (wavelengths larger than about 3 m), which suggest that image orientation is important for roughness assessment,
- further experiments are suggested to specify the UAV image acquisition requirements for soil roughness,

Paper IV has the following main contributions:

- a new physically rigorous method is suggested to estimate the total canopy transmittance from small-footprint airborne waveform LiDAR data,
- the methodology for calculating the transmittance within a single laser beam and cell-wise calculation is suggested,
- the canopy transmittance method is compared with the traditional gap fraction method.

Paper V has the following main contributions:

- a waveform stacking method is suggested to up-scale the small-footprint airborne LiDAR waveforms to simulate large-footprint (space-borne) LiDAR waveforms,
- the waveform stacking method gives a basis for deriving the canopy transmittance for space-borne LiDAR data.

Paper VI has the following main contributions:

- the analysis compares for the first time TLS-, ULS- and ALS-based roughness spectra as well as a roughness spectra derived from handheld images
- requirements on TLS scanning setup are imposed to derive accurate roughness spectra,

- frequency bands are derived over which the above roughness spectra: (a) can be used interchangeably and (b) are affected by the interpolation method
- effects of interpolation methods on the roughness spectrum are analysed.

### 3.1 Paper I

**Title:** Modeling the tree branch structure at very high resolution

**Authors:** Milenković, M., Eysn, L., Hollaus, M., Karel, W. and Pfeifer, N.

**Published in:** SilviLaser 2012 - Conference Proceedings, Paper ID SL2012-099

**Licence:** This manuscript version is made available under the Creative Commons Attribution 4.0 (CC BY 4.0) license

## Modeling the tree branch structure at very high resolution

Milutin Milenković, Lothar Eysn, Markus Hollaus, Wilfried Karel & Norbert Pfeifer

Vienna University of Technology, Institute of Photogrammetry and Remote Sensing,  
Gusshausstraße 27-29, 1040 Vienna, Austria; mm@ipf.tuwien.ac.at

Paper Number: SL2012-099

### 1. Introduction

Knowledge on the structure of vegetation is required in a number of applications. Depending on the scale at which the modeled processes occur or at which the parameters of interest are required, this can either be dominated by larger structures, e.g. a stand or plot, by single tree positions, or at finer details like the individual branching structure. At even finer spatial resolution individual leaves or needles can be described. Modeling as such can occur spatially explicit or as a distribution. In the first case of 3D modeling the available modeling methods use polygons or polyhedral surfaces, freeform curves and surfaces (Farin, 2002), or parametric primitives (Mäntylä, 1998) like, e.g., cylinders or, in the case of planar shapes, ellipses. These geometric elements are assembled in order to represent the geometric structure. Additional information, e.g. optical properties, can be attached to the individual elements. In the case of modeling by distributions, parameters of interest, e.g., the orientation of leaves, are modeled by describing their distribution, e.g. percentiles or average value and variance. Both types of models can – in principle – either be derived from measurements or constructed by assumptions on the structure of the modeled elements.

Radiative transfer modeling using ray tracing allows generating (simulating) synthetic images from a modeled 3D scene by forward modeling (Morsdorf et al, 2012). The scattering behavior within the canopy requires a model of the individual needles or leaves for producing faithful simulation results (e.g. Disney et al., 2010, Disney et al., 2006. Models for extracting the branch structure only from measurements were described, e.g., by Thies et al. (2004) and Bucksch and Lindenbergh (2008). Using only the available measurements of a terrestrial laser scanner (TLS) placed inside the forest and an orchard, respectively, these approaches are not able to model individual needles or leaves. One way to describe for example a forest stand including individual needles or leaves is to use software packages of computer graphics to generate artificially the foliage orientation and variability within the individual tree crowns. For this generation of virtual forest stands several assumptions and generalizations are required. Rutzinger et al. (2010), e.g., extract tree location, height, stem diameter and crown diameter from mobile laser scanning data and “grow” tree models (Weber and Penn, 1995) reaching the measured parameters. Côté et al. (2009) used for the reconstruction of 3D tree architecture from terrestrial LiDAR scans a generic conifer shoot model based on the model description of Smolander and Stenberg (2003). However, there is still a lack of detailed information concerning actual shoot structure as stated in Côté et al. (2009).

To overcome the limitation of actual shoot structure information, we present an approach for reconstructing exact geometric information on individual twigs, needles, and leaves from measurements. This reconstruction can be performed with sub-millimeter accuracy using a measuring arm in an indoor setting. At the current stage, the approach requires, next to the measurement itself, manual interaction. Individual needles and leaves as well as twig fragments are modeled in terms of their position, length and direction. Basics of the applied 3D modeling approaches were developed within the NEWFOR (Hollaus, 2012) project for a coarser scale (i.e. tree structure) and are adapted and improved for branch modeling within the 3D-VegetationLab project.

In Sec. 2 the measurement device and the sample branches, one coniferous and one deciduous,

are described. In Sec. 3 the methods are explained and the results are discussed in Sec. 4.

## 2. Study objects and data

### 2.1 Study objects

One coniferous and one deciduous branch are selected as objects for the modeling. Both branches belong to the end part of the corresponding tree limbs, and carry a typical structure of their species, which makes them – in principle – also suitable for cloning all over the tree. The objects also have similar structures in the sense that both branches are composed of one “primary” and several “secondary” branches.

The coniferous branch (Fig. 1) is taken from a fir tree (*Abies alba*) and is approximately 80 cm long and completely covered with needles. The “secondary” branches spread about 40 cm sideways from the “primary” one, mainly in one plane. They contain many shoots that are attached to them. While not of importance for the reconstruction method, the oldest part of the branch was estimated to an age of 5 years. The shoot location within a secondary branch was used to determine the age of the shoot, with the end shoots considered as first year shoots, whereas others decrease in the age while moving from the branch end towards the branch joint.

The deciduous branch (Fig. 2) comes from a European beech tree (*Fagus sylvatica*). Comparing to the coniferous branch, it is slightly bigger in size (c.a. 1 m in length), but has a similar planar spreading of the secondary branches. Twigs with attached leaves are sparsely distributed over the secondary branches making the object structure more “open” and less complex. Scanning of the branch indoors required a fast transportation of the cut branch to the measurement device because of the fast drying out process.

### 2.2 Measuring device

A measuring arm (METRIS MCA, 3600 M7) is used to acquire exact geometric information. The instrument used has a triangulation laser scanner mounted on its head, and therefore allows contactless object scanning. A laser stripe is constantly emitted and intersects with an object’s surface if pointed at it. This illuminated cross section is mapped by a camera and furthermore 3D coordinates of the illuminated area are derived. If the laser stripe is moved over the object, a so called “scanning strip” is recorded. Larger areas are covered by scanning several strips. The METRIS measuring arm provides automatically oriented scans of the object. The mounted scanner provides a point cloud that has different along- and across-strip resolution. The across-strip resolution depends upon both the laser strip width and the resolution of the camera, and goes up to 0.05 mm. The along-strip resolution, on the other hand, is usually about 0.5 mm, which is mainly driven by the moving speed of the arm’s scanning head. A slow movement of the head can significantly increase this value and provide a large number of acquired points. Due to its construction, the instrument has a limited operational range that allows scanning of objects up to 1.5 m in size. Besides, there is an operational limit which dictates the size of the acquired scan, i.e. the number of points that can be processed by the system.

### 2.3 Acquisition method

The arm’s resolution and operational range, on the one hand, and the objects’ structure and size, on the other hand, appear as the most prominent factors during the scanning. Those specific characteristics of the instrument and objects are the reason for introducing separate acquisition strategies for coniferous and deciduous branches.

#### 2.3.1 Coniferous branch

The complex structure of the conifer branch and its large extend (comparing to the operational range) affect both object stability and accessibility during the scanning procedure. Therefore, a two-stepped strategy is introduced to acquire a representative point cloud of the model. First, the overall structure is in the focus, then, each “secondary” branch is measured. In the first step, the main branch and large secondary branches are scanned using a number of scan strips and

ensuring overlaps between the scans. Then, the secondary branches are separated physically (i.e. cut) from the object and measured separately. Therefore, co-registration of all the scanned parts is required in the second step (Fig. 1).

The co-registration is done for each secondary branch independently, transforming its coordinate systems to the main branch's coordinate system. This procedure is done using the spherical heads of pins as targets that are present in both scans. Tree pins per each secondary branch are introduced in zones close to branch joints i.e. in the overlapping scan areas (Fig. 1). Based on the points that represent those targets, different spheres are fitted and then their centers are used for the co-registration. This acquisition approach also allows to model each secondary branch independently and latter to build the final model by merging all the models into one structure.

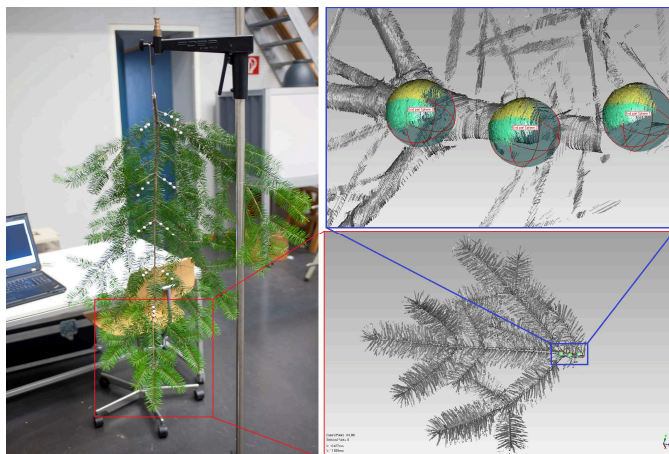


Figure 1: Left: conifer branch prepared for the measurement; Bottom right: detail showing the point cloud of a scanned (“secondary”) part; Top right: detail showing the spheres for co-registration.

The point cloud of the coniferous branch (Fig. 2, right) has over 40 million points. The branches are covered from both sides. As visible in Fig. 1 (bottom right), the first and second year shoot at the end of the tree are not perfectly symmetrical. This holds for the directions and lengths as well as for the branching structure.

### 2.3.2 Deciduous branch

The deciduous branch is scanned in one step because its sparse structure allows an easy access to the entire object. However, the area of the leaves and the high resolution of the scanner produce a large amount of data that exceeds the operational limit of the arm. Therefore, several smaller scans (i.e. files) are collected to cover the whole object. Since the object and scanner coordinate system were fixed during the scanning, there was no need for the final co-registration of these scans. The final point cloud of the deciduous branch is shown in Fig. 2 (left). It contains almost 50 Million points. The scans were only acquired from the leaf top and bottom side.

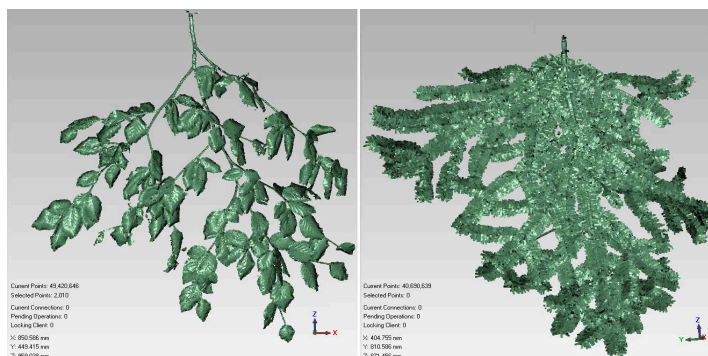


Figure 2: Left: Point cloud of the deciduous branch; Right: Point cloud of the coniferous branch

### 3. Methods

Needles and leaves are the elementary unit in modeling the coniferous and deciduous branch, respectively. Since it is not possible to represent them in a geometrically similar way, two separate methods are proposed to model those objects. Both methods start with a common task where the corresponding branch structures are modeled, and then, during the modeling of their elementary unit, they split into two independent procedures. Following this logic, the Sec. 3.1 will first discuss the extraction of the branch skeleton, and in Sec. 3.2 and Sec. 3.3 the proposed modeling methods are described.

#### 3.1 Modeling branch structure

The branch structures of the two objects are very similar, i.e. both have branch joints and cylindrical wooden parts that connect them. Thus, topologically correct 3D polylines are used as a model for both the coniferous and deciduous branch structure. Those polylines are digitized (manually) from the corresponding point clouds.

The open structure of the deciduous branch allows a fast digitization without interruptions of the entire object structure in one coordinate system, i.e. the object coordinate system (OCS). This included digitization of the leaf stalks.

The digitization of the coniferous branch structure is not so straightforward. The presence of needles disturbs the digitization process making the selection of stem points much more time consuming comparing to the deciduous branch. Therefore, an automatic procedure for point reduction is implemented before the digitization. The point cloud reduction is based on the voxel model derived from the scanned part and an estimation of a local voxel density. A property of the original point density is, that it is strongly influenced by the instrument's scanning pattern.

Voxelizing the data with an appropriate voxel size, the native structure of the object is emphasized rather than the scanning properties of the instrument. A voxel is considered as foreground (i.e. filled), if it contains at least one point from the original point cloud. The voxel density is the percentage of filled voxels in the 33-neighborhood of the center voxel (sphere of radius 2 in voxel space). An empirically driven thresholding on the local voxel density is done to reduce the starting point cloud. The used voxel size is 1 mm, which is close to the width of an average needle of the conifer branch. After the reduction procedure most of the needle points are removed from the starting data set, and the remaining points (mainly points from the stem) are used for digitizing the skeleton of the scanned part (Fig. 3). Since the co-registration of all the scanned parts is already done, the resulting 3D polyline structure is in a coordinate system of the conifer branch, i.e. in the OCS.

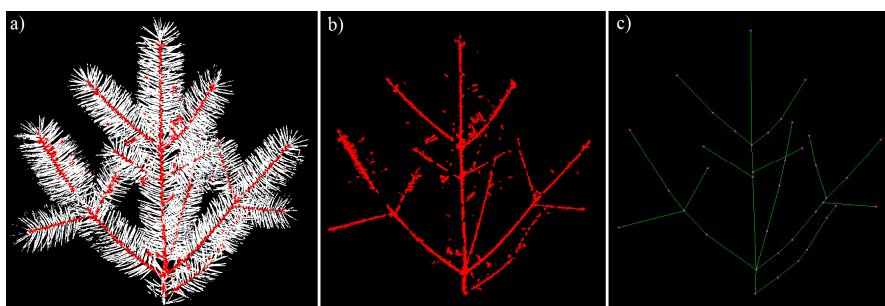


Figure 3: a) The classified original point cloud, based the thresholding the local voxel density; b) the reduced point cloud; c) the skeleton of the scanned part (right)

#### 3.2 Modeling the deciduous branch

For modeling the deciduous branch it is assumed, that the wooden structure is available as 3D polyline. Thus, only the leaves need to be modeled. For each leaf, a local point cloud is extracted. This is based on a bounding box which is extracted per leaf. Based on those local

point clouds, for each leaf an ellipse is estimated and used as a model for that leaf. Before estimating the ellipse, the regression plane is fitted through the leaf point cloud (Fig. 4, left). This provides the orientation of the leaf plane.

Next, the leaf point cloud is orthogonally projected to the regression plane and boundary leaf points are extracted from this data set. The ellipse parameters (center point, major and minor radius, and axis orientation) are estimated by fitting the ellipse through the leaf boundary points (see Figure 4, right). These parameters are transformed into a description suitable for including it in the model coordinate system (MCS): the normal vector of the regression plane, the ellipse center point, the end point of the longer radius of the ellipse, and the minor radius.

To establish a correct topology in the final model, the estimated ellipse is translated to the closest end point of the branch skeleton. In this way the native orientation of the leaf (the regression plane) is preserved. The translation parameters are resolved from the equality condition of the end point of the longer radius of the ellipse (tip of the leaf) in MCS and the closest end point of the branch skeleton in OCS.

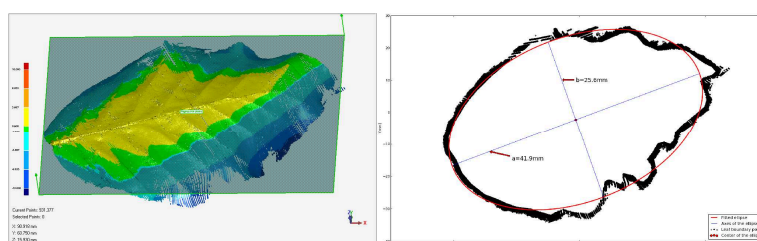


Figure 4: Left: The leaf point cloud with the regression plane; Right: the fitted ellipse displayed over the leaf boundary points

### 3.3 Modeling the coniferous branch

To handle the large data set, the modeling of all the scanned parts (the primary and the secondary branches) is performed independently and then, in the subsequent step, their models are combined into the final branch model. In the following a method for modeling of a shoot is presented. This method can either be applied to the entire branch, or the shoot can be cloned to populate the entire skeleton with the needles of the shoot model.

Using cloning is therefore a two step approach: (1) creating the shoot model, and (2) cloning the shoot model over the branch structure. A detailed workflow that includes also the skeleton modeling and all intermediate layers is illustrated in Figure 5. Since the proposed strategy allows an independent modeling of the scanned parts, only one is selected here to demonstrate the potential of the proposed method. The end part of the branch (see Figure 1) is taken because it has the most complex structure among other parts. Using a shoot model multiple times, enhances the efficiency of the modeling procedure. However, a typical data set needs to be selected when creating only one shoot model. This 3D model is assumed to be representative for all the shoots within the branch and used later, in the cloning step.

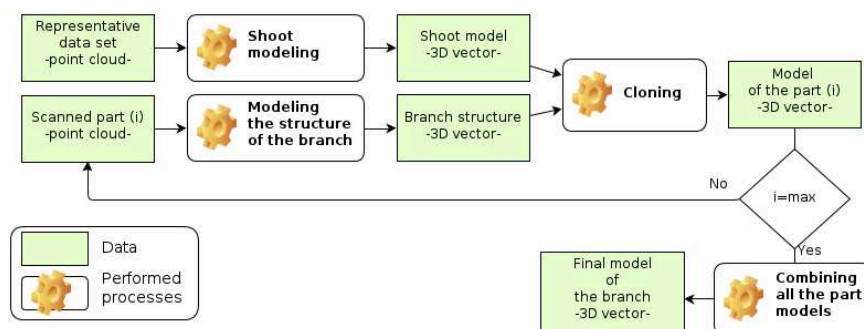


Figure 5: The workflow for modeling the branch

### 3.3.1 Modeling the shoot

A point cloud of a first year shoot (Fig. 6a) is selected as a representative data set for the shoot modeling by manually digitizing. Each needle is represented by a 3D line, with a starting and ending point, while the shoot's stem is represented by 3D polyline. Since the starting points of the needle lines are also the nodes of the stem poly line, the model is also topologically correct (Fig. 6b). The local coordinate system of the shoot model - the model coordinate system (MCS) - is defined with two reference points and one plane. The starting and ending point of the wooden part are selected as the reference points, whereas the regression plane fitted through the needle end points (Fig. 6c) is taken as the reference plane.

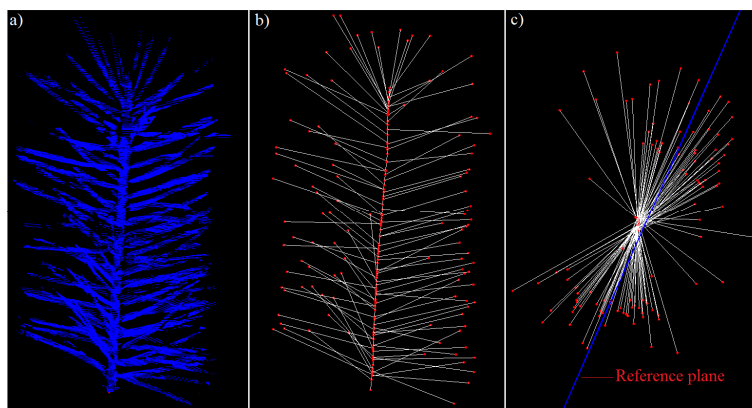


Figure 6: a) Point cloud of the representative shoot; b) the shoot model; c) the shoot model from the top view with the reference plane.

### 3.3.2 Cloning the shoot model

To build the conifer branch model by cloning, the shoot model is cloned over the branch skeleton. For each segment of the skeleton's polylines an appropriate part of the shoot model is firstly extracted and then cloned on this location. For example, segments that represent an end part of the skeleton are cloned with the whole shoot model, whereas middle segments are cloned only with a lower part of the shoot model. In case where the length of the skeleton segment exceeds the length of the shoot model, the lower part of the shoot model is used to bridge the remaining part of the segment.

The cloning procedure is performed by transforming the shoot model from MCS to OCS. Since the MCS is defined by the two points and one plane, the starting and ending point of the skeleton segment are used as the reference points, while a local plane is taken to resolve the orientation of the shoot model. The local plane is estimated for each skeleton segment independently, based on the local needle points filtered out during the point reduction procedure (see Sec. 3.1).

## 4. Results and discussion

In this Section the results of the cloning process are presented and discussed. The results are based on the shoot model shown in Fig. 6b, and the branch skeleton shown in Fig. 3c. The application of the above described modeling and cloning methods lead to the branch model shown in Fig. 7. The point cloud and the final branch model show a perfect correspondence for the location of the manually modeled shoot model (marked red in Fig. 7), exhibiting the same (ir)regularity of the needles especially at the end and with respect to their orientation out of the plane. The lower part of the shoot model shows a homogeneous density of needles. Therefore, this 1<sup>st</sup> year shoot could be cloned all over the manually extracted branch skeleton. At joints, where multiple sub branches connect, the 3D model, in some cases, exhibits more needles than the point cloud data suggests (Fig. 7).

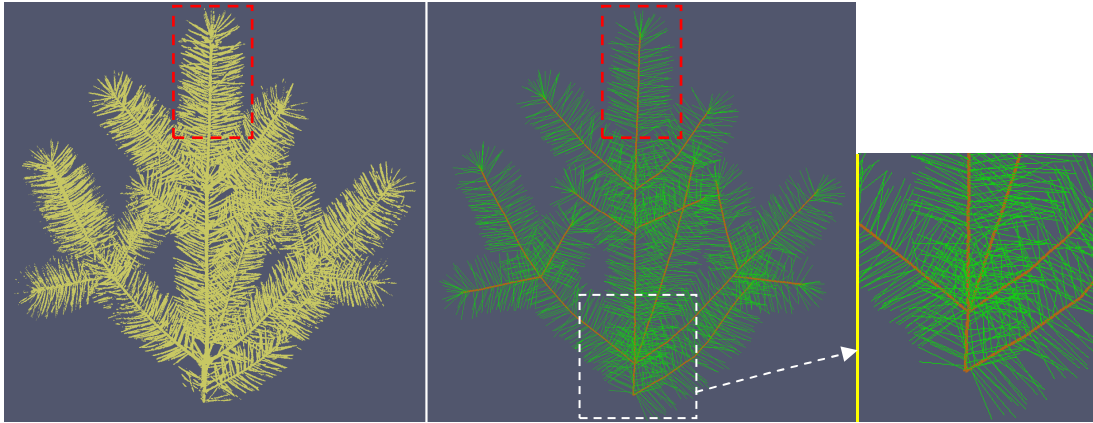


Figure 7: Point cloud of a coniferous twig versus its extracted 3D model. The red boxes show the shoot which was manually modeled and used for cloning; Left: Pointcloud; Middle: 3D model with classification into needles and branch structure; Right: Erroneous clumping of needles at joints

Considering the entire method of modeling, a number of steps include simplifications and cause differences between the geometric model and the acquired data. However, the entire method is data driven and allows modeling of the branch structure for each individual needle and leaf as well as the branches in between. A slight curvature of the needles was visually found in the data set but was neglected during modeling. The chosen model for a needle is the straight connection between the start and the end point of the needle. This rather simple model could be enhanced by using the average thickness of the needle for fitting an ellipsoid of revolution, which is favorable if the models are used i.e. for ray tracing analyzes where volumetric objects are preferred. However, also the orientation of the branch is available, which allows even more complex needle models to be applied, too.

Because the branch skeleton and the needle axis are digitized manually based on the point cloud, the location of the digitized elements is on the outer surface of the corresponding objects. If necessary, this error could be simply corrected by estimating or measuring the diameter of the corresponding object and translating the axis by half of the diameter. While a fitting approach would estimate the axis directly, the irregular point distribution, especially, in the case of a coniferous branch, poses an additional challenge to obtain a better geometric position in this way.

Concerning cloning, no 2<sup>nd</sup> year, 3<sup>rd</sup> year or even older shoots were used for this model. In general, the 1<sup>st</sup> year shoots have more needles than the older shoots and therefore an overestimation of the number of needles in the current cloned model is assumed. 2<sup>nd</sup> or 3<sup>rd</sup> year shoots could be simulated by reducing the number of needles before inserting the clone into the branch structure. Further investigations in this direction need to be performed.

Concerning the leaf model, the approximation of the leaf as an ellipse applies well to the beech leaves used in this study. However, the main consideration is a model with a small number of parameters, e.g. 5 in the case of an ellipse or 6 for a triangle. Fitting elements like an ellipse overcomes problems with gaps or inhomogeneous point densities in the acquired datasets. Alternative approaches include using the alpha-shape for the outline detection and the Douglas-Peucker algorithm for simplification in order to get a polygonal outline with a small number of points. Generally, the leaves are assumed to be flat which does not account for seasonality, although leaf curvature is visible in Fig. 4 (left). Again, ray tracing advocated for simple models.

## 5. Conclusion

Methods to model individual twigs, needles, and leaves, based on point clouds acquired with a measuring arm, at a high level of detail are presented. The model for coniferous branches

consists of 3D polylines with an additional classification, whether a line element represents a needle or belongs to the branch. Each line element can be transformed to a volumetric description by using their respective thickness value. The chosen model for representing a single leaf is an ellipse which acts as a good approximation for the complex leave structure. This study showed that the presented approach leads to promising results, which represent the real 3D branch structure based on measurements of the object. These detailed coniferous and deciduous 3D branch models can be used to build up larger twigs and branches by using cloning approaches. In this way virtual tree models can be enhanced or created that are used i.e. as input for radiative transfer and process modeling. While a faithful reconstruction is possible with the presented approach, measures of quality need to be derived before these results can be used in further applications. Likewise, for larger scenes to be modeled, the degree of automation needs to be increased.

### Acknowledgements

This study is partly financed by the ESA funded 3D-VegetationLab project and the project NEWFOR financed by the European Territorial Cooperation “Alpine Space”.

### References

- Bucksch, A., Lindenbergh, R. 2008. Campino – a skeletonization method for point cloud processing. *ISPRS Journal of Photogrammetry and Remote Sensing* 63(1), 115-127.
- Côté, J.-F., Widlowski, J.-L., Fournier, R. A., and Verstraete, M. M. 2009. The structural and radiative consistency of three-dimensional tree reconstructions from terrestrial lidar. *Remote Sensing of Environment*, 113(5), 1067-1081. Elsevier Inc. doi:10.1016/j.rse.2009.01.017
- Disney, M., Lewis, P., and Saich, P. 2006. 3D modelling of forest canopy structure for remote sensing simulations in the optical and microwave domains. *Remote Sensing of Environment* 100(1).
- Disney, M., Kalogirou, V., Lewis, P., Prieto-Blanco, A., Hancock, S., Pfeifer, M. 2010. Simulating the impact of discrete-return lidar system and survey characteristics over young conifer and broadleaf forests. *Remote Sensing of Environment* 114 (7), 1546-1560.
- Farin, G. 2002. *Curves and surfaces in CAGD*. 5<sup>th</sup> ed. Academic Press.
- Hollaus, M., Mücke, W., Eysn, L. 2012. Forest Structure And Stem Volume Assessment Based On Airborne Laser Scanning. *AMBIÊNCIA* (ISSN 2175-9405), accepted.
- Mäntlyä, M. 1998. *An introduction to solid modeling*. Computer Science Press.
- Morsdorf F. and 9 co-authors 2012. 3D-Vegetation Laboratory: A scientific support tool for accuracy assessment and prototyping of EO data and products. *Proceedings of ForestSat 2012*.
- Rutzinger, M., Pratihast, A.K., Oude Elberink, S., Vosselman, G., 2010. Detection and modelling of 3d trees from mobile laser scanning data. *Int. Archives of Photogrammetry and Remote Sensing*, Vol. XXXVIII/5, Newcastle upon Tyne. 520-525.
- Smolander, S., and Stenberg, P. 2003. A method to account for shoot scale clumping in coniferous canopy reflectance models. *Remote Sensing of Environment*, 88, 363-373. doi:10.1016/j.rse.2003.06.003
- Thies, M., Pfeifer, N., Winterhalder, D., and Gorte B.G.H. 2004. Three-dimensional reconstruction of stems for assessment of taper, sweep and lean based on laser scanning of standing trees. *Scandinavian Journal of Forest Research* 19 (6), 571-581.
- Weber, J, and Penn, J. 1995. Creation and rendering of realistic trees. *ACM International Conference on Computer Graphics and Interactive Techniques*, New York, United States, pp. 119-128.

## 3.2 Paper II

**Title:** Applying Terrestrial Laser Scanning for Soil Surface Roughness Assessment

**Authors:** Milenković, M., Pfeifer, N. and Glira, P.

**Published in:** Remote Sensing; 2015, Vol.7(2), pp. 2007-2045; doi:10.3390/rs70202007

**Licence:** This manuscript version is made available under the Creative Commons Attribution 4.0 (CC BY 4.0) license

Article

## Applying Terrestrial Laser Scanning for Soil Surface Roughness Assessment

Milutin Milenković \*, Norbert Pfeifer and Philipp Glira

Department of Geodesy and Geoinformation (GEO), Vienna University of Technology, Gußhausstraße 27-29, Vienna 1040, Austria; E-Mails: Norbert.Pfeifer@geo.tuwien.ac.at (N.P.); Philipp.Glira@geo.tuwien.ac.at (P.G.)

\* Author to whom correspondence should be addressed;

E-Mail: Milutin.Milenkovic@geo.tuwien.ac.at; Tel.: +43-1-58801-12254;

Fax: +43-1-58801-12299.

Academic Editors: Nicolas Baghdadi and Prasad S. Thenkabail

Received: 27 August 2014 / Accepted: 26 January 2015 / Published: 11 February 2015

---

**Abstract:** Terrestrial laser scanning can provide high-resolution, two-dimensional sampling of soil surface roughness. While previous studies demonstrated the usefulness of these roughness measurements in geophysical applications, questions about the number of required scans and their resolution were not investigated thoroughly. Here, we suggest a method to generate digital elevation models, while preserving the surface's stochastic properties at high frequencies and additionally providing an estimate of their spatial resolution. We also study the impact of the number and positions of scans on roughness indices' estimates. An experiment over a smooth and isotropic soil plot accompanies the analysis, where scanning results are compared to results from active triangulation. The roughness measurement conditions for ideal sampling are revisited and updated for diffraction-limited sampling valid for close-range laser scanning over smooth and isotropic soil roughness. Our results show that terrestrial laser scanning can be readily used for roughness assessment on scales larger than 5 cm, while for smaller scales, special processing is required to mitigate the effect of the laser beam footprint. Interestingly, classical roughness parametrization (correlation length, root mean square height (RMS<sub>h</sub>)) was not sensitive to these effects. Furthermore, comparing the classical roughness parametrization between one- and four-scan setups shows that the one-scan data can replace the four-scan setup with a relative loss of accuracy below 1% for ranges up to 3 m and incidence angles no larger than 50°, while two opposite scans can replace it over the whole plot. The incidence angle limit

for the spectral slope is even stronger and is  $40^\circ$ . These findings are valid for scanning over smooth and isotropic soil roughness.

**Keywords:** terrestrial laser scanning; triangulating scanner; surface roughness; spatial resolution; autocorrelation; roughness spectrum; correlation length; root mean square height; spectral slope

---

## 1. Introduction

Terrestrial laser scanners (TLSs) are designed to capture precise and detailed geometric information about natural and artificial objects. These instruments utilize the light detection and ranging (LiDAR) technique to collect point clouds with spatial resolution ranging from several millimeters up to several centimeters, depending on the object distance from the scanner [1]. Besides the geometry information (range, horizontal and vertical angles), some TLSs are able to register backscattered laser intensity, which then can be used to deduce the radiometric properties of the scanned objects [2].

Thanks to the above characteristics, terrestrial laser scanning has been successfully applied to many environmental applications, like forestry, hydrology and geomorphology. For example, tree stems and heights, canopy openness, 3D tree structure, as well as its change detection are just some of the forest-mapping aspects that have been addressed by the TLS data [3–6]. In hydrology and geomorphology, the TLS data have been used, e.g., to characterize the surface of gravel-bed river banks [7–9] or even submerged gravel beds [10], then to quantify depositional and erosional processes in dynamic and complex fluvial systems [11,12] or to classify complex morphological settings, as well as to monitor the landslide displacement [13,14]. Compared to these studies, the application of the TLS data for surface roughness assessment is, however, more challenging, since the surface features that should be described appear already at the millimeter scale, which is about the resolution limit of the contemporary TLSs [1]. Thus, special care should be taken during TLS data acquisition and processing to successfully describe these fine-scale roughness elements.

Surface roughness is a physical property of natural surfaces and also a parameter in many geophysical models. Since each physical process interacts with the specific group of surface features and under the specific range of scales, there is a high diversity in understanding, characterizing and even in naming the surface roughness among the corresponding disciplines. Some of the commonly-used terms are: hydraulic roughness, soil roughness, surface microtopography, snow surface roughness, aerodynamic roughness, *etc.* [15–20]. Soil roughness, for example, affects infiltration and runoff during a rain event, controls wind erosion and fluid flow and also influences the backscattered energy of radar signals [21,22]. Local surface features, like tillage structure, soil aggregates and particles, are considered to be directly related to the soil roughness, and in the corresponding roughness studies, they are typically described through their regional stochastic properties [23]. Hollaus *et al.* [24] distinguished between two different types of roughness, the surface and the terrain roughness, where the latter one describes objects that are 20 cm or more above the surface. Most of the soil roughness studies are concentrated exclusively on surface roughness, where it is additionally distinguished between a so-called “oriented” and a random

roughness geometry [16,18,23]. In this paper, assessment of the surface roughness associated with a bare soil plot with a random (isotropic) geometry will be analyzed.

There are several methods for soil roughness assessments that involve: (1) different soil height sampling techniques; and (2) different data analysis strategies. Traditional roughness sampling techniques are pin and mesh-board profilers, which collect individual soil roughness profiles with a length ranging from 0.5 m to 4 m and a regular sampling distance ranging from 5 mm to 10 mm along the profile direction [25,26]. A non-destructive alternative for the above roughness measurements are laser profilers. An example of this category is a laser profiler constructed by CESBIO (The Center for the Study of the Biosphere from Space) and ESA (European Space Agency), which is able to sample heights regularly at every 5 mm and collect up to 25 m-long profiles [27]. On the other hand, there is a number of studies where digital images and the stereo-photogrammetric techniques are applied to provide a two-dimensional sampling of soil heights (e.g., [18,28,29]). These data are used to generate regularly-structured digital elevation models (DEMs), which then serve as a base for the roughness analysis. The recent studies of Marzan *et al.* [16] and Bretar *et al.* [30] showed, for example, that DEMs with a millimeter grid size can be readily reconstructed with stereo-photogrammetry for plots of 6 m<sup>2</sup> to 12 m<sup>2</sup>. Terrestrial laser scanning is another technique capable of providing precise two-dimensional sampling of soil heights at a similar scale [20,31,32]. In the TLS studies of Barneveld *et al.* [33], as well as Nield *et al.* [34], the soil surface was analyzed even over a larger area (up to 120 m<sup>2</sup> and 144 m<sup>2</sup>, respectively), but this was at the cost of the DEM's resolution, i.e. the DEM's grid size was much coarser there (1 cm). On the other hand, in the study of Haubrock *et al.* [35], a 1 mm DEM of micro-erosion plots over ~1 m<sup>2</sup> was generated from data collected by an optical triangulating laser scanner. While all of the mentioned TLS studies apply multiple scanning to mitigate occlusions and improve the spatial resolution of the TLS data, the number of required scans and the resolution that will ensure a certain accuracy level of a roughness index were not investigated.

The sampled soil heights are used to analyze the stochastic properties of soil roughness. This can be done either: (1) in the spatial domain, e.g., by calculating the autocorrelation function [18,36] or variogram [16,17]; or (2) in the frequency domain, *i.e.*, using the roughness spectrum, which is the power spectrum of the sampled soil heights [22,37]. The latter is especially favorable for large datasets, but this approach also involves the discrete Fourier transform (DFT) for which an additional data aggregation into a regularly-structured DEM should be performed. Since the TLS sampling is irregular in the Euclidean space, the original TLS data should be first interpolated into a DEM and then analyzed by the DFT. This interpolation is usually accompanied with smoothing, which is most severe at high surface frequencies, where the most important roughness content is placed. Thus, optimally, the resulting DEM should preserve the stochastic properties of the original surface, as well as the spatial resolution of the original data. However, in roughness studies, the resolution of the used DEMs is usually determined only based on the point density or sometimes even arbitrarily and then reported by the DEM's grid size. This, however, cannot be applied on close-range TLS data, where the sampling is diffraction limited, and as shown by Lichti and Jamtsho [1], the resolution is a function of both the sampling interval and the laser beam footprint. Thus, such inappropriately-generated DEMs can lead to an inaccurate assessment of soil roughness. Besides, there are several theoretical studies that already showed that

some roughness indices, like the correlation length and the root mean square height, are sensitive to data resolution [38–40].

This paper presents the findings of an experiment where a TLS was applied to measure soil surface roughness on a plot with an isotropic, random geometry. Since the stochastic properties of bare isotropic soil surfaces were intensively studied in the past ([23,25,27,36,41], *etc.*), the focus of this paper is rather on the application of the terrestrial laser scanning for the assessment of soil surface roughness. Particularly, the paper suggests a method for generating a DEM that ensures that the surface's stochastic properties are preserved at high frequencies and provides additionally an estimate of the DEM's spatial resolution. Then, it is studied how the number and positions of scans, as well as the DEM resolution affects spatial correlation, the roughness spectrum and four selected roughness indices (correlation length, root mean square height (RMS<sub>h</sub>), power coefficient and spectral slope). Additionally, a small sub-plot is surveyed with an optical triangulating scanner (OTS), and then, the corresponding TLS and OTS roughness estimates are compared over this area.

The paper is organized as follows: Section 2 explains how the roughness plot was prepared and surveyed and how the laser scanning data were processed. Section 3 starts with presenting the main characteristics of the collected data and continues with reporting the results of this study. Then, in Section 4, the major findings from the Results section are discussed and compared with other studies. Furthermore, this section comments on the suitability of TLS for soil roughness assessment. Finally, conclusions are drawn in Section 5.

## **2. Materials and Methods**

An out-door experiment was conducted to test the potential of terrestrial laser scanning for the soil roughness description. The experiment involved the preparation, measurement and analysis of a bare soil roughness plot.

### *2.1. Roughness Preparation*

An isotropic roughness pattern was prepared on a 2.6 m × 3 m rectangular plot placed in the Botanical Garden of the University of Vienna, in late October, 2013. The plot was generally used as a seed bed for plant reserve growth and was composed of a bare loamy-sand soil, which was rich in organic materials and rather dark in color. The soil is part of the Danube river basin and, generally speaking, contains a notably large portion of sand compared to clay, which is present just in a small amount. The high presence of the organic matter is a consequence of more than 30 years of cultivation. Such an organic-rich soil generally has low reflectance at laser wavelengths compared to other soil types. This negatively affects the strength of the backscattered laser signal, as well as the signal-to-noise ratio, decreasing the quality of the resulting TLS measurements. Thus, the selected soil imposes rather unfavorable conditions for TLS scanning compared to other soil types.

To ensure an isotropic geometry within the plot, the soil was first prepared by a rotary cultivator and then flattened out with a rake. The resulting roughness was mainly driven by randomly-oriented and spatially-distributed soil particles and aggregates, most of them with a size of ~0.5 cm to 7 cm in diameter (Figure 1b,c). Additionally, some traces of the rake pulling process were present in some parts

of the plot. However, their magnitude and amount were too small to disturb the general isotropic and random nature of the plot. Finally, other roughness elements, like small gravel (up to 2 cm in diameter), as well as needles and leaves from the surrounding trees were also present in the plot, though all of them in a very small quantity (Figure 1c).

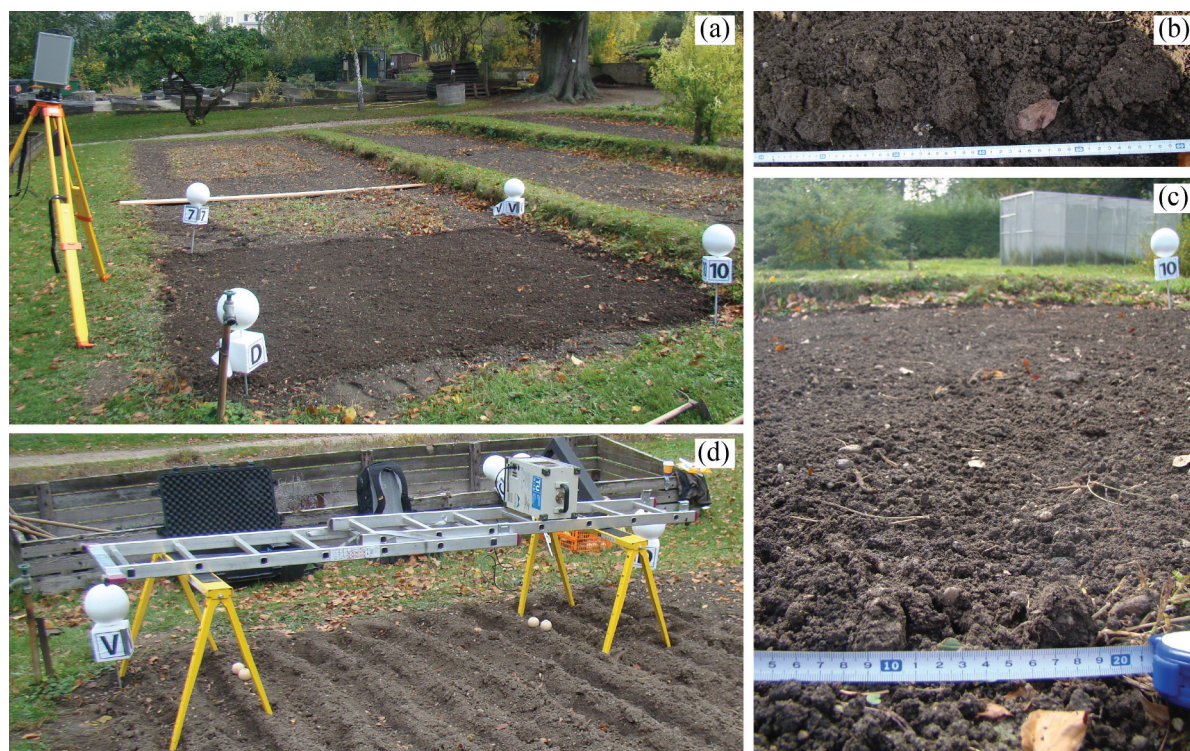


**Figure 1.** (a) Measurement setting of the TLS instrument over the analyzed plot; (b,c) soil aggregates and other roughness elements present within the plot; (d) measurement setting of the optical triangulating scanner (OTS) instrument (since a photo of the OTS setting over the analyzed plot was not available, this photo shows an identical OTS setting that was applied on another roughness plot, which is not considered in this paper).

## 2.2. Measurement Setup and Acquired Data

The roughness plot was measured immediately upon its formation. The measurements were performed with the Z + F IMAGER<sup>®</sup> 5006i, an amplitude-modulated continuous-wave (AM-CW) terrestrial laser scanner (TLS) that uses the phase comparison ranging technique. The instrument has a specified precision of 0.4 mm (relevant for targets with a reflectivity of 100%) and a small beam divergence (0.22 mrad), with a beam diameter at the exit of 3 mm [42]. The scanner also has a large vertical field of view (FoV) that starts at 75° below the horizon and which allows its positioning closer to the object. In addition to the TLS measurements, a subplot of ~0.3 m × 1.2 m was scanned by an optical triangulating laser scanner (OTS), Konica Minolta VIVID<sup>®</sup> 910i. This scanner provides data with a specified precision of 32 μm for the wide-lens scanning setup, which is one order of magnitude better than the specified precision of the TLS. On the other hand, the typical ground sampling distance

(GSD) of this instrument is less than 1 mm, which is far below the TLS's footprint in a close-range setup (up to 4 mm). Therefore, these data were considered as a reference and used for the validation of the roughness parameters derived from the TLS.

The measurement setup of the TLS is shown in Figure 1a. The measurements started on 23 October 2013 at 13:00 CET and finished approximately one hour later. The weather was mainly cloudy, but also with some short sunny intervals and without wind and rain. The plot was surveyed with 4 scan positions, each placed approximately halfway on the plot's edges and as close to the plot as the TLS's vertical FoV allows. The scanner was mounted on a standard wooden tripod adjusted at the maximum possible height ( $\sim 1.8$  m), which ensures the stability during the scanning. The scanning itself was performed in the "low noise" and "high power" mode, while the sampling resolution was set to "super high", *i.e.*, 20,000 measurements within the full vertical and horizontal circle [42]. Such a scanning mode requires 17 min per scan position to scan the complete FoV. In addition to this setting, 4 spherical targets (made of Styropor<sup>®</sup> and each with a radius of 10 cm) were installed at the 4 plot's edges. These targets were later used as tie points for the relative orientation of the 4 measured TLS scans. A similar setting was already applied successfully for a vegetation survey with the same TLS instrument [5]. During the complete surveying time, it was ensured that these targets were static and visible from each scan position.

The measurement setup of the OTS was slightly atypical. Since this is primarily an indoor instrument that has a relatively small FoV compared to the TLS, a special construction was installed over the subarea to survey a strip with several overlapping OTS scans. Unfortunately, a picture of this particular setup was not available, and thus, Figure 1d shows the identical setup over another roughness plot, which is not considered in this paper. As can be seen there, the construction acted as a platform made of two adjustable metal trestles, which were used to support a horizontally-positioned aluminum ladder. The OTS scanner was mounted on the ladder and faced down toward the soil at a relative height of  $\sim 0.7$  m. Additionally, the construction was covered by special ultra-light, first-aid blankets to introduce the indoor lightning conditions, which is required for successful scanning with the OTS. The surveying was then done by a successive ladder sliding and capturing individual OTS scans. The scans were acquired using the wide lens with a focal distance of 8 mm, which, for our setup, provided a rectangular object coverage of  $\sim 0.4$  m  $\times$  0.3 m and a ground pixel size of  $\sim 0.7$  mm. Alternatively, "tele" and "middle" lenses could have been used, as well. However, the increase in precision and resolution that they bring is minor and at the cost of the FoV, which would only increase the number of individual scans.

In total, 10 individual OTS scans were collected in the form of a strip and in the direction approximately parallel and close to one of the plot's edges. It was ensured that the successive scans had at least a 70% overlap along the larger edge of the OTS's FoV, which also determined the final strip length ( $\sim 1.2$  m). The strip width, on the other hand, was driven by the smaller edge of the OTS's FoV ( $\sim 0.3$  m at the ground). To resolve an initial co-registration between the OTS and TLS data, two small wooden spherical targets (3 cm in radius) were placed at the beginning and end of the OTS strip. They were firmly fixed to the ground by 20 centimeter-long screws and were visible in both OTS and TLS data. Later, in the preprocessing phase, these parts were excluded from the OTS data, which, together with slightly inclined strip directions to the plot's sides, restricted the effective area to 0.18 m  $\times$  1 m for the OTS strips.

### 2.3. Data Processing

TLS data were processed through two main steps. The first step aimed at extracting valid measurements (points) from the raw TLS data, while in the second step, these valid points for each of the 4 TLS scans were transformed into a common coordinate system. During the transformation, the soil heights were also detrended, which is the prerequisite for almost any roughness analysis [22,23]. This section explains each of these two main tasks in more detail.

#### 2.3.1. Pre-Processing

The pre-processing of the raw point clouds was done in the “Z + F Laser Control” software, similarly to the pre-processing done in [4]. Several predefined filters were applied to remove (1) irrelevant measurements, (2) low-quality measurements and (3) erroneous measurements, which are associated with the AM-CW ranging technique. First, points outside the plot area, *i.e.*, irrelevant points, were discarded by applying a simple polygon filter. Then, points with a small intensity value were removed from the data by an intensity filter with the default settings. These points have a low signal-to-noise ratio, and thus, they are generally considered as low-quality measurements [43]. Finally, points that are so-called mixed pixels were removed automatically by applying the mixed-pixel filter and single-pixel filter implemented in the software. These points are associated with an erroneous range value that appears when an AM-CW ranging system samples a target that has individual scatterers distributed along different ranges within the laser beam [43]. In soil roughness scanning, such cases appear, *e.g.*, when the laser beam illuminates simultaneously both the top of a large soil aggregate (first individual scatterer) and the underlying soil surface (second individual scatterer).

Depending on the reflectance, illuminated area and relative distance between the individual scatterers, the resulting range may appear anywhere along the laser’s line of sight, *i.e.*, in front, behind or between the soil aggregate’s top and the soil in the background. In all three cases, mixed-pixel points provide the false geometry of soil aggregates, while in the latter case, they cover the occluded area, providing also a false impression about the coverage and point density of the TLS data. Thus, the mixed pixels have to be removed before any data quality and roughness analysis. Figure 2 shows automatically detected mixed pixels (yellow points) in one of our TLS scans, applying the default settings suggested by the software. Although this filter setting performed the best in our case, *i.e.*, up to a 5-m range, it was also observed that the filters’ performance became questionable for larger ranges. Thus, automatic filtering of the mixed pixels may be an issue in the case of larger roughness plots.

#### 2.3.2. Data Transformation and Detrending

Each TLS or OTS scan is acquired in its own local coordinate system, which will be named here the sensor’s own coordinate system (SOCS). To analyze the two datasets jointly, all of the individual scans were transformed from their SOCSs into one common coordinate system, named here the object coordinate system (OCS). The transformation was done through three consecutive steps. First, the relative orientation was resolved independently among the TLS scans and among the OTS scans. This resulted in two point-cloud blocks, one from the TLS scans and another from the OTS scans, where each of them was built in its own block coordinate system (BCS). Then, in the second step, the OTS block was

co-registered globally to the TLS block. Finally, the co-registered scans were all transformed together from the TLS's BCS to the OCS.

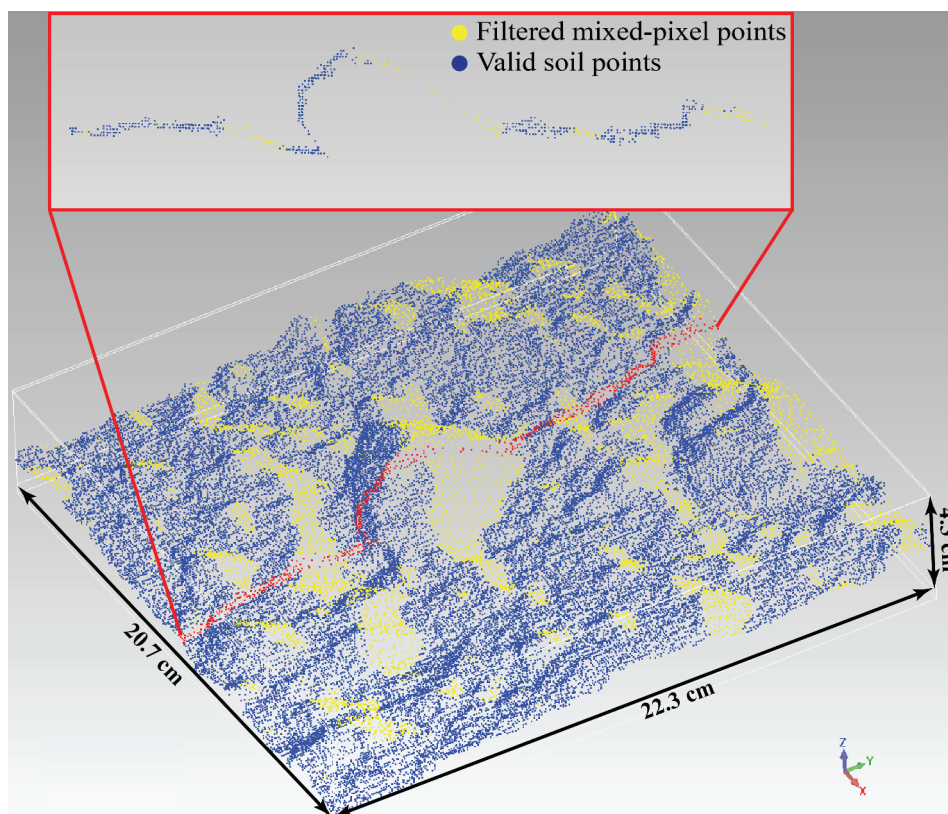


**Figure 2.** An example of automatically-detected mixed pixels (yellow points) in a single scan station. The top diagram shows a cross-section of mixed pixels taken approximately along the TLS's line of sight.

A coarse, relative orientation of the TLS scans was done using the 4 spherical targets installed at the plot's corners. These targets were measured semi-automatically in each TLS scan, and then, their centers were used as tie points to derive the transformation parameters (three rotation angles and three translation increments) for each TLS scan. This was done within an adjustment procedure implemented in the Z + F Laser Control software, where the scan taken from Position 1 (Scan 1) was fixed. This ensured that the resulting TLS block had a coordinate system identical to the SOCS of Scan 1. The average deviation between the corresponding tie points after the adjustment was 4.8 mm. Then, an additional fine relative orientation of the TLS scans was done using an in-house implementation of the iterative closest point (ICP) algorithm. As a result, the average 3ddistance between the corresponding points among each TLS scan pair ranged from 0.9 mm to 1.1 mm. The relative orientation of the OTS scans was also done by the same ICP algorithm, where one of the OTS scans was kept fixed. The average distance between the corresponding OTS points after the relative orientation was 0.1 mm.

The co-registration of the OTS to the TLS block was done through an initial co-registration followed by a fine co-registration. The initial co-registration was done using the 4 small spherical targets installed

at the OTS strip's corners. The spheres' centers, derived independently from the OTS and TLS block, were used as tie points in an adjustment that provided the 6 global parameters for the rigid body transformation between the two blocks. These parameters were then applied to transform each OTS scan into the TLS's BCS. Finally, a fine registration was performed with the mentioned ICP algorithm in which all of the TLS and OTS scans were co-registered autonomously to one another. The average 3D distance between all of the corresponding TLS and OTS points was 1.2 mm after applying the ICP.

Since roughness analysis should be performed on detrended heights, the co-registered scans were once more transformed into final OCS, where soil roughness heights were free from a global planar trend. This transformation was done by defining the z-axis of the OCS as parallel to the normal of an orthogonal-distance regression plane that was fit through all of the TLS points within the plot. The center of gravity of these points was taken to be the origin of the OCS, while the direction of one plot's side (defined with two large spheres) was taken as the x-axis of the OCS. This means that the z-coordinate of the measured points in the OCS represents the linearly detrended component of soil roughness heights. In practice, when large plots are considered (e.g., plot sides of 25 m or larger), the global trend may also appear to be different from planar, e.g., a higher order polynomial surface [36], and in this case, data should be accordingly detrended to arrive at roughness heights. The second and third order polynomial surfaces were also estimated for our plot, and their root mean square (RMS) of the fit errors were 11 mm and 10 mm, respectively, whereas for the linear fit, the RMS error was also 11 mm. Since the RMS errors are practically identical, the linear model was selected, because it is the simplest one and also in accordance with most of the roughness studies ([23,40,41], *etc.*).

#### 2.4. Roughness Analysis

Soil roughness was analyzed in both the spatial and frequency domain. To enable the conversion between the domains, gap-free digital elevation models (DEMs) were built, and discrete Fourier transform (DFT) was used. The roughness analysis itself was then performed on profiles, which were actually rows or columns of the generated DEMs. The focus of the analysis was on understanding the nature of spatial correlation associated with the profile heights, as well as on deriving the conventional roughness parametrization, *i.e.*, root mean square height ( $s$ ) and correlation length ( $l$ ).

##### 2.4.1. DEM Generation

Gap-free DEMs offer the regular structure of soil heights, which is the required data format for an application of the DFT. Thus, two different interpolation methods were consecutively applied to compute the interpolation at every grid node. First, the moving plane method was performed, providing an interpolation that is derived from the local regression plane estimated on all of the points within a circular neighborhood. The moving plane interpolation was selected, because the locally-inclined plane is a much more appropriate model for the soil surface compared to, e.g., the local horizontal plane, which is the case for the mean and median interpolators. Besides, the later interpolators also tend to provide step-like DEMs, which might additionally hamper the roughness assessment. The neighboring points used for the interpolation were the linearly-detrended measurements of soil heights given in the OCS, while the radius of the circular neighborhood is the data aggregation parameter, which controls the

amount of smoothing, *i.e.*, the resolution, of the interpolated DEM. Multiple radius sizes were applied to understand their influence on the soil roughness assessment and to select accordingly the optimal one for the DEM generation. The local regression plane was not possible to estimate for some grid nodes, because either there were not enough neighboring points (more than 3) or the neighboring points were too inclined (nearly vertical), providing a singular covariance matrix. For these grid nodes, the interpolation was computed from the corresponding triangular facets of a triangular irregular network (TIN) built on the grid nodes, which were interpolated by the moving plane interpolation in the previous step. Such an interpolation strategy was applied on different subsets of measurements, *e.g.*, on single TLS's scan, or two or four merged TLS's scans, providing the corresponding 1-mm gap-free DEMs, used in the subsequent analysis.

#### 2.4.2. Roughness Description

The interpolated profile heights (the DEM's rows or columns) are treated here as realizations of an isotropic, zero-mean process with a Gaussian probability distribution function. This is a conventional and widely-used roughness model [25,36,41], which, considering the plot size and that the roughness geometry was prepared, also appeared to be a reasonable assumption for our analysis. This model is completely described once the autocorrelation function (ACF) of the profile heights is known. This means that an empirical ACF should be first estimated, and then, the root mean square (RMS) height and the correlation length parameters should be determined from the applied ACF model.

In this paper, the empirical ACF was estimated in the same way as in [25,41], *i.e.*, as the Fourier transform of the power spectral density (the roughness spectrum) obtained as the periodogram. This is equivalent to:

$$\hat{r}(\tau_k) = \frac{1}{N} \sum_{i=0}^{N-k} z_i z_{i+k} \quad (1)$$

where  $\hat{r}(\tau_k)$  is the estimated ACF value for a lag  $\tau_k = k \cdot \Delta x$ , while  $\Delta x$  is the DEM's grid size, and  $N$  and  $k$  are the number of heights in the profile and the lag increment ( $k \in \mathbb{Z}_+$ , and usually less than  $N/2$ ), respectively;  $z_i$  is the profile height at position  $i$  in a DEM's row (or column). The RMS height ( $s$ ) was estimated as  $\sqrt{\hat{r}(0)}$ , the square root of the empirical ACF value at a lag of zero ( $k = 0$ ). This value was then used to calculate the normalized ACF:  $\hat{\rho}(\tau_k) = \hat{r}(\tau_k)/\hat{r}(0)$ . The shape of the  $\hat{\rho}$  is usually approximated either by a Gaussian or exponential function, and the correlation length  $l$  is then estimated as the lag for which  $\hat{\rho}(\tau_l) = e^{-1}$ , where  $\tau_l = l$ . In this study, both models, Gaussian and exponential, were always estimated per each profile, and the correlation length was derived from the one that had the smallest RMS error of the fit. This correlation length is here named the model correlation length  $l_m$ . Additionally, another correlation length value was estimated by interpolating the normalized ACF linearly between two consecutive lags ( $\tau_m$  and  $\tau_{m+1} = \tau_m + \Delta x$ ) [41]:

$$l_d = \tau_m + (e^{-1} - \rho(\tau_m)) \frac{\tau_{m+1} - \tau_m}{\rho(\tau_{m+1}) - \rho(\tau_m)}, \text{ where, } \tau_m \leq l_d \leq \tau_{m+1} \quad (2)$$

while  $l_d$  fulfills  $\hat{\rho}(l_d) = e^{-1}$  and is here named the direct correlation length. This value was used to determine spatial lags over which the model correlation length was estimated, *i.e.*, in the interval  $[0, 2l_d]$ . This interval was selected to avoid the impact of the oscillatory effects present in the empirical ACF when estimated from shorter profiles [39], while the interval itself was set according to [27,38].

### 2.4.3. Soil Spatial Correlation and Measurement Noise

The soil heights that are used in this study contain also random measurement errors. These errors are treated here as a stochastically-independent and spatially-uncorrelated additive component, *i.e.*, white noise. As such, the measurement noise may negatively affect the signal-to-noise ratio at high frequencies, and many soil roughness elements that should be described are actually present in this frequency region. Then, the assumed measurement noise has an ACF that approaches the delta function in the ideal case. Thus, the empirical ACF estimated from a noisy soil profile will be only biased at the zero lag  $\hat{\rho}(0)$ , while the ACF estimates at other lags will just become more uncertain than without the measurement noise. This means that the measurement noise just introduces more power into the roughness spectrum, resulting in an overestimation of the  $s$  parameter. For the correlation length, this means that the decorrelation by  $e^{-1}$  ( $\sim 37\%$ ) in the empirical ACF happens at a smaller lag compared to the profile without the noise, resulting in an underestimation of the  $l$  parameter. Following simple geometry, the amount of this underestimation will depend on the magnitude of the measurement noise, as well as on the local slope of the empirical ACF function around the  $\hat{\rho}(\tau_l)$ . Thus, the measurement noise simply biases the classical roughness parametrizations  $s$  and  $l$ , which was the reason for considering additional roughness parametrization in the analysis.

Two extra parameters were additionally included: one to observe the nature of the soil spatial correlation at small lags and another parameter to observe the nature of the soil roughness spectrum at high frequencies. The former parameter is the power coefficient  $p$  of the power-model ACF function that allows a better description of spatial correlations, which are neither exponential nor Gaussian [44]. The power model of the normalized ACF is given by:

$$\rho(\tau) = \exp[-(\tau/l_p)^p] \quad (3)$$

where  $l_p$  is the correlation length that can be estimated from this model. The parameter  $p$  describes the shape of the normalized ACF and usually takes values approximately from 1 (the exponential correlation) to 2 (the Gaussian correlation). In this study, the power coefficient  $p$  was used to analyze the change in the shape of the ACF in the interval  $[0, 2l_d]$ , *i.e.*, over the same spatial lags as for the model correlation length.

The second parameter is the so-called spectral slope  $\alpha$ , which is the slope of a regression line used to model the roughness spectrum given in the logarithmic scale [37]. This means that the power spectral density  $S(f)$ , *i.e.*, the roughness spectrum, of a surface should behave in the linear-scale frequency domain as:

$$S(f) = c \cdot f^{-\alpha} \quad (4)$$

where  $f$  is the spatial frequency and  $\log_{10}(c)$  is the intercept of the regression line in the logarithmic scale. Such a model of the roughness spectrum and its parametrization ( $\alpha$  and  $c$ ) are also often used as a description of soil roughness (e.g., [27,45] among others). In this study, the spectral slope was estimated only within a narrow frequency band close to the Nyquist frequency. Thus, it was not assumed that the model given by Equation (4) is valid over the whole frequency domain, but rather within this small frequency band. Besides, common soil roughness spectra (e.g., with exponential correlation) generally tend to perform a linear decay at the Nyquist's neighboring frequencies in the logarithmic

scale [37]. The lower limit of this band was set to correspond to the physical resolution limit of the scanning system, *i.e.*, the laser footprint diameter in the case of the TLS data, and two-times the GSD in the case of the OTS data. The upper limit was set to be one order of magnitude larger than the lower limit, which is approximately around the 20-mm wavelength. The upper and lower limits are here specified in the spatial domain, while in the frequency domain, they correspond to the lower frequency and higher frequency limits, respectively. This region is expected to be the most sensitive to the presence of the measurement noise, as well as to the smoothing operations accompanying the DEM interpolation, which will be shown and discussed later in Sections 3.4 and 4.2.

### 3. Results and Analysis

#### 3.1. Characteristics of the TLS Data

Table 1 reports the most important statistics of the acquired TLS point clouds within the plot. Values given in the range column represent the distance from the origin of the TLS’s coordinate system to the scanned objects within the plot. Point density, sampling interval and laser footprint diameter are reported for the furthest and the nearest 20-cm bands of the plot with respect to the corresponding scan position.

**Table 1.** The characteristics of the acquired TLS scans.

Name	Range (m)			Point Density (pts/cm <sup>2</sup> )		Sampling Interval (mm)		Footprint Diameter (mm)		Sampling Mode *
	min	mean	max	near	far	near	far	near	far	far
Scan 1	1.840	2.915	4.303	251	22	0.6	2.1	3.0	3.1	1.5
Scan 2	1.871	2.880	4.116	233	21	0.7	2.2	3.0	3.1	1.4
Scan 3	2.127	3.276	4.664	194	18	0.7	2.4	3.0	3.2	1.3
Scan 4	2.135	3.196	4.530	159	14	0.8	2.7	3.0	3.2	1.2

\* The sampling mode is the ratio of the laser footprint diameter to the sampling interval.

These values are given within the columns named “near” and “far”, respectively. The reported point density ( $D_{band}$ ) is the median value of the number of TLS points per cm<sup>2</sup> (pts/cm<sup>2</sup>) within the corresponding zone. The sampling interval ( $\Delta_{band}$ ) was then estimated from this point density by assuming a uniform point distribution within 1 cm<sup>2</sup>, *i.e.*,  $\Delta_{band}[mm] = 10/\sqrt{D_{band}}$ , where *band* stands either for the near or the far plot zone. The laser footprint diameter was calculated based on the non-linear expansion equation for the short ranges [46] and using minimum and maximum ranges for the near and far plot zones, respectively. Finally, the last column reports the ratio of the laser footprint diameter to the sampling interval. This value indicates the TLS sampling mode, and for values larger than one, the laser footprints of the adjacent rays were overlapping one another during the scanning, introducing the so-called correlated sampling [1]. As can be seen from Table 1, all of the TLS scans were acquired in the correlated sampling mode.

For merged scan data, the range and footprint statistics from Table 1 remain similar, while the median point density in the near and far plot zones changed to 220 pts/cm<sup>2</sup> and 329 pts/cm<sup>2</sup> for the merged opposite scan data and all four scans, respectively. The median point density within the whole plot

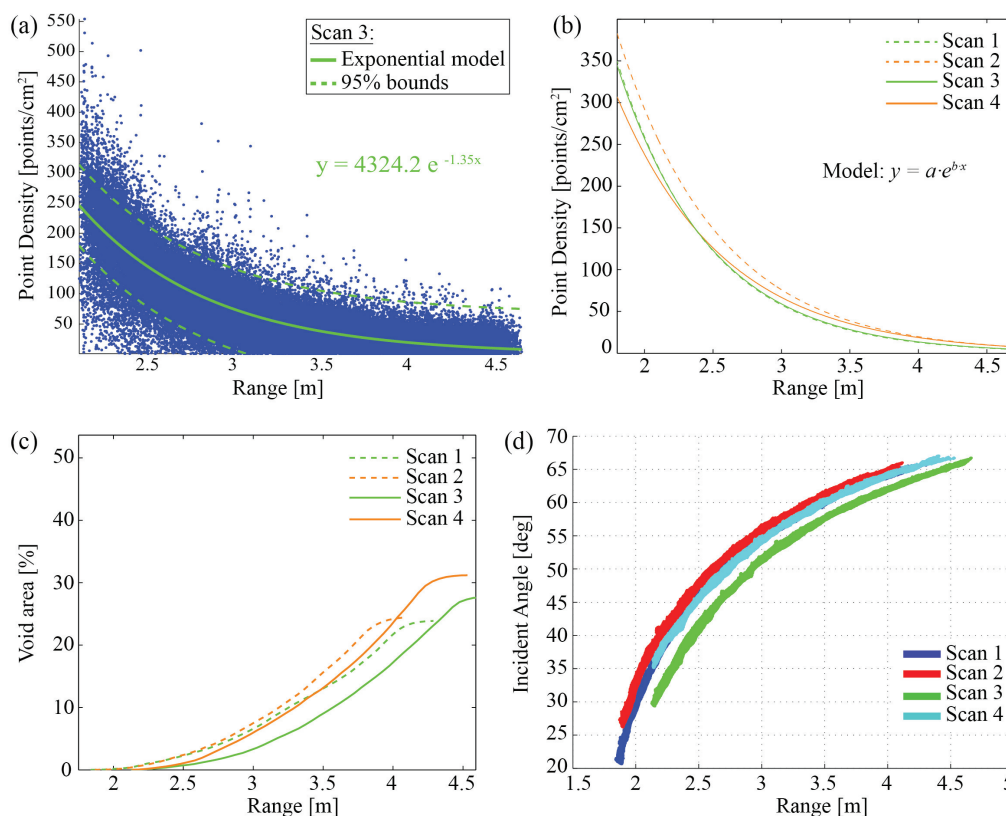
changed from 60 pts/cm<sup>2</sup> to 152 pts/cm<sup>2</sup> and 322 pts/cm<sup>2</sup> for the two opposite scans and all four scans, respectively. Thus, the spatial distribution of the points improved by including the opposite scans, while for all four scans, the densities at the plot edges become almost identical to the global plot density. All of the merged scan data also have the correlated sampling mode.

Figure 3a shows a scatter plot of the point density and mean range over the plot, both taken from corresponding 1-cm rasters, which were generated using the data of Scan 3. The high variability of the point density at short ranges (the near plot zone) is driven by the local incidence angle and a notably higher median point density compared to the far plot zone (Table 1). It can be also seen that the TLS's point density drops exponentially from the near to far plot zone. This was also confirmed by the remaining three TLS's scans, which are shown in Figure 3b. Figure 3c shows a cumulative void area over the range. The void area represents the proportion of cells that does not contain any TLS measurement in a 2-mm raster built over the whole plot. The cell size of 2 mm was selected to match approximately the sampling interval in the far plot zone ( $\Delta_{far}$ ). In this way, the void area values actually indicate the portion of the plot that was bridged by the TIN interpolation in the respective gap-free DEMs. As can be seen from Figure 3c, this happens between 20% to 35% of the plot area for the DEMs built from the individual TLS scans. It should be mentioned here that the void areas do not contain the footprint centers of the laser beams, but some of the void areas may still be covered by the footprints from the laser rays, the centers of which fall within the adjacent cells.

On the other hand, Soudarissanane *et al.* [47] showed in their experiment that incidence angles also affect the point density, as well as the signal-to-noise ratio of the measured points. Thus, the above results can be seen from this point of view instead of considering only the range. Figure 3d shows the scatter plot of the range and the incidence angle values for our four single scans. These functions can be used to deduce the incidence angle at which the void area or the point density changes due to a change in range. For example, void areas larger than 5% appear in Scan 3 at ranges larger than 3.2 m and incidence angles larger than 50° (Figure 3c,d). The deduction based on Figure 3d will be used later in the text whenever it is necessary to introduce certain restrictions on both the range and incidence angle. It should be noted that the incidence angle is here defined as the shortest angle measured in the vertical plane from the local normal to the laser beam vector in the OCS. The local normal was derived from the planar trend of the plot (Section 2.3.2) and was pointing upwards, *i.e.*, in the direction of the z-axis of the OCS. The direction of laser beam vector was set from the measurement point towards the origin of the TLS's coordinate system.

The range and incidence angle values describe also the relative position of the scanner to the measured object, *i.e.*, the measurement setup [47]. Thus, the clustering of range-incidence-angle functions for Scan 1, Scan 2 and Scan 4 in Figure 3d means that these scans have a similar measurement setup, whereas the range-incidence-angle function of Scan 3 is slightly biased to the right. This then means that Scan 3 performs the same incidence angles as other scans, but at slightly larger ranges, *i.e.*, it has the best measurement setup among the acquired TLS scans. This scan position was actually taken from the edge of the neighboring plot, which is slightly uplifted compared to our plot (the right side in Figure 1a and also the background area in Figure 1c). This gain in the instrument height with respect to the observed plot resulted in the better acquisition geometry of Scan 3, which is clearly reflected in Figure 3d. In the case that the instrument height improves even more (e.g., by increasing the height of the tripod),

the range-incidence-angle function would just be biased more to the right and cover smaller incidence angles. An ideal TLS measurement setup would result in a horizontal range-incidence-angle function at, e.g., 20° or a lower incidence angle. However, this is not possible due to the oblique acquisition architecture of the contemporary TLSs. On the other hand, the OTS data used in our experiment would appear as a vertical range-incidence-angle function at approximately a 0.7 m-range and with a length of several degrees starting from the 0° incidence angle.



**Figure 3.** (a) Change in point density over the range for the TLS Scan 3. The green line shows the fitted exponential model with its 95% confidence bounds; (b) The exponential models of the density drop over the range for the four single TLS scans; (c) The percentage of the void area over the range for the single TLS scans; (d) The relation between the range and the incidence angle within the plot for the single TLS scans. The incidence angles were calculated with respect to the planar trend of the plot.

Figure 4b,c shows how the void area was spatially distributed within the plot for Scan 1 and for the two opposite scans (Scan 1 and Scan 3) merged into one common point cloud (Scans 1&3), respectively. Figure 4b shows that 24.1% of the plot area was interpolated by the TIN method in the gap-free DEM generated from Scan 1. As can be seen there, most of the void area is concentrated in the far plot zone, *i.e.*, at ranges larger than 4 m. Figure 4c shows that when the data from the opposite scan are additionally used, the occlusions are significantly reduced within the plot. The red regions marked by yellow

rectangles in Figure 4b,c are places where the small wooden sphere (used in the block co-registration) were installed.

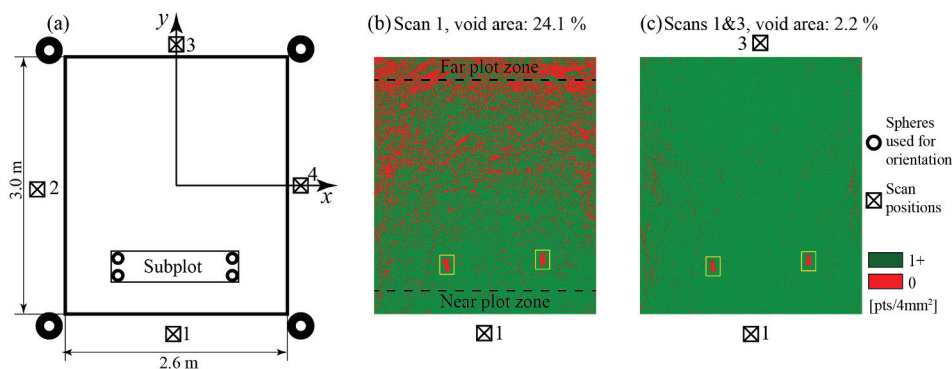


**Figure 4.** (a) The scheme of the scan positions with respect to the plot coordinate system. The spatial distribution of the 2-mm cells where there were no TLS measurements in the data from Scan 1 (b) and from the two merged scans: Scan 1 and Scan 3 (c).

### 3.2. Overview of DEM Sets

The analysis presented in the paper is based on a series of differently-generated DEMs. These DEM sets differ in the data source used for their generation, e.g., OTS or TLS point clouds, or, further, in the case of the TLS data, in the number of scans used. Then, there are DEM sets generated over different subparts of the plot or even over the whole plot area (see Figure 4a). Furthermore, some DEM sets were generated using different neighborhood sizes for the DEM interpolation. To overcome this complexity, Table 2 gives an overview of all of the DEM sets, organized according to the particular objectives of the performed analysis.

**Table 2.** The overview of the DEM sets used for the analysis.

Name	Objective	Section	Data Source	Used Scans	Analyzed Area	Profiling	Neighb. <sup>1</sup>	DEMs <sup>2</sup>
Set 1	Effects of Neighborhood Size on Soil Roughness	3.3	TLS	4 Scans	subplot (0.18 m × 1 m)	x-axis	16	16
Set 2.1				Scan 1			41	41
Set 2.2				Scan 3			41	41
Set 2.3	Optimization of Neighborhood	3.4	TLS	Scans 1&3 <sup>3</sup>	subplot (0.18 m × 1 m)	x-axis	41	41
Set 2.4	Size Using Spectral Slope			Scans 2&4 <sup>3</sup>			41	41
Set 2.5				4 Scans			41	41
Set 2.6			OTS	-			21	21
Set 3	Comparison of Soil Roughness Derived from OTS and TLS	3.5	OTS and TLS	Scan 1; Scan 3; 4 Scans Scans 1&3; Scans 2&4	subplot (0.18 m × 1 m)	x-axis	1	6
Set 4	TLS Directional Pattern and Profile Sampling	3.6	TLS	Scans 1&3; Scans 2&4; 4 Scans	subarea (1 m × 1 m)	x-axis y-axis	1	3
Set 5	Single vs. Multiple TLS Scanning and Soil Roughness	3.7	TLS	Scan 1; Scan 3 Scans 1&3; 4 Scans	plot (2.6 m × 3 m)	x-axis y-axis	1	4

<sup>1</sup> The Neighb. column shows the number of neighborhood sizes used for DEM interpolation; <sup>2</sup> The DEMs column shows the number of DEMs that the corresponding DEM set contains. <sup>3</sup> The ampersand indicates that two opposite scans are merged into a single point cloud.

As can be seen from Table 2, the coming sections will follow the mentioned objectives and will use the introduced nomenclature in Table 2. Nevertheless, the DEM sets will be explained in detail within each section; thus, Table 2 should just give a general overview of the performed analysis and the respective datasets.

### 3.3. Effects of Neighborhood Size on Soil Roughness

DEM Set 1 was used to analyze the effects of the neighborhood size parameter used during the moving plane interpolation step. As can be seen from Table 2, this set contains DEMs generated from all four merged TLS scans and over the rectangular subplot area ( $0.18 \text{ m} \times 1 \text{ m}$ ) surveyed with the OTS scanner. The DEMs were interpolated as explained in Section 2.4.1 setting the neighborhood diameter size for each DEM within the set differently. In total, the neighborhood size was set 16 times, taking values from 1 mm up to the 100 mm, while the grid sizes of the 16 resulting DEMs were always set to 1 mm. For the analyzed subplot, this means that each DEM contained 180 rows with 1000 soil heights regularly spaced at 1 mm from one another over the 1-m row length.

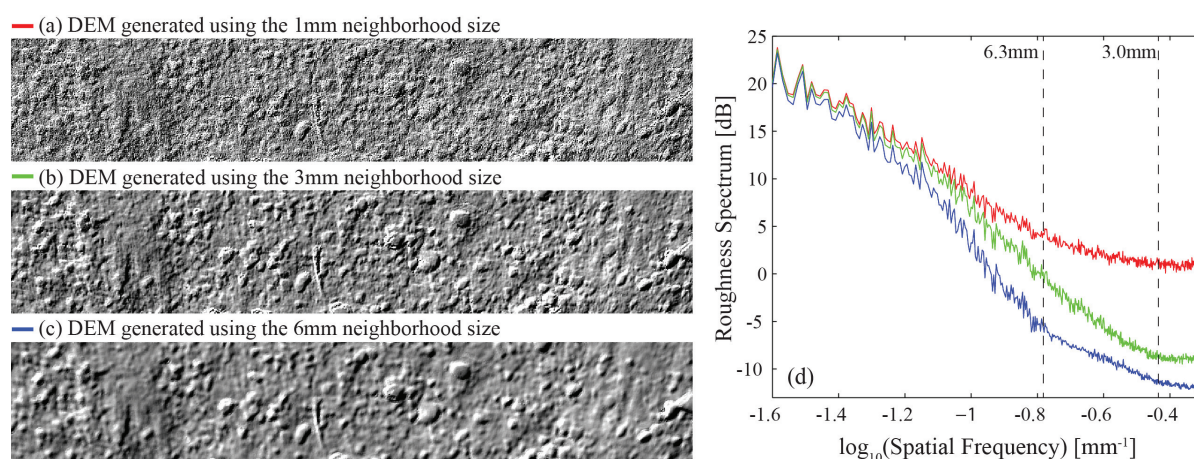
#### 3.3.1. Roughness Spectrum

Figure 5a–c shows the shaded heights of three DEMs selected from DEM Set 1. These DEMs were interpolated using the neighborhood diameters of 1 mm, 3 mm and 6 mm, and will be called here 1-mm DEM, 3-mm DEM and 6-mm DEM, respectively. Based on the given shadings, it looks like the 1-mm DEM contains all of the relevant elements of the soil roughness, which are, however, buried in noise. In the 3-mm DEM, this noise is significantly reduced, while the relevant soil roughness elements are still preserved. The latter is, however, not the case for the 6-mm DEM, where small soil aggregates, as well as the noise are not visible any more. The noise dominating in the 1-mm DEM is actually the measurement noise, which is, due to the extremely small neighborhood size, reflected in the DEM's heights. Generally, the applied moving plane interpolation behaves similarly to the moving average, *i.e.*, as a low-pass filter, and thus, the size of the neighborhood area regulates how much of both measurement noise and roughness features will be smoothed out in the resulting surface.

The smoothing effect driven by the neighborhood size can be better seen in the frequency domain. Figure 5d shows the mean roughness spectra of the three DEMs, which were estimated with the Fourier transform applied on the DEMs' rows. As was expected, the spectrum of 1-mm DEM (the red curve) has the highest power, thanks to the portion of the measurement noise that is reflected due to the small neighborhood size. The spectrum of the 3-mm DEM (the green curve) performs along all of the frequencies between the spectra from 1-mm and 6-mm DEMs. Since the RMS height is equal to the area below the roughness spectrum [22], the resulting estimates of roughness parameter  $s$  will be biased from one another proportionally to the area between their corresponding roughness spectra. Another interesting point is that the roughness spectrum of the 3-mm DEM performs a white noise roll-off at wavelengths smaller than 3 mm (the right dashed vertical line in Figure 5d). This behavior of the roughness spectrum indicates that the applied grid size is probably smaller than the resolution of our data, which then caused such informationless behavior below 3 mm. The same roll-off can also be seen in the spectrum of the 1-mm DEM. There, the spectrum continues to perform an inclination towards the

white noise, even over a broader frequency band, which is due to a weak signal-to-noise ratio coming from the small neighborhood size.

The roll-off of the spectrum from the 6-mm DEM has a completely different shape. It starts around 6 mm (which is actually equal to its neighborhood size) and declines slower than the 3-mm DEM's spectrum in the same frequency band. Furthermore, the variability of the 6-mm DEM's spectrum is significantly reduced along the roll-off frequencies compared to lower frequencies. The low variability in this frequency band is perfectly in accordance with the use of the interpolation step, since the associated interpolation (a low-pass filter) affects such frequencies more than those far before its cut-off frequency. This suggests that the shape of the 6-mm roughness spectrum may not reflect the inherent soil spatial correlation well at these frequencies. Finally, the deformation of the 6-mm spectrum exists also in the opposite direction, towards low frequencies. However, the shapes of the 3-mm and 6-mm spectra are very similar there, though the latter appears to be more inclined. This will generally introduce bias in the spectral slope when it is estimated within this frequency band. It should be also mentioned that the starting frequency in Figure 5d ( $\log_{10}(f) = -1.6 \text{ mm}^{-1}$ ) is the place where the relative difference between the 3-mm and 6-mm roughness spectra becomes less than 10%, while the left vertical dashed line marks the frequency where this difference is at the maximum.



**Figure 5.** DEMs interpolated from all four scans and using three different neighborhood settings (a–c) and the mean roughness spectra estimated from these three DEMs (d).

The above example showed the importance of the neighborhood size setting when laser scanning data and DEMs are used in soil roughness analysis. Although all of the considered DEMs should represent the same soil roughness, it is apparent from Figure 5 that they will lead to different roughness estimates, as well as different natures of soil spatial correlation at high frequencies. Thus, an optimization is required to arrive at a suitable neighborhood size, which will minimize the impact of the measurement noise and oversmoothing on the roughness spectrum at high frequencies. The determination of such a neighborhood size is discussed in Section 3.4.

### 3.3.2. Roughness Indices

The impact of the neighborhood diameter size on the roughness indices was analyzed from DEM Set 1. Figure 6a–e shows box plots of the roughness indices  $l_d$ ,  $l_m$ ,  $s$ ,  $p$  and  $\alpha$  (Sections 2.4.2 and 2.4.3) estimated from the 16 DEMs of DEM Set 1. Thus, each box-plot compares 16 sets of 180 index’s values estimated from the 180 rows of the corresponding DEMs. In Figure 6a–e, these sets are denoted by the neighborhood size of the corresponding DEM and plotted over the x-axes of the box plots. It should be noted that the selected neighborhood sizes within the TLS series do not have a constant increment, which can be also seen on the x-axes of the box-plots.

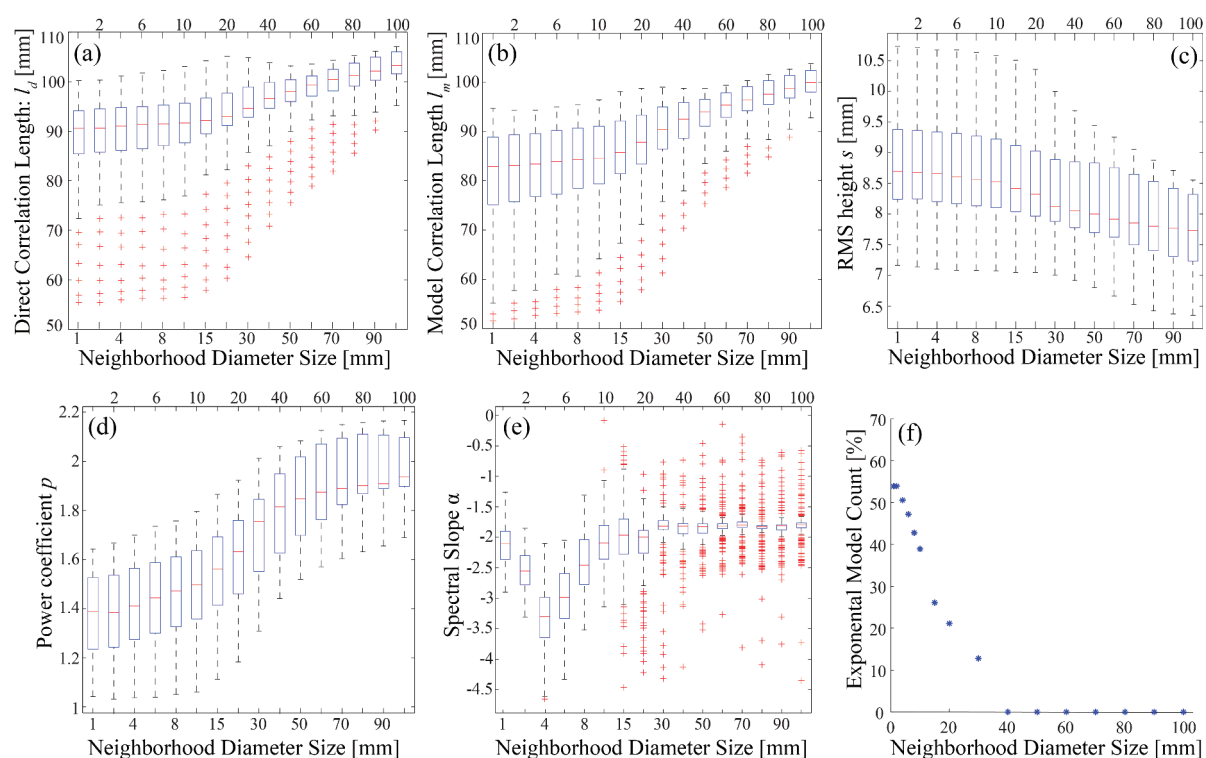


**Figure 6.** (a–e) Roughness indices  $l_d$ ,  $l_m$ ,  $s$ ,  $p$  and  $\alpha$  as a function of the neighborhood diameter; (f) The percentage of the exponentially correlated profiles as a function of the neighborhood diameter; The parameters were estimated from the DEM Set 1, where only Scan 1 was used.

Figure 6b shows that the median of the model correlation length  $l_m$  enlarged from 83.4 mm to 87.9 mm for the 4 mm and 20 mm neighborhoods, respectively, which is an increase larger than 5%. On the other hand, the dispersion in the correlation length decreased by 25% for the same neighborhoods. The mentioned dispersion actually reflects the spatial variability of the correlation length within the subplot, which then means that a DEM with neighborhood sizes of 20 mm or larger does not depict this soil property well any more. The observed changes in the correlation length and its variability happened because small soil aggregates were smoothed out by increasing the neighborhood size, *i.e.*, soil variability is reduced, resulting in the observed: (1) underestimation of the inherent variability of the

correlation length; and (2) overestimation of the inherent correlation length. It should be also mentioned that the model correlation length constantly underestimate the direct correlation length, which for the 4-mm DEM was about 8%. This may indicate that the applied ACF model does not perfectly describe soil correlations locally, *i.e.*, at lags similar to the correlation length value.

The RMS height parameter reacted opposite of the correlation length, *i.e.*, constantly decreasing while increasing the neighborhood size. The smoothing of the small soil aggregates caused the 5% relative decrease in both the  $s$  value and its dispersion between the 4-mm and 20-mm neighborhoods. This is slightly surprising, since it is generally considered that the correlation length is more difficult to estimate than the RMS height [23,36,39,41]. This, however, does not seem to be the case here, *i.e.*, for the over-smoothing effect caused by non-optimal data aggregation.

Figure 6d shows how the power coefficient  $p$  changes when small soil elements are smoothed out. When all of the relevant soil elements are present in the DEM, the soil heights within the subplot shows a tendency towards an exponential spatial correlation. This is generally the case for isotropic soil roughness analyzed at similar scales [25,27,36]. However, as soon as the neighborhood size increases,  $p$  starts to converge to a Gaussian spatial correlation. This means that the over-smoothing effect may also lead to misinterpretation of the soil spatial correlation when a large neighborhood size is selected. This can also be seen in Figure 6f, where the number of exponentially-correlated rows per each DEM is reported. This number was calculated by comparing the RMS errors of the Gaussian and exponential autocorrelation fits per each row and counting the number of rows where the RMS error of the exponential fit was smaller. Figure 6f shows that the 4-mm DEM has almost an equal number of exponentially- and Gaussianly-correlated rows. This is also consistent with the  $p$  values, the median of which is 1.4, while their dispersion is large enough to allow both correlation models. In other words, there are many profiles with a  $p$  value larger than 1.5, which most likely caused the RMS error of the Gaussian fit to be smaller compared to the exponential fit. The DEMs with a smaller neighborhood size have slightly more exponentially correlated rows, which may be due to the measurement noise that is still present in these DEMs. On the other hand, the DEMs with 40-mm or larger neighborhoods do not have any more exponentially-correlated rows, and their  $p$  values are 1.8 or larger. Finally, the 5% relative error of parameter  $p$  happened already between the 4-mm and 10-mm neighborhoods, which is slightly earlier compared to the previous indices.

The most interesting results, however, come from the spectral slope  $\alpha$  (Figure 6e). This roughness index shows a global minimum for the 4-mm DEM and then features almost a constant median for the neighborhoods larger than 20 mm. As was discussed in Section 3.3.1, the measurement noise, as well as the roll-off effects cause the roughness spectrum to be more inclined towards a white spectrum than towards its inherent inclination at high frequencies. Therefore, the DEM where the measurement noise and the roll-off effects are minimized is the one that has the highest inclination of the roughness spectrum. This corresponds to the minimum of the spectral slope (Figure 6e). This offers the possibility for an optimization of the spectral slope with respect to the neighborhood size, which is explored in the next section.

### 3.4. Neighborhood Size and Spectral Slope

The behavior of the spectral slope around its global minimum is analyzed here in more detail. This was done using DEM Sets 2.1, 2.2, ...and 2.6 (Table 2). The first five DEM sets are based on the TLS data, while Set 2.6 is based on the OTS data. Further, the first two TLS sets were built from single TLS scans, *i.e.*, DEM Set 2.1 from Scan 1 and DEM Set 2.2 from Scan 3. Then, DEM Sets 2.3 and 2.4 were built from the point clouds where two opposite TLS scans were merged, *i.e.*, combining Scan 1 and Scan 3 into Scans 1&3, as well as Scan 2 and Scan 4 into Scans 2&4. DEM Set 2.5 was built using all of the TLS points, *i.e.*, the points collected from the four scans.

Figure 7 shows the spectral slope values estimated from the six DEM sets. These sets contain a much larger number of DEMs due to a finer setting of the neighborhood diameter size. For the five TLS sets, this parameter cover values from 1.5 mm to 5.5 mm, and for the OTS set, from 1 mm to 3 mm, but always with the same increment of 0.1 mm. This resulted in 41 and 21 DEMs per each TLS and the OTS series, respectively. The different span in the neighborhood size caused the x-axis of the OTS set (Figure 7f) to have slightly different limits from the x-axes in the TLS sets (Figure 7a–e). The y-axes, however, are identical in all of the figures.

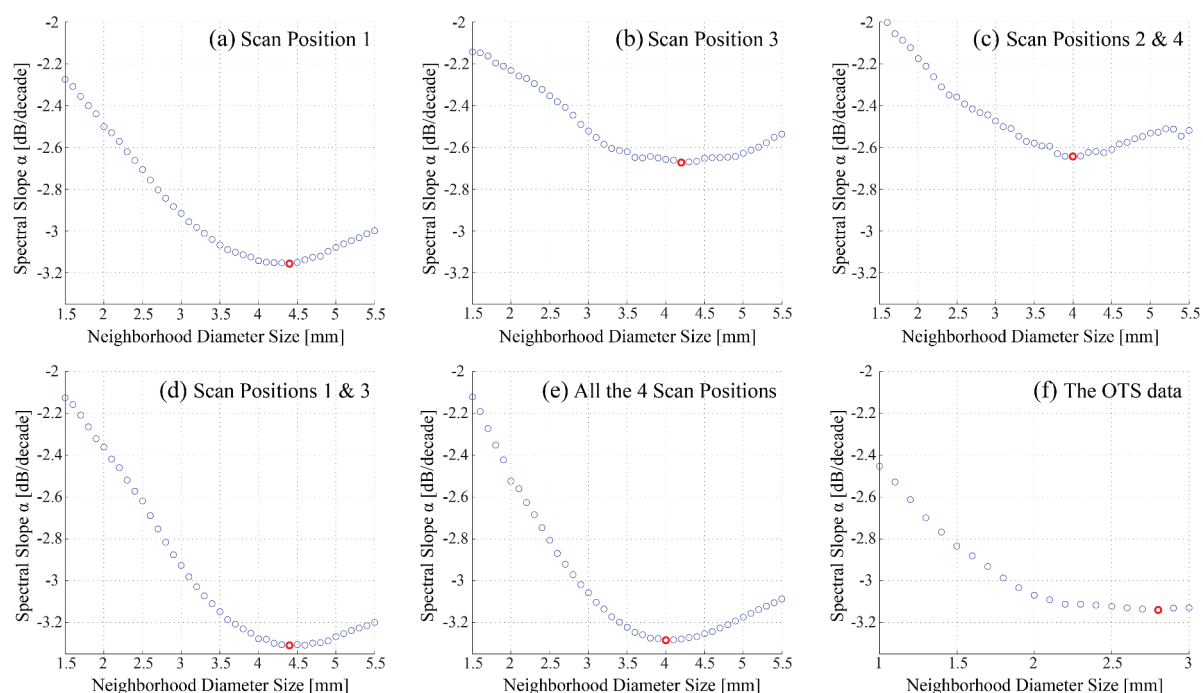


**Figure 7.** The local minima in the spectral slope calculated for: (a) DEM Set 2.1, (b) DEM Set 2.2, (c) DEM Set 2.4, (d) DEM Set 2.3, (e) DEM Set 2.5 and (f) DEM Set 2.6.

As can be seen from Figure 7, the spectral slope confirmed the global minima (the red circles) for all six sets and under the much more intense neighborhood sizes. It is only the OTS set that seems to be not large enough to materialize the rising side of the minimum well. However, this will not affect the

analysis, since the focus is on the global minimum here. The spectral slope values at the global minimum for the DEM sets based on Scan 1, Scans 1&3 and the four scans are consistent with one another, as well as with the OTS set (Figure 7a,d–f). Scans 1&3 and the four scans caused an underestimation in the spectral slope with a relative error of about 5% comparing to the OTS data. Scan 1, on the other hand, caused a slight overestimation (around 1%) of the spectral slope. One of the reasons for the slightly larger relative error of the estimates based on the merged scans could be the errors that follow the relative orientation of the TLS scans. Another factor could be the unfavorable measurement setup of Scan 3. As can be seen in Table 3, Scan 3 has incidence angles that are not smaller than 60°, while Scan 1 (with the relative error of the spectral slope within 1%) has incidence angles not larger than 40°. Two TLS sets, one based on Scan 3 and another on Scans 2&4, appeared to be inconsistent with the remaining three TLS sets, providing a large bias (15% relative error) in the spectral slope compared to the OTS data. The reasons for such surprising results will be discussed in the next section.

**Table 3.** The statistics of the range and incidence angle within the subplot.

Name	Range (m)			Inc. Angle (°)		
	min	mean	max	min	mean	max
Scan 1	2.097	2.177	2.273	33.9	36.7	40.0
Scan 2	2.576	2.935	3.378	49.0	54.5	60.2
Scan 3	3.844	3.932	4.026	60.5	61.4	62.4
Scan 4	2.667	3.494	3.038	49.3	54.5	60.1

For the five TLS sets, the global minimum happens at the neighborhood sizes between 4 mm and 4.5 mm, while for the OTS set, it happens even earlier, at 2.8 mm. Following the analysis from the two previous sections, these values identify the DEMs where almost all of the relevant soil elements should be present, while most of the measurement noise should already be filtered out. This means that these DEMs contain the most complete and accurate level of detail on the soil roughness among all of the generated DEMs in this study. Additionally, these DEMs minimize the spectral slope, *i.e.*, maximize the fractal dimension, at high frequencies, and therefore, they were selected as the most appropriate for the subsequent analysis.

### 3.5. Comparison of Soil Roughness Derived from OTS and TLS Data

The comparison of the two datasets was done over the subplot area and based on six DEMs (DEM Set 3 in Table 2), each of them selected from the corresponding DEM Sets 2.1, 2.2, ... and 2.6. The selection was done according to the optimal neighborhood sizes determined in Section 3.4. Shaded models of these DEMs are shown in Figure 8. The shading in Figure 8a is based on the OTS data and visually looks like the one that contains the highest level of detail on the soil roughness among the selected DEMs. This was generally expected, since (according to the specifications) this instrument should provide higher resolution data with a smaller measurement noise compared to the TLS scanner. Furthermore, the OTS point cloud covers the subplot continuously, which means that there was no need

to bridge the no data regions with the TIN interpolation. This is not the case with the two DEMs based on the single TLS scans (Figure 8e,f).

The unfavorable acquisition geometry (high incidence angles and low point density) of Scan 3 caused the corresponding DEM to have a completely deformed geometry at scales up to the largest soil aggregate (Figure 8f). These two factors are much more favorable in the case of Scan 1, and therefore, the corresponding DEM (Figure 8e) does not contain extremely large occlusions, while the point density is almost enough to ensure the same level of detail as in the OTS DEM.

The DEMs from two opposite scans do not have problems with occlusion any more (Figure 8c,d). However, they perform certain pattern, which seems to “elongate” the soil aggregates’ edges in a particular direction. For the DEM based on Scans 2&4, the elongation of the soil aggregates is along the larger subplot side, which also corresponds to the direction of the laser line of sight within the subplot. For the DEM based on Scans 1&3, this elongation is along the smaller subplot side, which is again the direction of the laser line of sight. The same effect can be also seen in the individual scans. The first explanation for this effect is the interpolation over the shadow area of a scan. A shadow appears along the line of sight. A second possible explanation for this directional pattern may be the nature of the AM-CW ranging technique, *i.e.*, mixed pixels. In the preprocessing step, the mixed pixels were removed, but only for the case when the laser beam illuminates the top of a soil aggregate and the background soil. However, when the laser beam illuminates the bottom of a soil aggregate, as well as the foreground soil, the resulting range is derived from a sum of the two phasors corresponding to each of the two scatterers. This then leads to a range that is slightly shorter than it should be and, eventually, makes the soil aggregates more elongated in the direction of the line of sight. As can be seen in Figure 8b, when a DEM is based on all four scans, this directional pattern is not visible any more. The shadow areas of one scan are typically filled up by points from another scan. This improvement, however, is at the cost of the soil roughness details, which becomes slightly less than in the case of, *e.g.*, the DEM based on Scan 1 (Figure 8e). Especially at edges, points from the poorer acquisition geometry cause this (small) degradation. Two yellow rectangles in Figure 8b,e delineate the area where this loss in roughness is visible in the respective shadings.

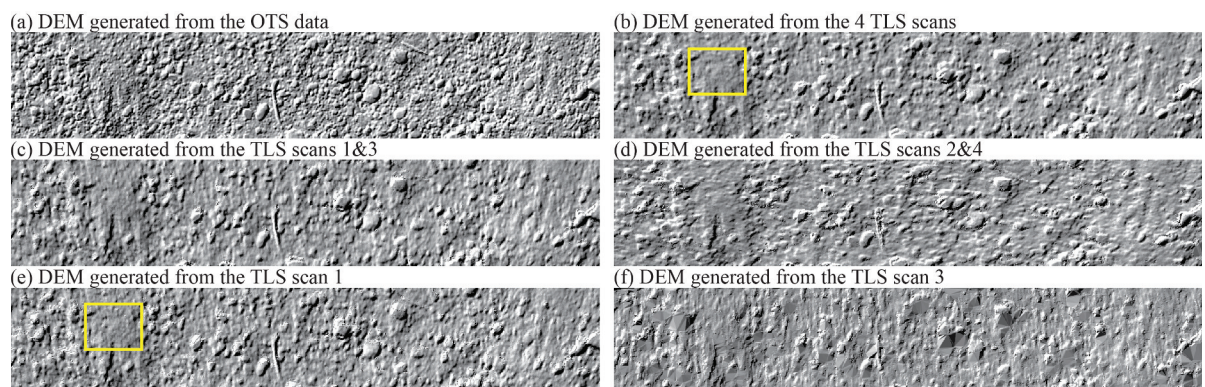


**Figure 8.** The six optimal DEMs for which the spectral slope was minimized and which were selected from: (a) Set 2.6, (b) Set 2.5, (c) Set 2.3, (d) Set 2.4, (e) Set 2.1 and (f) Set 2.2; The DEMs cover the area of the subplot, *i.e.*, 0.18 m × 1 m.

The difference observed in the DEMs' shadings are also analyzed in the frequency domain by comparing the DEMs' roughness spectra. Figure 9 shows the mean spectra of each TLS DEM after subtracting the mean spectra of the OTS DEM. It was assumed that the OTS DEM depicts the soil roughness in the greatest detail among the six selected DEM, and thus, it was taken as a reference for the comparison. As can be seen from the figure, the relative difference between the OTS power spectrum and almost all TLS spectra does not exceeds 1 dB at wavelengths larger than 50 mm. The 1-dB difference appears slightly earlier and later only for Scan 3 and Scan 1, respectively. The spectrum of Scan 1 has generally the smallest difference for the OTS spectra over the whole frequency domain, which reach their maximum of 4 dB at approximately the 6.5-mm wavelength. This confirms the convincing visual impression of the corresponding shaded model, where the level of soil roughness detail appeared to be almost as rich as in the OTS shading. The spectra based on (1) Scans 1&3 and (2) on the four scans behave similarly to Scan 3, only with a larger maximum difference of 4.8 dB, as well as 6 dB, respectively. On the contrary, the spectra differences of (1) Scan 3 and (2) Scans 2&4 appeared slightly different, indicating that their corresponding DEMs also perform a different spatial geometry. This was already noted in the visual comparison of their shadings in Figure 8.

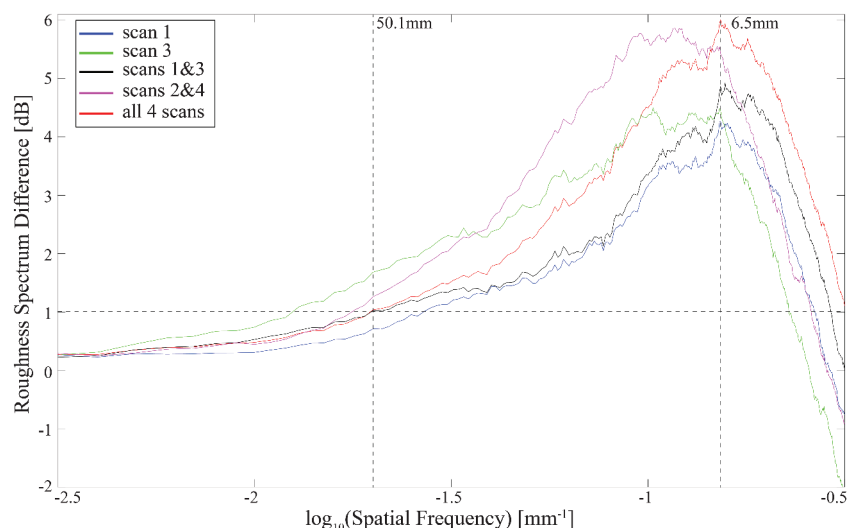


**Figure 9.** Relative difference of the five TLS roughness spectra with respect to the OTS roughness spectra.

The question is now how these differences in geometry of the DEMs affect the roughness indices. Part of the answer is already given by Figure 7, where the spectral slope was analyzed. The consistency in the spectral slope among the OTS and the three TLS datasets is most probably the consequence of sampling the profiles perpendicularly to the laser line of sight. This means that even a difference of 4 dB at the 6.5-mm wavelength in the roughness spectrum cannot introduce a change in the spectral slope larger than 1%, as long as the profiles are sampled perpendicularly to the TLS's directional pattern. However, when the profiles are sampled along the line of sight (the DEM based on Scans 2&4), the spectral slope can be underestimated by 15%. The same amount of underestimation also happens when the scan position

is set more apart from the subplot (Scan 3). Such data are accompanied by large occlusions and large incidence angles, which are the main reasons for the observed underestimation.

The response of the remaining three indices on the directional pattern is shown in Figure 10. Again, index values estimated from the individual rows of the six DEMs are presented there with the corresponding box-plots. Additionally, the 5% bounds around the median of the OTS estimates are marked by the dashed horizontal red lines. The medians of  $s$  and  $l$  turned out not to be so sensitive for the mentioned deformation in DEM geometry, while in the medians of  $p$ , the deformations were reflected slightly, but not so clearly as for the spectral slope. This means that as long as the errors in the roughness spectrum are below 1 dB at wavelengths larger than 50 mm, the RMS height and the correlation length cannot change by more than 5%, when they are estimated from 1-m profiles. It should be also mentioned that the observed sensitivity of the parameters  $\alpha$  and  $p$  may come from the fact that they are estimated from a relatively narrow high-frequency band, which is generally more affected by the DEM deformation, while  $s$  and  $l$  are estimated from a broader band, where the magnitudes at low frequencies are much larger and, thus, predominantly influence the resulting values.

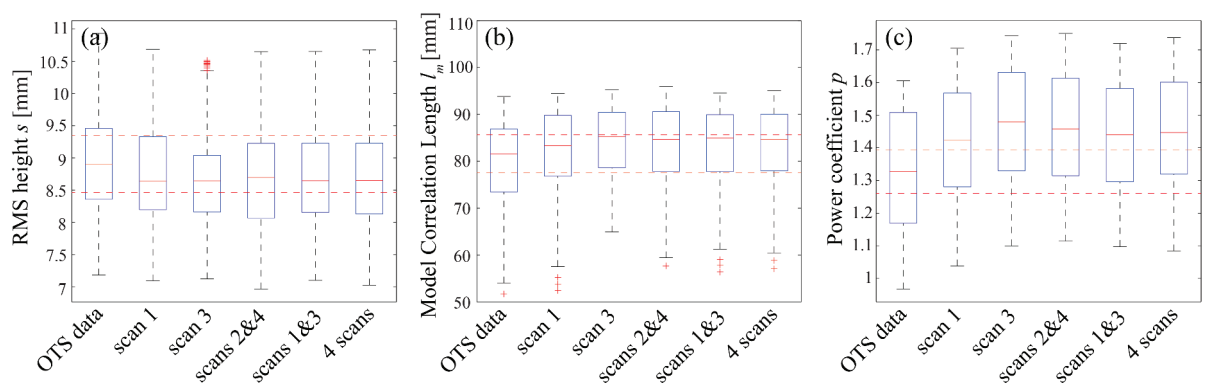


**Figure 10.** The values of (a) root mean square height, (b) model correlation length and (c) power coefficient, estimated from the rows of the six optimal DEMs and presented as box-plots.

### 3.6. TLS Directional Pattern and Profile Sampling

As is shown in the previous section, the directional pattern has only a significant impact at high frequencies and, consequently, on the indices that are estimated from this domain ( $\alpha$  and  $p$ ). Additionally, the results suggested that the sampling across the directional pattern can compensate for the consequent uncertainties in the index's values. To offer more comprehensive support for the above statements, additional analysis was carried out on three 1-m<sup>2</sup> subareas within the plot. Since the roughness estimates are a function of the profile length [25,27,36,39,40], squared areas were selected to allow an easier comparison of the estimates. Figure 11a shows the locations of these subareas, which were selected to be close either to one plot side or to the center of the plot. Per each subarea, three different DEMs were generated always using the 4-mm neighborhood: first, based on all four scans, second based on Scans 1&3 and third based on Scans 2&4 (DEM Set 4 in Table 2). Since the subareas were squares, the roughness spectra, as well as the roughness indices were estimated independently from both DEMs'

rows and columns. This means that the consistency of the index parameters was tested in both directions, along the x-axis (using the DEM's rows) and along the y-axis (using the DEM's columns).

Figure 11b shows three mean roughness spectra estimated from the rows of the three corresponding DEMs generated for Subarea 3. Considering the relative scan positions to the plot, this means that the spectrum based on Scans 1&3 (Spectrum 1&3) was estimated from the profiles sampled across the directional pattern, while the spectrum based on Scans 2&4 (Spectrum 2&4) was estimated from the profiles sampled along the directional pattern. The spectrum based on four merged TLS scans (four-scan spectrum) was considered here as the reference, since, according to Section 3.5, the directional pattern is not visible any more in its DEM, while its estimates are still consistent with the OTS estimates. To allow a better interpretation, an additional figure was prepared (Figure 11c), where the four-scan spectrum was subtracted independently from Spectrum 1&3 and Spectrum 2&4. The dotted and full lines are used there to indicate the differences of the spectra estimated along the x- and y-axis, respectively.

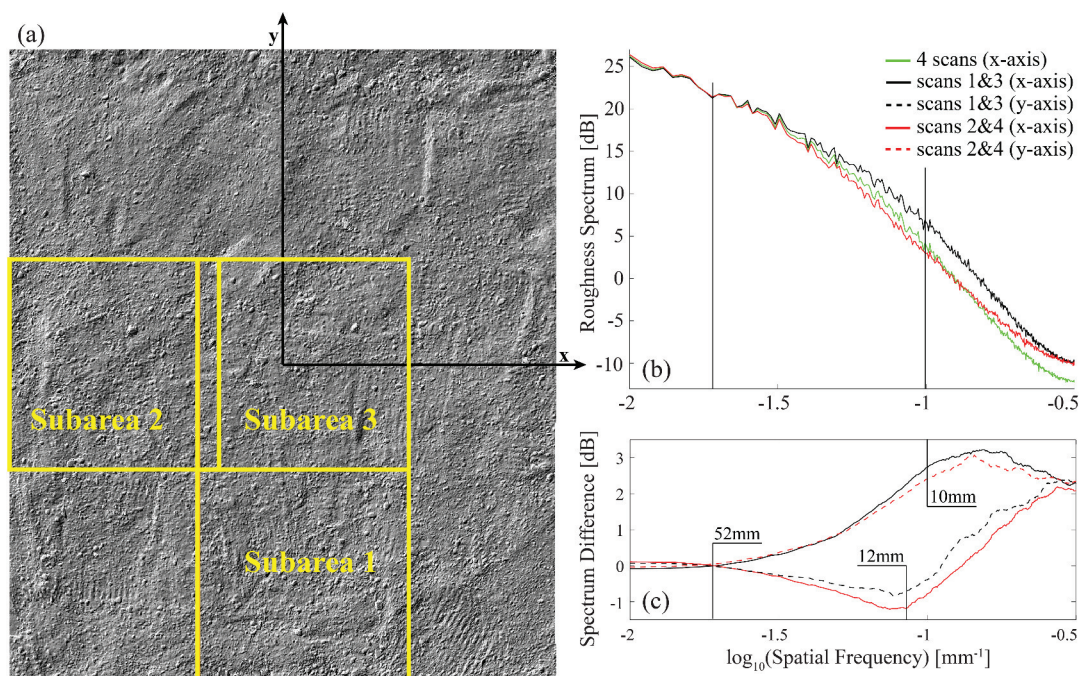


**Figure 11.** (a) Three subareas of the plot where the directional pattern was analyzed; (b) The roughness spectra of Subarea 3 estimated from the rows, *i.e.*, along the x-axis, of the three DEMs; (c) The differences of the roughness spectra with respect to the four-scan roughness spectrum, estimated along the x-axis (the full lines), as well as along the y-axis (dashed lines); The legend of the (b) is also valid for the (c).

As can be seen from Figure 11b,c, all of the spectra are almost identical at wavelengths larger than 50 mm, demonstrating that the directional effects are negligible within this frequency band. However, this is not the case for the frequency band that corresponds to the wavelengths between 50 mm and 10 mm, where Spectrum 1&3 and Spectrum 2&4 departed in opposite directions from the four-scan spectrum. This means that independently of the profile sampling strategy, the spectral slope, as well as the spatial correlation will be highly inconsistent within this frequency band due to the TLS's directional

pattern. The RMS height, on the other hand, will be in the same frequency band, either overestimated or underestimated, depending on whether the profiles are sampled across or along the directional pattern, respectively. The spectrum based on the across profiling, *i.e.*, Spectrum 1&3, continues to overestimate the four-scan spectrum almost constantly along all of the wavelengths smaller than 10 mm, which demonstrates that the two datasets perform the same nature of spatial correlation within this frequency band, while having biased RMS height values from one another. This is not the case for the along profiling, *i.e.*, Spectrum 2&4, which intersects the four-scan spectrum in the same frequency band. The same behavior of the roughness spectra was also observed for the other two subareas (the results are not presented here).

The roughness index values were also estimated for all three subareas and from the same DEMs. Figure 12 reports only the values estimated over Subarea 3, since the other two subareas confirm the same findings. The index values are displayed as box-plots grouped into two sections: the first is named the x-axis section, indicating that the values were estimated from the DEMs' rows, while the second is named the y-axis section, indicating that the values were estimated from the DEMs' columns. The box-plots' names reflect the TLS scans, which were used to generate the DEMs. It should be noted that each box-plot summarizes 1000 index values estimated from 1 m-long profiles.

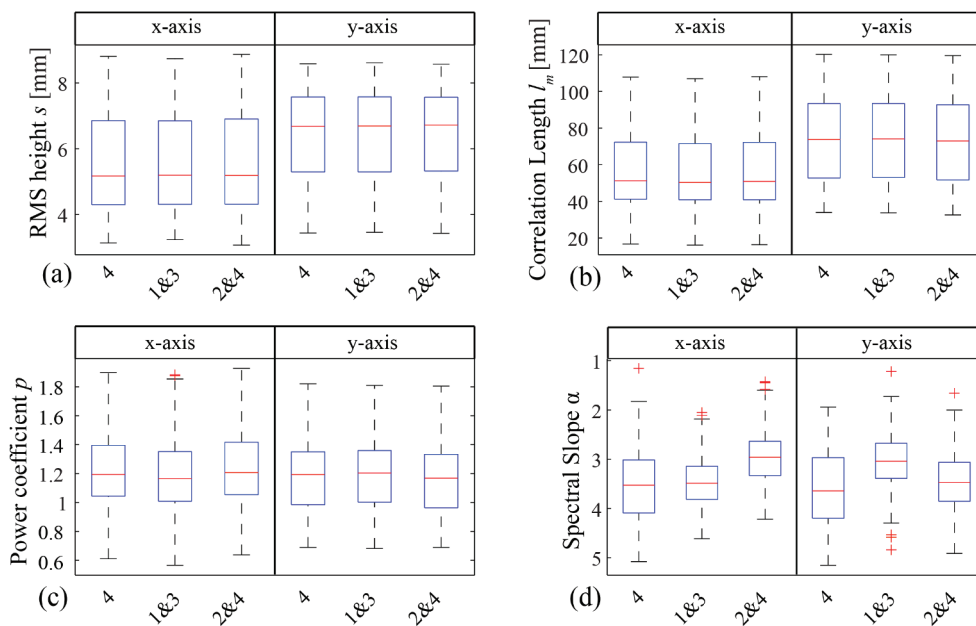


**Figure 12.** The values of (a) RMS height, (b) model correlation length, (c) power coefficient and (d) spectral slope, estimated independently, once from the rows (x-axis section) and another time from the columns (y-axis section), over Subarea 3. The names of each box-plot show the scans used to generate the DEMs: all four scans (4), the merged Scan 1 and Scan 3 (1&3) and the merged Scan 2 and Scan 4 (2&4).

As can be seen from Figure 12a,b, the box-plots within each section are consistent with one another, regardless of whether the profiles are sampled across or along the directional pattern (Box-plots 1 and 3 and 2 and 4). On the other hand, the index values estimated from the rows (the x-axis section) and

then from the columns (the y-axis section) are biased against one another, which reflects the degree of spatial anisotropy within Subarea 3. The consistency of the box-plots within each section for the RMS height and the correlation length confirm the observation from Section 3.5 that these two parameters are not sensitive to the TLS's directional deformations. The same conclusion can also be drawn for the parameter  $p$  based on Figure 12c, where the box-plots are also consistent. Interestingly, for the  $p$  parameter, the box-plots for the profiles sampled along the x-axis, as well as along the y-axis are also consistent, which indicates that this parameter does not reflect the spatial anisotropy observed by  $s$  and  $l_m$ . Finally, Figure 12d demonstrates that only the spectral slope parameter is again found to be sensitive to the directional pattern. There, the box-plots related to the along profiling (Box-plots 2 and 4 in the x-axis section and Box-plots 1 and 3 in the y-axis section) are inconsistent with the other two box-plots by more than 15%. Interestingly, the parameters  $\alpha$  and  $p$  also showed that the soil is isotropic at high frequencies, which is probably due to a rather round form of soil aggregate, as well as its random spatial distribution within the subarea.

The above analysis demonstrated that the directional pattern has little impact on wavelengths larger than 50 mm. For smaller wavelengths, *i.e.*, with values comparable to the size of the soil roughness elements, this pattern causes an overestimation in the roughness spectrum. This happens at high frequencies, where the roughness magnitudes are generally small. Therefore, this overestimation corresponds to a relative error in the correlation length and in the RMS height under 5%. If, however, the nature of soil spatial correlation up to the 50-mm lag is important to characterize, then either all four TLS's scans or two opposite scans and profiles sampled across the laser line of sight should be used to estimate the spatial correlation at this scale.

### 3.7. Comparison of Soil Roughness Derived from Single and Multiple TLS Scans

This section analyzes whether two opposite scans or even a single scan can replace the data from the four merged TLS scans, while preserving a similar accuracy for the  $s$  and  $l$  parameters. To answer this, four DEMs were generated over the whole plot (2.6 m  $\times$  3 m) using four different scan configurations: (1) single Scan 1; (2) single Scan 3; (3) merged Scan 1 and Scan 3; and (4) all four scans. These DEMs that belong to Set 4 in Table 2, were interpolated using and were interpolated using the 4-mm neighborhood setting, which corresponds to the optimal neighborhood size derived for the four-scan configuration in Section 3.4. This neighborhood was selected because the DEM based on the four-scan configuration was taken here as the reference. The four-scan DEM actually offers the best representation over the whole plot among the alternative DEMs. This is because the OTS data were not available for the whole plot, while the single-scan DEMs are not accurate in the far plot zone (Section 3.5). The two-scan DEMs (Scans 1&3 and Scans 2&4), on the other hand, have a directional pattern (Section 3.6), which was not the case for the selected four-scan DEM.

Figure 13a shows how the profile's heights taken from a single or two opposite scans are correlated with the heights of the same profile derived from all four scans. The profile's number is counted in the direction of the plot's y-axis, which means that profile Number 1 is closer to Scan Position 1, while profile Number 3000 is closer to Scan Position 3 (Figure 4). Since the whole plot was analyzed, this

means that the profile length was 2.6 m. Figure 13b,c reports the relative accuracy of the indices  $s$  and  $l_m$  (estimated from single or two opposite scans) with respect to their values estimated from the four scans. The negative relative errors mean underestimation, while the positive values mean overestimation of the index values with respect to the four scans.

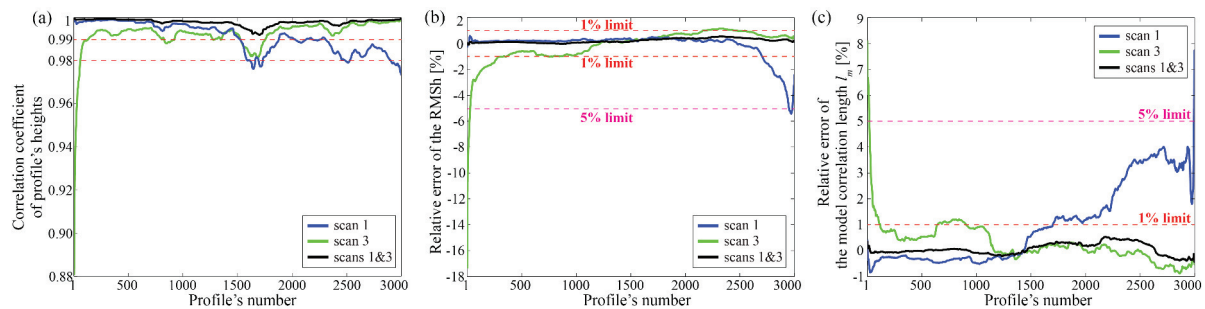


**Figure 13.** Comparison of (a) profile heights, (b) RMS height and (c) model correlation length, estimates based on single scans (green and blue lines) or two opposite scans (black lines) with respect to the corresponding estimates based on the four scans. The analyzed profiles have a direction parallel to the plot's x-axis.

Figure 13 shows that the combination of two opposite scans can fully replace the four-scan setting with a relative error in both roughness parameters of less than 1%. Furthermore, the DEM's heights interpolated from the two opposite scans are almost identical to the DEM's heights interpolated from the four scans (their correlation is better than 99% for all of the profiles within the plot). The relative errors of the indices estimated from the individual scans have a different behavior when the location of the profile departs from the scan position. Figure 13b,c shows that profiles closer to the scan position (the near field) slightly overestimate the index values derived from the four scans, as well as from the two opposite scans. Then, approximately after half of the plot, they start with the underestimation, which systematically increases till the end of the plot, which is opposite of the scan position. For example, the relative error of the RMSH for Scan 3 and Scan 1 exceeds the 1% limit at profile Numbers 358 and 2705, which happens approximately at scanning ranges larger than 4.2 m and 3.9 m, respectively. For the single scans, the point density gets lower and the incidence angles, as well as the ranges become larger in the far field. As shown in Section 3.5, this even smooths out larger soil aggregates, resulting in the observed underestimation of  $s$ . On the other hand, in the near field, the single scans have an optimal acquisition geometry, which allows one to depict slightly greater level of detail compared to the merged scans, where the points from the poorer acquisition geometry are added. These factors caused the observed overestimation of  $s$  in the near field. As expected, completely the opposite happened with the model correlation length. The individual scans first underestimate  $l_m$  based on the four scans, and then, in the further plot zone, they continue with systematical overestimation. For Scan 1, the 1% overestimation limit of this index happens at profile Number 1703, which corresponds approximately to the range of 3.0 m and an incidence angle of 55° (Figure 13c,d). Interestingly, the relative error of the model correlation length estimated from Scan 3 fluctuates around a 1% limit almost in the whole second part of the plot. A similar behavior of the relative errors and height correlations, which are reported in

Figure 13, was also observed when Scan 2, Scan 4, Scans 2&4 and the four scans were analyzed together (these results are, however, not shown here).

#### 4. Discussion

##### 4.1. Optimal Neighborhood Size and the EIFOV

The spatial resolution of the DEMs used in this study should be limited by the the resolution of TLS data used for their interpolation. On the other hand, Section 3.4 showed that although the DEMs' grid size was set to 1 mm, their spatial resolution was rather driven by the neighborhood size defined during the interpolation. Thus, the question is whether the optimal neighborhood size is consistent with a theoretical resolution measure for TLS point clouds, e.g., with the effective instantaneous field of view (EIFOV) suggested by Lichti and Jamtsho [1].

Figure 14 shows the EIFOV values calculated over the TLS ranges observed within our plot. The values were calculated by imposing the same assumptions on the system modulation transfer function (MTF) as in [1]. The blue curve comes from the theoretical sampling calculated from the horizontal angular increment specified for the “super-high” sampling mode of the Z + F IMAGER® 5006i instrument and assuming a perpendicular laser beam on the object. The latter is, of course, not the case for our measurement setup, and therefore, a corrected EIFOV (green line) was also calculated based on the point density that was directly estimated from individual TLS scans and which was already reported in Figure 3. Additionally, the optimal neighborhood sizes deduced for Scan 1 and Scan 3 (Section 3.4) are plotted at the ranges that correspond to the respective distances of these two scan positions with respect to the subplot. The optimal neighborhood sizes of the merged TLS data are not plotted here, because their neighboring points may have completely different ranges.

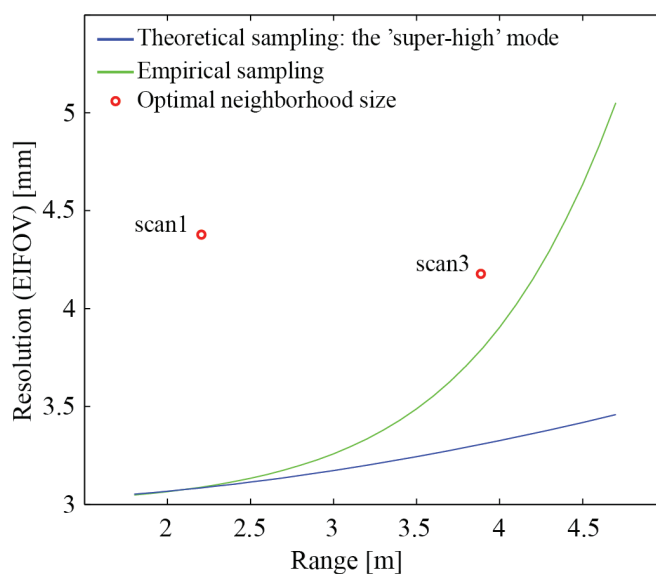


**Figure 14.** The effective instantaneous field of view (EIFOV) of an individual scan collect by Z + F IMAGER® 5006i over the ranges observed within the analyzed plot.

As can be seen from Figure 14, the optimal neighborhood sizes overestimate the spatial resolution of the individual TLS point clouds within the plot. This was expected, because the modulation transfer function associated with the applied interpolation method additionally lowers the spatial resolution of the DEMs compared to the point clouds. Another interesting result is that the uncertainty of the corrected EIFOV due to the range is about 2 mm within the plot. Compared to Figure 7 (Section 3.4), this value also corresponds to the uncertainty of the neighborhood size that is associated with the 1% relative error in the optimal spectral slope value. Such a variation in the neighborhood size does not change the relative errors of the  $s$  and  $l$  by more than 2%, as is shown by Figure 6 in Section 3.3.2. This means that the EIFOV and the optimal neighborhood size are consistent with one another for the applied measurement setting. Thus, the EIFOV value can also be used to determine the optimal neighborhood size under the 5-m TLS ranges. On the other hand, the optimization of the neighborhood size presented in Section 3.4 can then be seen as a practical approach to optimize the spatial resolution of a DEM interpolated from point clouds collected up to the 5-m TLS range.

#### 4.2. Optimal DEM and the Fractal Dimension

The optimization done in Section 3.4 ensures that the resulting DEM minimizes the spectral slope at high frequencies. This roughness index is directly related to the fractal dimension  $D$ , which (when estimated from the profiles) is given by [48]:  $D = (5 - \alpha)/2$ . Thus, it can be also formulated that the optimization in Section 3.4 maximizes the fractal dimension of the high-frequency roughness elements, while the measurement noise, as well as the loss in roughness detail are minimized. The optimization then leads to DEMs that will have an optimal resolution, as well as a distinctive stochastic property associated with the spatial correlation of the high-frequency roughness elements. The only assumption made to arrive at these optimal DEMs was that the roughness magnitudes should behave similarly to fractals in this frequency band. Thus, it was not assumed that the model given by Equation (4) is valid over the whole frequency domain, but rather within a small band. This is a fair assumption, especially for the soil surfaces, where the roughness is found to be predominantly exponentially correlated [25,36]. For such a spatial correlation, it is already known that its roughness spectrum approaches the fractal model at high frequencies [37]. Nevertheless, the experiment performed in this study certainly cannot answer whether the fractal dimension at high frequencies can be optimized for surfaces that have spatial correlations different from the exponential. A special study that will consider a wide range of surface roughness patterns should be carried out in order to answer this question.

It should be also mentioned that the interpolation strategy applied to ensure the gap-free conditions in the optimal DEM might not be appropriate for all applications. Large soil aggregates imposed occlusions on the TLS line of sight, and the occluded areas were later interpolated using the TIN method, which certainly does not describe the shape of the soil aggregates correctly. However, the results from Section 3.5 showed that these effects do not affect the  $s$  and  $l$  parameters significantly. Only in the case when the roughness at high frequencies should be described may the interpolation method have a significant impact. As was shown in Section 3.4 for large occlusions (e.g., Scan 3), the spectral slope value can be completely misinterpreted when estimated from the high frequencies. Another case where the interpolation may have a significant impact is the non-correlated sampling, *i.e.*, when the

average distance between neighboring points is larger than the laser beam footprint. In such cases, the choice of the interpolator will control the modulation of the roughness spectra much more strongly, and thus, stochastic interpolators, like Kriging, might be more appropriate. Nevertheless, the moving plane interpolation still remains a reasonable choice to model soil roughness within the 4-mm neighborhood from TLS data acquired in the correlated sampling mode.

#### 4.3. Conditions on the Laser Beam Footprint

The results in Section 3.3.2 show how the roughness values react when the spatial resolution of DEMs is reduced by enlarging the neighborhood size. Generally speaking, the same effect may also appear when a series of point clouds with a decreasing spatial resolution are used instead of the series of DEMs interpolated using different neighborhood values. Therefore, the result in Section 3.3.2 can also be seen as a way of simulating how the loss in point cloud resolution influences the index values. This then offers a possibility to introduce the conditions on TLS sampling under certain index's accuracy, as was done for the case of an ideal sampling in [38,39].

As is shown in Section 3.3.2, both  $s$  and  $l$  change by more than 5% when the neighborhood size increases from 4 mm to 20 mm. As the neighborhood size is an estimate of the spatial resolution (Figure 14), the above statement can be extrapolated on TLS point clouds. In this case, this would mean that the point cloud of 20-mm or a lower spatial resolution may introduce a relative error in both  $s$  and  $l$  that is larger than 5%. For the contemporary TLSs, which are rather diffraction- than sampling-limited, this would mean that the laser footprint should be under 20 mm to fulfill the 5% standard in the relative error. Particularly, for the TLS used in this study, such a condition on the laser footprint is fulfilled under a 45-m range. However, such a surprisingly weak condition on the TLS range is only valid in the case of an ideal acquisition geometry, *i.e.*, when the sampling line of sight is perpendicular to the object. Thus, this condition cannot be applied when the standard TLS tripods are used. The reason for allowing such a large laser footprint diameter can be due to the insensitivity of the  $s$  and  $l$  parameters on the very small roughness components, which was reported within Section 3.3.2. Thus, for roughness studies where the spatial correlation at high frequencies is important, this condition has to be revised according to the parameters that are more sensitive to the changes in this frequency band, *e.g.*,  $\alpha$  or  $p$ . For such applications, the optimal DEM from Section 3.4 offers the best trade-off between the measurement noise and the roll-off effects. Thus, the applied 5% standard on the relative error actually limits the departure of the considered point cloud from the point cloud that reflects the high frequency roughness the best.

The sampling conditions are usually not instrument oriented, but rather, expressed in terms of the correlation length. For example, Oh and Kay [39] found that the sampling interval should be at least 0.2 of the correlation length to obtain the index values with  $\pm 5\%$  precision. For the median correlation length ( $l_d = 118$  mm) estimated from all of the rows within the plot, this would mean that the spatial resolution should be  $\sim 50$  mm or better. Comparing this to the 5% condition on the laser footprint diameter (20 mm), it appears that the latter is more than two-times stronger, which was generally expected, because of the additional modulation due to the laser beam. In another theoretical study, Ogilvy and Foster [38] found that the sampling interval must be less than one tenth of the correlation length to detect the exponential nature of the spatial correlation around the origin, *i.e.*, at small lags. For our plot, this would mean that

the spatial resolution should be  $\sim 12$  mm or better to depict the exponential nature of the high-frequency roughness. In our study, the inherent nature of the spatial correlation at high frequencies was ensured by the optimization of the fractal dimension in this band, providing the optimal DEMs with a resolution between 4 mm and 4.5 mm, which is almost three-times better than the condition suggested by [38]. Ogilvy and Foster [38] also stated that when the sampling interval is larger than two thirds of the correlation length, the exponentially-correlated roughness may be misinterpreted as a Gaussian. For our experiment, this means that the spatial resolution should be larger than 150 mm to misinterpret the exponentially-correlated rows with a Gaussian. This condition can be best compared with the change in the  $p$  parameter and in the number of exponentially-correlated rows, reported in Figure 6d,f, respectively. The latter figure showed that at a spatial resolution around 40 mm or lower, all of the profiles performs the Gaussian spatial correlation, while the 5% relative error in  $p$  happens already at the spatial resolution around 10 mm. This is again more than three-times stronger than the condition suggested by [38].

It should be noted that the above condition on the TLS spatial resolution was derived from the correlation length estimated from the 2.6-m profiles of a smooth isotropic soil roughness plot. Such short profiles generally lead to the underestimation of the inherent correlation length of an isotropic soil roughness [25,27,36,39,40]. Thus, the imposed restriction on the TLS resolution is rather valid for roughness studies performed over similar isotropic roughness and at similar scales. To introduce more general conditions, which are independent of, e.g., the plot scale or roughness magnitude, a more extensive analysis should be done.

#### *4.4. Suitability and Limitations of TLS in Soil Roughness*

Terrestrial laser scanning was shown to be appropriate for soil roughness analysis according to several aspects. First, TLS offers high-resolution point clouds with low measurement noise at the plot scale. Section 3.4 showed that the spatial resolution of our optimal DEMs is between 4 mm and 4.5 mm, which is, e.g., more than ten times better than the ideal sampling condition imposed by Oh and Kay [39]. The TLS's resolution is also more than ten-times smaller than the wavelength of the C-band ( $\sim 5.7$  cm), which is, according to Ulaby *et al.* [22], sufficient for the application of modeling the backscatter of C- and L-band radar satellites. Then, the average 3D distance between the corresponding points among each TLS scan pair ranged from 0.9 mm to 1.1 mm, which is a good indicator for the TLS's relative accuracy within the plot. As shown by Lievens *et al.* [40], these relative accuracies do not have a significant impact on the soil moisture retrieval from the radar backscatter. Another of the TLS's advantages is that many standard processing tools are already available for processing raw TLS data [49,50]. As was demonstrated in this study, all of the important preprocessing tasks were successfully carried out by applying the standard software settings. Then, TLS is an active remote sensing technique, which allows measurements at any time of the day. Finally, the TLS is portable and needs a maximum of 20 min per station for scanning.

There are also certain limitations that are associated with TLS. The most striking one is certainly the directional pattern, which is a consequence of the AM-CW ranging technique. However, this feature is not only a problem for the AM-CW TLS, but also for other ranging techniques. For example, in the case of pulsed TLS, the measured range results from the decomposition of the transmitted pulse convolved

with the surface [51], which again affects the accuracy of the estimated range for the mixed pixels. Then, stereo imaging is also associated with an averaging within the pixel (the aperture diffraction limit) or even over several pixels when the circle of confusion is not optimally set [52]. On the other hand, Sections 3.5 and 3.6 demonstrated that the directional pattern does not affect the roughness spectrum at wavelengths larger than 50 mm, introducing a relative error in the  $s$  and  $l$  parametrization smaller than 5%. Therefore, two different applications of TLS in soil roughness have to be distinguished when this instrument is used: large-scale roughness analysis (scales larger than 50 mm) and small-scale roughness analysis (scales up to 50 mm). In the former application, the TLS data can be freely used, while in the latter application, a special profiling strategy should be applied to deal with the effects due to the directional pattern. As was shown in Section 3.6, either all the four TLS scans or two opposite scans and profiles sampled across the laser line of sight should be used to estimate the spatial correlation of the small-scale roughness. Such a strategy will also reduce the occluded area within a plot, which is also a drawback when only one TLS scan is used. Finally, the line of sight should be, as much as possible, perpendicular to the object, because this will minimize the occlusions, as well as the smoothing due to the laser footprint. In such cases, the laser footprint will have a circular shape rather than the elliptical one, which should then introduce a more isotropic smoothing in the object space. This can be easily achieved by increasing the height of the scanner, e.g., by using large tripods or by scanning from platforms when possible. Such a measurement setup would dramatically improve the incidence angles within the plot, shifting the range-incidence-angle functions notably to the right compared to the functions given in Figure 3d. This may also positively affect the quality of the resulting scans, increasing the point density and reducing mixed-pixel effects and the signal-to-noise ratio [47].

TLS is also suitable for scanning plots larger than  $2.6 \text{ m} \times 3 \text{ m}$ . However, this requires better planning of the measurement setup, where factors, like the roughness index accuracy, resolution (point density, as well as the laser beam footprint) and void area, have to be considered. We analyzed these factors in terms of the range and the incidence angle for our  $2.6 \text{ m} \times 3 \text{ m}$  plot and for the case of smooth, isotropic soil roughness. Thus, certain rules of thumb for both the range and incidence angle can be drawn from the presented results. Section 3.7 showed that for the ranges up to 3 m and the incidence angles smaller than  $55^\circ$ , the four-scan estimates of the model correlation length can be replaced with the single-scan estimates with a loss of 1% in the relative accuracy. Then, Section 3.5 showed that the spectral slope values estimated from the scan with high incidence angles (Scan 3, Figure 7b and Table 3) are notably biased against the OTS estimates of the spectral slope. This, however, was not the case for the scan where the incidence angles were no larger than  $40^\circ$  (Scan 1, Figure 7a and Table 3). It was also shown that a void area larger than 5% happens for some scans, even at the 2.5-m range and incidence angles below  $50^\circ$  (Figure 3c). On the other hand, Sections 3.4 and 4.1 showed that DEMs with 4-mm resolution can be reconstructed over the whole plot. This means that there are no further constraints on the range and the incidence angle, which come from the data resolution, *i.e.*, when the TLS data are acquired under the correlated sampling mode.

Based on the given findings, it can be concluded that the maximum recommended range is 3 m, which comes from the accuracy of the roughness index. The maximum recommended incidence angle is  $50^\circ$ , when the classical roughness parametrization ( $s$  and  $l_m$ ) is estimated. This limit comes from the maximum allowed void area of 5%. However, when the spectral slope is estimated, the maximum

recommended incidence angle is  $40^\circ$ . These recommendations, for example, can be considered when defining an effective area of a single scan and a number of scans required to survey large plots. The results also showed that two opposite scans (separated slightly more than 3 m from one another) can be used to survey large plots. This would mean that plots of 3 m in width and practically any length can be easily scanned with TLS. The distance between consecutive scan positions is, however, recommended to be no larger than 2.5 m, since this ensures an overlapping of the neighboring effective areas larger than 50%. Nevertheless, this parameter should be optimized with respect to the accumulation of the systematic errors of the relative orientation between the models [52].

The above findings are valid for smooth isotropic soil roughness. In case of larger isotropic or oriented soil roughness, some of the above conditions might become even stronger. This can be especially the case for the void area and, consequently, the point density, because large roughness elements introduce more occlusions. This might also increase the mixed-pixel effects, as well as the directional patterns discussed in Section 3.5. On the other hand, for other rough surfaces, like gravel, many roughness elements may be expected to be larger than the laser beam footprint at the 3-m range, and thus, the measurements might be more reliable. Nevertheless, these cases require additional experimentation to be answered.

## 5. Conclusions

In this study, a four-scan TLS setup was applied to study a smooth and isotropic soil roughness pattern over a  $2.6 \text{ m} \times 3 \text{ m}$  plot. A new method was introduced to generate DEMs that preserves the surface's stochastic property at high frequencies. The method optimizes the neighborhood size during the DEM interpolation, while minimizing the spectral slope, *i.e.*, maximizing the fractal dimension, of the roughness's high frequencies. The derived neighborhood sizes turned out to be also a good indicator of the DEM's spatial resolution. The acquired data allowed generating such DEMs at a 4-mm spatial resolution over the whole plot, which was then used as a base for roughness analysis. Soil roughness was analyzed in both the spatial and frequency domain and using four different roughness indices: root mean square height  $s$ , correlation length  $l$ , power coefficient  $p$  and spectral slope  $s$ . Additionally, a  $0.18 \text{ m} \times 1 \text{ m}$  subplot was surveyed with an optical triangulating scanner, and these data were used to evaluate the TLS-derived roughness.

The analysis showed that the roughness spectra estimated from the TLS and OTS data correspond to one another up to a spatial wavelength of 5 cm. Thus, TLS can be readily used for roughness assessment on this or larger scales, while for a smaller scale roughness assessment, special processing is required to mitigate the effect of the laser beam footprint. The latter involves two strategies: (1) using four scans collected from each side of the plot to generate the DEMs; or (2) using two opposite scans and then profiles that are perpendicular to the laser line of sight. Interestingly, the classical roughness parametrization (correlation length and root mean square height) turned out not to be sensitive to these distortions in the roughness spectrum, probably because they are more driven by low-frequency roughness. Thus, to detect such a small-scale roughness, the indices should be estimated from the high frequencies, where this roughness is well reflected.

The results also showed that the correlation length and the root mean square height values estimated from the four TLS scans can be replaced with the estimates from a single TLS scan acquired under

the maximum 3-m range and an incidence angle no larger than  $55^\circ$  without losing more than 1% in the relative accuracy of  $s$  and  $l_m$ . The estimates of two opposite scans can even replace the four-scan estimates over the whole plot area and under the same 1% relative accuracy loss. On the other hand, the spectral slope estimated from the single scan with incidence angles no larger than  $40^\circ$  was consistent with the estimates based on the OTS data. Additionally, the results showed that a decrease in the DEM's resolution from 4 mm to 20 mm may introduce a relative error in both the  $s$  and  $l$  indexes larger than 5%. Furthermore, the DEM's with a spatial resolution that is 12 mm or better can depict the exponential nature of the spatial correlation, while the DEMs with a resolution of 40 mm or lower cause the exponentially-correlated surface to appear as Gaussian. These values are more strict than the ones reported in previous theoretical studies.

The above results are derived for an oblique TLS scan acquired from classical geodetic tripods and for smooth and isotropic soil roughness conditions. Based on the presented analysis on the index accuracy, resolution and void area, a range up to 3 m and an incidence angle below  $50^\circ$  can be recommend when  $s$  and  $l$  should be estimated. For the spectral slope, the incidence angle limit is even stronger and should be no larger than  $40^\circ$ .

### **Acknowledgments**

The basics for this research were funded by the European Regional Development Fund (ERDF) in the framework of the Alpine Space Program within the project, NEWFOR (NEW technologies for a better mountain FORest timber mobilization). The experiment and the analysis leading to the presented results have received funding from the European Community's Seventh Framework Programme (FP7/2007–2013) under Grant Agreement No. 606971.

The authors also would like to thank Frank Schumacher, Thomas Backhausen and Prof. Michael Kiehn from the Botanical Garden of the University of Vienna, for making their facilities available and helping with the preparation of the roughness patterns. Many thanks are also given to Anke Schroiff and Karolina Korzeniowska, who helped during the measurements. Finally, the authors would like to thank the anonymous reviewers for their valuable comments and suggestions.

### **Author Contributions**

Milutin Milenković identified the research questions, planned the experiment, carried out the measurements, performed most of the data pre-processing, carried out the data analysis, wrote the manuscript and coordinated the review process. Norbert Pfeifer proposed the overall research field, supervised the data pre-processing and analysis, helped with writing the manuscript and commented on the manuscript. Philipp Glira performed the fine co-registration of the OTS and TLS blocks.

### **Conflicts of Interest**

The authors declare no conflicts of interest.

## References

1. Lichti, D.D.; Jamtsho, S. Angular Resolution of Terrestrial Laser Scanners. *Photogramm. Rec.* **2006**, *21*, 141–160.
2. Kaasalainen, S.; Krooks, A.; Kukko, A.; Kaartinen, H. Radiometric Calibration of Terrestrial Laser Scanners with External Reference Targets. *Remote Sens.* **2009**, *1*, 144–158.
3. Olofsson, K.; Holmgren, J.; Olsson, H. Tree Stem and Height Measurements Using Terrestrial Laser Scanning and the RANSAC Algorithm. *Remote Sens.* **2014**, *6*, 4323–4344.
4. Seidel, D.; Fleck, S.; Leuschner, C. Analyzing Forest Canopies with Ground-Based Laser Scanning: A Comparison with Hemispherical Photography. *Agric. For. Meteorol.* **2012**, *154–155*, 1–8.
5. Eysn, L.; Pfeifer, N.; Ressler, C.; Hollaus, M.; Graf, A.; Morsdorf, F. A Practical Approach for Extracting Tree Models in Forest Environments Based on Equirectangular Projections of Terrestrial Laser Scans. *Remote Sens.* **2013**, *5*, 5424–5448.
6. Kaasalainen, S.; Krooks, A.; Liski, J.; Raunonen, P.; Kaartinen, H.; Kaasalainen, M.; Puttonen, E.; Anttila, K.; Mäkipää, R. Change Detection of Tree Biomass with Terrestrial Laser Scanning and Quantitative Structure Modelling. *Remote Sens.* **2014**, *6*, 3906–3922.
7. Hodge, R.; Brasington, J.; Richards, K. *In Situ* Characterization of Grain-Scale Fluvial Morphology Using Terrestrial Laser Scanning. *Earth Surf. Process. Landf.* **2009**, *34*, 954–968.
8. Wang, C.K.; Wu, F.C.; Huang, G.H.; Lee, C.Y. Mesoscale Terrestrial Laser Scanning of Fluvial Gravel Surfaces. *IEEE Geosci. Remote Sens. Lett.* **2011**, *8*, 1075–1079.
9. Brasington, J.; Vericat, D.; Rychkov, I. Modeling River Bed Morphology, Roughness, and Surface Sedimentology Using High Resolution Terrestrial Laser Scanning. *Water Resour. Res.* **2012**, *48*, doi:10.1029/2012WR012223.
10. Smith, M.; Vericat, D.; Gibbins, C. Through-Water Terrestrial Laser Scanning of Gravel Beds at the Patch Scale. *Earth Surf. Process. Landf.* **2012**, *37*, 411–421.
11. Milan, D.J.; Heritage, G.L.; Hetherington, D. Application of a 3D Laser Scanner in the Assessment of Erosion and Deposition Volumes and Channel Change in a Proglacial River. *Earth Surf. Process. Landf.* **2007**, *32*, 1657–1674.
12. Williams, R.D.; Brasington, J.; Vericat, D.; Hicks, D.M. Hyperscale Terrain Modelling of Braided Rivers: Fusing Mobile Terrestrial Laser Scanning and Optical Bathymetric Mapping. *Earth Surf. Process. Landf.* **2014**, *39*, 167–183.
13. Ghuffar, S.; Székely, B.; Roncat, A.; Pfeifer, N. Landslide Displacement Monitoring Using 3D Range Flow on Airborne and Terrestrial LiDAR Data. *Remote Sens.* **2013**, *5*, 2720–2745.
14. Brodu, N.; Lague, D. 3D Terrestrial Lidar Data Classification of Complex Natural Scenes Using a Multi-Scale Dimensionality Criterion: Applications in Geomorphology. *ISPRS J. Photogramm. Remote Sens.* **2012**, *68*, 121–134.
15. Dorn, H.; Vetter, M.; Höfle, B. GIS-Based Roughness Derivation for Flood Simulations: A Comparison of Orthophotos, LiDAR and Crowdsourced Geodata. *Remote Sens.* **2014**, *6*, 1739–1759.

16. Marzahn, P.; Seidel, M.; Ludwig, R. Decomposing Dual Scale Soil Surface Roughness for Microwave Remote Sensing Applications. *Remote Sens.* **2012**, *4*, 2016–2032.
17. Darboux, F.; Davy, P.; Gascuel-Oudou, C.; Huang, C. Evolution of Soil Surface Roughness and Flowpath Connectivity in Overland Flow Experiments. *CATENA* **2002**, *46*, 125–139.
18. Taconet, O.; Ciarletti, V. Estimating Soil Roughness Indices on a Ridge-and-Furrow Surface Using Stereo Photogrammetry. *Soil Tillage Res.* **2007**, *93*, 64–76.
19. Kukko, A.; Anttila, K.; Manninen, T.; Kaasalainen, S.; Kaartinen, H. Snow Surface Roughness from Mobile Laser Scanning Data. *Cold Reg. Sci. Technol.* **2013**, *96*, 23–35.
20. Hugenholtz, C.H.; Brown, O.W.; Barchyn, T.E. Estimating Aerodynamic Roughness ( $z_0$ ) From Terrestrial Laser Scanning Point Cloud Data Over Un-Vegetated Surfaces. *Aeolian Res.* **2013**, *10*, 161–169.
21. Huang, C.h.; Bradford, J.M. Depressional Storage for Markov-Gaussian Surfaces. *Water Resour. Res.* **1990**, *26*, 2235–2242.
22. Ulaby, F.; Moore, R.; Fung, A. *Microwave Remote Sensing: Active and Passive*; Vol. II; Artech House: Boston, MA, USA, 1982.
23. Verhoest, N.E.; Lievens, H.; Wagner, W.; Álvarez-Mozos, J.; Moran, M.S.; Mattia, F. On the Soil Roughness Parameterization Problem in Soil Moisture Retrieval of Bare Surfaces from Synthetic Aperture Radar. *Sensors* **2008**, *8*, 4213–4248.
24. Hollaus, M.; Aubrecht, C.; Höfle, B.; Steinnocher, K.; Wagner, W. Roughness Mapping on Various Vertical Scales Based on Full-Waveform Airborne Laser Scanning Data. *Remote Sens.* **2011**, *3*, 503–523.
25. Mattia, F.; Davidson, M.; Le Toan, T.; D’Haese, C.; Verhoest, N.; Gatti, A.; Borgeaud, M. A Comparison Between Soil Roughness Statistics Used in Surface Scattering Models Derived from Mechanical and Laser Profilers. *IEEE Trans. Geosci. Remote Sens.* **2003**, *41*, 1659–1671.
26. Jester, W.; Klik, A. Soil Surface Roughness Measurement-Methods, Applicability, and Surface Representation. *CATENA* **2005**, *64*, 174–192.
27. Davidson, M.; Toan, T.L.; Mattia, F.; Satalino, G.; Manninen, T.; Borgeaud, M. On the Characterization of Agricultural Soil Roughness for Radar Remote Sensing Studies. *IEEE Trans. Geosci. Remote Sens.* **2000**, *38*, 630–640.
28. Rieke-Zapp, D.H.; Nearing, M.A. Digital Close Range Photogrammetry for Measurement of Soil Erosion. *Photogramm. Rec.* **2005**, *20*, 69–87.
29. Blaes, X.; Defourny, P. Characterizing Bidimensional Roughness of Agricultural Soil Surfaces for SAR Modeling. *IEEE Trans. Geosci. Remote Sens.* **2008**, *46*, 4050–4061.
30. Bretar, F.; Arab-Sedze, M.; Champion, J.; Pierrot-Deseilligny, M.; Heggy, E.; Jacquemoud, S. An Advanced Photogrammetric Method to Measure Surface Roughness: Application to Volcanic Terrains in the Piton de la Fournaise, Reunion Island. *Remote Sens. Environ.* **2013**, *135*, 1–11.
31. Perez-Gutierrez, C.; Álvarez-Mozos, J.; Martíñez-Fernández, J.; Sanchez, N. Comparison of a Multilateral-Based Acquisition with Terrestrial Laser Scanner and Profilometer Technique for Soil Roughness Measurement. In Proceedings of the 2010 IEEE International Geoscience and Remote Sensing Symposium (IGARSS), Honolulu, HI, USA, 25–30 July 2010; pp. 2988–2991.

32. Eitel, J.U.; Williams, C.J.; Vierling, L.A.; Al-Hamdan, O.Z.; Pierson, F.B. Suitability of Terrestrial Laser Scanning for Studying Surface Roughness Effects on Concentrated Flow Erosion Processes in Rangelands. *CATENA* **2011**, *87*, 398–407.
33. Barneveld, R.J.; Seeger, M.; Maalen-Johansen, I. Assessment of Terrestrial Laser Scanning Technology for Obtaining High-Resolution DEMs of Soils. *Earth Surf. Process. Landf.* **2013**, *38*, 90–94.
34. Nield, J.M.; King, J.; Wiggs, G.F.S.; Leyland, J.; Bryant, R.G.; Chiverrell, R.C.; Darby, S.E.; Eckardt, F.D.; Thomas, D.S.G.; Vircavs, L.H.; Washington, R. Estimating Aerodynamic Roughness Over Complex Surface Terrain. *J. Geophys. Res. Atmos.* **2013**, *118*, 12948–12961.
35. Haubrock, S.N.; Kuhnert, M.; Chabrillat, S.; Güntner, A.; Kaufmann, H. Spatiotemporal Variations of Soil Surface Roughness From In-Situ Laser Scanning. *CATENA* **2009**, *79*, 128–139.
36. Callens, M.; Verhoest, N.E.C.; Davidson, M. Parameterization of Tillage-induced Single-scale Soil Roughness from 4-m Profiles. *IEEE Trans. Geosci. Remote Sens.* **2006**, *44*, 878–888.
37. Dierking, W. Quantitative Roughness Characterization of Geological Surfaces and Implications for Radar Signature Analysis. *IEEE Trans. Geosci. Remote Sens.* **1999**, *37*, 2397–2412.
38. Ogilvy, J.A.; Foster, J.R. Rough Surfaces: Gaussian or Exponential Statistics? *J. Phys. D Appl. Phys.* **1989**, *22*, 1243–1251.
39. Oh, Y.; Kay, Y.C. Condition for Precise Measurement of Soil Surface Roughness. *IEEE Trans. Geosci. Remote Sens.* **1998**, *36*, 691–695.
40. Lievens, H.; Vernieuwe, H.; Álvarez-Mozos, J.; De Baets, B.; Verhoest, N.E. Error in Radar-Derived Soil Moisture due to Roughness Parameterization: An Analysis Based on Synthetical Surface Profiles. *Sensors* **2009**, *9*, 1067–1093.
41. Davidson, M.; Mattia, F.; Satalino, G.; Verhoest, N.; Le Toan, T.; Borgeaud, M.; Louis, J.; Attema, E. Joint Statistical Properties of RMS Height and Correlation Length Derived from Multisite 1-m Roughness Measurements. *IEEE Trans. Geosci. Remote Sens.* **2003**, *41*, 1651–1658.
42. Zoller+Fröhlich Technical Data z + f IMAGER 5006i. Available online: [http://www.geodis.cz/doc\\_product/datasheet/datenblatt\\_imager\\_5006i.pdf](http://www.geodis.cz/doc_product/datasheet/datenblatt_imager_5006i.pdf) (accessed on 3 February 2015).
43. Langer, D.; Mettenleiter, M.; Härtl, F.; Fröhlich, C. Imaging Ladar for 3-D Surveying and CAD Modeling of Real-World Environments. *Int. J. Robot. Res.* **2000**, *19*, 1075–1088.
44. Li, Q.; Shi, J.; Chen, K. A Generalized Power Law Spectrum and its Applications to the Backscattering of Soil Surfaces Based on the Integral Equation Model. *IEEE Trans. Geosci. Remote Sens.* **2002**, *40*, 271–280.
45. Mattia, F.; Le Toan, T.; Davidson, M. An Analytical, Numerical, and Experimental Study of Backscattering from Multiscale Soil Surfaces. *Radio Sci.* **2001**, *36*, 119–135.
46. Weichel, H. *Laser Beam Propagation in the Atmosphere*; SPIE Optical Engineering Press: Washington, DC, USA, 1990.
47. Soudarissanane, S.; Lindenbergh, R.; Menenti, M.; Teunissen, P. Scanning Geometry: Influencing Factor on the Quality of Terrestrial Laser Scanning Points. *ISPRS J. Photogramm. Remote Sens.* **2011**, *66*, 389–399.
48. Berry, M.V.; Lewis, Z.V. On the Weierstrass-Mandelbrot Fractal Function. *Proc. R. Soc. Lond. Ser. A Math. Phys. Sci.* **1980**, *370*, 459–484.

49. Otepka, J.; Ghuffar, S.; Waldhauser, C.; Hochreiter, R.; Pfeifer, N. Georeferenced Point Clouds: A Survey of Features and Point Cloud Management. *ISPRS Int. J. GeoInf.* **2013**, *2*, 1038–1065.
50. Pfeifer, N.; Mandlbürger, G.; Otepka, J.; Karel, W. OPALS—A Framework for Airborne Laser Scanning Data Analysis. *Comput. Environ. Urban Syst.* **2014**, *45*, 125–136.
51. Wagner, W.; Ullrich, A.; Ducic, V.; Melzer, T.; Studnicka, N. Gaussian Decomposition and Calibration of a Novel Small-Footprint Full-Waveform Digitising Airborne Laser Scanner. *ISPRS J. Photogramm. Remote Sens.* **2006**, *60*, 100–112.
52. Kraus, K. *Photogrammetry—Geometry from Images and Laser Scans*, 2nd ed.; De Gruyter: Berlin, Germany, 2007.

© 2015 by the authors; licensee MDPI, Basel, Switzerland. This article is an open access article distributed under the terms and conditions of the Creative Commons Attribution license (<http://creativecommons.org/licenses/by/4.0/>).

### 3.3 Paper III

**Title:** A comparison of UAV and TLS data for soil roughness assessment

**Authors:** Milenković, M., Karel, W., Ressler, C. and Pfeifer, N.

**Published in:** ISPRS Ann. Photogramm. Remote Sens. Spatial Inf. Sci., III-5:  
pp.145-152, <https://doi.org/10.5194/isprs-annals-III-5-145-2016>, 2016

**Licence:** ©2016. Authors. This manuscript version is made available under the Creative Commons Attribution 3.0 (CC BY 3.0) license

## A COMPARISON OF UAV AND TLS DATA FOR SOIL ROUGHNESS ASSESSMENT

M. Milenković<sup>a,\*</sup>, W. Karel<sup>a</sup>, C. Ressel<sup>a</sup>, N. Pfeifer<sup>a</sup>,

<sup>a</sup> Dept. of Geodesy and Geoinformation, Vienna University of Technology, Gußhausstraße 27-29, 1040 Vienna, Austria  
(Milutin.Milenkovic, Wilfried.Karel, Camillo.Ressel, Norbert.Pfeifer)@geo.tuwien.ac.at

Commission V, WG V/5

**KEY WORDS:** Autocorrelation function, Correlation length, Power spectral density, Fractal dimension, Error propagation, Bundle adjustment

### ABSTRACT:

Soil roughness represents fine-scale surface geometry which figures in many geophysical models. While static photogrammetric techniques (terrestrial images and laser scanning) have been recently proposed as a new source for deriving roughness heights, there is still need to overcome acquisition scale and viewing geometry issues. By contrast to the static techniques, images taken from unmanned aerial vehicles (UAV) can maintain near-nadir looking geometry over scales of several agricultural fields. This paper presents a pilot study on high-resolution, soil roughness reconstruction and assessment from UAV images over an agricultural plot. As a reference method, terrestrial laser scanning (TLS) was applied on a 10 m x 1.5 m subplot. The UAV images were self-calibrated and oriented within a bundle adjustment, and processed further up to a dense-matched digital surface model (DSM). The analysis of the UAV- and TLS-DSMs were performed in the spatial domain based on the surface autocorrelation function and the correlation length, and in the frequency domain based on the roughness spectrum and the surface fractal dimension (spectral slope). The TLS- and UAV-DSM differences were found to be under  $\pm 1$  cm, while the UAV DSM showed a systematic pattern below this scale, which was explained by weakly tied sub-blocks of the bundle block. The results also confirmed that the existing TLS methods leads to roughness assessment up to 5 mm resolution. However, for our UAV data, this was not possible to achieve, though it was shown that for spatial scales of 12 cm and larger, both methods appear to be usable. Additionally, this paper suggests a method to propagate measurement errors to the correlation length.

### 1. INTRODUCTION

Roughness is a property of surfaces, required to understand and model interaction at these surfaces, e.g. in hydraulics, radar remote sensing, or soil erosion. The assessment of roughness has been traditionally performed by mechanical profiling (Mattia et al., 2003), but this is naturally restricted by the length of the ruler and the effort to place it at different locations. With efficient methods for acquiring point clouds at high resolution like terrestrial laser scanning (TLS) and high density image matching (Lichti and Jamtsho, 2006) (Rothermel et al., 2012) (Rieke-Zapp and Nearing, 2005), new possibilities for assessing roughness arise. The range envelope for which roughness should be quantified depends on the application. In radar remote sensing, but likewise in the optical domain, the backscattering behavior depends on the roughness in relation to the wavelength (Ulaby et al., 1986). As an example, Sentinel-1 has a wavelength of 5.5 cm. Thus, the roughness between a few mm and up to several decimeters should be modeled.

The shape of a rough surface can be modeled as a random process, as a scalar function of the X- and Y-coordinate (Verhoest et al., 2008). Assessing the roughness therefore requires the study of a larger area. Using again the example of Sentinel-1, which has a resolution of 5 m x 20 m, a highly detailed surface model should be derived for an extent of several multiples of 20 m.

Terrestrial laser scanning has proven to be a suitable tool for modeling the roughness at the required scales. Positioning the TLS at large height above the ground, and restricting the ranges used, guarantees that roughness content placed close to the Nyquist frequency is assessed with 5% accuracy or better (Milenković et al.,

2015). However, for larger areas this procedure is less practicable due to the number of required stand points. Airborne acquisition, in contrast, allows large area coverage. However, standard photogrammetric flights cannot provide the resolution required. Lower flying heights would be necessary to reach it.

Using a UAV these low flying heights become possible: the airborne close range approach. Above that, low cost components (small UAVs, consumer cameras), make this approach interesting. However, little work has been performed on very high resolution mapping of irregular surfaces by UAVs. In (Eltner et al., 2013), UAV images with 2-4 mm ground sampling distance (GSD) were used to provide cm to sub-cm accurate DSMs for multi-temporal soil erosion monitoring. Also (Mancini et al., 2013) reported that UAV data with 6 mm resolution was acquired to monitor beach dune geometry. The heights reconstructed from this UAV data were within a few centimeters compared to the heights of a TLS data set used as the reference.

The aim of this article is to investigate if the quality obtained by TLS can be achieved also by light weight UAV image based acquisition. Specifically, in this paper data is acquired over a plot of bare soil, by TLS and with images from a UAV. The surface model from TLS serves as a reference and the model from the images is compared against it. This comparison is performed on the basis of roughness measures.

### 2. EXPERIMENT SETUP AND DATA

#### 2.1 Experiment Setup

TLS and UAV data were collected over an agricultural field, located just beyond the city border of Vienna, Austria. The measurements were performed one after another in a single day in

\*Corresponding author

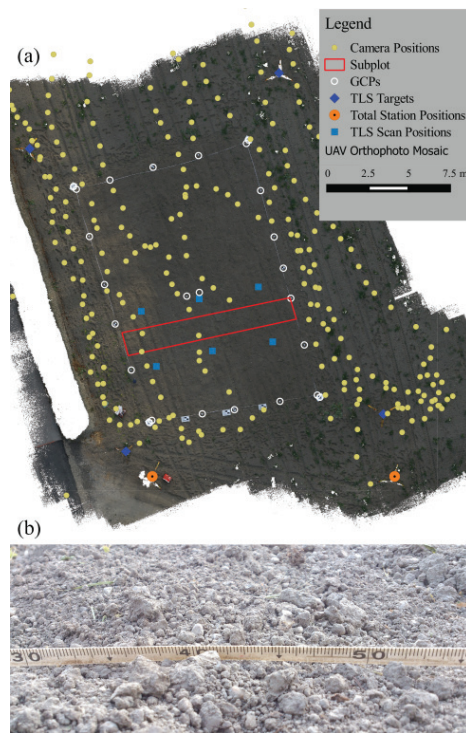


Figure 1: (a) The agricultural plot with the UAV and TLS measurement setup; (b) An image of the fine-scale roughness elements present in the plot.

June 2015. The weather was mostly sunny with some short cloud interruptions and without rain, but with wind that was strong enough to prevent the UAV from flying in autopilot mode.

The experimental setup is shown in Figure 1a, where the orthophoto derived from the UAV images was used as background. The large rectangular plot delineated by the ground control points (GCPs, the white circles in Figure 1a) was surveyed with the UAV images, while a subplot of ca. 10 m x 1.5 m (the red rectangle) was surveyed with the TLS. Additionally, total station measurements were performed to define a local datum, i.e. to derive coordinates of the GCPs in the local object coordinate system. The GCPs were symmetrically distributed around the plot and separated at maximum 3 m from one another. This, rather small, GCP spacing was selected to minimize systematic deformations in the object space due to residual errors in the images.

The agricultural soil plot contained roughness elements over several scales. The most prominent ones were low-frequency periodic surface components (2 to 3 cm in the amplitude) which were introduced with a mechanical, seed-bed preparation tool. On top of these components, there were randomly distributed soil clods (soil aggregates up to a few centimeters), very fine soil grains (Figure 1b), and a number of small, individual vegetation patches (up to a few decimeters). Since the purpose of this study was to characterize the bare soil roughness, this vegetation was removed from the plot before data acquisition.

## 2.2 UAV Images

The images were collected with a Sony  $\alpha$  ILCE-6000, an interchangeable lens camera mounted on an octocopter (Figure 4). The camera's sensor size is 23.5 mm x 15.6 mm, which corresponds to pixel size of 3.9  $\mu$ m. The camera was combined with a

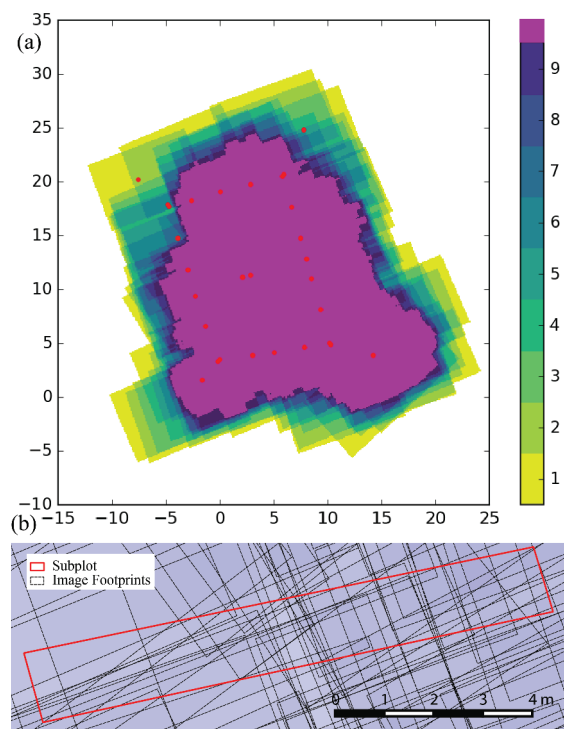


Figure 2: (a) Image density map (the GCPs are plotted as red dots); (b) Image footprints within the subplot.

zoom lens Sony AF E 16-70mm 4.0 ZA OSS, the focal length of which was 52 mm during image acquisition.

Due to strong wind, the flight was performed manually and as much as possible parallel to the two longer sides of the plot. The flight took 13 minutes to acquire 254 images, which were predominately distributed along the two longer sides of the plot, but with some of them also distributed along the plot's central axis (Figure 1). Thus, the acquired images were not distributed in the well-known regular strip pattern. Nevertheless, as shown in Figure 2a, the plot was covered everywhere with at least 9 images. The average flying height was 22 m, which resulted in a ground sampling distance (GSD) below 2 mm. The images were self-calibrated in a bundle block adjustment procedure.

The image resolution was then examined based on the edge spread function, also known as edge response (Perko et al., 2004)(Jacobsen, 2009). The edge spread function was calculated by the QuickMTF software ([www.quickmtf.com](http://www.quickmtf.com)) using the special test charts (provided by the software company) which were printed and fixed to flat plates on the ground during image acquisition (Figure 3a-b). The estimated modulation transfer functions for each color are shown in Figure 3. According to the 50 % modulation threshold, the reported resolution is 6 pixels, which is approximately 12 mm in the object space. This resolution is notably lower compared to the images' GSD (ca. 2 mm). One of the reasons for this degradation of image resolution is motion blur which is most probably caused by an inappropriate shutter time setting and vibration of the UAV.

## 2.3 TLS Data

In this experiment, the data collected with a Z + F Imager 5010c served as reference. Generally, UAV images observe soil from above, providing better viewing geometry compared to TLS data

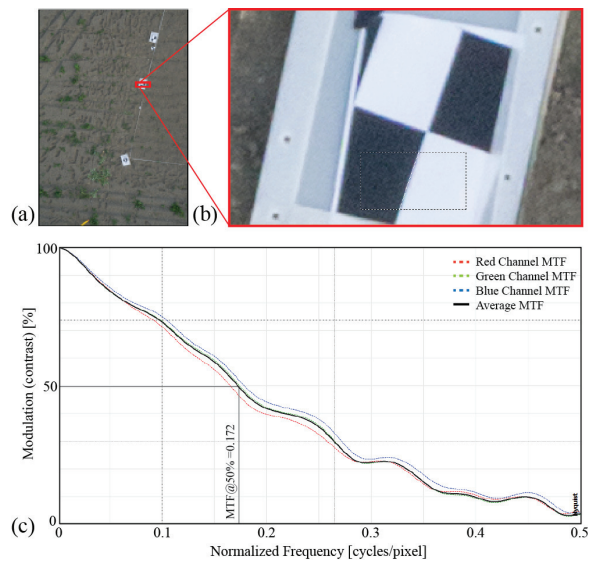


Figure 3: The modulation transfer function (MTF) corresponding to the edge spread function (measured in the in-flight direction) of an acquired image.

taken from classical geodetic tripods. However, UAV images are collected in a kinetic mode, which degrades the resolution by several pixels due to motion blur. On the other hand, the scanner itself is static and a single measurement takes less than one microsecond. Moreover, the TLS was applied here from a high tripod (instrument height  $>2.5\text{m}$ ) and with small ranges ( $<6\text{m}$ ), which provided more favorable viewing geometry and higher resolution compared to classical TLS setups and our UAV data.

**2.3.1 Measurement Setup** The subplot was scanned with 6 scan positions in total, where 3 of them were taken along each of the two longer sides of the subplot. To minimize occlusions and incidence angles, the scan positions were set approximately opposite to one another and the scanner was placed on a high tripod (Figure 4). The instrument height ranged from 2.55 m to 2.72 m. Scanning was performed in the high-quality and high-sampling mode, providing 10000 range measurements per full circle. The scanning started at 19:10 CET and completed in 50 minutes, taking on average 9 minutes per station.

The TLS points collected within the subplot have the following characteristics. 95 % of the points have a range smaller than 4.5 m. Since the scanner has a precise laser beam (3 mm beam diameter at the exit and a divergence of 0.3 mrad), the diameter of the laser-beam footprint was below 5 mm all over the subplot. 90% of the points have an incidence angle below  $52^\circ$ , which fulfills the requirements suggested by (Milenković et al., 2015) for TLS in roughness applications. The average point density within the subplot is 85 points/m<sup>2</sup>, while 90% of the subplot has at least 40 points/m<sup>2</sup>, i.e. the point spacing within the subplot is 1.5 mm or smaller. This means that the laser-beam footprints of neighboring points were overlapping one another, which is also known as the correlated sampling mode where the resolution of the TLS data is rather limited by the laser beam footprint (Lichti and Jamtsho, 2006) and (Milenković et al., 2015). This means that the resolution of this TLS data is approximately 5 mm.

**2.3.2 TLS Data Pre-Processing** The six raw TLS scans were first preprocessed in “Z + F Laser Control” software where the mixed-pixel and single-pixel filters were applied. These filters

remove points with erroneous range values happened when the laser beam of a phase-comparison laser scanner illuminates several objects distributed along the laser line of sight (Langer et al., 2000). For our surface, this mostly happened when the laser beam simultaneously illuminated the top of a soil clod and the soil surface in the background. In addition to these filters, the intensity filter was applied to remove points with an intensity smaller than 1 %. These points are generally less accurate because their range determination is associated with a small signal to noise ratio (Langer et al., 2000).

The parameter values used in the above filters (mixed-pixel, single-pixel and intensity) are the default values recommended by the “Z + F Laser Control” software. This default parameter setting was already found to be appropriate for soil-roughness preprocessing (Milenković et al., 2015).

### 3. METHODS

#### 3.1 UAV Data Processing

The UAV imagery was oriented and the camera was calibrated using OrientAL (Karel et al., 2013). Missing any direct sensor orientation data, processing started with a variation of Structure-from-Motion (SfM) (Torr and Zisserman, 2000): image feature points are detected in each image and their neighborhoods are described, after which point pairs with similar descriptors are matched between image pairs. Relative image pair orientations are computed and outlier matches discarded. For an initial image pair, object points are forward intersected and both camera orientations and object points are optimized in a bundle block adjustment. Subsequently, additional images are added to the block one after another by spatial resection and further object points are triangulated, until all images have been oriented. Aiming at the error-free and precise orientation of all images, robust methods are employed at all stages, and intermediate bundle block adjustments are executed after the addition of further images. Already the pairwise image matching takes place in Euclidean space, using an approximate interior orientation derived from Exif data. In contrast to other software packages, OrientAL estimates a variable set of lens distortion parameters, depending on their signif-



Figure 4: The TLS and UAV instruments used in this experiment.

inance and stability, and to better handle perspective image distortion, we use Affine SIFT features (Morel and G.Yu, 2009), which are not only scale and rotation invariant, but also invariant to affine distortion. Finally, the maximum admissible image point residual norm is not a fixed parameter, but is derived from the data itself.

Using these relative image orientations, we forward intersect the GCPs into model space using their manual image observations, apply the resulting similarity transform to the bundle block, and introduce additional observations for the GCPs in image and object space, taking into account their stochastic nature. While we assumed the standard deviations of feature point image observations a priori to be 1 pix, image observations of control points were given the higher precision of 0.1 pix due to their higher definition accuracy. Observations of control point coordinates in object space were assigned a standard deviation of 1 mm a priori. This resulted in median residual norms for feature image points of 0.46 pix, for GCP image points of 0.97 pix, and for GCP object points of 14 mm. The rather large residuals of GCP image points may be a result of the weak block geometry with 2 flight strips of extremely high overlap along-track, but low overlap across-track.

### 3.2 Data Co-Registration

Before interpolation and data comparison, it was necessary to bring the UAV and TLS data into the same local object coordinate system (LOCS). This was done through several co-registration steps. First, the individual TLS scans were georeferenced to the LOCS with the help of the control points measured with the total station. This procedure was performed using an adjustment procedure implemented in “Z + F Laser Control” software. Then, in an additional step, the individual TLS scans were co-registered to one another using a variant of the iterative closest point (ICP) algorithm implemented in the software OPALS (Ghira et al., 2015). This step minimizes the point-to-surface distance among all the scans, and for our 6 scans data, the standard deviation of this distance after the ICP procedure was 0.8 mm. This value is just two times the specified measurement noise of the Z + F IMAGER 5010c scanner, which suggests at very good co-registration of the TLS scans. The six TLS scans were then merged into one TLS point-cloud block.

The UAV images were oriented through a bundle adjustment procedure where the GCP coordinates measured with the total station were also used as observations. Thus, the resulting exterior camera parameters were already in the LOCS. This means that the densely matched points as well as the automatically derived UAV DSM are both in the LOCS. Still, in order to remove any remaining residual errors in the absolute orientation and to optimize the relative orientation between UAV DSM and TLS DSM, another ICP run was applied to both DSMs. The standard deviation of the final point-to-surface distances between UAV DSM and the TLS block was 4 mm.

### 3.3 Detrending and DSM Interpolation

Roughness analysis is generally performed on detrended heights. Thus, the UAV and TLS data were additionally detrended here using the regression plane fitted through the TLS points within the subplot. This means that the detrended UAV and TLS heights were calculated as the normal residuals to the regression plane, while the planar coordinates were additionally reduced to the center of gravity of the TLS points.

The TLS DSM was interpolated from the detrended TLS point-cloud block. The interpolation was done for a 1 mm grid spacing

and with the moving plane interpolation applied to points within a 2.5 mm neighborhood radius. This neighborhood size was selected to match the size of the laser beam footprint within the plot. The UAV DSM was automatically produced by the SURE software (Rothermel et al., 2012), where the bundle results were supplied as input.

### 3.4 Roughness Assessment

Surface roughness is treated here in two ways: (a) through the so-called classical parametrization, i.e. as a zero-mean Gaussian process characterized by the root mean square (RMS) height, autocorrelation function (ACF) and correlation length ( $l$ ) (Verhoest et al., 2008), and (b) as a band-limited random fractal surface characterized by the spectral slope ( $\alpha$ ), i.e. fractal dimension  $D = \frac{5-\alpha}{2}$  (Davidson et al., 2003). Both parametrizations were estimated as in (Milenković et al., 2015), i.e. from linearly-detrended soil-roughness profiles sampled as rows of the TLS and UAV DSMs.

For the classical parametrization, first the empirical autocorrelation function was derived, with its value for a lag  $\tau_k$  calculated as:

$$\hat{r}(\tau_k) = \frac{1}{N-k} \sum_{i=1}^{N-k} z_i z_{i+k} \quad (1)$$

where  $\tau_k = k \cdot \Delta x$  with  $k$  being the lag increment, and  $\Delta x$  being the DSM’s grid size.  $N$  is the number of height samples in a DSM row, while  $z_i$  and  $z_{i+k}$  are the DSM row heights at positions  $i$  and  $i+k$ , respectively. The RMS height  $s$  was estimated as  $s^2 = \hat{r}(0)$ , while the correlation length  $l$  was calculated as in (Davidson et al., 2003), i.e. directly interpolating the normalized autocorrelation function  $\rho(\tau_k) = \hat{r}(\tau_k)/\hat{r}(0)$ :

$$l = \tau_m + (e^{-1} - \rho(\tau_m)) \frac{\tau_{m+1} - \tau_m}{\rho(\tau_{m+1}) - \rho(\tau_m)}, \quad (2)$$

where  $\tau_m \leq l \leq \tau_{m+1}$  and  $\rho(\tau_m) \leq e^{-1} \leq \rho(\tau_{m+1})$ .

For the fractal parametrization, it was necessary first to estimate the power spectral density (the roughness spectra). This was done by calculating the assembly-average of the hamming-windowed periodograms derived from the sampled DSM rows (Milenković et al., 2015). Based on the derived roughness spectra, the spectral slope  $\alpha$  is calculated as the slope of a regression line used to approximate the roughness spectrum on the logarithmic scale and within a particular frequency band (Dierking, 1999). In the linear-scale frequency domain, the latter is equivalent to:

$$S(f) = c \cdot f^{-\alpha} \quad (3)$$

where  $f$  is the spatial frequency,  $\log_{10}(c)$  is the intercept of the regression line, and  $S(f)$  is the roughness spectrum.

**3.4.1 Roughness Levels of Detail** The roughness level of detail present in the TLS- and UAV-DSM is judged in two ways: (a) qualitatively, by visual comparison of the DSMs’ shaded models, and (b) quantitatively, by calculating the difference of the estimated UAV and TLS roughness spectra. The roughness spectra difference can reveal the spatial wavelengths (scales) over which two corresponding DSMs share the same roughness information. According to the study of (Oh and Kay, 1998), which is based on synthetic data, the roughness spectra difference should be below 1 dB for accurate prediction of the microwave backscatter strength.

### 3.5 Autocorrelation Function and Error Propagation

The TLS DSM and UAV DSM which are used to derive the autocorrelation functions are not free from measurement and inter-

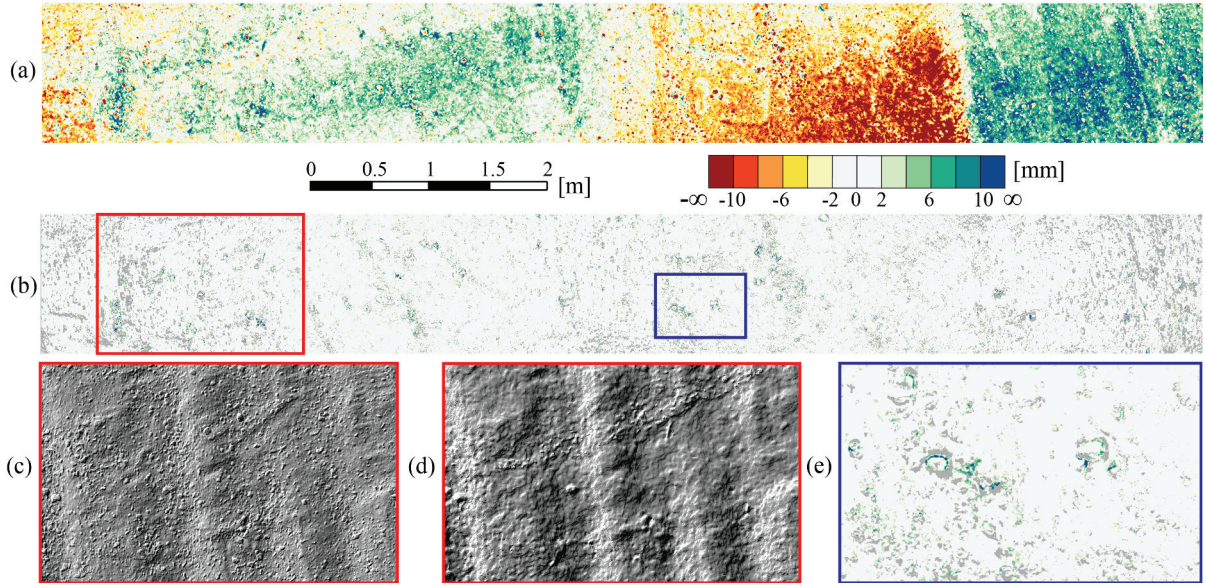


Figure 5: (a) Difference map between the TLS- and the UAV-DSM; (b) Min-max distance map derived from the DSMs of six overlapping single-TLS scans; (c) and (d) are shaded TLS- and UAV-DSM, respectively, from the region marked by the red rectangle in (b); (e) is the zoom-in to the blue rectangle in (b).

polarization errors. Thus, this section considers how these errors can be quantified and propagated further to the autocorrelation estimates.

For the TLS DSM, the height errors are quantified with the moving-plane interpolation error  $\sigma_z$ . This error is derived for each grid position by propagating the RMS error of the plane adjustment procedure of the neighboring points during the interpolation process. Since the neighborhood used in our case is small (2.5 mm radius), the interpolation error can be seen as a mixture of the measurement noise as well as the modeling error caused by a planar approximation of roughness elements like soil clods.

For the UAV DSM, the height error is quantified as the standard deviation ( $\sigma_{MAD}$ ) derived from the median of absolute differences of the dense-matched point's heights within 6 mm neighborhood radius. The dense-matched points are one of the outputs provided by SURE, and they are calculated while matching a base image with several neighboring images (Rothermel et al., 2012). This means that for each pixel of a base image there are several reconstructed heights corresponding to the neighboring image pairs. Therefore, the DSM heights (also provided by SURE) can be seen as a median-like filter of the matched points. The  $\sigma_{MAD}$  estimation radius (6 mm) was set according to the image resolution in the object space (ca. 12 mm).

$\sigma_z$  and  $\sigma_{MAD}$  are available for each height of the TLS DSM and UAV DSM, respectively. Based on Eq.(1), it is possible to propagate  $\sigma_z$  and  $\sigma_{MAD}$  further to the autocorrelation values for each particular lag. This can be easily done when Eq.(1) is seen as linear combination, i.e. as a product of a row vector  $\mathbf{h}_k^\top$  and a column vector  $\mathbf{z}$ :

$$\hat{r}(\tau_k) = \frac{1}{N-k} \sum_{i=1}^{N-k} z_i z_{i+k} = \mathbf{h}_k^\top \cdot \mathbf{z}, \quad (4)$$

where:

$$\mathbf{h}_k = \frac{1}{N-k} \begin{bmatrix} \mathbf{0} \\ z_1 \\ \vdots \\ z_{N-k} \end{bmatrix}, \text{ and } \mathbf{z} = \begin{bmatrix} z_1 \\ z_2 \\ \vdots \\ z_N \end{bmatrix},$$

while the first  $k$  elements of  $\mathbf{h}_k$  are zeros. For the zero-lag autocorrelation  $\hat{r}(0)$ , it holds:  $\mathbf{h}_0 = \frac{1}{N}\mathbf{z}$ . Following the error propagation law for  $\mathbf{h}_k$  and  $\mathbf{z}$  (both contain individual random variables), the expression for the variance of a single-lag autocorrelation value  $\hat{r}(\tau_k)$  is:

$$\hat{\sigma}_{r_k}^2 = \mathbf{h}_k^\top \cdot \Sigma_{zz} \cdot \mathbf{h}_k + \mathbf{z}_k^\top \cdot \Sigma_{\mathbf{h}_k \mathbf{h}_k} \cdot \mathbf{z}_k \quad (5)$$

$\Sigma_{zz}$  is a full diagonal matrix containing variances  $\sigma_{z_i}^2$ , while  $\Sigma_{\mathbf{h}_k \mathbf{h}_k}$  is the same as  $\Sigma_{zz}$ , but with the first  $k$  diagonal elements equal to zero. Finally, to compute the variance of  $\hat{r}(\tau_k)$  for the TLS DSM, the  $\sigma_{z_i}^2$  values are replaced with  $\sigma_z^2$ , while in case of the UAV DSM, the  $\sigma_{MAD}^2$  is used instead.

## 4. RESULTS AND ANALYSIS

### 4.1 Accuracy of Data Co-Registration

Improper data co-registration may lead to false roughness analysis. Thus, two elevation-difference rasters were prepared to report on the co-registration accuracy: one to check the co-registration of the individual TLS scans, and another to check the co-registration of the TLS DSM and UAV DSM.

The co-registration of the individual TLS scans was checked with the minimum-maximum elevation difference (range) for each pixel of a set of six overlapping DSMs interpolated from the individual TLS scans. Figure 5b shows the color-coded range map for our 6 TLS scans over the subplot with a pixel size of 1 mm. Since the range values are non-negative, the colors correspond only to the right half of the given color palette. The gray values show the

areas which contain just one individual TLS DSM, and they occupy about 30% of the plot. The 95% of the remaining area contains range values below 2 mm, which indicates a very good co-registration of the TLS scans. The remaining 5% of large range values occurs mostly around the soil clod edges, which can be seen in Figure 5e. This is because the moving-plane interpolation with a neighborhood radius of 2.5 mm (the interpolation method used for the DSM interpolation) does not perform well on soil clod borders. However, these are generally known interpolation artifacts that can not be easily overcome with our TLS data.

Figure 5a shows the color-coded elevation differences between the UAV DSM and the TLS DSM. Due to the ICP minimization between the two DSMs performed in the preprocessing step, the differences are on average zero, and 90% of the differences are within  $\pm 9$  mm. However, within this accuracy range, there are also large systematic patterns in the difference map. After careful examination, it was found that borders between regions of positive and negative differences correspond to image borders (see Figure 2b). Residual image orientation errors may be responsible for that. These orientation errors could be caused by insufficient overlap between individual image sub-blocks. Additionally, during the image acquisition, the image stabilization was switched on to reduce motion blur, which caused unstable inner geometry of the camera, and consequently, difficulties to determine a single distortion model valid for all images. With an accuracy of  $\pm 9$  mm this UAV DSM is only sub-optimal. Still, within this accuracy bound, the UAV DSM can be used for the comparison with the TLS DSM. However, this experience raises the awareness that the acquisition of the UAV images should be conducted with much more care - especially regarding the stability of the inner image geometry. For an identical image set with a stable inner geometry, the accuracy of the UAV DSM should be expected to be notably higher, and without the systematic effects shown in Figure 5a.

#### 4.2 Roughness Assessment in Frequency Domain

The TLS and UAV DSMs of the whole plot are analyzed here in the frequency domain. Figure 6 shows two roughness spectrum lines derived from the TLS DSM (red) and UAV DSM (blue), respectively. They are the ensemble-average, hamming-windowed periodograms derived from 100 rows of the corresponding DSMs. To make interpretation easier, the periodograms were further smoothed with the moving average with the span of 100 elements. This procedure preserves the general trend of the periodogram while removing the undesirable variability associated with this estimator. The black line in Figure 6 shows the difference between the TLS- and UAV-based periodograms.

There are 4 frequency bands where the roughness spectra perform differently. These bands are separated with the three vertical dashed lines in Figure 6. The very right band (from the Nyquist up to the 5 mm wavelength) of the TLS spectrum shows a white-noise (horizontal) roll-off, indicating that there is no further information contained. This is fully consistent with the resolution of the TLS DSM, i.e. with the diameter of the laser footprint which was up to 5 mm within the subplot. These frequencies are present in the periodogram because the TLS DSM was unnecessarily interpolated to 1 mm grid even though the resolution of the data itself was lower (5 mm). However, this was performed just to have an additional estimate of the resolution of our control data set, and to illustrate that the Nyquist frequency does not necessarily indicate the resolution of a DSM. Additionally, it can be seen that the roughness spectrum at these frequencies is below -20 dB, which is several orders of magnitude smaller than the TLS measurement noise. This indicates that the measurement noise is

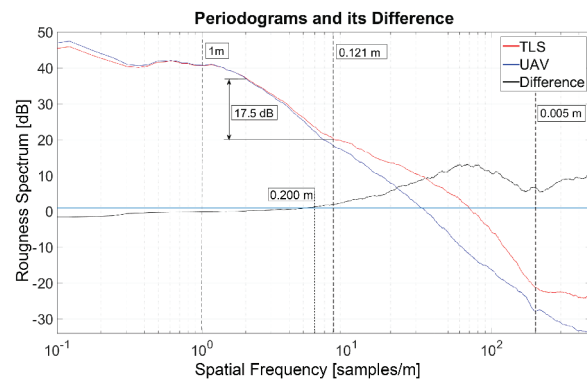


Figure 6: The PSD functions

filtered out from the TLS point cloud during the DSM interpolation. Thus, it shows that the TLS data are appropriately modeled.

From the spectra difference, it can be shown that the roughness spectra are similar in the first two frequency bands up to the 1 dB limit (the blue horizontal line in Figure 6). The 1 dB limit was selected according to a study of (Oh and Kay, 1998). This practically means that the TLS DSM can be readily replaced with the UAV DSM when the relevant roughness content is placed along wavelengths up to 20 cm. For shorter wavelengths (from 20 cm till 5 mm), the TLS roughness spectrum contains much more roughness information than the UAV spectrum. This can also be seen in the two shaded DSMs (Figure 5c and 5d), which clearly show that the TLS DSM contains much more roughness elements at these scales compared with the UAV DSM, where they are smoothed out. The latter effect is most probably a consequence of image resolution and orientation errors which directly influence the DSM.

In the second frequency band (from 1 m to 12 cm wavelengths), both spectra exhibit a linear (fractal) nature, while the power of the UAV DSM drops faster (17.5 dB per 0.5 of decade) compared with the TLS power drop (17.5 dB per 0.6 of decade). The latter is equivalent to the spectral slope values of 3.5 and 2.6 for the UAV- and TLS-DSM, respectively. Thus, in this frequency band, the UAV DSM has a slightly higher spectral slope (smaller fractal dimension) compared with the TLS DSM. This shows that even though the underlying surface is identical for both data sets, the UAV and TLS data suggest two families of surfaces with different stochastic properties. This, in turn, may cause an inconsistent prediction of the microwave backscatter energy from the same surface.

Finally, in the very left frequency band (from DC till 1 m wavelength), the UAV spectrum is on top of the TLS spectrum, which is opposite to its behavior along the remaining frequencies. This shows that UAV spectra has more power at these frequencies compared with the TLS DSM, which is a consequence of the systematics present in the UAV DSM (Figure 5a).

#### 4.3 Roughness Assessment in Spatial Domain

The TLS and UAV DSMs of the whole plot are also analyzed in the spatial domain by comparing individual profiles and their autocorrelation functions. Figure 7a shows single height profiles sampled at the identical location in the TLS DSM (red line) and UAV DSM (blue line). From the zoomed-in area (Figure 7b), it can be clearly seen that TLS profiles reconstructed much more roughness level of detail compared with the UAV profile. This is particularly true for the soil aggregates up to 3 mm in size, which

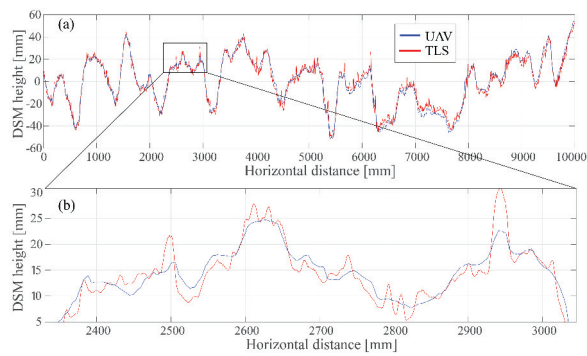


Figure 7: (a) Single TLS and UAV height profiles sampled at identical location from the corresponding DSMs; (b) Zoom-in to portions of the profiles in (a).

are completely smoothed out in the UAV profile (e.g. section from 2.6 m to 2.7 m, Figure 7b). However, due to the systematic errors in the UAV DSM, this did not have an effect on the profiles' RMS height values, where the RMS height of the UAV profile ( $s_{uav} = 22$  mm) was found even larger than the RMS height ( $s_{tls} = 20$  mm) of the TLS profile.

The correlation length, as a measure of roughness, was determined for both data sets. As can be seen in Figure 8 the shapes of the autocorrelation functions are similar, and the faster drop was explained as result of the finer details visible in the TLS data. The correlation length determined from the UAV images is thus approximately 15% larger than for the TLS data. In this article error propagation was used to forward the uncertainty of elevation to uncertainty of the autocorrelation function and further to the precision of the estimated correlation length. Given the lower accuracy of the image based surface model, the precision of the corresponding correlation length is poorer, too, but still only a few percent of the correlation length. This uncertainty is much lower than the offset in correlation length between the two methods. This suggests, that this error estimate is too optimistic, and a likely cause is that correlations between the individual elevation measures remained unconsidered (diagonal matrix in Eq (5)).

## 5. DISCUSSION AND CONCLUSIONS

In this experiment, a UAV data set was analyzed for soil roughness assessment. The images used in the experiment had a resolution of 12 mm, which is low compared to the GSD of 2 mm. The reason was the motion blur and poor lighting conditions, which led to a loss of sharpness at the individual pixel level. Terrestrial laser scanning was used as a reference method here, which does not suffer from these two effects.

Although in this experiment the TLS was selected as the reference, point clouds based on overlapping images taken very close to the object and using static acquisition can be more accurate. For example, the vertical accuracy and GSD of an image block taken 1 m apart from the object and with a contemporary camera and a normal-angle lens, can be a few tenths of mm (Kraus, 2007). This is notably better than the TLS co-registration accuracy and the laser footprint, both found here to be of a few mm. Thus, in further experiments, static and very close-range overlapping imaging can be considered as the reference as well.

In Figure 5a systematic errors in the surface model derived from dense image matching became apparent, under the assumption that the TLS data serves as reference. That these systematic errors

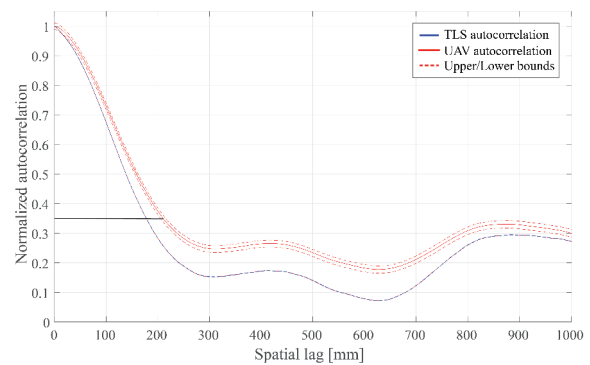


Figure 8: Normalized autocorrelation functions based on the TLS DSM and UAV DSM. The red dashed lines show the  $3\sigma$  bounds of the propagated errors.

are related to the bundle block adjustment or the dense matching is further supported by the comparison of the pattern of Figure 5a to Figure 2b, which shows the overlap as grey tone and the image borders. Changes from negative to positive errors occur at regions where the overlap strongly drops. Thus, we conclude that images within the bundle formed a sub-block which has strong ties within itself, but poorer ties to neighboring sub-blocks. In this context it is noted that clods and soil grains may look differently from different perspectives, e.g. due to cast shadow, near vertical elements, etc. This would introduce high correlation between some images, which is not considered in the stochastic model of the bundle block adjustment used here.

Based on the performed analysis, one conclusion is that obtaining very high resolution images of natural bare soil surfaces with UAV remains challenging with low-cost components. The stability of the camera is of concern, which can be enhanced (turning off auto-focus, stabilizer, etc.) with suitable cameras. However, the limited stability of consumer cameras is generally known. Secondly, flying has to support image acquisition, thus avoiding motion blur due to forward motion or vibrations. Additionally, the experiment suggests that a regular block layout of the images within the block could prevent systematic errors due to forming of sub-blocks within the bundle block adjustment.

The experiment uses the methods suggested in (Milenković et al., 2015) for processing TLS data to assess surface roughness. The results are consistent with the previous study, and thus, confirm the suggested method and show that it is extendable for TLS data taken from high tripods and over a larger area. We could not prove that the low-cost UAV images considered in this experiment can deliver the same level of detail and accuracy as current TLS systems (resolution of 5mm), although improvement can be expected. However, for spatial scales of 12cm and larger (Figure 6), both methods appear to be usable.

The experiment is also complementing the study of (Eltner et al., 2013). Both studies contribute to the same aim, i.e. developing methods for very high resolution modeling of terrain surfaces. The results of both studies are generally similar, though the GCP accuracy achieved in (Eltner et al., 2013) is apparently better compared to our results, and no systematic errors were reported there. The systematic errors in our experiments originate in (relatively) weakly tied sub-blocks of the bundle block. On the other hand, the TLS reference of this article has a co-registration error below 2 mm, and together with the data resolution of 5 mm, this makes it well usable as reference data. Further experimentation is necessary to build a more comprehensive understanding of the strengths and weaknesses of different approaches, and how to

use them in synergy.

#### ACKNOWLEDGEMENTS

The research leading to these results has received funding from the European Community's Seventh Framework Programme ([FP7 / 2007 - 2013 ]) under grant agreement no 606971.

We would also like to thank Melanie Rašković for helping with measurements of the ground control points as well as Peter Dorninger and Clemens Nothegger from 4D-IT GmbH for collecting the UAV images.

#### REFERENCES

- Davidson, M., Mattia, F., Satalino, G., Verhoest, N., Le Toan, T., Borgeaud, M., Louis, J. and Attema, E., 2003. Joint statistical properties of rms height and correlation length derived from multisite 1-m roughness measurements. *Geoscience and Remote Sensing, IEEE Transactions on* 41(7), pp. 1651–1658.
- Dierking, W., 1999. Quantitative roughness characterization of geological surfaces and implications for radar signature analysis. *Geoscience and Remote Sensing, IEEE Transactions on* 37(5), pp. 2397–2412.
- Eltner, A., Mulrow, C. and Maas, H.-G., 2013. Quantitative measurement of soil erosion from tfs and uav data. *ISPRS - International Archives of the Photogrammetry, Remote Sensing and Spatial Information Sciences XL-1/W2*, pp. 119–124.
- Glira, P., Pfeifer, N., Briese, C. and Ressel, C., 2015. A correspondence framework for als strip adjustments based on variants of the icp algorithm. *Photogrammetrie - Fernerkundung - Geoinformation* 2015(4), pp. 275–289.
- Jacobsen, K., 2009. Effective resolution of digital frame images. In: *International Archives of the Photogrammetry, Remote Sensing and Spatial Information Sciences*.
- Karel, W., Doneus, M., Verhoeven, G., Briese, C., Ressel, C. and Pfeifer, N., 2013. Oriental - automatic geo-referencing and orthorectification of archeological aerial photographs. In: *ISPRS Annals of the Photogrammetry, Remote Sensing and Spatial Information Sciences, II-5/W1*.
- Kraus, K., 2007. *Photogrammetry – Geometry from Images and Laser Scans*. 2 edn, De Gruyter.
- Langer, D., Mettenleiter, M., Härtl, F. and Fröhlich, C., 2000. Imaging lidar for 3-d surveying and cad modeling of real-world environments. *The International Journal of Robotics Research* 19(11), pp. 1075–1088.
- Lichti, D. D. and Jamtsho, S., 2006. Angular resolution of terrestrial laser scanners. *The Photogrammetric Record* 21(114), pp. 141–160.
- Mancini, F., Dubbini, M., Gattelli, M., Stecchi, F., Fabbri, S. and Gabbianelli, G., 2013. Using unmanned aerial vehicles (uav) for high-resolution reconstruction of topography: The structure from motion approach on coastal environments. *Remote Sensing* 5(12), pp. 6880.
- Mattia, F., Davidson, M., Le Toan, T., D'Haese, C., Verhoest, N., Gatti, A. and Borgeaud, M., 2003. A comparison between soil roughness statistics used in surface scattering models derived from mechanical and laser profilers. *Geoscience and Remote Sensing, IEEE Transactions on* 41(7), pp. 1659–1671.
- Milenković, M., Pfeifer, N. and Glira, P., 2015. Applying terrestrial laser scanning for soil surface roughness assessment. *Remote Sensing* 7(2), pp. 2007.
- Morel, J. and G.Yu, 2009. ASIFT: A new framework for fully affine invariant image comparison. *SIAM Journal on Imaging Sciences*.
- Oh, Y. and Kay, Y. C., 1998. Condition for precise measurement of soil surface roughness. *Geoscience and Remote Sensing, IEEE Transactions on* 36(2), pp. 691–695.
- Perko, R., Klaus, A. and Gruber, M., 2004. Quality comparison of digital and film-based images for photogrammetric purposes. In: *International Archives of Photogrammetry, Remote Sensing and Spatial Information Sciences*.
- Rieke-Zapp, D. H. and Nearing, M. A., 2005. Digital close range photogrammetry for measurement of soil erosion. *The Photogrammetric Record* 20(109), pp. 69–87.
- Rothermel, M., Wenzel, K., Fritsch, D. and Haala, N., 2012. SURE: Photogrammetric surface reconstruction from imagery. In: *Proceedings LC3D Workshop, Berlin, December 2012*.
- Torr, P. H. and Zisserman, A., 2000. Feature based methods for structure and motion estimation. In: *Vision Algorithms: Theory and Practice*, Springer, pp. 278–294.
- Ulaby, F., Moore, R. and Fung, A., 1986. *Microwave Remote Sensing: Active and Passive*. Artech House microwave library, Addison-Wesley Publishing Company, Advanced Book Program/World Science Division.
- Verhoest, N. E., Lievens, H., Wagner, W., Álvarez-Mozos, J., Moran, M. S. and Mattia, F., 2008. On the soil roughness parameterization problem in soil moisture retrieval of bare surfaces from synthetic aperture radar. *Sensors* 8(7), pp. 4213–4248.

### 3.4 Paper IV

**Title:** Total canopy transmittance estimated from small-footprint, full-waveform airborne LiDAR

**Authors:** Milenković, M., Wagner, W., Quast, R., Hollaus, M., Ressler, C., Pfeifer, N.

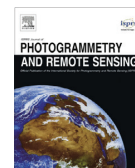
**Published in:** ISPRS Journal of Photogrammetry and Remote Sensing, 128, 2017, 61 – 72, <http://dx.doi.org/10.1016/j.isprsjprs.2017.03.008>

**Licence:** © 2017 ISPRS Inc. Published by Elsevier B.V. All rights reserved. This manuscript version is made available under the Attribution-NonCommercial-NoDerivatives 4.0 International (CC-BY-NC-ND 4.0) license, <http://creativecommons.org/licenses/by-nc-nd/4.0/>



Contents lists available at ScienceDirect

ISPRS Journal of Photogrammetry and Remote Sensing

journal homepage: [www.elsevier.com/locate/isprsjprs](http://www.elsevier.com/locate/isprsjprs)

## Total canopy transmittance estimated from small-footprint, full-waveform airborne LiDAR



Milutin Milenković\*, Wolfgang Wagner, Raphael Quast, Markus Hollaus, Camillo Ressel, Norbert Pfeifer

Department of Geodesy and Geoinformation (GEO), Technische Universität Wien (TU Wien), Gußhausstraße 27-29, 1040 Vienna, Austria

### ARTICLE INFO

#### Article history:

Received 13 July 2016

Received in revised form 20 March 2017

Accepted 21 March 2017

#### Keywords:

Airborne laser scanning

LiDAR waveforms

Vegetation structure

Canopy cover

Monoplotting

Point cloud classification

### ABSTRACT

Canopy transmittance is a directional and wavelength-specific physical parameter that quantifies the amount of radiation attenuated when passing through a vegetation layer. The parameter has been estimated from LiDAR data in many different ways over the years. While early LiDAR methods treated each returned echo equally or weighted the echoes according to their return order, recent methods have focused more on the echo energy. In this study, we suggest a new method of estimating the total canopy transmittance considering only the energy of ground echoes. Therefore, this method does not require assumptions for the reflectance or absorption behavior of vegetation. As the oblique looking geometry of LiDAR is explicitly considered, canopy transmittance can be derived for individual laser beams and can be mapped spatially. The method was applied on a contemporary full-waveform LiDAR data set collected under leaf-off conditions and over a study site that contains two sub regions: one with a mixed (coniferous and deciduous) forest and another that is predominantly a deciduous forest in an alluvial plain. The resulting canopy transmittance map was analyzed for both sub regions and compared to aerial photos and the well-known fractional cover method. A visual comparison with aerial photos showed that even single trees and small canopy openings are visible in the canopy transmittance map. In comparison with the fractional cover method, the canopy transmittance map showed no saturation, i.e., there was better separability between patches with different vegetation structure.

© 2017 International Society for Photogrammetry and Remote Sensing, Inc. (ISPRS). Published by Elsevier B.V. All rights reserved.

### 1. Introduction

Light detection and ranging (LiDAR) has been proven to be an excellent technique for vegetation structure mapping. This is a result of the direct ranging and multiple-echo detection capabilities of airborne LiDAR, which allows the observation of the signal contribution from different vegetation layers. Such information has been well explored over recent decades for mapping vegetation structural properties and forestry applications in general (Maltamo et al., 2014).

One method of characterizing vegetation structure is using canopy transmittance  $T_c$ . This is a spectral and directional physical parameter that quantifies how much radiation is attenuated when passing through a vegetation layer. The strength of this attenuation depends on the interaction of radiation with vegetative elements

(e.g., leaves, needles, branches, etc.). Therefore, canopy transmittance is closely related to other vegetation structural parameters such as the leaf area index (LAI) and directional gap fraction  $P(\theta)$  (Bréda, 2003).  $T_c$  can be used as an indirect method to estimate LAI (Bréda, 2003). The relationship between  $T_c$  and LAI is normally modeled by the Beer-Lambert law, where an exponential attenuation of the radiation is assumed (Monsi and Saeki, 2005).  $T_c$  can be derived for a certain canopy depth  $d$  or for the total canopy layer. The former is useful for analyzing the vertical distribution of vegetation structure, while the latter is addressed as the total canopy transmittance.  $T_c$  also has its own angular and spectral pattern because physical and structural properties of vegetation (reflectance, absorbance, etc.) are different for different propagation directions (incident angle  $\theta$  and azimuth  $\omega$ ) and radiation wavelengths  $\lambda$ , i.e.  $T_{c,\lambda}(\theta, \omega)$ .

When estimated with airborne LiDAR,  $T_c$  refers to a particular direction and wavelength. This is because an airborne LiDAR sensor transmits and observes laser radiation (e.g., 1064 nm) at specific transmitted/observed directions, i.e., scan angles. Contemporary sensors observe with narrow beams (0.25 mrad) and at high pulse repetition rate (up to 800 kHz), which for lower flying heights can

\* Corresponding author.

E-mail addresses: [Milutin.Milenkovic@geo.tuwien.ac.at](mailto:Milutin.Milenkovic@geo.tuwien.ac.at) (M. Milenković), [Wolfgang.Wagner@geo.tuwien.ac.at](mailto:Wolfgang.Wagner@geo.tuwien.ac.at) (W. Wagner), [Raphael.Quast@geo.tuwien.ac.at](mailto:Raphael.Quast@geo.tuwien.ac.at) (R. Quast), [Markus.Hollaus@geo.tuwien.ac.at](mailto:Markus.Hollaus@geo.tuwien.ac.at) (M. Hollaus), [Camillo.Ressel@geo.tuwien.ac.at](mailto:Camillo.Ressel@geo.tuwien.ac.at) (C. Ressel), [Norbert.Pfeifer@geo.tuwien.ac.at](mailto:Norbert.Pfeifer@geo.tuwien.ac.at) (N. Pfeifer).

<http://dx.doi.org/10.1016/j.isprsjprs.2017.03.008>

0924-2716/© 2017 International Society for Photogrammetry and Remote Sensing, Inc. (ISPRS). Published by Elsevier B.V. All rights reserved.

give more than 20 samples per  $m^2$  with the footprint size below 0.5 m, depending on flying altitude. Such high-resolution estimates of  $T_c$  are useful in many environmental applications. For example,  $T_c$  is an input parameter for snow melt models (Musselman et al., 2013; Moeser et al., 2014). The relationship between  $T_c$  and LAI is used to map tree defoliation (Solberg et al., 2006) or to characterize the habitat for certain species (Clawges et al., 2008; Sasaki et al., 2016). In addition,  $T_c$  can be used for biomass estimation (Lefsky et al., 1999).

The LiDAR-based  $T_c$  and directional gap fraction  $P(\theta)$  are commonly assumed to be equivalent (Ni-Meister et al., 2001; Hopkinson and Chasmer, 2009; Armston et al., 2013). The LiDAR-based  $P(\theta)$  is understood as the probability of an infinitesimally small laser beam to be directly transmitted through the canopy along the direction  $\theta$  (Armston et al., 2013; Ni-Meister et al., 2001). This parameter can be calculated as, e.g., the portion of ground to total number of echoes and is also referred to as the laser penetration rate (Solberg et al., 2006). A complement to this measure is calculated as the portion of vegetation to total number of echoes and is referred to as the canopy fractional cover ( $f_{Cover}$ ) (Morsdorf et al., 2006; Riano et al., 2004). In some studies, the term  $f_{Cover}$  is also referred as canopy closure (Harding et al., 2001).

There are many methods to estimate canopy transmittance (or gap fraction) from LiDAR data. They can be grouped according to whether LiDAR waveforms or LiDAR returns are analyzed. Some of the first waveform-based methods were suggested by Lefsky et al. (1999), Harding et al. (2001) and Parker et al. (2001) for a large footprint full-waveform LiDAR sensor known as SLICER (Scanning LiDAR Imager of Canopies by Echo Recovery). This methodology involves raw-waveform normalization by its total energy and a fixed adjusting factor to correct for the difference in canopy and ground reflectance at 1064 nm. Canopy transmittance at certain canopy depth  $d$  is then estimated by accumulating the normalized and reflectance-corrected waveforms (also known as Canopy Height Profiles - CHP) from the canopy top till depth  $d$  and subtracting it from 1 (Parker et al., 2001). Ni-Meister et al. (2001) suggested a physical framework for using such uncalibrated (raw) waveforms to directly derive the gap probability (the gap fraction). This method also requires knowledge of the ground and canopy reflectance ratio. Armston et al. (2013) extended this method to small-footprint LiDAR waveforms. They suggested a data-driven method to estimate the ground and canopy reflectance ratio by modeling a linear relationship between the integrated energy from the LiDAR pulses with only ground or only vegetation returns. The robustness of this approach was confirmed by Chen et al. (2014) where different forest conditions are considered. Armston et al. (2013) also identified that the total gap-fraction can be derived using only ground returns, but this framework has not been analyzed in detail yet. Lindberg et al. (2012) extended the CHP method of Lefsky et al. (1999) for small-footprint LiDAR waveforms by applying an intensity correction based on the Beer-Lambert law before the normalization and aggregation step. The correction was applied to compensate for the shielding effect of higher vegetation layers, and the results showed that the correction improved the vegetation volume estimate. Recently, Fieber et al. (2015) adopted the CHP method of Harding et al. (2001) and applied the data-driven reflectance ratio from Armston et al. (2013) to aggregated, small-footprint LiDAR waveforms. This study confirmed better performance of the data-driven reflectance ratio to the fixed reflectance ratio for LAI derivation.

The return-based methods for canopy transmittance have two main steps: (a) classification to ground and canopy returns and (b) calculation of the fraction of ground or canopy returns to the total number of returns for a spatial cell. The abovementioned methods of Solberg et al. (2006) and Morsdorf et al. (2006) have

been mostly used in the last decade. In Morsdorf et al. (2006), it is also suggested to consider first and last returns independently and to derive two  $f_{Cover}$  maps. Solberg et al. (2009) suggested combining the first and last returns and using fixed weights to account for single- and multiple-return observations. Hopkinson and Chasmer (2009) used the intensity from the returns as weights and calculated a so-called intensity ratio, i.e., the sum of all the canopy returns intensity to total returns intensity. This measure is similar to the CHP methods, but it is performed return-wise. They also suggested an alternative method where square-root corrections are applied for “two-way energy transmission” and for the multiple returns. Finally, Muss et al. (2011) aggregated the LiDAR returns and intensity into larger footprints to create so-called pseudo-waves and analyzed them with the waveform-based methods.

This study suggests a new method for canopy transmittance that considers only the energy from ground returns. Such an approach allows the use of uncalibrated LiDAR waveforms. Compared with the previous methods, it does not require the vegetation-ground reflectance correction or an assumption for the vegetation extinction coefficient. This is because the energy of the ground returns is normalized by an energy approximated from the single ground returns found in the vicinity of the ground returns. The method estimates total canopy transmittance per laser beam and per spatial cell based on single-strip, full-waveform airborne LiDAR data.

The study is organized as follows. Section 2.1 reviews briefly the basics of full-waveform LiDAR theory, and Sections 2.2 and 2.3 present the theoretical framework of our method. Section 3 presents the full-waveform airborne LiDAR data as well as data used for the comparison (aerial and ground photos). Section 4 explains how the method was practically implemented on the full-waveform LiDAR data. Section 5 presents the results of the comparison with an existing gap-fraction LiDAR method. Section 6 discusses the limitations of the method and this study. Finally, Section 7 presents the main conclusions drawn from the comparison.

## 2. Theory

### 2.1. Full-waveform theory

A full-waveform LiDAR sensor detects the backscattered radiant flux  $[W]$  at regular time intervals (e.g., 1 ns) and converts it into a digitized signal, i.e., the full-waveform. Following the radar equation, the recorded waveform represents the convolution of the transmitted-pulse waveform and the response function of a cluster of scatterers illuminated by the laser beam (Wagner et al., 2006; Jutzi and Stilla, 2006). When scanning over vegetation, however, the transmitted pulse interacts with several clusters of scatterers placed at different ranges along the scanning direction. In this case, the resulting waveform is the convolution of the transmitted pulse with a series of response functions centered at the clusters' ranges. To arrive at an analytical solution for such waveforms, Wagner et al. (2006) approximated both the transmitted pulse and the response functions with Gaussian functions. Following this approximation, the received radiant energy  $Q_r$  of a transmitted laser pulse is then given as:

$$Q_r = \int_{-\infty}^{+\infty} P_r(t) dt = \int_{-\infty}^{+\infty} \left[ \sum_{i=1}^N \hat{P}_i \cdot e^{-\frac{(t-t_i)^2}{\sigma_i^2}} \right] dt \quad (1)$$

where  $P_r(t)$  is the recorded waveform given by its instantaneous amplitudes. It is assumed that the amplitude is linearly proportional to the radiant flux incident on the receiver. The assumption

on Gaussian shape of the pulse returns is in most cases appropriate for the infrared LiDAR sensors and natural objects. However, it is also observed that the fitting accuracy of the Gaussian model gets worse for weak returns, i.e., returns with a small amplitude (Wagner et al., 2006).

The sum within the rectangular brackets in Eq. (1) emphasizes that the received energy is approximated by a finite number  $N$  of Gaussian clusters. Each detected cluster  $i$  is associated with its amplitude  $\hat{P}_i$ , standard deviation  $s_{p,i}$ , and the time  $t_i$ . The latter is the round-trip time that corresponds to the range  $R_i$ . The detected clusters are also called echoes (or returns), and their parameterization (amplitude  $\hat{P}_i$ , echo width  $s_{p,i}$ , and the range  $R_i$ ) is estimated from the recorded full-waveform signal (Wagner et al., 2006; Roncat et al., 2011; Jutzi and Stilla, 2006). Eq. (1) can be further expressed as:

$$Q_r = \sum_{i=1}^N \hat{P}_i \int_{-\infty}^{+\infty} e^{-\frac{(t-t_i)^2}{s_{p,i}^2}} dt = \sum_{i=1}^N \hat{P}_i \cdot s_{p,i} \cdot \sqrt{2\pi} \quad (2)$$

where  $s_{p,i}\sqrt{2\pi}$  is the area below the unit-amplitude Gaussian echo with the standard deviation  $s_{p,i}$  and centered at the range  $R_i$ . Consequently, the energy of an individual echo  $i$  is then given as:

$$Q_i = \hat{P}_i \cdot s_{p,i} \cdot \sqrt{2\pi} \quad (3)$$

Each of the  $N$  detected echoes has its own spatial location  $(x_i, y_i, z_i)$ , where  $i = 1, \dots, N$  in a world coordinate system. This is readily derived by a direct georeferencing procedure where flight trajectory information is considered (Skaloud and Lichti, 2006). The spatial location allows one to distinguish whether the echo comes from a ground or vegetation cluster, provided that a digital terrain model exists (Fig. 1a). In general, a LiDAR waveform can contain both ground and vegetation echoes. Such waveforms will be referred to here as vegetation-ground waveforms. However,

there are also waveforms which contain only vegetation echoes or only ground echoes, and they will be referred here as vegetation waveforms and ground waveforms, respectively. The waveform's energy received from the vegetation or ground layer can then be calculated by summing up the individual energies (Eq. (3)) of the vegetation or ground echoes detected in the waveform.

Generally, the echo energy  $Q_i$  (and the waveform) is not necessarily identical when a cluster is observed from different heights or by different sensors and flight campaigns. Therefore, Wagner (2010) suggested to use the backscattering coefficient  $\gamma$  [ $\text{m}^2 \cdot \text{m}^{-2}$ ], i.e. the scattering cross-section normalized by the beam area perpendicular to the propagation direction. This physical quantity is inherent to the object and is closely related to the bidirectional reflectance distribution function  $f$  (BRDF):

$$\gamma = 4\pi \langle f \rangle \cos(\theta) = 4\pi \frac{\langle L_s \rangle}{E_i} \cos(\theta), \quad (4)$$

where  $\langle f \rangle$  is the bidirectional reflectance function (BRDF) averaged for the incident and scattered solid angles (Wagner, 2010).  $\theta$  is the scattering angle, which is also identical to the incident angle of the laser beam due to the quasi collinear backscatter geometry of airborne LiDAR. According to Nicodemus et al. (1977),  $\langle f \rangle$  can be further expressed through the ratio of the average radiance  $\langle L_s \rangle$  of the scattered solid angle and the irradiance  $E_i$ .

The backscattering coefficient  $\gamma_i$  of a cluster  $i$  is also related to the energy  $Q_i$  of the corresponding echo observed from the LiDAR waveform. This relationship is given by the calibration equation (Wagner, 2010):

$$\gamma_i = C_{cal} \cdot \frac{R_i^2}{\sqrt{2\pi}} \cdot Q_i, \quad (5)$$

where  $C_{cal}$  is the calibration constant. It is noted that Eq. (5) is expressed slightly different than in Wagner (2010), but both

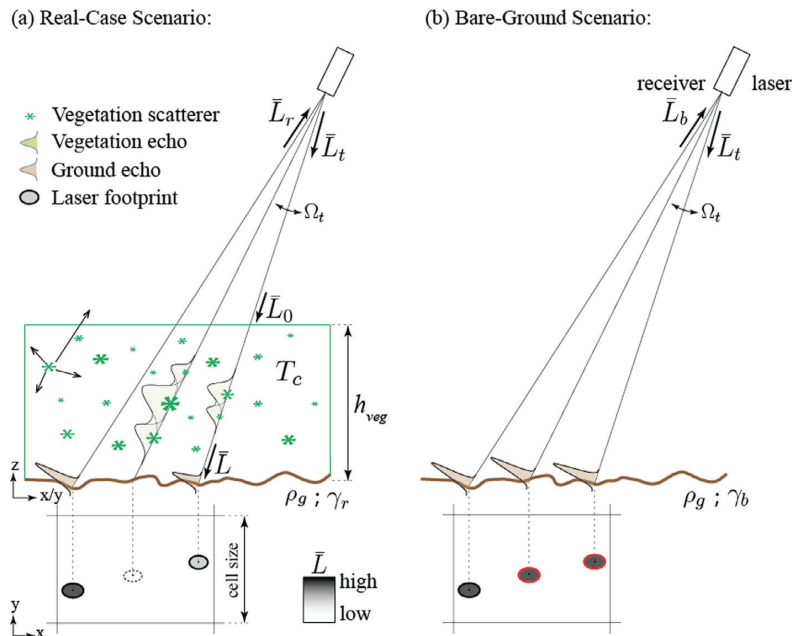


Fig. 1. Three waveform types (ground waveforms, vegetation waveforms, and vegetation-ground waveforms) shown for: (a) the real and (b) the hypothetical scanning scenarios. The bottom figure is the top view of the ground layer. The three laser footprints, corresponding to the three waveform types, are colored according to their average radiance incident on the ground layer  $\bar{L}$ . The footprints with the red frame in (b) indicate waveform types for which the ground echo energy was approximated. (For interpretation of the references to colour in this figure legend, the reader is referred to the web version of this article.)

expressions are in principle equivalent. Here, the calibration constant includes all the sensor parameters and the transmission factors, while the term  $\sqrt{2\pi}$  is added to express the calibration equation in terms of the energy of Gaussian echoes.

## 2.2. Beam-wise canopy transmittance

The LiDAR sensor transmits concentrated laser photons inside a conical beam of a transmitted solid angle  $\Omega_t$ . These photons have an average transmitted radiance  $\bar{L}_t^i$ :

$$\bar{L}_t^i = \frac{1}{\Omega_t} \int_{\Omega_t} L d\Omega, \quad (6)$$

where  $L$  is the radiance [ $\text{W} \cdot \text{m}^{-2} \cdot \text{sr}^{-1}$ ], which is invariant along a differential solid angle  $d\Omega$  unless there is extinction. During the propagation through a vegetation layer (Fig. 1a), some of the photons are scattered by vegetative elements like leaves, needles, twigs, branches, etc. This causes the average radiance incident upon the ground layer  $\bar{L}^i$  to be smaller than the average radiance incident on the vegetation layer  $\bar{L}_0^i$ . The ratio of these two variables is commonly called the canopy transmittance  $T_c$ :

$$T_c = \frac{\bar{L}^i}{\bar{L}_0^i} \quad (7)$$

LiDAR pulses typically produce both vegetation and ground echoes, and they correspond to vegetation-ground waveforms (Section 2.1). However, there are laser beams for which  $\bar{L}_0^i = \bar{L}^i$ , i.e., the average radiance is not attenuated after passing the vegetation layer. This can occur, e.g., when canopy gaps are larger than the laser beam footprint, producing only ground echoes. Such beams correspond to the ground waveforms, and their canopy transmittance is 1. In contrast, there are laser beams for which  $\bar{L}^i = 0$ , i.e., all transmitted photons are scattered by the vegetation producing only vegetation echoes. These beams correspond to the vegetation waveforms, and their canopy transmittance is 0.

For vegetation-ground waveforms, Eq. (7) cannot be directly applied because the average radiances  $\bar{L}^i$  and  $\bar{L}_0^i$  are neither known nor directly observed. To overcome this problem, we introduce a hypothetical scenario where the identical scanning is performed, but now assume that all the vegetation has been removed (Fig. 1b). This will be referred as the bare-ground scenario, while the scenario in Fig. 1a will be referred as the real-case scenario. Under the real-case scenario, the canopy transmittance for the vegetation-ground waveforms can be expressed as the average radiance  $\bar{L}_r^i$  scattered from the ground and incident on the receiver for the real-case scenario normalized by the average radiance  $\bar{L}_b^i$  scattered from the ground and incident on the receiver for the bare-ground scenario:

$$T_c = \frac{\bar{L}_r^i}{\bar{L}_b^i} = \frac{\bar{L}_t^i \cdot \eta_{atm}^2 \cdot T_c \cdot \rho_g}{\bar{L}_t^i \cdot \eta_{atm}^2 \cdot \rho_g}, \quad (8)$$

where  $\eta_{atm}^2$  is the two-way atmospheric attenuation factor and  $\rho_g$  is the ground reflectance. The canopy transmittance  $T_c$  refers to the one-way attenuation factor, which is in accordance with the assumptions made in Ni-Meister et al. (2001). Note that the vegetative elements are treated as opaque.

The average radiances  $\bar{L}_r^i$  and  $\bar{L}_b^i$  in Eq. (8) can be further normalized by the irradiance  $E_i$ . These ratios are actually equivalent to the BDRF averaged in Eq. (4), which then gives:

$$T_c = \frac{\bar{L}_r^i/E_i}{\bar{L}_b^i/E_i} = \frac{\gamma_r}{\gamma_b}, \quad (9)$$

where  $\gamma_b$  is the bare-ground backscattering coefficient, and  $\gamma_r$  is the backscattering coefficient of the same ground but under the vegetation layer. The average radiance ( $L_s$ ) scattered from the ground layer from Eq. (4) is replaced by  $\bar{L}_r^i$  and  $\bar{L}_b^i$  for the real-case and bare-ground scenario, respectively. Finally,  $\gamma_r$  and  $\gamma_b$  are further expressed by the calibration Eq. (5) in terms of the ground-echo energy, which gives:

$$T_{c,i} = \frac{\bar{L}_r^i}{\bar{L}_b^i} = \frac{\gamma_r}{\gamma_b} = \frac{Q_{r,i}}{Q_{b,i}} \quad (10)$$

This expression shows that the canopy transmittance for a laser beam  $i$  can be calculated by normalizing the energy  $Q_{r,i}$  of the ground echo  $i$  in the beam's waveform observed in the real-case scenario by the energy  $\tilde{Q}_{b,i}$  of the same echo that would be observed in the bare-ground scenario. The tilde sign indicates that the latter echo energy is not observed but approximated. Here, the energy  $\tilde{Q}_{b,i}$  is approximated from the observed, single ground echoes, i.e., it is estimated by interpolating from the energies of the neighboring ground waveforms. In contrast, the energy  $Q_{r,i}$  is known and given by Eq. (3) because all echoes are observed by full-waveform LiDAR under the real-case scenario.

It is noted that the normalization step in Eq. (10) cancels out the calibration constant  $C_{cal}$ , which allows one to use the ground-echo energies estimated directly from the uncalibrated LiDAR waveforms.

## 2.3. Canopy transmittance mapping

Canopy transmittance can be also calculated per spatial cell and mapped spatially. Similar to laser beams, this can be done strip-wise and considering only ground echoes. Following Eq. (10), the canopy transmittance  $T_k$  for a cell  $k$  is given as:

$$T_{c,k} = \frac{Q_{r,k}}{Q_{b,k}}, \quad (11)$$

where  $k$  is the linear index of the cell and  $Q_{r,k}$  is the total ground energy observed within the cell in the real-case scenario. Similar to the beam-wise case,  $\tilde{Q}_{b,k}$  is not observed and is an approximation of the total ground energy within the cell for the bare-ground scenario.

The total energy  $Q_{r,k}$  is the sum of the energies of all ground echoes observed within the cell. As ground echoes can only come from the ground waveforms and the vegetation-ground waveforms,  $Q_{r,k}$  is given by:

$$Q_{r,k} = \sum_1^{n_1} Q_{r,i}^g + \sum_1^{n_2} Q_{r,i}^{vg} \quad (12)$$

where  $Q_{r,i}^g$  ( $Q_{r,i}^{vg}$ ) is the energy of a ground echo  $i$  in the cell detected from a ground (vegetation-ground) waveform, while  $n_1$  ( $n_2$ ) is the number of the ground echoes within the cell detected from the ground (vegetation-ground) waveforms.

The approximated total energy  $\tilde{Q}_{b,k}$  is the sum of the energies of all ground echoes that would be observed within the cell under the bare-ground scenario. In this scenario, all three waveform types provide only ground echoes. Therefore,  $\tilde{Q}_{b,k}$  is given by:

$$\tilde{Q}_{b,k} = \sum_1^{n_1} \tilde{Q}_{b,i}^g + \sum_1^{n_2} \tilde{Q}_{b,i}^{vg} + \sum_1^{n_3} \tilde{Q}_{b,i}^v \quad (13)$$

where, the number of ground echoes detected in the ground, vegetation-ground, and vegetation waveforms within the cell  $k$  are given by  $n_1$ ,  $n_2$ , and  $n_3$ , respectively. The energy  $\tilde{Q}_{b,i}^g$  is equal

to the energy  $Q_{r,i}^g$ , while  $\tilde{Q}_{b,i}^v$  ( $\tilde{Q}_{b,i}^{vg}$ ) is the energy of a ground echo  $i$  that would be detected by a vegetation (vegetation-ground) waveform under the bare-ground scenario. The tilde symbol indicates that these energies are approximated. The approximation is done as in the beam-wise case (Section 2.2), i.e., interpolating from the energies of the neighboring single ground echoes ( $Q_{r,i}^g$ ).

It is important to note that the laser beams of the vegetation waveforms never reached the ground layer. These beams have to be projected to the ground layer to calculate the locations of their ground echoes realized under the bare-ground scenario. For the beams corresponding to ground and vegetation-ground waveforms, this is not necessary because they already provide at least one ground echo. Moreover, laser beams generally have different looking geometry within an airborne LiDAR strip. Their looking geometry changes from the nadir to low-oblique depending on the laser beam position within a scan line. This means that laser beams enter each cell at a different incident angle, while its variability within the cell is rather low. Moreover, the laser beams enter each cell at different azimuth angles. Therefore, the canopy transmittance should be assigned with an average incident  $\theta_k$  and an average azimuth  $\omega_k$  angle of the laser beams within the cell  $k$ . The final equation for the canopy transmittance  $T_{c,k}(\theta_k, \omega_k)$  for the cell  $k$  is then given as:

$$T_{c,k}(\theta_k, \omega_k) = \frac{\sum_1^{n_1} Q_{r,i}^g + \sum_1^{n_2} Q_{r,i}^{vg}}{\sum_1^{n_1} Q_{r,i}^g + \sum_1^{n_2} \tilde{Q}_{b,i}^{vg} + \sum_1^{n_3} \tilde{Q}_{b,i}^v} \quad (14)$$

### 3. Study site and data

The study site covers an area around the lower course of the river Pielach in Lower Austria (N48°12'48", E15°22'20"; WGS84). The area contains two sub regions with different vegetation characteristics: (a) a region with mixed forest and (b) a region with deciduous forest in an alluvial plain. These regions are shown in Fig. 4a, while their aerial photos are shown in Fig. 4b and c. The region with mixed forest contains patches with rather homogeneous coniferous or deciduous forest as well as some open areas, such as meadows and forest- and regional-roads. Some of the deciduous forest patches contain individual (detached) coniferous trees. The alluvial region contains predominately deciduous forest and shrubs as well as some open areas, such as meadows, bare ground, and water bodies.

The study data includes: (a) airborne LiDAR full-waveform data, (b) aerial photos, and (c) ground photos with their coordinates. The area was flown on January 14, 2016, under leaf-off conditions, and with a Riegl LMS-Q1560 full-waveform sensor mounted together with an aerial digital camera on the airplane. Aerial photos were

collected simultaneously with the full-waveform data. The Riegl LMS-Q1560 full-waveform sensor operates at the 1064 nm laser wavelength and is a so-called dual channel scanner, collecting two scans simultaneously per single flight strip. In addition, the scanner supports multiple-time-around processing. Each scan provides parallel scan lines with a  $\pm 30^\circ$  field of view, which reduces to  $\pm 29^\circ$  in the lateral flight direction because the two scanning planes are tilted against one another by  $28^\circ$ . Our LiDAR data were collected from an average flight height of 600 m above the ground and with a pulse repetition rate of 400 kHz. The data include one lateral strip and several strips acquired parallel to the river axis with a 80% strip overlap. The resulting point density of the last echoes in a single scan was at least four points per  $m^2$  over 90% of the strip's area. The sensor also collected up to seven echoes per laser beam, while the laser footprint size was smaller than 18 cm over the whole area. The airborne photos were collected with the Phase One IXA-R 180 camera and a 50 mm lens, which resulted in a ground sampling distance of approximately 7 cm. The airborne photos are used to inspect the plausibility and the level of detail in the canopy transmittance map.

On the day of the airborne data acquisition, seven spots were visited in the field. These spots were selected to document the diverse vegetation structure found in the area. For each spot, its coordinates were recorded by differential GPS measurements, and an upwards-looking ground photo was taken. Four ground photos were taken in the alluvial region at spots with the deciduous, leaf-off vegetation. The remaining three photos were taken inside a coniferous patch in the mixed-forest region. Fig. 4 shows the locations of the spots within the study site. Table 1 summarizes basic LiDAR statistics of the echoes located within a 50 m radius from the spots. The ground photos were collected to document the vegetation structure at the particular locations, which should help later in interpreting the results. However, the photos were acquired at an arbitrary azimuth and at a coarse approximation of zenith direction, which made them useful only for a qualitative interpretation of the results.

### 4. Methodology

Several processing steps are required to progress from raw LiDAR waveforms to a transmittance map. These steps involve pre-processing of the full-waveform LiDAR data (beam georeferencing and echo detection), classification of both echoes and waveforms, projection of the beams corresponding to the vegetation waveforms, interpolation of the echo energies for the bare-ground scenario, and finally, calculation of the canopy transmittance by Eq. (14). The subsequent subsections discuss these steps. Additionally, the last subsection presents an existing LiDAR gap-fraction method used for comparison with the transmittance map.

**Table 1**  
Basic statistics for a single scan and merged LiDAR scans. The values are derived from echoes selected within a 50 m radius around the validation spots.

Spot	Merged scans				Single scan								
	Num. –	$f_{cover}^a$ [%]	$h$ [m] <sup>b</sup> max	$h_{DTM}$ [m]	Num. –	$f_{cover}^a$ [%]	$h$ [m] <sup>b</sup> [m]	$\theta$ [deg] <sup>c</sup>			$\omega$ [deg] <sup>d</sup>		
								Min	Median	Max	Min	Median	Max
1	649520	23.0	15.808	215.045	43621	27.6	15.721	17.5	21.4	26.0	–53.3	–50.5	–47.4
2	893250	44.0	38.693	215.720	62674	46.5	38.387	2.0	5.7	11.6	133.7	145.5	183.0
3	921070	40.4	37.642	214.219	69565	43.3	37.384	4.3	8.7	13.6	–71.9	–60.1	–52.8
4	1008500	43.7	36.941	215.773	87432	45.5	36.645	2.1	4.4	9.1	–168.1	–78.7	–63.5
5	1189100	71.6	25.881	243.138	90977	74.3	25.756	14.2	19.1	24.1	–56.8	–55.0	–53.6
6	1158900	72.4	25.545	242.054	90262	74.5	25.122	12.5	17.3	22.3	–57.6	–55.3	–53.6
7	1158100	74.2	31.289	240.598	101440	74.5	31.041	5.9	10.9	16.2	–65.0	–57.8	–54.7

<sup>a</sup> Percentage of vegetation echoes.

<sup>b</sup> Echo height above the terrain.

<sup>c</sup> Incident angle of the beam vector.

<sup>d</sup> Azimuth of the beam vector.

#### 4.1. LiDAR preprocessing

Preprocessing of the LiDAR data was performed strip-wise. Raw full-waveform LiDAR data were given per strip, in form of waveforms and in the scanner coordinate system. This means that each laser beam was represented by its waveform, scan angle, and GPS time. The waveform itself was given by its instantiations amplitude values, each of them associated with the time elapsed between pulse transmission and amplitude recording. The preprocessing started with the extraction of individual echoes from the raw waveforms by applying the Gaussian decomposition method (Wagner et al., 2006). Additionally, waveform information like echo number within the waveform, total number of echoes within the waveform, echo amplitude  $\hat{P}_i$ , echo width  $s_{p,i}$ , and range  $R_i$  were assigned to each detected echo. Moreover, multiple echoes detected within a single waveform were assigned to the GPS time of the corresponding transmitted pulse (laser shot). Direct georeferencing (Skaloud and Lichti, 2006) was performed to transform the detected echoes from the scanner to a world coordinate system. This was performed considering the flight trajectory (described by Global Navigation Satellite System and Inertial Measurement Unit data) and the mounting information of the LiDAR system. The direct georeferencing provided the detected echoes as separate point clouds corresponding to individual LiDAR strips in the ETRS89/UTM 33N coordinate system. The overall geometry of the LiDAR block was then improved by strip adjustment using the least squares method (Ressl et al., 2011). The complete preprocessing was done in the software OPALS (Orientation and Processing of Airborne Laser Scanning data) (Pfeifer et al., 2014).

#### 4.2. Echo classification

To apply Eq. (14), it is necessary to perform the following two steps: (a) echo classification to ground and vegetation and (b) identification of the three waveform types (ground waveforms, vegetation-ground waveforms, and vegetation waveforms). The classification of the echoes into ground and vegetation was done according to the relative height of the echoes with respect to a digital terrain model (DTM). The DTM was derived from the georeferenced point cloud using the robust filtering method implemented in the software SCOP++ (Kraus and Pfeifer, 1998). All echoes that were placed more than 0.5 m away from the DTM were classified as vegetation, while the remaining echoes were classified as ground.

The three waveform types were identified by querying the point cloud of all the detected echoes and their attributes. The querying was performed according to the echo geolocation with respect to the DTM and the echo position within the waveform, which is illustrated in Fig. 2. The ground waveforms were identified with the single ground echoes (Fig. 2a), i.e., the ground echoes whose number-of-echoes value was 1. The vegetation-ground waveforms were identified by selecting the last ground echoes that share identical laser shot with at least one vegetation echo. These ground echoes will be referred as the last-of-multiple ground echoes (the

gray asterisks in Fig. 2). The vegetation waveforms were identified by the last echoes that were located in vegetation (the dark blue asterisks in Fig. 2). These particular vegetation echoes will be referred as the last-in-vegetation echoes. It is noted that the detected echoes and their attributes were available as an OPALS data manager instance that was built and updated by new attributes during the preprocessing. The OPALS data manager allows efficient access to large point clouds and handles arbitrary attributes associated with the point geometry (Otepka et al., 2013).

As discussed in Section 2.3, for the beams corresponding to the vegetation waveforms, it is necessary to calculate its intersection with the ground layer. Therefore, the last-in-vegetation echoes were projected to the ground layer, i.e., the DTM. These projected points represent ground echoes that would be detected from the vegetation waveforms in the bare-ground scenario. These projected points will be referred to as the synthetic ground echoes.

#### 4.3. Echo monoplotting

One way to determine the synthetic ground echoes is to project the last-in-vegetation echoes to the ground by simply using the vertical as a projection ray and to intersect it with the DTM. This means that the projected echoes will preserve the same planar position and get a new height according to the value from the intersected DTM cell. Such a projection model is straightforward, but also neglects the geometry of the laser beams. To overcome this, the last-in-vegetation echoes were projected to the DTM using monoplotting.

Monoplotting is a well-known photogrammetric method that intersects the projection ray of an image point with a DTM (Kraus, 2007). The main inputs for this procedure are the image coordinates of the point, the image's exterior and interior parameters, and a DTM. To apply this technique here, it is necessary to know the last-in-vegetation echo, the laser-beam vector, and the DTM, all given in the same world coordinate system, i.e., in our case, the ETRS89/UTM 33N. The laser-beam vector is assigned to the raw waveform data in the scanner coordinate system (the GPS time and the scan angle), which is then transformed into the world coordinate system during the direct georeferencing and the strip adjustment. All inputs are available then for the monoplotting of the last-in-vegetation echoes. Fig. 3 shows the monoplotting and vertical projection of the last-in-vegetation echoes (the dark blue points) for the full-waveform LiDAR data of a single tree. The red points in Fig. 3a-c are projected with monoplotting, while the red points in Fig. 3d-f are vertically projected. For the vertical projection case (Fig. 3f),  $T_{ck}$  is calculated for the vertical rectangular prism (the dashed black lines). For the monoplotting case (Fig. 3c),  $T_{ck}$  is calculated for the oblique rectangular prism, which follows the laser-beam geometry.

#### 4.4. Echo energy in the bare-ground scenario

As discussed in Sections 2.2 and 2.3, the echo energy  $\tilde{Q}_{b,i}$  that would be observed under the bare-ground scenario is interpolated

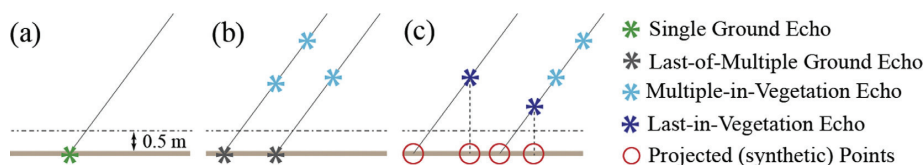
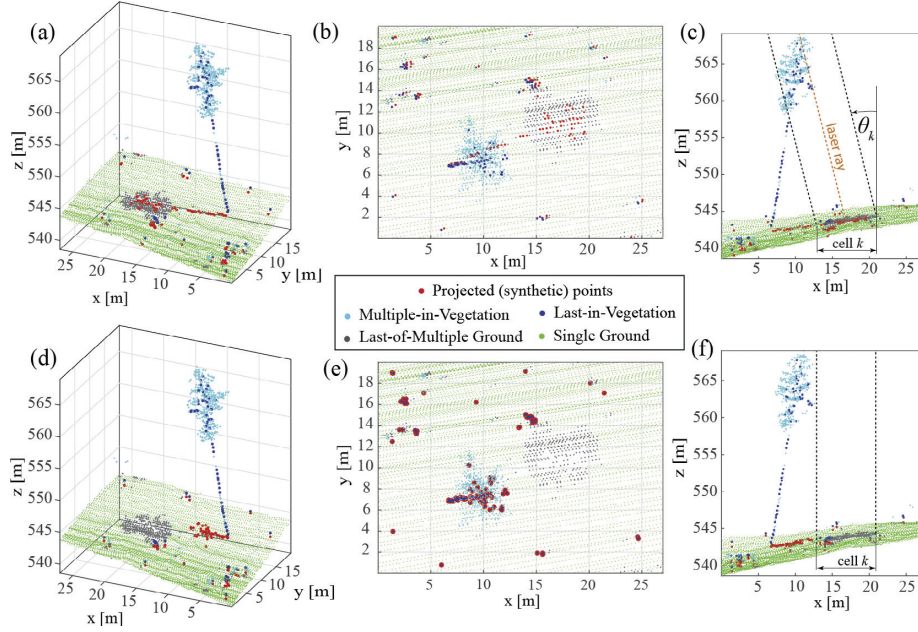


Fig. 2. Echo categories given for: (a) the ground waveforms, (b) the vegetation-ground waveforms, and (c) the vegetation waveforms. Horizontal brown lines represent the terrain, while horizontal dash-dotted lines show the border between the vegetation and ground. The full black lines represent laser beams. (For interpretation of the references to colour in this figure legend, the reader is referred to the web version of this article.)



**Fig. 3.** Echo categories and monoplotting (a, b, and c) vs. vertical projection (d, e, and f) shown on LiDAR data of a single tree (outside the study area). Figures (c) and (f) show the aggregation geometry in the scanner coordinate system (the consequence of monoplotting) and in the Euclidean coordinate system (the consequence of the vertical projection), respectively. The  $x$  and  $y$  coordinates are reduced by 598945 and 5285980, respectively.

from the energy  $Q_{r,i}^g$  of the neighboring single ground echoes. As  $\tilde{Q}_{b,i}^g = Q_{r,i}^g$ , it is necessary to interpolate only the energies  $\tilde{Q}_{b,i}^{vg}$  and  $\tilde{Q}_{b,i}^v$  of the ground echoes coming from the vegetation-ground waveforms and the vegetation waveforms, respectively. This practically means that  $\tilde{Q}_{b,i}^{vg}$  should be interpolated at the locations of the last-of-multiple ground echoes, while  $\tilde{Q}_{b,i}^v$  should be interpolated at the locations of the synthetic ground echoes. In both cases, the interpolation was done locally by averaging the energies  $Q_{r,i}^g$  of the single ground echoes within a circular neighborhood centered at the interpolation point.

To properly set the neighborhood radius, the distance from a last-of-multiple ground echo to its nearest-neighbor single ground echo was analyzed for our data set. It was found that 99% of the last-of-multiple ground echoes in a single LiDAR scan have at least one single ground echo within a 2.1 m neighborhood radius. To consider more than one single-ground echo, the neighborhood radius was eventually set to 5 m. A neighborhood size that is too small may lead to an empty neighborhood, while in the opposite case, local ground properties might be lost.

It is noted that the neighborhood radius is only used when the energy of ground echoes is estimated for the bare-ground scenario. If the density of LiDAR data is high, the canopy transmittance still can be aggregated by Eq. (14) at cells with sizes smaller than the neighborhood radius.

#### 4.5. Comparison

$T_c$  is estimated at particular incident and azimuth angles, with a laser wavelength of 1064 nm and by sensing downwards, i.e., towards the ground. Such measurement conditions are difficult to mimic with a field-based sensor. Therefore,  $T_c$  was (a) compared visually with the aerial photos, and (b) compared against the existing LiDAR gap-fraction method.

#### 4.5.1. Comparison with the existing method

The  $T_c$  map is compared with the fractional cover ( $f_{Cover}$ ) map suggested by Morsdorf et al. (2006). The  $f_{Cover}$  map is derived by normalizing the number of vegetation echoes  $N_{veg}$  by the total number of echoes  $N_{total}$  observed within a spatial cell:

$$f_{Cover} = \frac{N_{veg}}{N_{total}} \quad (15)$$

As recommended in Morsdorf et al. (2006), two  $f_{Cover}$  maps were calculated: one only from the first echoes ( $f_{Cover}^{First}$ ) and another only from the last echoes ( $f_{Cover}^{Last}$ ). The vegetation and ground echoes were separated as in our method (Section 4.2). It is noted that single echoes are at the same time the first and the last echoes. Therefore, both the  $f_{Cover}^{First}$  map and the  $f_{Cover}^{Last}$  map consider the single echoes. The correlation (and differences) between the  $T_c$  map and the two  $f_{Cover}$  maps were analyzed with scatter plots.

## 5. Results

### 5.1. Canopy transmittance and aerial photos

A canopy transmittance map with a cell size of 2 m was calculated based on the methodology described in Section 4 and from a single LiDAR scan of the test site. Fig. 4a, b, and c show this transmittance map and two aerial photos of the alluvial- and mixed-forest regions, respectively. The aerial photos were slightly modified (with histogram stretching and saturation adjustment) to improve the separability between the coniferous and deciduous forest patches. Visual comparison suggests that the  $T_c$  values close to 0 correspond to vegetation, while the values close to 1 correspond to open areas, i.e., bare ground, meadows, roads, and water. Moreover, within the vegetation, the  $T_c$  map separates clearly the patches with deciduous or coniferous forest. This can be seen in the mixed-forest region (the red rectangle in Fig. 4). There, the

deciduous-forest patches have on average a higher transmittance ( $T_c > 0.4$ ) compared with the coniferous-forest patches ( $T_c < 0.3$ ). The  $T_c$  map can also distinguish individual deciduous or coniferous trees. Fig. 4e shows three isolated conifers inside a deciduous-forest patch (C1, C2, and C3). These trees are also visible in the  $T_c$  map shown in Fig. 4d. Moreover, the two figures show that local canopy gaps/openings (G1 and G2) are also present in the  $T_c$  map.

### 5.2. Canopy transmittance and the $f_{Cover}$ method

Two fractional cover maps were calculated: one only based on the first echoes  $f_{Cover}^{First}$  and another only based on the last echoes  $f_{Cover}^{Last}$ . Both maps were generated for a cell size of 2 m, which was also the case for the  $T_c$  map. The cell values of  $f_{Cover}^{First}$  ( $f_{Cover}^{Last}$ ) show the fraction of the first (last) echoes in the vegetation within a vertical prism with a 2 m square base. Each  $f_{Cover}$  map was then compared with the  $T_c$  map. This was done with scatter plots of the cell values over the two regions: (a) the mixed-forest region (coniferous and deciduous) and (b) the alluvial-forest region (predominately deciduous). For each region, two scatter plots were derived: one based on  $T_c$  and  $f_{Cover}^{First}$  values and another based on  $T_c$  and  $f_{Cover}^{Last}$  values. The regions were manually delineated on the map.

Fig. 5 shows results of the comparison over the mixed-forest region. The  $f_{Cover}^{First}$  map (Fig. 5b) appeared to be more saturated com-

pared with the  $T_c$  map (Fig. 5a). This saturation can be also seen in the corresponding scatter plot (Fig. 5d) where 58% of the data have  $f_{Cover}^{First}$  values range from 0.8 to 1, i.e., only 20% of its dynamic range. The same data, however, cover over 85% of the  $T_c$  values (from 0 to 0.85). Therefore, the  $T_c$  map does not show the saturation for high fractional cover as the  $f_{Cover}^{First}$  map shows. The  $f_{Cover}^{Last}$  map (Fig. 5c), in contrast, does not show the saturation at high fractional cover values ( $f_{Cover}^{Last} > 0.6$ ). This map is also more similar to the  $T_c$  map, which is manifested by a linear trend within this domain ( $f_{Cover}^{Last} > 0.6 \wedge T_c < 0.3$ ) in the corresponding scatter plot (Fig. 5e). However, the  $f_{Cover}^{Last}$  map shows a slight saturation for low fractional cover: almost 50% of the data have  $f_{Cover}^{Last} < 0.2$ , and 90% of this data is stretched from 0.53 to 1 in the  $T_c$  map. Therefore, the  $f_{Cover}^{Last}$  map does not show saturation in the high fractional cover domain but has a slight saturation in the low fractional cover domain compared to the  $T_c$  map.

The difference between the  $T_c$  and  $f_{Cover}$  maps are emphasized by their values at spots 5, 6, and 7 shown in Fig. 5d-e. The upward-looking ground photos of those spots (the figures in the bottom panel of Fig. 5) document totally different canopy gap conditions. The photo at spot 7 was taken to document the canopy gaps for an extremely dense, coniferous stand. The photo at spot 5 was taken to document a local canopy gap, while the spot 6 photo was taken just a few meters from spot 5, deeper in the same coniferous forest stand. However, spots 5 and 6 have distinct  $f_{Cover}$  values, but very similar  $T_c$  values. As the  $f_{Cover}$  values refer to the

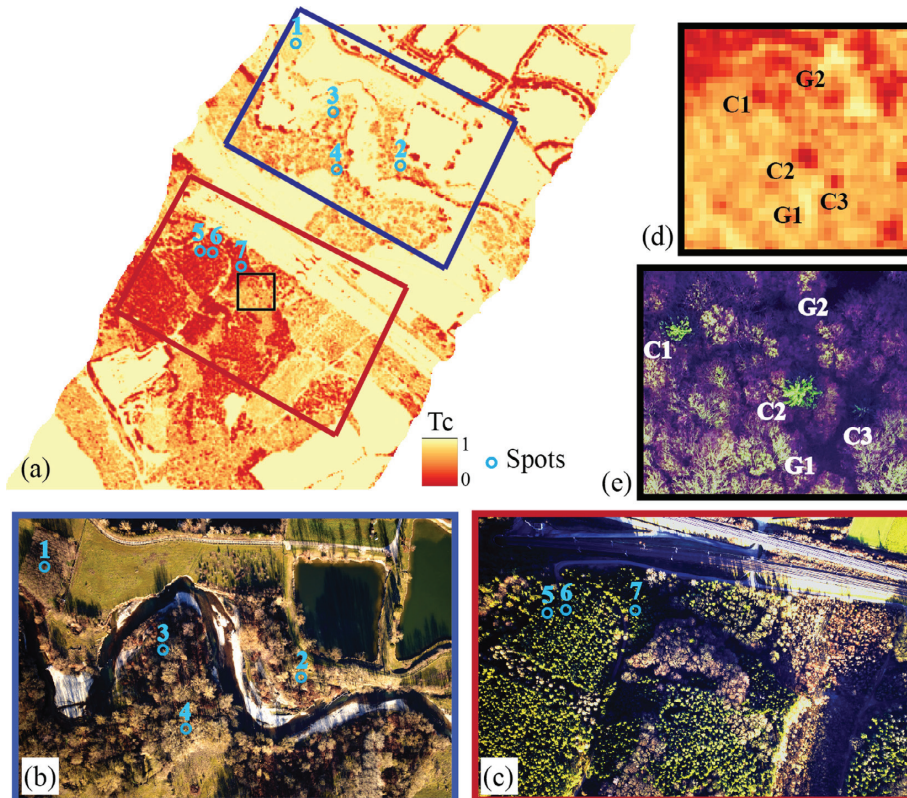
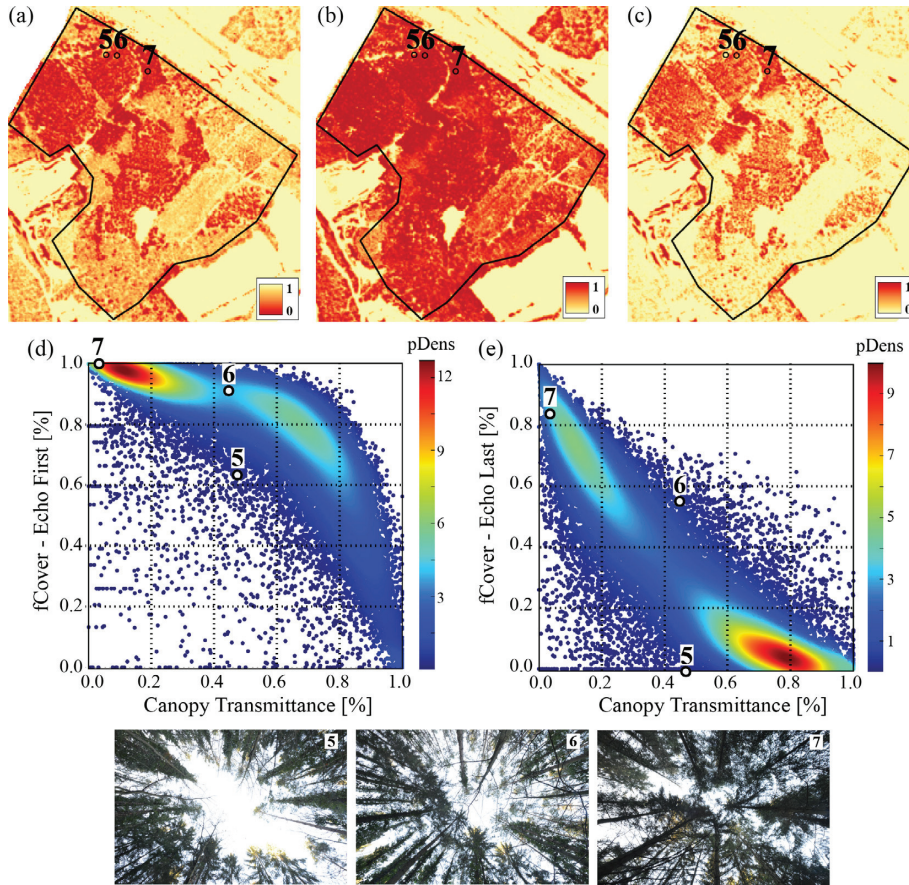


Fig. 4. (a) The total canopy transmittance map over the area of interest and with the locations where the ground images were taken. (b) Aerial image of the alluvial-forest region. (c) Aerial image of the mixed-forest region. The tree shadows on the aerial images point to the north. (d) The  $T_c$  map of the area marked by the black rectangle in (a), and corresponding zoom-in of the aerial photo (e). C1, C2, and C3 point to the individual coniferous trees, while G1 and G2 point to the two largest gaps in the area.



**Fig. 5.** Comparison of fractional cover and  $T_c$  over the mixed-forest region: (a) total canopy transmittance map, (b) first-echo  $f_{Cover}$  map, (c) last-echo  $f_{Cover}$  map, (d,e) scatter plots of  $T_c$  and  $f_{Cover}$  values, respectively. It is noted that  $f_{Cover}$  values are negatively correlated to the  $T_c$  values. Figures in the bottom row show the upward-looking ground photos for spots 5, 6, and 7.

vertical-prism neighborhood, their  $f_{Cover}$  values reflect what is observed in the central part of the photos (the zenith direction). In contrast, the  $T_c$  values refer to a highly oblique-prism neighborhood ( $\omega = 23^\circ, \theta = 55^\circ$ , Table 1), and their  $T_c$  values describe the non-central part of the photos along the laser-beam azimuth direction. Thus, the  $T_c$  values are correctly similar to one another as they refer to the similar stand part placed at the particular direction ( $\omega = 23^\circ, \theta = 55^\circ$ ) from the spot location.

Fig. 6 shows results of the comparison over the alluvial-forest region. Here, the  $f_{Cover}^{First}$  map (Fig. 6b) does not show any saturation, i.e., it offers more separability than the  $T_c$  map (Fig. 6a). About 50% of the data range from 0.8 and 1 in the  $T_c$  map, while 95% of this data range from 0 to 0.65 in the  $f_{Cover}^{First}$  map. However, the  $f_{Cover}^{Last}$  map (Fig. 6c) has a saturation at low fractional cover values ( $f_{Cover}^{Last} < 0.1$ , Fig. 6e). There are 72% of  $f_{Cover}^{Last}$  values in this domain, and 95% of this data is stretched from 0.61 to 1  $T_c$  values. This saturation shows that almost every laser shot left its last echo at or close to the ground in the alluvial, leaf-off forest. Therefore, the  $f_{Cover}^{Last}$  map erroneously suggests that the canopy structure is low in the alluvial-forest region, which is in contrast to the  $T_c$  and  $f_{Cover}^{First}$  maps. This saturation might be sensitive to laser beam divergence or laser wavelength.

Different directional characteristics of  $T_c$  and  $f_{Cover}$  are also shown by the photos taken in the alluvial-forest region (the bot-

tom panel of Fig. 6). The photo at spot 2 was taken in the middle of a local canopy gap, and as the central part of the photo suggests, the  $f_{Cover}$  values are zero. However, the  $T_c$  of spot 2 is slightly less than 1. This is because the oblique scanning ( $\theta = 6^\circ, \omega = 146^\circ$ , Table 1) intercepts a portion of the canopy top present in the non-central part of the photo (the canopy height is ca. 38 m, Table 1). The photo at spot 3 also documents a local canopy gap, but the non-central and right part of the photo is vegetation-free. However, the corresponding  $f_{Cover}$  values are the largest among all the spots. This is because the cluster of tall trees in the left part of the photo is placed along the laser-beam direction around spot 2 ( $\theta = 9^\circ, \omega = 60^\circ$ ). The photo for spot 3 is the only one among all photos in which the middle-top part is oriented approximately to the north, i.e.,  $\omega = 60^\circ$  corresponds to the direction of the tree cluster.

## 6. Discussion

### 6.1. Relation of $T_c$ to existing concepts

The  $T_c$  method suggested here provides wavelength-specific, directional, and physically well-defined values. They are derived from radiometric and geometric LiDAR observations, while the  $f_{Cover}$  values are purely geometrical. Such  $T_c$  values are relevant

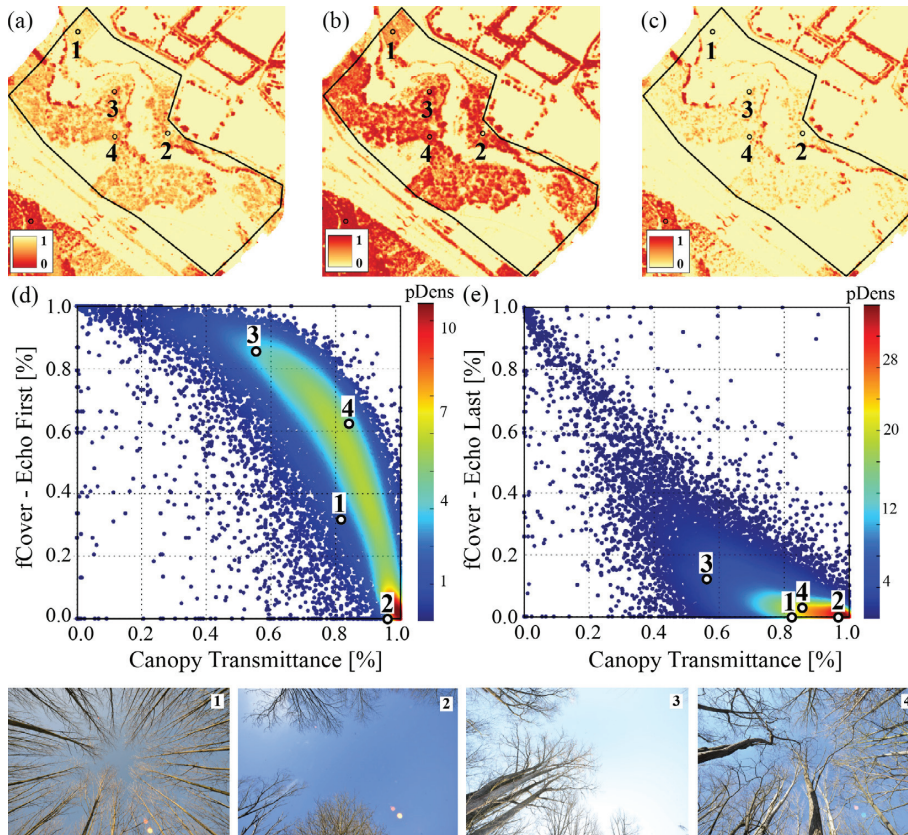


**Fig. 6.** Comparison of fractional cover and  $T_c$  over the alluvial-forest region: (a) total canopy transmittance map, (b) first-echo  $f_{Cover}$  map, (c) last-echo  $f_{Cover}$  map, (d,e) scatter plots of  $T_c$  and  $f_{Cover}$  values, respectively. The open area was masked out before the preparation of scatter plots. Figures in the bottom row show the upward-looking ground photos for spots 1, 2, 3, and 4.

for canopy radiation studies, as in the concept of spectral invariants (Huang et al., 2007; Stenberg et al., 2016). This concept suggests modeling photon-canopy interaction by the canopy interception, the recollision, and the escape probabilities and derives variables that are wavelength-independent (in the solar domain) and more specific to the canopy structure. Our  $T_c$  values are wavelength-specific, but the airborne LiDAR sensors can operate at different laser wavelengths (e.g., 531 nm, 1064 nm, and 1550 nm). The corresponding, wavelength-specific,  $T_c$  values could then be used for modeling transmittance in the spectral invariant methods.

Section 5.2 showed that the  $f_{Cover}$  map for the first echoes is saturated in dense coniferous stands. This is also observed in earlier studies and explained by the insensitivity of the first echoes to canopy gaps smaller than the footprint (Solberg et al., 2009; Morsdorf et al., 2006). In addition, the study of Korhonen et al. (2011) showed that  $f_{Cover}^{First}$  represents the between-crown gaps. The  $f_{Cover}^{Last}$  and  $T_c$  maps derived here appear to be promising for quantification of the within-crown gaps and, indirectly, the leaf area index. However, this should be validated against the angular gap fraction measures from, e.g., hemispherical photos or canopy gap analyzers.

## 6.2. $T_c$ method

The suggested  $T_c$  method uses the energy of single ground echoes to normalize the observed, ground-echo energy. Therefore,

the method requires single ground echoes. The method also involves two further parameters: (a) the height threshold used to select ground echoes (Section 4.2) and (b) the cell size used to aggregate the echo energies (Section 2.3). In contrast, LiDAR acquisition planning involves decisions (selection of sensor type and flying height) that, in turn, define properties of the resulting  $T_c$  map. These aspects are discussed here.

The method was tested using a full-waveform LiDAR data set collected by a specific sensor and under leaf-off conditions. However, there are also cases where the availability of ground echoes is reduced. For example, scanning over leaf-on and dense vegetation may largely reduce the number of ground echoes. The number and type (single or last-of-multiple) of ground echoes will primarily depend on the canopy gaps as well as the laser footprint size. Generally, there can be three possible cases: (a) there are no ground echoes, (b) there are the last-of-multiple ground echoes as well as the single-ground echoes in their vicinity, and (c) there are only the last-of-multiple ground echoes, but no single-ground echoes in their vicinity. In the first case,  $T_c$  is zero, which is handled well in our method, because the monoplotting is used to project the last-in-vegetation echoes to the ground, and the zero energy is assigned to them. The second case is also handled by our method, because there are some single-ground echoes in the vicinity that can be used to normalize the energy of the last-of-multiple ground echoes. Therefore, the only challenging case is the third case, i.e., when there are no single-ground echoes in the vicinity of the last-of-multiple ground echoes. This can be overcome, e.g.,

by increasing the neighborhood size used to search for the single ground echoes (Section 4.4). However, local ground properties (e.g., reflectance) might be lost with a large neighborhood size. As reported in Armston et al. (2013), Chen et al. (2014), and Fieber et al. (2015), this may happen when the spatial variation of ground reflectance happens at scales smaller than the neighborhood size used to select the single ground echoes. Nevertheless, this limitation is generally valid for all the methods that consider the echo energies.

The height threshold used to select ground echoes was set here to 0.5 m, and the same value is used in Armston et al. (2013) and Chen et al. (2014). The threshold values of 0.3 m, 0.4 m, 0.6 m, and 0.7 m were also tested. It was observed that the  $T_c$  values increased for the height thresholds smaller than 0.5 m, while the opposite happens for the height thresholds larger than 0.5 m. Nevertheless, the mean  $T_c$  values changed less than 2%, for each threshold setting. It is noted that this parameter also depends on the accuracy and the level of detail of the DTM. The DTM accuracy, in contrast, depends on the LiDAR filtering strategy, while for leaf-on conditions and dense vegetation, the accuracy may be lower compared to the leaf-off conditions. These aspects should be considered when setting the height threshold. The cell size used to aggregate the echo energies was set to 2 m. Larger cell sizes of 5 m and 10 m were also tested, but the main trend of the scatter plots in Fig. 5 and in Fig. 6 was preserved. It is only the dispersions of the  $T_c$  and  $F_{cover}$  values that were reduced by increasing the cell size. No systematic change of the values was noted. Theoretically,  $T_c$  can be also derived on the laser-beam level. Nevertheless, an appropriate cell size is to be defined by the application requirements.

The sensor properties affect the number of ground points. For example, scanning over the same vegetation conditions, season, and flying height with sensors having different laser-beam divergence results in a different number of ground points. The selection of flying height, therefore, defines the directional properties of the resulting  $T_c$  values. Furthermore, airborne LiDAR sensors operate at different laser wavelengths (e.g., 531 nm, 1064 nm, and 1550 nm), and thus, the observed echo energies depend on the ground spectral properties. In line with that, Morsdorf et al. (2008) reported that  $f_{cover}$  values may be affected by the scanning angle and the footprint size.

Finally, the method could be improved by considering more advanced strategies for the selection of single ground echoes. For example, before the selection, single ground echoes can be classified according to their backscattering coefficient or the ground reflectance derived from it. These properties would, however, require the radiometric calibration of the single ground echoes (Wagner, 2010). Diverse selection strategies of the single ground echoes would also allow for an uncertainty analysis of the  $T_c$  values.

## 7. Conclusions

In this study, a new method is presented for calculating directional, total canopy transmittance from small-footprint, full-waveform LiDAR data. The transmittance values derived by the method have a clear physical and geometrical meaning, which is relevant for canopy radiation studies. The suggested method considers only the energy of ground echoes. The canopy transmittance is then estimated by normalizing this energy by an energy approximated from the single ground echoes. Such normalization is beneficial for two reasons. First, there is no need to calibrate waveforms, because the calibration constant cancels out in the energy ratio. Second, assumptions on the vegetation scattering characteristics (reflectance and extinction) are not required,

because only the energy backscattered from the ground layer is considered. In contrast, the  $T_c$  method requires single ground echoes, and their number may be reduced when scanning under leaf-on conditions or over dense forest. This can be overcome, e.g., by a large neighborhood size used to search for the single ground echoes.

The method was applied to a contemporary full-waveform LiDAR data set and under leaf-off conditions. The study site contains two sub regions: (a) a region with mixed (coniferous and deciduous) forest and (b) a region with alluvial (predominately deciduous) forest. The resulting canopy transmittance map was compared with aerial photos and the well-known, fractional cover method. The comparison of the canopy transmittance map with the fractional cover map was done independently for each region and for two versions of the fractional cover: one where only first echoes were considered and another where only last echoes were considered. For the mixed region, the fractional cover maps showed some saturation compared with the canopy transmittance map. The first-echo fractional cover map was saturated at high fractional cover values (>0.8), while the last-echo fractional cover map was slightly saturated at low fractional cover values (<0.2). For the alluvial region (deciduous forest with leaf-off conditions), the first-echo fractional cover map showed less saturation than the canopy transmittance map, while the last-echo fractional cover map was again slightly saturated.

The results show that the method provides canopy transmittance values that are not saturated over mixed forests compared to the existing fractional cover method. The focus for future work should be on a quantitative validation of the transmittance values derived by the method. The  $T_c$  values have a clear physical and geometrical meaning, which is relevant for further canopy radiation studies or derivation of biophysical parameters, such as leaf area index.

## Acknowledgements

The authors would like to thank Martin Wieser for his help in acquiring the ground photos and Andreas Roncat and Gottfried Mandlbürger for valuable discussions on the radiometric properties of the LiDAR data set. The authors would also like to thank the company, RIEGL Laser Measurement Systems GmbH, for providing the data for this study.

The research leading to these results has received funding from the European Community's Seventh Framework Programme ([FP7/2007–2013]) under grant agreement no 606971.

## References

- Armston, J., Disney, M., Lewis, P., Scarth, P., Phinn, S., Lucas, R., Bunting, P., Goodwin, N., 2013. Direct retrieval of canopy gap probability using airborne waveform lidar. *Remote Sensing Environ.* 134, 24–38 <http://www.sciencedirect.com/science/article/pii/S003442571300062X>.
- Bréda, N.J.J., 2003. Groundbased measurements of leaf area index: a review of methods, instruments and current controversies. *J. Exp. Botany* 54 (392), 2403–2417 <http://jxb.oxfordjournals.org/content/54/392/2403.abstract>.
- Chen, X., Disney, M., Lewis, P., Armston, J., Han, J., Li, J., 2014. Sensitivity of direct canopy gap fraction retrieval from airborne waveform lidar to topography and survey characteristics. *Remote Sensing Environ.* 143, 15–25 <http://www.sciencedirect.com/science/article/pii/S0034425713004501>.
- Clawges, R., Vierling, K., Vierling, L., Rowell, E., 2008. The use of airborne lidar to assess avian species diversity, density, and occurrence in a pine/aspen forest. *Remote Sensing Environ.* 112 (5), 2064–2073. *Earth Observations for Terrestrial Biodiversity and Ecosystems Special Issue* <http://www.sciencedirect.com/science/article/pii/S0034425708000291>.
- Fieber, K.D., Davenport, I.J., Tanase, M.A., Ferryman, J.M., Gurney, R.J., Becerra, V.M., Walker, J.P., Hacker, J.M., 2015. Validation of canopy height profile methodology for small-footprint full-waveform airborne lidar data in a discontinuous canopy environment. *ISPRS J. Photogram. Remote Sensing* 104, 144–157 <http://www.sciencedirect.com/science/article/pii/S092427161500060X>.

- Harding, D., Lefsky, M., Parker, G., Blair, J., 2001. Laser altimeter canopy height profiles: methods and validation for closed-canopy, broadleaf forests. *Remote Sensing Environ.* 76, 283–297.
- Hopkinson, C., Chasmer, L., 2009. Testing lidar models of fractional cover across multiple forest eczones. *Remote Sensing Environ.* 113 (1), 275–288 <http://www.sciencedirect.com/science/article/pii/S0034425708003106>.
- Huang, D., Knyazikhin, Y., Dickinson, R.E., Rautiainen, M., Stenberg, P., Disney, M., Lewis, P., Cescaati, A., Tian, Y., Verhoef, W., Martonchik, J.V., Myneni, R.B., 2007. Canopy spectral invariants for remote sensing and model applications. *Remote Sensing Environ.* 106 (1), 106–122 <http://www.sciencedirect.com/science/article/pii/S0034425706002847>.
- Jutzi, B., Stilla, U., 2006. Range determination with waveform recording laser systems using a wiener filter. *ISPRS J. Photogram. Remote Sensing* 61 (2), 95–107 <http://www.sciencedirect.com/science/article/pii/S0924271606001080>.
- Korhonen, L., Korpela, I., Heiskanen, J., Maltamo, M., 2011. Airborne discrete-return lidar data in the estimation of vertical canopy cover, angular canopy closure and leaf area index. *Remote Sensing Environ.* 115 (4), 1065–1080 <http://www.sciencedirect.com/science/article/pii/S0034425710003494>.
- Kraus, K., 2007. *Photogrammetry – Geometry from Images and Laser Scans*. De Gruyter.
- Kraus, K., Pfeifer, N., 1998. Determination of terrain models in wooded areas with airborne laser scanner data. *ISPRS J. Photogram. Remote Sensing* 53 (4), 193–203 <http://www.sciencedirect.com/science/article/pii/S0924271698000094>.
- Lefsky, M.A., Harding, D., Cohen, W., Parker, G., Shugart, H., 1999. Surface lidar remote sensing of basal area and biomass in deciduous forests of eastern maryland, (USA). *Remote Sensing Environ.* 67 (1), 83–98 <http://www.sciencedirect.com/science/article/pii/S0034425798000716>.
- Lindberg, E., Elofsson, K., Holmgren, J., Olsson, H., 2012. Estimation of 3d vegetation structure from waveform and discrete return airborne laser scanning data. *Remote Sensing Environ.* 118, 151–161 <http://www.sciencedirect.com/science/article/pii/S003442571100410X>.
- Maltamo, M., Næsset, E., Vauhkonen, J., 2014. *Forestry Applications of Airborne Laser Scanning: Concepts and Case Studies*. Managing Forest Ecosystems. Springer, Netherlands <https://books.google.se/books?id=i3vGBAAQBAJ>.
- Moesser, D., Roubinek, J., Schleppl, P., Morsdorf, F., Jonas, T., 2014. Canopy closure, {LAI} and radiation transfer from airborne lidar synthetic images. *Agric. Forest Meteorol.* 197, 158–168 <http://www.sciencedirect.com/science/article/pii/S0168192314001506>.
- Monsi, M., Saeki, T., 2005. On the factor light in plant communities and its importance for matter production. *Ann. Botany* 95 (3), 549–567. note that this reference is an English translation of the original article published in German in 1953 <http://aob.oxfordjournals.org/content/95/3/549.short>.
- Morsdorf, F., Frey, O., Meier, E., Itten, K.I., Allgöwer, B., 2008. Assessment of the influence of flying altitude and scan angle on biophysical vegetation products derived from airborne laser scanning. *Int. J. Remote Sensing* 29 (5), 1387–1406 <http://dx.doi.org/10.1080/01431160701736349>.
- Morsdorf, F., Kötz, B., Meier, E., Itten, K., Allgöwer, B., 2006. Estimation of LAI and fractional cover from small footprint airborne laser scanning data based on gap fraction. *Remote Sensing Environ.* 104 (1), 50–61 <http://www.sciencedirect.com/science/article/pii/S0034425706001751>.
- Muss, J.D., Mladenoff, D.J., Townsend, P.A., 2011. A pseudo-waveform technique to assess forest structure using discrete lidar data. *Remote Sensing Environ.* 115 (3), 824–835 <http://www.sciencedirect.com/science/article/pii/S0034425710003275>.
- Musselman, K.N., Margulis, S.A., Molotch, N.P., 2013. Estimation of solar direct beam transmittance of conifer canopies from airborne lidar. *Remote Sensing Environ.* 136, 402–415 <http://www.sciencedirect.com/science/article/pii/S0034425713001752>.
- Ni-Meister, W., Jupp, D.L.B., Dubayah, R., 2001. Modeling lidar waveforms in heterogeneous and discrete canopies. *IEEE Trans. Geosci. Remote Sensing* 39 (9), 1943–1958.
- Nicodemus, F.E., Richmond, J.C., Hsia, J.J., Ginsberg, I.W., Limperis, T., 1977. *Geometrical Considerations and Nomenclature for Reflectance*. US Department of Commerce, National Bureau of Standards, Washington, D.C.
- Otepka, J., Ghuffar, S., Waldhauser, C., Hochreiter, R., Pfeifer, N., 2013. Georeferenced point clouds: a survey of features and point cloud management. *ISPRS Int. J. Geo-Inf.* 2 (4), 1038 <http://www.mdpi.com/2220-9964/2/4/1038>.
- Parker, G.G., Lefsky, M.A., Harding, D.J., 2001. Light transmittance in forest canopies determined using airborne laser altimetry and in-canopy quantum measurements. *Remote Sensing Environ.* 76 (3), 298–309 <http://www.sciencedirect.com/science/article/pii/S003442570000211X>.
- Pfeifer, N., Mandlbürger, G., Otepka, J., Karel, W., 2014. {OPALS} a framework for airborne laser scanning data analysis. *Comput. Environ. Urban Syst.* 45, 125–136 <http://www.sciencedirect.com/science/article/pii/S0198971513001051>.
- Ressl, C., Pfeifer, N., Mandlbürger, G., 2011. Applying 3d affine transformation and least squares matching for airborne laser scanning strips adjustment without gnss/imu trajectory data. *ISPRS – International Archives of the Photogrammetry, Remote Sensing and Spatial Information Sciences XXXVIII-5/W12*, pp. 67–72. <<http://www.int-arch-photogramm-remote-sens-spatial-inf-sci.net/XXXVIII-5-W12/67/2011/>>.
- Riano, D., Valladares, F., Condes, S., Chuvieco, E., 2004. Estimation of leaf area index and covered ground from airborne laser scanner (lidar) in two contrasting forests. *Agric. Forest Meteorol.* 124 (34), 269–275 <http://www.sciencedirect.com/science/article/pii/S0168192304000449>.
- Roncat, A., Bergauer, G., Pfeifer, N., 2011. B-spline deconvolution for differential target cross-section determination in full-waveform laser scanning data. *ISPRS J. Photogram. Remote Sensing* 66 (4), 418–428 <http://www.sciencedirect.com/science/article/pii/S0924271611000244>.
- Sasaki, T., Imanishi, J., Fukui, W., Morimoto, Y., 2016. Fine-scale characterization of bird habitat using airborne lidar in an urban park in japan. *Urban Forestry Urban Greening* 17, 16–22 <http://www.sciencedirect.com/science/article/pii/S1618866715300145>.
- Skaloud, J., Lichti, D., 2006. Rigorous approach to bore-sight self-calibration in airborne laser scanning. *ISPRS J. Photogram. Remote Sensing* 61 (1), 47–59 <http://www.sciencedirect.com/science/article/pii/S0924271606000682>.
- Solberg, S., Brunner, A., Hanssen, K.H., Lange, H., Næsset, E., Rautiainen, M., Stenberg, P., 2009. Mapping {LAI} in a norway spruce forest using airborne laser scanning. *Remote Sensing Environ.* 113 (11), 2317–2327 <http://www.sciencedirect.com/science/article/pii/S0034425709001862>.
- Solberg, S., Næsset, E., Hanssen, K.H., Christiansen, E., 2006. Mapping defoliation during a severe insect attack on scots pine using airborne laser scanning. *Remote Sensing Environ.* 102 (34), 364–376 <http://www.sciencedirect.com/science/article/pii/S0034425706000964>.
- Stenberg, P., Mttus, M., Rautiainen, M., 2016. Photon recollision probability in modelling the radiation regime of canopies a review. *Remote Sensing Environ.* 183, 98–108 <http://www.sciencedirect.com/science/article/pii/S0034425716302140>.
- Wagner, W., 2010. Radiometric calibration of small-footprint full-waveform airborne laser scanner measurements: basic physical concepts. *ISPRS J. Photogram. Remote Sensing* 65 (6), 505–513. *ISPRS Centenary Celebration Issue* <http://www.sciencedirect.com/science/article/pii/S0924271610000626>.
- Wagner, W., Ullrich, A., Ducic, V., Melzer, T., Studnicka, N., 2006. Gaussian decomposition and calibration of a novel small-footprint full-waveform digitising airborne laser scanner. *ISPRS J. Photogram. Remote Sensing* 60 (2), 100–112 <http://www.sciencedirect.com/science/article/pii/S0924271605001024>.

### 3.5 Paper V

**Title:** Influence of Footprint Size and Geolocation Error on the Precision of Forest Biomass Estimates from Space-Borne Waveform LiDAR

**Authors:** Milenković, M., Schnell, S., Holmgren, J. Ressler, C., Lindberg, E., Hollaus, M., Pfeifer, N. and Olsson, H.

**Published in:** Remote Sensing of Environment, Vol. 200, pp.74-88,  
<https://doi.org/10.1016/j.rse.2017.08.014>, 2017

**Licence:** © 2017 Elsevier Inc. All rights reserved. This manuscript version is made available under the Attribution-NonCommercial-NoDerivatives 4.0 International (CC-BY-NC-ND 4.0) license,  
<http://creativecommons.org/licenses/by-nc-nd/4.0/>



Contents lists available at ScienceDirect

## Remote Sensing of Environment

journal homepage: [www.elsevier.com/locate/rse](http://www.elsevier.com/locate/rse)

## Influence of footprint size and geolocation error on the precision of forest biomass estimates from space-borne waveform LiDAR



Milutin Milenković<sup>a,\*</sup>, Sebastian Schnell<sup>b,c</sup>, Johan Holmgren<sup>b</sup>, Camillo Ressler<sup>a</sup>, Eva Lindberg<sup>b</sup>, Markus Hollaus<sup>a</sup>, Norbert Pfeifer<sup>a</sup>, Håkan Olsson<sup>b</sup>

<sup>a</sup> Department of Geodesy and Geoinformation (GEO), Technische Universität Wien, Gußhausstraße 27-29, 1040 Vienna, Austria

<sup>b</sup> Department of Forest Resource Management, Swedish University of Agricultural Sciences, SLU Skogsmarksgränd, Umeå SE-90183, Sweden

<sup>c</sup> Forest Inventory and Remote Sensing, Faculty of Forest Sciences, University of Goettingen, Buesgenweg 5, 37077 Goettingen, Germany

## ARTICLE INFO

## Keywords:

Satellite LiDAR  
Biomass  
Large footprint  
Waveform stacking  
Forest inventory  
Model-assisted estimation  
Hybrid inference

## ABSTRACT

Space-borne LiDAR systems can potentially assist large-area assessments of forest resources, in particular when a subset of the acquired LiDAR footprints is combined with field surveys of forest stand characteristics at footprint location. When combined, space-borne LiDAR geolocation error and the footprint size may however have considerable effects on the estimation accuracy of forest stand variables, such as aboveground biomass (AGB). The aim of this study was to draw recommendations for future space-borne LiDAR systems, which should deliver data for unbiased AGB assessments. The recommendations were drawn from AGB estimations based on space-borne LiDAR waveforms simulated over a 1300 ha large study site in southern Sweden. Large-footprint, nadir-looking satellite waveforms were simulated by stacking individual small-footprint, airborne LiDAR waveforms observed near a predefined sampling pattern. The stacked waveforms, represented by their metrics, were used as input for a two-phase systematic sampling in combination with model-assisted estimation or hybrid inference for estimating AGB and its variance. The second-phase sample included 264 inventory plots, whereas the first-phase sample included 1010 sample locations, where satellite waveforms were simulated. After simulating satellite waveforms with different footprint sizes and analyzing the AGB variance, the recommendation is to have a footprint size that is similar to the size of the field plots used for collecting reference data, i.e. 20 m diameter in our case. For the optimal footprint size, AGB was estimated with a precision of 2.9 Mg per hectare (2.9% of the average). The results also showed that variance estimates increased constantly with increasing geolocation error. For a geolocation error of 14 m, variance estimates increased by 17%, which justifies investing additional efforts in minimizing it.

## 1. Introduction

Space-borne LiDAR (Light Detection and Ranging) systems dedicated for estimation of vegetation are expected and needed in the future. Such systems will regularly provide samples of vegetation height information for all parts of the globe, and offer opportunities for estimation of aboveground biomass (AGB) and related variables over large areas.

The Geoscience Laser Altimeter System (GLAS) on board of the Ice, Cloud, and Land Elevation Satellite (ICESat) collected unprecedented global data on three-dimensional (3D) forest canopy structure during its mission from 2003 to 2007. It exploited the LiDAR principle, i.e. transmitting a laser pulse and recording of its time-delay, to receive 3D data from the Earth's surface. Although not specifically designed for vegetation mapping, ICESat/GLAS measurements have successfully

been used for national to global assessments of basic forest stand characteristics, such as canopy height (Lefsky, 2010), growing stock volume (Maselli et al., 2014; Nelson et al., 2009), aboveground biomass (Boudreau et al., 2008; Margolis et al., 2015; Nelson et al., 2017), and aboveground carbon (Neigh et al., 2013).

The upcoming missions, ICESat-II and GEDI (the Global Ecosystem Dynamics Investigation), will provide a very dense, near global sampling of canopy heights. The ATLAS instrument on board of the ICESat-II satellite will record a certain number of elevation measurements for each footprint using a single photon counting technique. Single pulses of the ATLAS instrument will be split up into six parallel tracks arranged in three pairs with a distance between pairs of 3.3 km. Within beams, the single footprints will be separated by a distance of 0.7 m and will have a diameter of 14 m (Abdalati et al., 2010; Gwenz et al., 2016). The GEDI mission will collect large-footprint waveforms along

\* Corresponding author.

E-mail address: [Milutin.Milenkovic@geo.tuwien.ac.at](mailto:Milutin.Milenkovic@geo.tuwien.ac.at) (M. Milenković).

<http://dx.doi.org/10.1016/j.rse.2017.08.014>

Received 17 March 2017; Received in revised form 24 July 2017; Accepted 4 August 2017  
0034-4257/ © 2017 Elsevier Inc. All rights reserved.

10 parallel tracks with a spacing of about 600 m. Within tracks, the waveforms will be recorded every 25 m over 25 m large footprints (NASA, 2016). ICESat data has already been used for large-area forest resource assessments (Nelson et al., 2017), and more applications are expected to come with ICESat-II and GEDI, and there is a large potential to further develop this technology in order to create fully operational and redundant systems that are tailor-made for national and international forest biomass assessments.

The application of space-borne LIDAR (SL) data for forest monitoring typically requires field collected reference data and suitable modeling strategies for predicting field-observed stand characteristics from SL measurements (Nelson et al., 2017). For developing prediction models, a link between field and SL data is required, which can either be done by measuring ground data directly under SL observations (Montesano et al., 2015; Nelson et al., 2009) or by using an additional data source, such as airborne laser scanning (ALS) for an indirect linkage between field and SL data (Margolis et al., 2015; Nelson et al., 2017). From a survey sampling perspective, the SL measurements form a first sample phase, as they do not fully cover the Earth's surface, which introduces a sampling error attached to estimates derived from such data. For the case of directly linking field and SL data, field observations are sub-sampled within the first sample phase and estimation of target variables and their uncertainties can be done using design-based inference with model-assisted estimation (Gregoire et al., 2011) or by using a so called hybrid approach (Ståhl et al., 2016). If field data is not covered by SL data (the indirect case), the uncertainties from two models (e.g. field to ALS and ALS to SL) need to be considered during estimation. In this case the hybrid three-phase estimators developed by Holm et al. (2017) may be applied. More detail on LiDAR sampling for forest applications can be also found in Wulder et al. (2012).

The spatial mismatch between SL data and field plots as well as the plot size itself are expected to have considerable effects on model fit and the accuracy of AGB estimates. These effects were, for example, studied for ALS data by Gobakken and Næsset (2009) and Frazer et al. (2011). Gobakken and Næsset (2009) found that stem volume estimates were already severely affected by geolocation errors of 5 m and that errors were especially a problem when small field plots were used. Similar conclusions were later drawn by Frazer et al. (2011), further stating that plot size is a critical design parameter in LiDAR studies affecting (1) the precision and accuracy of AGB estimates, (2) the precision and accuracy of LiDAR metrics, and (3) the negative effect of geolocation error. The recommendation from the study was towards the usage of larger plot sizes in comparison to what is common in forest inventories of temperate and boreal zones (see Tomppo et al., 2010 for common plot sizes). The influence of mismatch between the plot size and pixel size was studied in Rejou-Mechain et al. (2014) using 30, globally distributed, large field plots (8–15 ha). The study, however, assumed remote sensing data which have no measurement errors, i.e. measurements retrieved the exact value of AGB density as measured in the field plots. The analysis showed that a plot size smaller than a remote sensing pixel causes considerable calibration errors, which was explained by large spatial variability in mean AGB density for plot sizes smaller than 0.25 ha.

For large-footprint, space-borne systems studies about the effects of footprint size and positional accuracy are however still few. Pang et al. (2011) studied the effects of footprint size and off-nadir pointing on the precision of canopy height estimates by means of simulation. They concluded that footprints with a diameter between 25 m and 30 m would be ideal to level the effects of vegetation height and terrain slope on waveform length. This footprint size corresponds well with what is commonly used for field plot size in forest inventories of temperate and boreal climate and also with the footprint size that will be used by the future GEDI system. Furthermore, this footprint size was also recommended for the laser altimeter planned for DESDynI mission (Hall et al., 2011). However, the study by Pang et al. (2011) does not handle the influence of geolocation error on estimation of forest variables with

large-footprint LiDAR sensors. Goncalves et al. (2017) varied the locations of field plots and used Monte Carlo simulations and binomial distribution to estimate the biomass difference due to the introduced spatial mismatch between field plots and GLAS footprints in Amazon forest. Their analysis showed that the plot-footprint overlap should be larger than 75% (50%) for primary (secondary) forest to have a geolocation error < 20%. However, the study by Goncalves et al. (2017) does not handle the influence of the footprint size on estimation of forest variables.

Several studies have used simulated SL data to prepare future space missions. The simulations are usually based either on (1) a radiative transfer model (Gastellu-Etcheberry et al., 2015; Montesano et al., 2015; North et al., 2010), or (2) on data from airborne sensors (Gwenzi et al., 2016). The radiative transfer model approach requires assumptions on physical geometrical properties of vegetation, whereas the data approach requires corrections for the sensor characteristics affecting the recorded signal. Blair and Hofton (1999) modeled large-footprint LiDAR waveform data using a vertical distribution of intercepted surfaces approximated with data from a small-footprint LiDAR system. The returned waveform from the large-footprint system was obtained using a composition of elementary pulses reflected from each element within the large footprint. They modeled the elementary reflections with the spatial intensity properties of a large-footprint system using a normal distribution over finite vertical and horizontal distances and convolved the sum of elementary reflections with a Gaussian approximation of the impulse response of a large-footprint system to obtain “pseudo-waveforms”. High correlations were observed when simulated large footprints were compared with data from the airborne large-footprint system “Laser Vegetation Imaging Sensor” (LVIS). They concluded that the simulated waveforms could be useful for pre-launch simulations of upcoming space-borne LiDAR systems. Duong et al. (2009) have shown that ALS can very well explain ICESat waveforms of 70 m footprint. However, as discrete points were used, the blurring effect of waveforms (ca. 5 ns duration) was not found for clearly defined objects (e.g. horizontal ground).

The overall objective of this paper is to study the effect of footprint size and geolocation error on AGB estimates obtained from a first-phase sample of simulated SL footprints and a smaller second-phase sample of co-registered field plots. The method for SL waveform simulation is based on a spatial integration of the interactions of individual laser pulses and the object, i.e. small-footprint waveforms found within a large-footprint, SL beam cone. This, so-called waveform stacking, involves range corrections for the flight trajectory and oblique looking. Thus, the primary difference between airborne and space-borne waveforms we consider lies in the footprint size, whereas the length and shape of the airborne system response (emitted pulse recorded by the detector) “define” the length of pulses from simulated space-borne waveforms. To emphasize that the SL waveforms are simulated, they will be referred here as simulated space-borne LiDAR (SSL) waveforms. To study the effect of footprint size and geolocation errors on AGB estimates, nadir-looking SSL waveforms with different footprint sizes were simulated for a predefined monitoring strategy. The advantage of studying a real site is the large amount of ground reference data available. From the SSL waveforms, various waveform metrics were derived, which provided the input for the AGB estimation including uncertainty analyses. Based on the outcome of these analyses recommendations were drawn for the design of future SL systems rather than to simulate a particular sensor.

The paper is structured in the following way. First, we present the study site and data used for the simulation of SL waveforms. Second, we describe the methods for SL waveform simulation. Third, metrics for predicting AGB are defined and derived from the SSL waveforms. Fourth, the framework for estimating AGB and its uncertainty is introduced and results are presented and discussed. Finally, conclusions and recommendations with respect to forestry applications are drawn for future SL systems.

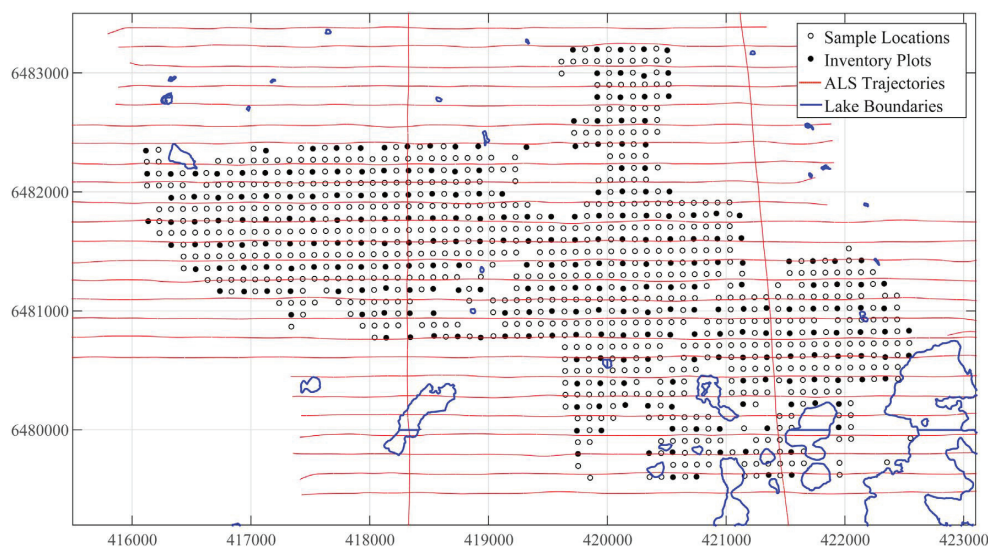


Fig. 1. Simulated space-borne LiDAR (SSL) sampling design and inventory strategy employed in the case study for estimating average aboveground biomass in the study area. The open circles together with the closed circles are the first-phase sample of SSL observations, whereas the filled circles only are the second-phase field measurements. The red lines show the strip trajectories of the small-footprint, full-waveform, airborne LiDAR data, used to simulate large-footprint SL waveforms. The coordinate reference system is SWEREF99 TM. (For interpretation of the references to color in this figure legend, the reader is referred to the web version of this article.)

## 2. Study site and data

### 2.1. Study site and forestry inventory data

The test site Remningstorp is located in the south of Sweden (58°30' N, 13°40' E). The estate covers about 1300 ha of managed forest land. Prevailing tree species are Norway spruce (*Picea abies*), Scots pine (*Pinus sylvestris*) and birch (*Betula* spp.). The topography is flat with a ground elevation between 120 and 145 m above sea level. During summer 2014, 264 field plots with a radius of 10 m were distributed evenly using a square grid with 200 m spacing (Fig. 1, the filled circles). On these plots, stem diameter at breast height (dbh) and tree species were registered for all trees with dbh  $\geq$  40 mm, while tree height was measured for a sample of trees. The coordinates of the plot centers were measured with differential GNSS (Global Navigation Satellite System). In addition to the field data, a manual interpretation of the land use/land cover of the Remningstorp area was available from an experienced photo interpreter. The data was used to limit the analysis to productive forest lands.

### 2.2. Airborne laser scanning data

Full-cover waveform ALS data were available for the entire study area and used for simulating SL waveforms. The data were collected with a RIEGL LMS-Q680i scanner on 14th of September 2014. In total, there were 27 ALS strips covering the forest inventory plots. The majority (25) of the ALS strips were recorded in an east-west direction and the remaining two in a north-south direction (Fig. 1). The east-west strips were separated from one another by approximately 150 m, and the average flight height above the terrain was 305 m. As this scanner has a scan angle range of  $\pm 30^\circ$ , the average swath width was 352 m, while the strip overlap was about 55%.

Single ALS strips were collected with mean point densities of last returns ranging between 25 and 28 points per  $m^2$ . The footprint diameter at the ground was  $< 21$  cm over the whole area, while the average footprint diameter was 15 cm. The scanner was further using a wavelength of 1550 nm to transmit laser pulses of 5 ns (the full width at the half maximum of the amplitude). This corresponds to a range

resolution of 0.75 m (Wagner et al., 2006). The RIEGL LSM-Q680i sensor supports multiple time around (MTA) ranging, i.e. it operates with multiple pulses in the air, which then causes range ambiguity for the returns (Rieger and Ullrich, 2011). Practically, this means that the scanner does not operate with a single pulse repetition rate (PRR), but changes the PRR constantly among a preset mean PRR. For our data, the mean PRR was set to 360 kHz, while the highest and lowest PRR were set to 374 kHz and 348 kHz, respectively. These PRRs caused the range ambiguities of 401 m and 431 m, respectively. The maximum range of our ALS data was 433 m. This means that there were at maximum two pulses at the same time in the air, i.e. two MTA zones for our data set.

The ALS data were further processed, return-wise, in the sensor's manufacturer software to derive individual returns, and subsequently, a digital terrain model (DTM). There were up to 10 discrete returns per transmitted pulse after the processing. The returns were filtered using the algorithm suggested by Axelsson (1999), resulting in a 1 m grid DTM of the study area. The DTM as well as the georeferenced returns were projected to the SWEREF99 TM coordinate system.

## 3. Methodology

The methodology includes three major steps: waveform simulation, calculation of waveform metrics and AGB estimation.

We employed a two-phase sampling strategy for AGB estimation, where the first phase includes a systematic sample of 1010 satellite plots with simulated waveform data, while the second-phase sample includes a systematic sub-sample of 264 field plots. The initial SSL sampling grid contained also plots over arable land and other non-forest land-use categories (e.g. lakes); such plots were consequently excluded from the analysis. For the field plots, both inventory and simulated waveform data were available. The systematic sampling was designed in the following way: satellite orbits are assumed to run in a north-south direction and have a spacing of 100 m. Within orbits, every 100 m an observation was made, so that each field plot is covered with SSL data. Additionally, there are SSL observations in-between field observations (Fig. 1).

For the second-phase sample (the field plots), a direct link between field data and waveform metrics was established. Such an inventory

strategy has been used in connection with ICESat-I data, where SL waveforms were searched in the field for collecting ground reference data (Montesano et al., 2015; Nelson et al., 2009). SL is considered a large-area sampling tool in forest surveys, operating at continental to global scale. In our study, we mimic the implementation of one possible inventory strategy for a much smaller geographic region due to limited availability of data for waveform simulations and restrictions concerning computation time. The focus is on the influence of varying footprint size and geolocation error of SSL waveforms on final AGB estimates.

### 3.1. Waveform simulation

The simulation of SL waveforms was done by stacking individually recorded airborne LiDAR waveforms that were located within a larger footprint. The objective was to simulate nadir-looking waveforms whose large footprints are centered at the middle points of the SSL sample plots and the field plots, respectively. In total, 1010 SL large-footprint waveforms were simulated at the corresponding sample locations.

Several processing steps are required to go from raw small-footprint airborne LiDAR waveforms to large-footprint SSL waveforms. The processing involves assigning the MTA zone to recording blocks, waveform geo-referencing, selection of waveforms within the sample plots, range corrections and stacking. This subsection starts by presenting the structure and properties of the raw waveform data, and then, follows the mentioned processing steps. The subsection ends by presenting the metrics derived from the stacked waveforms, which will be used for AGB estimation.

#### 3.1.1. LiDAR waveforms and recording blocks

The RIEGL LMS-Q680i LiDAR sensor recorded the amplitude of the backscattered energy from a transmitted laser pulse at every nanosecond. This waveform sampling frequency corresponds to a range of 15 cm, i.e. a double way distance of 30 cm. The amplitudes collected over a short period (usually 80 ns, or 160 ns, corresponding to 24 m and 48 m, respectively) forms a signal, i.e. a waveform, which is then stored by the system in recording blocks (Riegl, 2013). The recording blocks are grouped by corresponding preceding laser pulses and are assigned with auxiliary waveform information. This means that several recording blocks can be stored under a single transmitted pulse.

The raw LiDAR waveform data were stored strip-wise, and individual recording blocks, as well as their auxiliary information, were accessed by a waveform extraction library (the RiWaveLib) provided by the manufacturer.

#### 3.1.2. Assigning recording blocks to corresponding laser pulses

The used LiDAR sensor utilizes MTA ranging, which requires resolving the range ambiguities of the recording blocks. Methods for resolving the MTA range ambiguities are suggested for the return-wise data processing by Rieger and Ullrich (2011) and Lu et al. (2015). We borrowed the idea of using a DTM for this task, but had to extend the method to raw LiDAR waveforms.

The range ambiguities occurred when new laser pulses were transmitted before the sample block of the preceding pulse was recorded. This practically means that a specific sample block did not necessarily correspond to the preceding laser pulse. In such a case, the sample block had to be assigned to another, earlier laser pulse. As our LiDAR data had at maximum two pulses in the air at the same time (Section 2.2), there were just two possibilities: a recording block had to be related either to the preceding pulse, or to the one before the preceding pulse.

The range ambiguities of our recording blocks were resolved in the following manner. First, the maximum amplitude return was extracted from each sample block. Then they were assigned with the range relative to their preceding laser pulses. Combining these ranges with the unit beam vectors, a point cloud in the scanner coordinate system was

derived. This point cloud was then transformed by direct geo-referencing to a world coordinate system, in our case SWEREF99 TM. Finally, the georeferenced heights of the maximum-amplitude returns were compared with the DTM (Section 2.2). As expected, the return heights clustered into two groups: one close to the terrain, i.e. in MTA zone 2, and another one erroneously ( $> 200$  m) away from the terrain (closer to the flight trajectory), i.e. in MTA zone 1.

The maximum amplitude returns close to the terrain have the correct range, and thus, their recording blocks are related to the preceding pulse. On the other hand, the remaining returns apparently have an erroneous range. The above procedure was repeated for the ranges derived relative to the one before the preceding pulse. Finally, the points close to the terrain (in MTA zone 2) from both version of ranges were combined into a single, georeferenced point cloud with correctly assigned ranges. This point cloud was also assigned with sample block identifiers as well as the auxiliary data (e.g. amplification settings, recording times of the recording blocks, and unit laser beam vectors in both sensor and world coordinate system). Such a geo-referenced, maximum-amplitude point cloud was derived for each strip.

#### 3.1.3. Selection of recording blocks for waveform stacking

To select all recording blocks for a SSL sample location, the nearest LiDAR strip was first identified using the strips' trajectories, i.e. finding a strip trajectory, which is the closest (in the x-y plane) to the sample location. The selection of the recording blocks near to the sample location was based on the geo-referenced maximum-amplitude point cloud (Section 3.1.2). All the recording blocks with maximum-amplitude returns that were located inside a circular neighborhood centered at the sample location were selected. The radius of this circular neighborhood was treated as a variable in a later stage, when different footprint sizes were simulated. The selected maximum-amplitude returns contained also the recording indices of the corresponding recording blocks and their laser pulses, which was then used to access the waveforms. Two different channels were used for the recording blocks: (a) the so-called high power (low amplification) channel, and (b) low power (high amplification) channel. Here, only the recording blocks recorded by the high-power channel were considered for stacking.

#### 3.1.4. Range corrections

During the scanning, the absolute position and orientation of the scanner constantly changed, which is described by the flight trajectory. On the other hand, the ranges, i.e. the x-axes of the recording blocks (waveforms), are always defined relative to the instantaneous scanner location. This means that the recording blocks are misaligned when compared according to their original ranges. Therefore, range corrections for the scanner position and orientation are to be applied before the stacking of the recording blocks. The range correction for the scanner position, i.e. the range offset, was derived with respect to a reference point  $T_0$ , set to define the origin of the corrected ranges. The range correction for the scanner orientation was derived with respect to the vertical, as the objective was to simulate the nadir-looking waveforms.

For a sample block  $i$  selected for the stacking at the sample location  $j$ , the corrected range  $R_i'$  was calculated as:

$$R_i' = R_i \cos \alpha_i + \Delta R_i, \quad (1)$$

where  $R_i$  is the original range,  $\alpha_i$  is the nadir angle of the laser beam vector and  $\Delta R_i$  is the range offset. The first term  $R_i \cos \alpha_i$  is the range correction term for the orientation of the scanner. Fig. 2 shows schematically the corresponding geometry as well as the range corrections for a particular location and a sample block. The point  $T_i$  represents an instantaneous position of the scanner, while the vector  $\vec{T_i T_i}$  represents the laser beam vector. The figure also shows a reference point  $T_0$ , which was defined as the mean (of the coordinates) of the trajectory points corresponding to the GPS times of all the recording blocks selected for

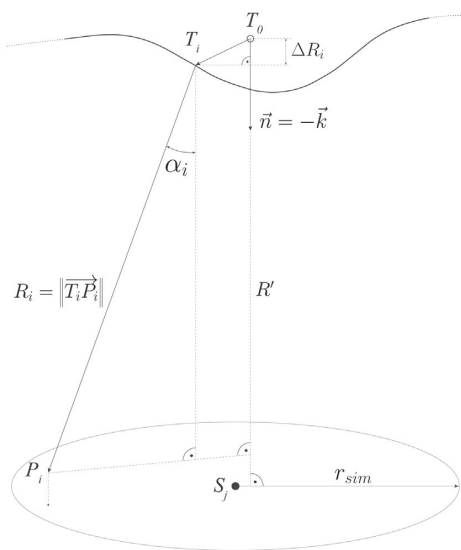


Fig. 2. Scanning geometry and the range corrections shown schematically for a particular sample location  $S_j$ , and the recording block  $i$ . The point  $T_0$  is the reference point introduced for the range correction, whereas the point  $T_i$  is the position of the scanner at the trajectory during the recording of the block  $i$ . The point  $P_i$  shows the geolocation of an instantaneous amplitude sample within the recording block  $i$ , whereas  $R_i$  is its range.  $\alpha_i$  is the nadir angle of the laser beam vector for the block  $i$ .

the stacking. The range offset  $\Delta R_i$  was calculated as the magnitude of the vector  $\overrightarrow{T_0 T_i}$  projected to the unit nadir vector ( $\vec{n} = -\vec{k}$ ):  $\Delta R_i = \|\overrightarrow{T_0 T_i} \cdot \vec{n}\|$ .

The nadir angle  $\alpha_i$  depends on the plot size (the simulation radius  $r_{sim}$ ) as well as the planar displacement between  $S_j$  and  $T_0$  (the nadir angle of the vector  $\overrightarrow{T_0 S_j}$ ). For 98% of the SSL sample locations  $S_j$ , the nadir angle of the vector  $\overrightarrow{T_0 S_j}$  was below  $2^\circ$ , whereas the maximum nadir angle was  $14^\circ$  for all  $S_j$ . This corresponds to the range corrections of 0.1% and 3%, respectively.

### 3.1.5. Recording blocks aggregation (stacking)

Instantaneous amplitudes of the selected recording blocks were aggregated according to their corrected ranges. A 15 cm binning of the nadir axis from the reference point  $T_0$  was introduced, and amplitudes with ranges falling in particular bins were accumulated. Amplitudes smaller than a noise threshold were not considered. Here, the noise threshold of 15 DN was applied, which corresponds to the maximum amplitude among the records at the end of unimodal recording blocks.

For each sample location, an aggregated waveform was derived. The aggregated waveforms were normalized by the number of the selected recording blocks at the particular sample location. This resulted into a mean, nadir-looking, large-footprint waveform per sample location. These simulated waveforms were used for the further analysis.

## 3.2. Waveform metrics and simulated waveform sets

### 3.2.1. Waveform metrics

The most common waveform metrics used in previous biomass studies are those considering the vertical distribution of the waveform's energy (e.g., Duong et al., 2009; Lefsky et al., 1999; Popescu et al., 2011; Sun et al., 2008). Typical examples are canopy heights that correspond to certain energy quantiles. Before deriving such waveform metrics, the start and end of individual waveforms has to be defined. These two waveform features refer to the canopy top and the ground, respectively. For the simulated nadir waveforms the range difference

between the canopy top and the ground is the canopy height. The waveform start was defined as the range bin where the mean waveform amplitude exceeded zero for the first time, i.e. the raw amplitude exceeded the noise threshold. The waveform end was defined as the range bin corresponding to 99% of the waveform area (energy), integrated from the waveform start, i.e. the canopy top. The 99% quantile was used instead of the hard noise threshold because it showed to be less sensitive to trailing noise, which appears just after the last terrain amplitudes. The energy metrics derived here included three canopy heights. First, the total canopy height ( $h_{100}$ ) calculated as the distance between the start and end of the waveform. Second, the height of median energy ( $h_{HOME}$ ) calculated as the distance from the waveform end to the bin where 50% of the waveform area occurs. Third, the canopy height ( $h_{95}$ ) calculated similarly as the HOME, but at 95% of the waveform energy (integrated from the waveform end).

In addition to the energy metrics, a peak analysis was performed to derive peak metrics. The waveform peaks were identified using the *findpeaks* function in the Signal Processing Tool Box of the Matlab R2016b software (MATLAB, 2016). The peak metrics derived here included three parameters. The first peak parameter is a peak-to-peak distance ( $d_{p2p}$ ). For bimodal waveforms, i.e. waveforms with two peaks,  $d_{p2p}$  is uniquely defined. However, for multimodal waveforms (more than two peaks),  $d_{p2p}$  was calculated as the distance from the first to the last peak. For unimodal peaks, i.e. (a single peak detected),  $d_{p2p}$  was replaced with the full waveform width at half of the peak magnitude (FWHM). The remaining two peak parameters are: (i) the amplitude of the last peak ( $a_{last}$ ), and (ii) the full width at half of the last-peak magnitude ( $d_{FWHM}$ ).

The values of the six waveform parameters were derived for all SSL plots in the first sample phase, and were used for regression analyses for assessing AGB.

### 3.2.2. Waveform sets

The impacts of footprint size and geolocation error were analyzed independently and with different waveform sets. To analyze the impact of footprint size on biomass estimates and their corresponding variance estimates, eight waveform sets were generated using different search radius values (Section 3.1.3). Each set contained 1010 SSL waveforms. The radius values ranged from 2.5 m to 20 m, with increments of 2.5 m, mimicking different footprint sizes. These eight waveform sets, represented by their waveform metrics, were used as input for the biomass model to derive the footprint size that minimizes the biomass variance estimates.

To analyze the impact of geolocation error on variance estimates, a single waveform set was generated using the footprint size that minimized the biomass variance estimates. This set contained 1010 SSL waveforms as before, and additionally 24 SSL waveforms around each sample location to simulate geolocation errors. This resulted in 25,250 SSL waveforms in total. The locations of the 24 additional SSL waveforms were distributed systematically using a  $5 \times 5$  nodes grid around each sample location. The node spacing was set to 5 m, while the grid sides were parallel to the x- and y-axis of the world coordinate system. This provided geolocation errors of up to  $\pm 10$  m along the x- and y-axis, and up to  $\pm 14.1$  m along the main diagonal. Fig. 3 shows several SSL sample locations and the corresponding grids of 24 additional locations used for analyzing the impact of the geolocation error.

### 3.3. Case study: application of space-borne LiDAR data in forest surveys

The 33 waveform sets (8 for the footprint simulation and 25 for the geolocation error simulation) were combined with the systematic sample of  $n_H = 264$  field plots to estimate the biomass of our study area. We employed a two-phase design, where the first phase is a systematic sample of  $n_t = 1010$  single-waveform satellite plots. The second-phase sample includes the 264 field plots, for which a direct link between field data and waveform metrics was established.

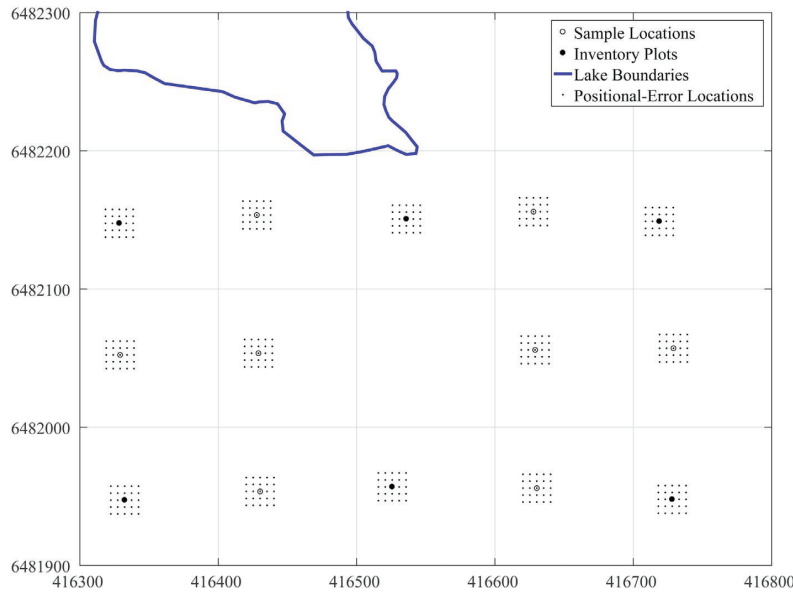


**Fig. 3.** A zoomed-in view into the SSL sample locations and the inventory plots. The smaller grey dots around the SSL sample locations are the additional sample locations introduced to assess the impact of geolocation error. The dots form local grids with a grid spacing of 5 m. Note that the SSL sample locations also includes the Inventory plot locations.

For the second-phase sample (field plots), we have a full set of information; i.e. AGB was predicted from field measurements using the models from [Marklund \(1988\)](#) and SSL metrics were available from the waveform simulation. For the remaining first-phase sample plots we have only SSL metrics available and AGB was predicted using a model that was developed from the ground reference data. The model had the following form:  $y_i = \beta_0 + \beta_1 d_{p2p} + \beta_2 h_{HOME} + \beta_3 h_{95} + \epsilon_i$ , and parameter values were estimated using the generalized least squares technique ([McCulloch et al., 2008](#)) as implemented in the nlme R-package ([Pinheiro et al., 2016](#)). To avoid back-transformation bias and to tackle heteroscedasticity, residual variance was modeled as a function of the  $h_{HOME}$  predictor variable. The chosen model was selected from all possible linear models, not considering interaction terms, that could be built with our six waveform metrics (in total 63 possible combinations). The models were fit to the waveform set that had no geolocation error and a footprint size that corresponded to the size of the field plots (10 m radius). As selection criteria, Bayes information criterion and residual standard error were used.

The selected model was then fit to all 32 waveform sets individually, and model fits were evaluated using model efficiency (ME) and root mean square error (RMSE), where

$$ME = 1 - \frac{SS_{res}}{SS_{mean}} \quad (2)$$

and

$$RMSE = \sqrt{\frac{SS_{res}}{n_{II} - n_{var}}} \quad (3)$$

with  $SS_{res} = \sum_{i=1}^{n_{II}} (y_i - \hat{y}_i)^2$ ,  $SS_{mean} = \sum_{i=1}^{n_{II}} (y_i - \bar{y})^2$ , and  $n_{var}$  denoting the number of model parameters. To further check if models were correctly specified, graphs of observed AGB plotted against model predictions were constructed in two ways: (1) original pairs of observations and predictions and (2) group means of observed and predicted values. For the latter pairs of observations and predictions ( $y_i, \hat{y}_i$ ) were ordered with respect to  $\hat{y}_i$  and then grouped into categories of ten observations. For each category, averages of observed and predicted AGB were calculated and plotted against each other. For correctly specified models, points should follow the 1:1 line with intercept 0 and slope 1, e.g. [McRoberts et al. \(2013\)](#). Graphs for the footprint waveform

sets are provided in [Appendix A](#), and for the geolocation waveform sets, graphs are provided in [Appendix B](#).

For estimating average biomass density  $\bar{y}$  of the study area and its variance, two inferential frameworks were applied: (1) model-assisted estimation under design-based inference and (2) hybrid inference combining the inferential frameworks model-based and design-based ([Ståhl et al., 2016](#)). The two-phase sampling model-assisted estimator for  $\bar{y}$  is ([Mandallaz, 2008](#), p. 80)

$$\hat{\bar{y}}_{ma} = \frac{1}{n_I} \sum_{k \in S_I} \hat{y}_k + \frac{1}{n_{II}} \sum_{k \in S_{II}} \hat{\epsilon}_k \quad (4)$$

where  $\hat{y}_k$  is AGB in Mg per hectare of population element  $k$  predicted from the regression model, and  $\hat{\epsilon}_k$  is the model residual  $\hat{\epsilon}_k = y_k - \hat{y}_k$ . A variance estimator for  $\hat{\bar{y}}_{ma}$  is ([Mandallaz, 2008](#), p. 81)

$$\hat{V}(\hat{\bar{y}}_{ma}) = \left(1 - \frac{n_{II}}{n_I}\right) \frac{\sum_{k \in S_{II}} \left(\hat{\epsilon}_k - \frac{\sum_{k \in S_{II}} \hat{\epsilon}_k}{n_{II}}\right)^2}{(n_{II}(n_{II} - 1))} + \frac{\sum_{k \in S_{II}} \left(\hat{y}_k - \frac{\sum_{k \in S_{II}} \hat{y}_k}{n_{II}}\right)^2}{(n_I(n_{II} - 1))} \quad (5)$$

Under hybrid inference,  $\bar{y}$  is estimated using the following estimator ([Ståhl et al., 2016](#)):

$$\hat{\bar{y}}_{hy} = \frac{1}{n_I} \sum_{i \in S_I} \hat{y}_k \quad (6)$$

Under sampling designs that use equal inclusion probabilities, as in our case, and for models for which  $\sum \hat{\epsilon}_k$  is zero, the two estimators from Eqs. (4) and (6) will yield identical results (e.g., [Magnussen, 2015](#)).

For the variance of  $\hat{\bar{y}}_{hy}$  we have a design-based component from the sample nature of satellite observations and a model-based component, since AGB for phase-one units without field data was predicted using a model. Although, systematic sampling is the widely accepted standard in surveys of natural resources, it has the drawback that no unbiased variance estimator exist due the fact that many second-order inclusion probabilities are zero. The most common strategy is to treat sampling units as they were selected randomly and to apply the according variance estimator for simple random sampling. This approach will yield conservative estimates that overestimate the variance of the total estimator (e.g., [Ene et al., 2013](#)); the degree of overestimation is unknown. In our case this is not relevant, since the design-based variance component is fixed (the sampling design does not change) and our focus is

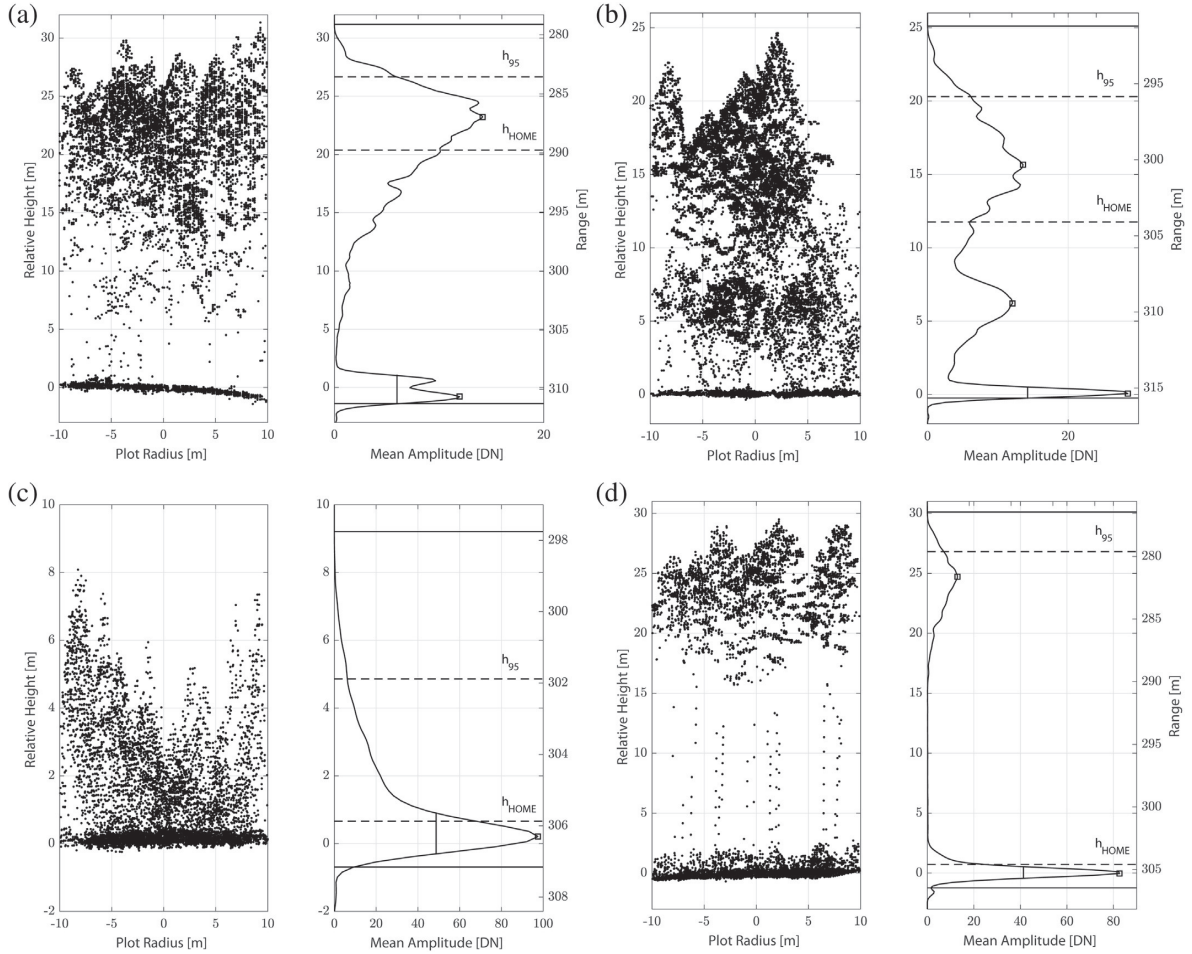


Fig. 4. Examples of SSL waveforms stacked using the radius of 10 m for four different field plots. The start and end of the waveforms are shown by upper and lower, solid horizontal lines, respectively. The dashed horizontal lines show  $h_{HOME}$  and  $h_{95}$  levels. The detected peaks are marked by the black squares, whereas  $d_{FWHM}$  of the last peak is shown by the vertical line. Note that the limits of the waveform amplitude axis are different for each subfigure, but the axis is always split in the increments of 20 DN to make relative comparison easier.

on the model-based variance component, which is influenced by footprint size and geolocation error. A variance estimator is

$$\widehat{V}(\widehat{Y}_{hy}) = \widehat{V}_{db} + \widehat{V}_{mb} \quad (7)$$

where  $\widehat{V}_{db} = \frac{1}{n_I} \sum_{S_I} \frac{(\widehat{y}_k - \widehat{y})^2}{n_I - 1}$  is the simple random sampling without replacement estimator for the design-based component of total variance, and  $\widehat{V}_{mb} = \frac{1}{n_I} \widehat{\sigma}_e^2 + \nu' X \widehat{C} \nu (\widehat{\beta})' X' \nu$  is the respective model-based component (Magnussen et al., 2016, Eq. 6). Here,  $X$  is the design matrix of the model with dimensions  $n_I \times p + 1$ , where  $p$  is the number of predictors,  $\nu$  is a  $n_I \times 1$  matrix of entries with the value  $1/n_I$ , and  $\widehat{\sigma}_e^2$  is the estimated residual variance calculated as  $\widehat{\sigma}_e^2 = \sum_{S_{II}} w_i^2 e_i^2 / (n_{II} - n_{var})$ . The weights  $w_i$  are used in the generalized least squares regression to account for heteroscedasticity and are derived from the residual variance model. Note that for large-area (national to global) surveys,  $\widehat{\sigma}_e^2$  is small compared to the second term in  $\widehat{V}_{mb}$  and can be ignored (Ståhl et al., 2016). For a more intuitive interpretation of results, variance estimates are transformed to standard error estimates by taking the square root ( $SE = \sqrt{\widehat{V}(\widehat{Y})}$ ).

## 4. Results and discussion

### 4.1. Simulated waveforms and selection of waveform metrics

Fig. 4 shows nadir-looking waveforms stacked using the radius of 10 m centered at four different field plot locations. Additionally, the figure shows corresponding georeferenced ALS returns, plotted in the  $xz$  plane. The coordinates are given relative to the field plot center. The  $z_{S_j}$  coordinate of a field plot center  $S_j$  was derived from the LIDAR DTM. The waveform's range is plotted vertically, while the mean amplitude of the stacked waveform is plotted horizontally. As the waveforms have nadir-looking geometry, the range is also expressed as the relative height (shown on the left vertical axis) used to plot the returns. The relative height for a nadir range  $R_i'$  was calculated as:  $z_{T_0} - R_i' - z_{S_j}$  (see Fig. 2). Note the different limits of the vertical axis for the four sub-figures.

As shown by Fig. 4, the stacked waveforms reflect different vegetation structure well. Fig. 4a shows a typical two-layer plot with high vegetation and the corresponding bi-modal waveform. This plot is also slightly sloped, which resulted in a broader ground part of the waveform. It can also be seen that the peak detection algorithm is robust, as the sub-dominant ground peak was omitted. Fig. 4b shows a plot with

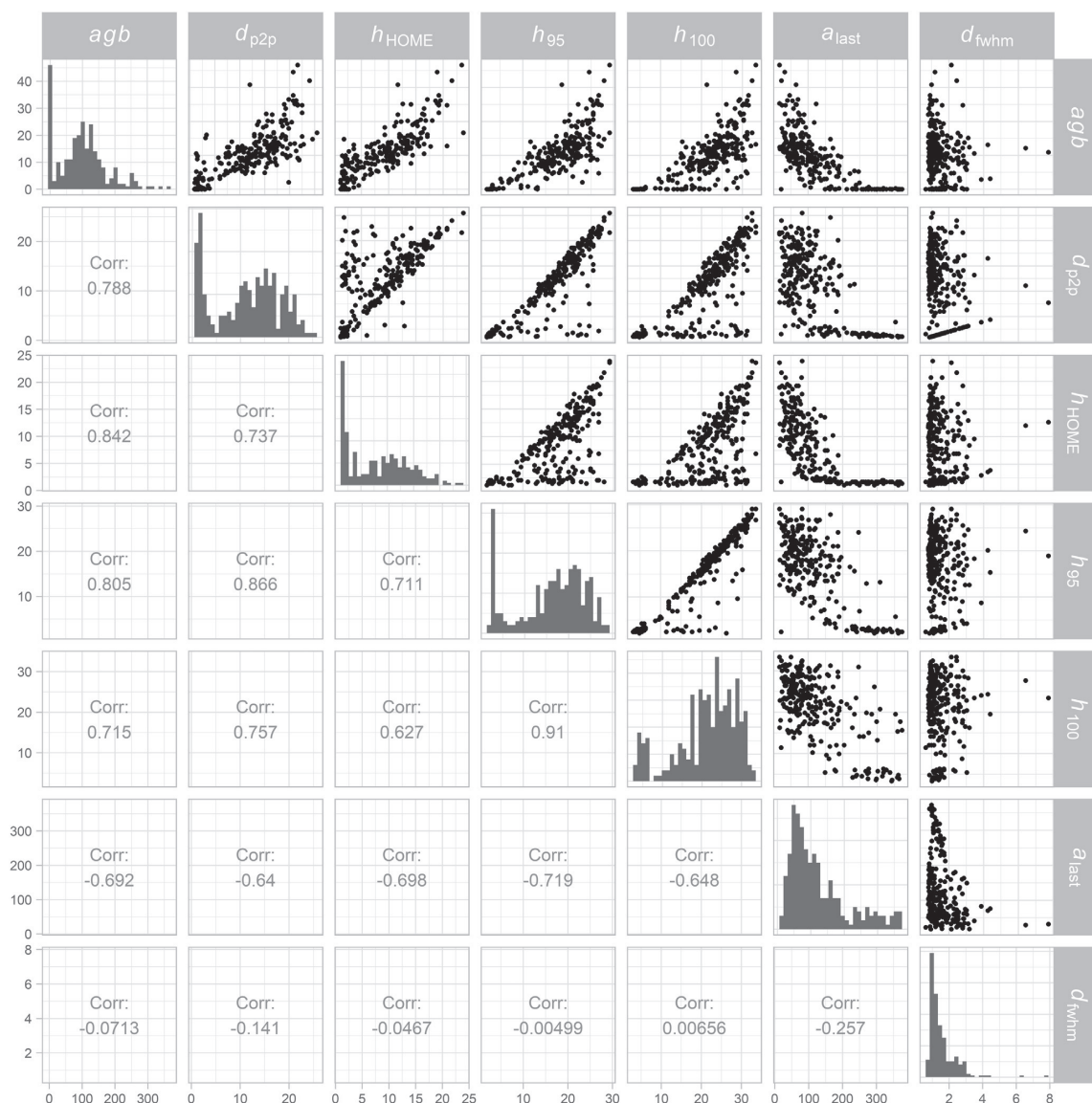


Fig. 5. Scatterplot matrix of waveform metrics and field-observed AGB.

high vegetation and understory that resulted in a multimodal waveform with three peaks identified. For this waveform, the ground part is much narrower as the terrain is flat within the plot. Finally, Fig. 4c shows a plot with dense low vegetation, which resulted in a unimodal waveform where the ground and vegetation part are mixed.

Fig. 4 also shows that the waveform metrics are robust for each of the three waveform types. The 99% energy quantile used to define the waveform end successfully filtered out the trailing noise of the waveform in Fig. 4d. For the rest of the examples, the 99% quantile was found just slightly inside the ground part, but is still enough robust to define the end of the waveform well. The  $h_{100}$ ,  $h_{95}$  and  $h_{HOME}$  metrics reflect the canopy height well, and, as shown later in Fig. 5, have very high correlation ( $> 0.7$ ) with the field AGB. Only in Fig. 4d,  $h_{HOME}$  is very close to the ground, erroneously suggesting low AGB within the plot. This plot was select as the one that is far away from the main trend

in the scatter plot of  $h_{HOME}$  and AGB values (Fig. 5). For comparison, the plot in Fig. 4a (also a bimodal waveform), is placed close to the main trend and has similar field AGB. The reason for small  $h_{HOME}$  in Fig. 4d is a large amplitude of the ground peak, which makes the median energy less sensitive to the vegetation height and more close to the ground. Nevertheless, Fig. 5 shows that erroneous  $h_{HOME}$  values appeared just for a few plots, while the majority of the plots showed a high correlation (0.84) with field-observed AGB.

Fig. 5 shows a scatter plot matrix for AGB and all waveform metrics. The metrics were derived from the 10 m radius waveforms for all of the 264 field plots. In the scatter plot matrix, Pearson's correlation coefficient of variable pairs is reported below the main diagonal, while on the main diagonal, the distributions of variable values are provided in the form of histograms. Table 1 summarizes the statistics of the three predictors used for AGB prediction by sample phase. There is a small

**Table 1**

Summary statistics of predictor variables used in the biomass estimation model, separated by sampling phases: cv – coefficient of variation, skew – skewness, kurt – kurtosis. The footprint radius for feature extraction was 10 m.

	n		Min	Max	Mean	cv	skew	kurt
Field	264	$d_{p2p}$	0.9	25.5	11.1	0.62	-0.11	-1.23
		$h_{HOME}$	1.2	23.7	8.1	0.71	0.44	-0.92
		$h_{95}$	2.1	29.1	16.1	0.47	-0.53	-0.85
Satellite	746	$d_{p2p}$	0.9	30.0	11.5	0.62	-0.03	-1.13
		$h_{HOME}$	0.9	24.3	8.3	0.72	0.43	-1.06
		$h_{95}$	1.8	33.0	17.3	0.43	-0.54	-0.58
All	1010	$d_{p2p}$	0.9	30.0	11.4	0.62	-0.05	-1.14
		$h_{HOME}$	0.9	24.3	8.3	0.71	0.43	-1.02
		$h_{95}$	1.8	33.0	17.0	0.44	-0.55	-0.63

**Table 2**

Model fit statistics, AGB density estimates and estimated standard errors in dependence of footprint size: *ME* – model efficiency, *RMSE* – root mean square error,  $\hat{y}$  – estimated biomass density,  $\widehat{SE}(\hat{y}_{ma})$  – model-assisted standard error estimate,  $\widehat{SE}(\hat{y}_{hy})$  – hybrid-inference standard error estimate.

Footprint radius [m]	<i>ME</i>	<i>RMSE</i> [Mg ha <sup>-1</sup> ]	$\hat{y}$ [Mg ha <sup>-1</sup> ]	$\widehat{SE}(\hat{y}_{ma})$ [Mg ha <sup>-1</sup> ]	$\widehat{SE}(\hat{y}_{hy})$ [Mg ha <sup>-1</sup> ]
2.5	0.62	45.9	101.1	3.4	4.1
5.0	0.71	39.6	101.4	3.2	3.3
7.5	0.78	35.1	101.9	3.0	2.9
10.0	0.80	33.4	101.3	2.9	2.8
12.5	0.78	34.6	100.8	2.9	2.9
15.0	0.76	36.7	100.6	3.0	2.9
17.5	0.73	38.3	100.7	3.1	3.1
20.0	0.71	39.8	100.6	3.2	3.1

difference in the mean values between only-field and only-satellite waveform metrics, where the metrics from the field-sample were slightly smaller.

4.2. Case study

By fitting the AGB prediction model to each of the waveform sets and consecutively applying the estimators, we obtained estimates of AGB density and corresponding standard errors. Results are summarized in Tables 2 and 3. As the difference of AGB estimates from Eqs. (4) and (6) was close to zero ( $1.4 \times 10^{-14}$  on average), results are summarized under one column with generic notation  $\hat{y}$ . From Table 2 it is obvious that the best model fits and lowest standard errors were achieved for footprint sizes that are close to the actual field plot size (i.e. from 7.5 m to 12.5 m). Regarding geolocation error (Table 3), standard error estimates generally increase with increasing distance of displacement, although substantial variation was observed among waveform sets of common distance but different direction of displacement (Fig. 6). The lowest standard error was consequently observed when there was a perfect match between SSL and field data.

In both cases, geolocation error and footprint size, variation in

standard error estimates are largely explained by changes in model-fit statistics (*ME* and *RMSE*) as expected from the estimators. Point ( $\hat{y}$ ) estimates from either model-assisted estimation or hybrid inference are almost identical as the applied sampling design used equal inclusion probabilities for selecting SL and field data (Magnussen, 2015). Interval ( $\widehat{SE}$ ) estimates, however, showed some differences between the two inferential frameworks. It appears that, in particular, the hybrid approach for variance estimation is more affected by decreasing model quality due to mismatches in either footprint size or geolocation (Fig. 6 for geolocation error). In case of varying footprint size, differences in standard error estimates are only clearly visible for the smallest footprint size of 2.5 m (Table 2). The other footprint sizes used seemed to be close enough to the actual field plot size, so that the decrease in model quality was not strong enough to lead to a notable difference between the two inferential frameworks.

The hybrid standard error estimates varied, further, also consistently more among the different directions of displacement when the distance was kept constant (Fig. 6). The cause for this behavior can be found in the fundamentally different inferential frameworks. While with design-based inference (here with model-assisted estimation), the population is considered to be fixed and randomization enters through the random selection of samples following a predefined probability sampling design, model-based inference assumes that the population is a realization of a random process and that the sample is fixed instead (Magnussen, 2015; Ståhl et al., 2016). Uncertainty under the model-based paradigm arises from estimating model parameters and from lack-of-fit residuals, while with model-assisted estimation, uncertainty comes from the variation between population parameter estimates from different samples (Magnussen, 2015). For the latter case, the quality of the model does typically not affect the approximately unbiasedness of the estimators (Magnussen, 2015). In the model-based case, however, inference relies on correctly specified models. Regarding the hybrid estimator in our study, we observed that estimates of the design-based component (Eq. (7)) were relatively stable across the different conditions tested here, while the model-based component reacted heavily on changes on the estimated uncertainty of model parameter estimates caused by geolocation error and discrepancies in footprint size. Such a difference between variance estimates from either design-based with model-assisted estimation and model-based inference was also observed by Saarela et al. (2016) when studying the effect of geolocation errors in a Monte-Carlo simulation study. The differences vanished, however, with increasing sample size. As a note of caution, we would like to mention that our results and conclusions are based on one single sample out of the many possible samples that could be drawn from our population. More detailed conclusions about the behavior of the hybrid variance estimator when model quality decreases due to mismatches between datasets, would require a Monte-Carlo simulation study. Such simulation studies typically require that target and auxiliary variables are available for all population elements. With respect to simulating satellite waveforms, the computational burden was, however, too heavy for the current study.

For point estimates, we further observed some variation among

**Table 3**

Model fit statistics, AGB density estimates and estimated standard errors in dependence of horizontal displacement distance (the footprint radius was fixed to 10 m). Results for different directions of the same displacement are averaged. Abbreviations are as follows: *ME* – model efficiency, *RMSE* – root mean square error,  $\hat{y}$  – estimated biomass density,  $\widehat{SE}(\hat{y}_{ma})$  – model-assisted standard error estimate,  $\widehat{SE}(\hat{y}_{hy})$  – hybrid-inference standard error estimate.

Displacement [m]	Number of observations	<i>ME</i>	<i>RMSE</i> [Mg ha <sup>-1</sup> ]	$\hat{y}$ [Mg ha <sup>-1</sup> ]	$\widehat{SE}(\hat{y}_{ma})$ [Mg ha <sup>-1</sup> ]	$\widehat{SE}(\hat{y}_{hy})$ [Mg ha <sup>-1</sup> ]
0.0	1	0.80	33.4	101.3	2.9	2.8
5.0	4	0.75	36.9	101.0	3.1	3.3
7.1	4	0.73	38.8	100.0	3.1	3.5
10.0	4	0.67	42.6	100.3	3.3	3.8
11.2	8	0.65	43.6	100.0	3.3	4.0
14.1	4	0.60	47.2	100.5	3.5	4.4

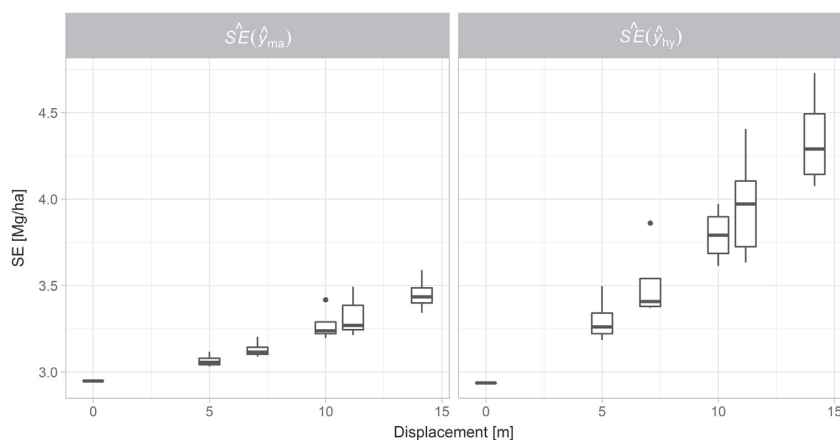


Fig. 6. Estimated standard errors of AGB estimates in dependence of horizontal displacement distance between field and satellite observations (the footprint radius was fixed to 10 m). The left panel gives estimates following the model-assisted estimator and the right panel following hybrid-inference. Differences among observations of the same displacement are due to different directions of displacement.

values from the different waveform sets. For example, the lowest AGB density observed in Table 2 is 100.6 Mg per hectare, while the largest value observed is 101.9 Mg per hectare. This variation can be entirely attributed to differences in the simulated waveforms from including different ALS data in the simulations by changing footprint size. This directly affects parameter estimates and thus point and interval estimates of AGB density. In combination with zero model residual sums and equal inclusion probabilities, the model-assisted correction factor in Eq. (4), as already mentioned, has no effect. Note, however, that the individual point estimates lie well within each other's confidence intervals. The same applies to the results in Table 3.

For sake of comparison, the field-based estimate of AGB was 97.1 Mg per hectare with an estimated standard error of 4.6 Mg per hectare. Thus, by including SSL data to facilitate AGB estimation in the manner shown here, the relative standard error of estimation was reduced by approx. 37% in the best case. The rather small difference of the field-based point estimate in comparison to the SSL supported estimates can be explained by the summary provided in Table 1. The slightly larger model predictor variables on SSL-only plots resulted in, on average, larger model predictions. Otherwise, the statistics in Table 1 show that the forest conditions in the two sets are comparable.

### 5. Conclusions

In this study we analyzed the effect of simulated LiDAR footprint size and geolocation error on AGB estimates. The AGB estimates were obtained from a first phase sample of simulated SL footprints and a smaller second phase sample of co-registered field plots. The large-footprint, nadir-looking SL waveforms were simulated by spatial integration of the small-footprint ALS waveforms found within the SSL beam cone. The shape of the simulated waveforms reflected well different forest structure, whereas the height metrics derived from the SSL waveforms showed high correlation (> 0.7) with the AGB of the field plots.

Simulating space-borne LiDAR waveforms with different footprint size, we showed that the size of field plots should match the footprint

size of the satellite observations. The other way around, we could also say that future space-borne LiDAR missions should be planned in a way that footprint sizes match field plot sizes commonly used in forest inventories. The larger the mismatch, the more the modeling efforts are affected in both directions (under or oversized footprints or field plots, respectively).

We saw a clear effect of geolocation error in the sense that standard errors increased with increasing horizontal displacement. The largest standard error estimate was 17% larger than the smallest standard error estimate if model-assisted estimation was used. For model-based inference, the estimated difference was 36%. It is, thus, important that future LiDAR satellites designed for operational forest monitoring will provide accurate coordinates, preferably sub meter, for the position of the laser footprints. Since the field data generally will be obtained after the LiDAR data, it is the coordinate for the actual footprint, and not the possibility to beforehand hit a specific target that is of importance. The results in this article is however dependent on the properties of the test site (temperate forest in southern Sweden). In homogenous forest areas such an effect can somewhat be dampened by autocorrelation, meaning that nearby points tend to be similar in the stand characteristics. In fragmented areas (forest, non-forest), however, or intensively managed forest areas (clear cut systems, even-aged plantation forest), correlation lengths can be short and areas in the immediate neighborhood of the field sample location can have completely different properties.

### Acknowledgments

The research leading to these results has received funding from the European Community's Seventh Framework Programme ([FP7/2007–2013]) under the Advanced\_SAR project (grant agreement no. 606971). We thank Björn Nilsson for conducting the manual photo interpretation of the Remningstorp estate that was needed for limiting the analysis to productive forest lands. We also thank Andreas Roncat for valuable discussions and clarifications of raw waveform data structure and the waveform extraction library.

Appendix A

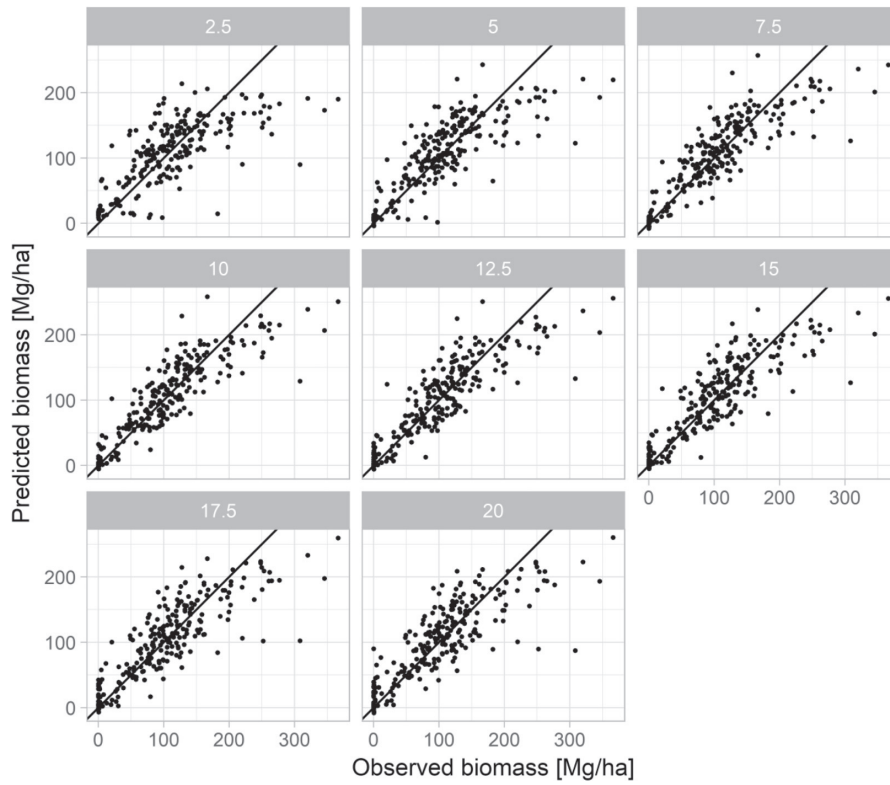


Fig. A.1. Model validation – footprint size. Graphs of predicted vs. observed AGB, here for the footprint size waveform sets. The radius of the footprint is given above the single scatter plots in m. The radius of the field plots was 10 m.

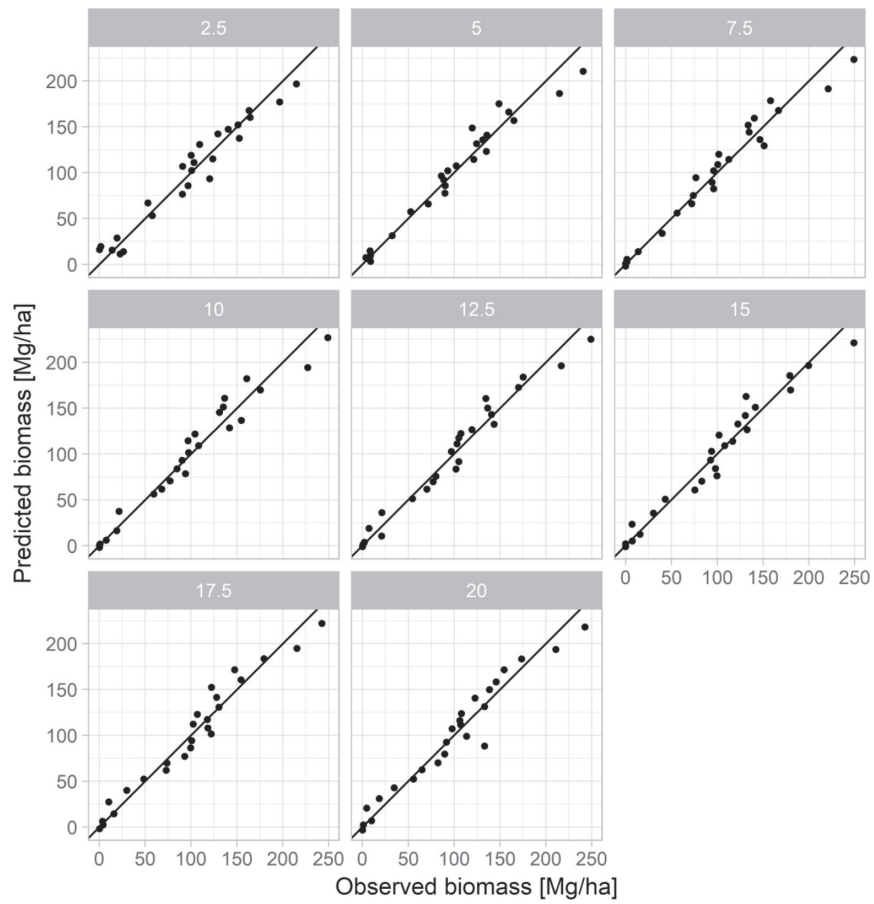


Fig. A.2. Model validation – footprint size. Group means of predicted vs. observed AGB, here for the footprint size waveform sets. The radius of the footprint is given above the single scatter plots in m. The radius of the field plots was 10 m.

Appendix B

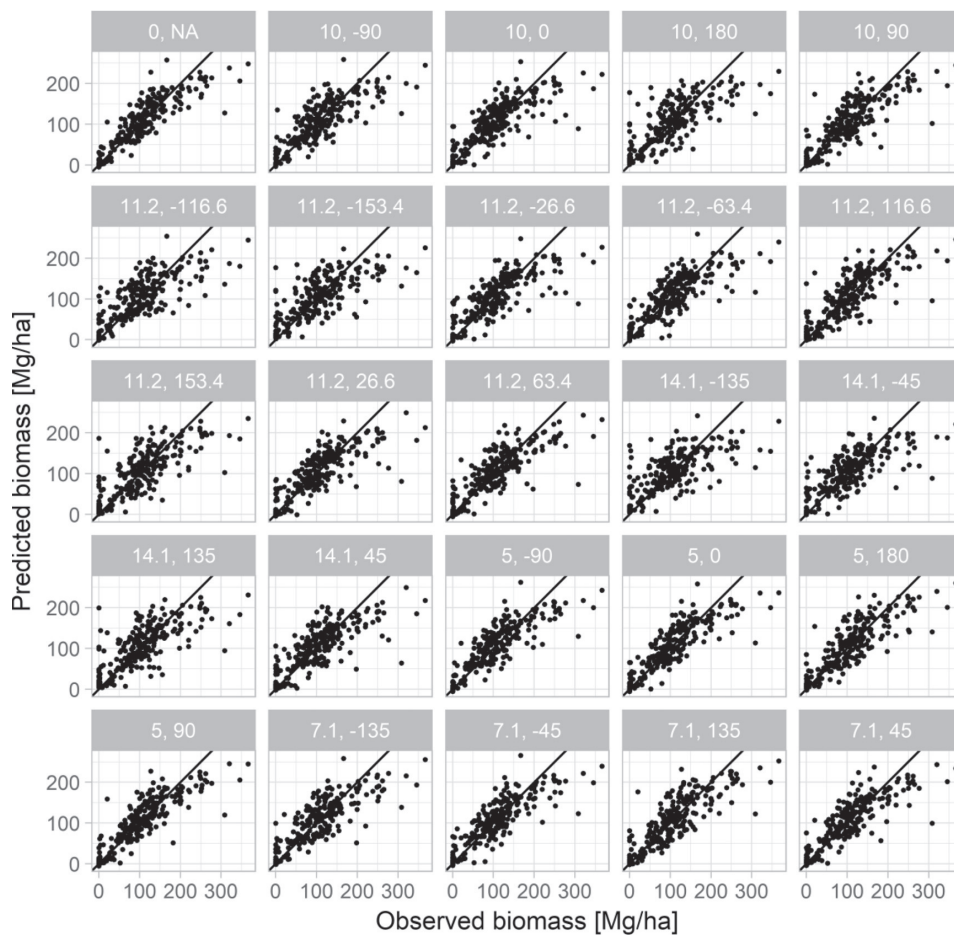


Fig. B.1. Model validation – Geolocation error. Graphs of predicted vs. observed AGB, here for the geolocation error waveform sets. Above the single scatter plots the displacement distance in m and the direction of displacement in degrees are given. The footprint radius was fixed to 10 m, and the field plot radius was 10 m.

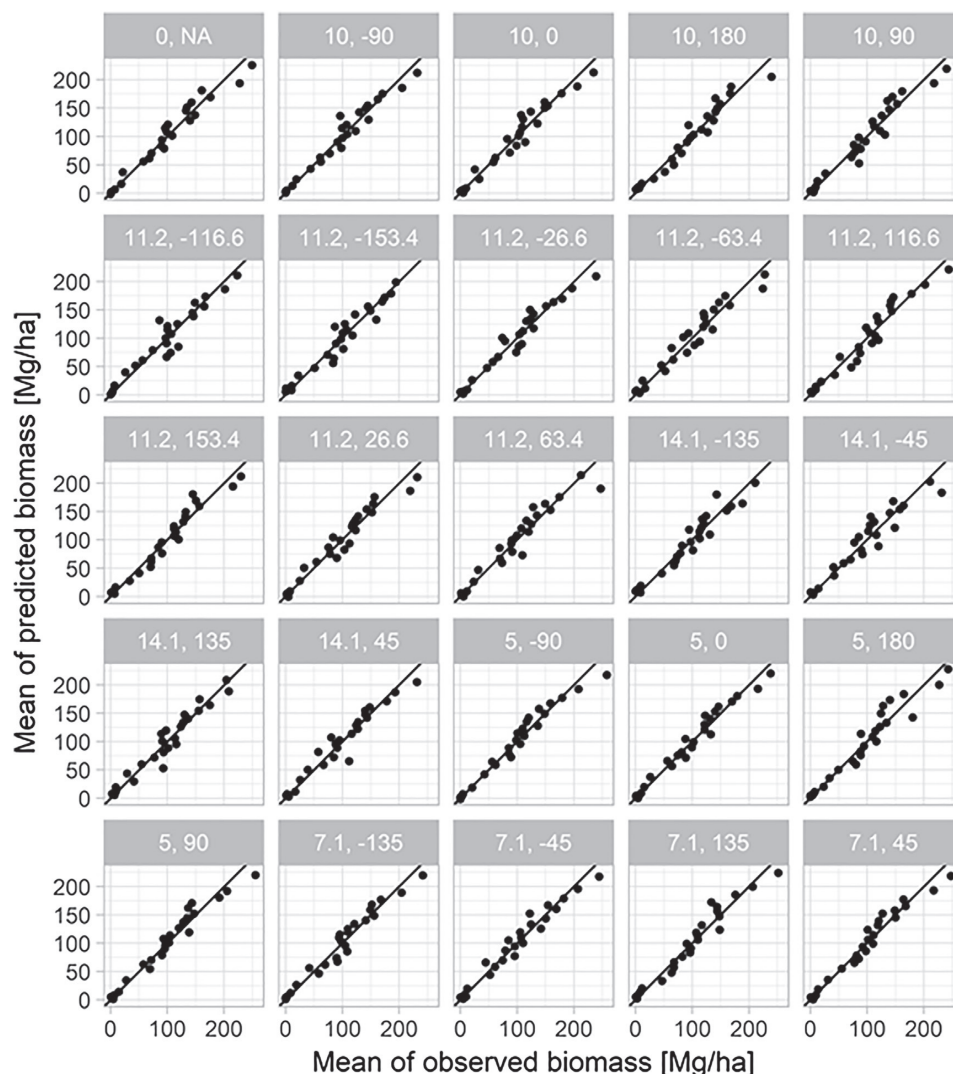


Fig. B.2. Model validation – Geolocation error. Group means of predicted vs. observed AGB, here for the geolocation error waveform sets. Above the single scatter plots the displacement distance in m and the direction of displacement in degrees are given. The footprint radius was fixed to 10 m, and the field plot radius was 10 m.

## References

- Abdalati, W., Zwally, H.J., Bindenschadler, R., Csatho, B., Farrell, S.L., Fricker, H.A., Harding, D., Kwok, R., Lefsky, M., Markus, T., Marshak, A., Neumann, T., Palm, S., Schutz, B., Smith, B., Spinhirne, J., Webb, C., 2010. The ICESat-2 laser altimetry mission. *Proc. IEEE* 98, 735–751.
- Axelsson, P.E., 1999. Processing of laser scanner data - algorithms and applications. *ISPRS J. Photogramm. Remote Sens.* 54, 138–147.
- Blair, J.B., Hofton, M.A., 1999. Modeling laser altimeter return waveforms over complex vegetation using high-resolution elevation data. *Geophys. Res. Lett.* 26, 2509–2512.
- Boudreau, J., Nelson, R., Margolis, H., Beaudoin, A., Guindon, L., Kimes, D., 2008. Regional aboveground forest biomass using airborne and spaceborne LiDAR in Québec. *Remote Sens. Environ.* 112, 3876–3890.
- Duong, H., Lindenbergh, R., Pfeifer, N., Vosselman, G., 2009. ICESat full-waveform altimetry compared to airborne laser scanning altimetry over The Netherlands. *IEEE Trans. Geosci. Remote Sens.* 47, 3365–3378.
- Ene, L.T., Næsset, E., Gobakken, T., Gregoire, T.G., Ståhl, G., Holm, S., 2013. A simulation approach for accuracy assessment of two-phase post-stratified estimation in large-area LiDAR biomass surveys. *Remote Sens. Environ.* 133, 210–224.
- Frazer, G.W., Magnussen, S., Wulder, M.A., Niemann, K.O., 2011. Simulated impact of sample plot size and co-registration error on the accuracy and uncertainty of LiDAR-derived estimates of forest stand biomass. *Remote Sens. Environ.* 115, 636–649.
- Gastellu-Etchegorry, J.P., Yin, T.G., Lauret, N., Cajfinger, T., Gregoire, T., Grau, E., Feret, J.B., Lopes, M., Guilleux, J., Dedieu, G., Malenovsky, Z., Cook, B.D., Morton, D., Rubio, J., Durrieu, S., Cazanave, G., Martin, E., Ristorcelli, T., 2015. Discrete anisotropic radiative transfer (DART 5) for modeling airborne and satellite spectro-radiometer and LiDAR acquisitions of natural and urban landscapes. *Remote Sens.* 7, 1667–1701.
- Gobakken, T., Næsset, E., 2009. Assessing effects of positioning errors and sample plot size on biophysical stand properties derived from airborne laser scanner data. *Can. J. For. Res.* 39, 1036–1052.
- Goncalves, F., Treuhaff, R., Law, B., Almeida, A., Walker, W., Bacchini, A., dos Santos, J.R., Graca, P., 2017. Estimating aboveground biomass in tropical forests: field methods and error analysis for the calibration of remote sensing observations. *Remote Sens.* 9.
- Gregoire, T.G., Stahl, G., Næsset, E., Gobakken, T., Nelson, R., Holm, S., 2011. Model-assisted estimation of biomass in a LiDAR sample survey in Hedmark County, Norway. *Can. J. For. Res.* 41, 83–95.
- Gwenzi, D., Lefsky, M.A., Suchdeo, V.P., Harding, D.J., 2016. Prospects of the ICESat-2 laser altimetry mission for savanna ecosystem structural studies based on airborne simulation data. *ISPRS J. Photogramm. Remote Sens.* 118, 68–82.
- Hall, F.G., Bergen, K., Blair, J.B., Dubayah, R., Houghton, R., Hurr, G., Kellndorfer, J.,

- Lefsky, M., Ranson, J., Saatchi, S., Shugart, H.H., Wickland, D., 2011. Characterizing 3D vegetation structure from space: mission requirements. *Remote Sens. Environ.* 115, 2753–2775.
- Holm, S., Nelson, R., Ståhl, G., 2017. Hybrid three-phase estimators for large-area forest inventory using ground plots, airborne lidar, and space lidar. *Remote Sens. Environ.* 197, 85–97.
- Lefsky, M.A., 2010. A global forest canopy height map from the moderate resolution imaging spectroradiometer and the geoscience laser altimeter system: a global forest canopy height map. *Geophys. Res. Lett.* 37 (n/a-n/a).
- Lefsky, M.A., Harding, D., Cohen, W.B., Parker, G., Shugart, H.H., 1999. Surface lidar remote sensing of basal area and biomass in deciduous forests of eastern Maryland, USA. *Remote Sens. Environ.* 67, 83–98.
- Lu, H., Pang, Y., Li, Z.Y., Chen, B.W., 2015. An Automatic Range Ambiguity Solution in High-Repetition-Rate Airborne Laser Scanner Using Prior Terrain Prediction. *IEEE Geosci. Remote Sens. Lett.* 12, 2232–2236.
- Magnussen, S., 2015. Arguments for a model-dependent inference? *Forestry* 88, 317–325.
- Magnussen, S., Frazer, G., Penner, M., 2016. Alternative mean-squared error estimators for synthetic estimators of domain means. *J. Appl. Stat.* 43, 2550–2573.
- Mandallaz, D., 2008. *Sampling Techniques for Forest Inventories*. Chapman & Hall/CRC, Boca Raton, FL.
- Margolis, H.A., Nelson, R.F., Montesano, P.M., Beaudoin, A., Sun, G., Andersen, H.-E., Wulder, M.A., 2015. Combining satellite lidar, airborne lidar, and ground plots to estimate the amount and distribution of aboveground biomass in the boreal forest of North America. *Can. J. For. Res.* 45, 838–855.
- Marklund, L.G. (Ed.), 1988. *Biomass Functions for Pine, Spruce and Birch in Sweden*. Dep. of For. Surv..
- Maselli, F., Chiesi, M., Mura, M., Marchetti, M., Corona, P., Chirici, G., 2014. Combination of optical and LiDAR satellite imagery with forest inventory data to improve wall-to-wall assessment of growing stock in Italy. *Int. J. Appl. Earth Obs. Geoinf.* 26, 377–386.
- MATLAB, 2016. *Signal Processing Toolbox: Release Notes (R2016b)*. The MathWorks.
- McCulloch, C.E., Searle, S.R., Neuhaus, J.M., 2008. *Generalized, Linear, and Mixed Models*, 2nd ed. Wiley, Hoboken, N.J.
- McRoberts, R.E., Naesset, E., Gobakken, T., 2013. Accuracy and precision for remote sensing applications of nonlinear model-based inference. *IEEE J. Sel. Top. Appl. Earth Observ. Remote Sens.* 6, 27–34.
- Montesano, P.M., Rosette, J., Sun, G., North, P., Nelson, R.F., Dubayah, R.O., Ranson, K.J., Kharuk, V., 2015. The uncertainty of biomass estimates from modeled ICESat-2 returns across a boreal forest gradient. *Remote Sens. Environ.* 158, 95–109.
- NASA, 2016. *GEDI - High Resolution Ranging of Earth's Forests and Topography On ISS*. NASA Science.
- Neigh, C.S.R., Nelson, R.F., Ranson, K.J., Margolis, H.A., Montesano, P.M., Sun, G., Kharuk, V., Naesset, E., Wulder, M.A., Andersen, H.-E., 2013. Taking stock of circumboreal forest carbon with ground measurements, airborne and spaceborne LiDAR. *Remote Sens. Environ.* 137, 274–287.
- Nelson, R., Boudreau, J., Gregoire, T.G., Margolis, H., Naesset, E., Gobakken, T., Ståhl, G., 2009. Estimating Quebec provincial forest resources using ICESat/GLAS. *Can. J. For. Res.* 39, 862–881.
- Nelson, R., Margolis, H., Montesano, P., Sun, G., Cook, B., Corp, L., Andersen, H.-E., deJong, B., Pellat, F.P., Fickel, T., Kauffman, J., Prisley, S., 2017. Lidar-based estimates of aboveground biomass in the continental US and Mexico using ground, airborne, and satellite observations. *Remote Sens. Environ.* 188, 127–140.
- North, P.R.J., Rosette, J.A.B., Suarez, J.C., Los, S.O., 2010. A Monte Carlo radiative transfer model of satellite waveform LiDAR. *Int. J. Remote Sens.* 31, 1343–1358.
- Pang, Y., Lefsky, M., Sun, G., Ranson, J., 2011. Impact of footprint diameter and off-nadir pointing on the precision of canopy height estimates from spaceborne lidar. *Remote Sens. Environ.* 115, 2798–2809.
- Pinheiro, J., Bates, D., DebRoy, S., Sarkar, D., Team, R.C., 2016. *nlme: Linear and Nonlinear Mixed Effects Models*.
- Popescu, S.C., Zhao, K., Neuenchwander, A., Lin, C., 2011. Satellite lidar vs. small footprint airborne lidar: Comparing the accuracy of aboveground biomass estimates and forest structure metrics at footprint level. *Remote Sens. Environ.* 115, 2786–2797.
- Rejou-Mechain, M., Muller-Landau, H.C., Detto, M., Thomas, S.C., Le Toan, T., Saatchi, S.S., Barreto-Silva, J.S., Bourg, N.A., Bunyavechewin, S., Butt, N., Brockelman, W.Y., Cao, M., Cardenas, D., Chiang, J.M., Chuyong, G.B., Clay, K., Condit, R., Dattaraja, H.S., Davies, S.J., Duque, A., Esufali, S., Ewango, C., Fernando, R.H.S., Fletcher, C.D., Gunatilleke, I.A.U.N., Hao, Z., Harms, K.E., Hart, T.B., Herault, B., Howe, R.W., Hubbell, S.P., Johnson, D.J., Kenfack, D., Larson, A.J., Lin, L., Lin, Y., Lutz, J.A., Makana, J.R., Malhi, Y., Marthews, T.R., McEwan, R.W., McMahon, S.M., McShea, W.J., Muscarella, R., Nathalang, A., Noor, N.S.M., Nytch, C.J., Oliveira, A.A., Phillips, R.P., Pongpattananurak, N., PUNCHI-Manage, R., Salim, R., Schurman, J., Sukumar, R., Suresh, H.S., Suwanvecho, U., Thomas, D.W., Thompson, J., Uriarte, M., Valencia, R., Vicentini, A., Wolf, A.T., Yap, S., Yuan, Z., Zartman, C.E., Zimmerman, J.K., Chave, J., 2014. Local spatial structure of forest biomass and its consequences for remote sensing of carbon stocks. *Biogeosciences* 11, 6827–6840.
- Rieger, P., Ullrich, A. (Eds.), 2011. *Resolving Range Ambiguities in High-repetition Rate Airborne Lidar Applications*, (pp. 81860A-81860A-81868).
- Riegl, 2013. *Waveform Extraction Library*. © RIEGL Laser Measurement Systems GmbH, Horn, Austria Printed on: March, 18, 2013.
- Saarela, S., Schnell, S., Tuominen, S., Balázs, A., Hyyppä, J., Grafström, A., Ståhl, G., 2016. Effects of positional errors in model-assisted and model-based estimation of growing stock volume. *Remote Sens. Environ.* 172, 101–108.
- Ståhl, G., Saarela, S., Schnell, S., Holm, S., Breidenbach, J., Healey, S.P., Patterson, P.L., Magnussen, S., Naesset, E., McRoberts, R.E., Gregoire, T.G., 2016. Use of models in large-area forest surveys: comparing model-assisted, model-based and hybrid estimation. *For. Ecosyst.* 3, 1–11.
- Sun, G., Ranson, K.J., Kimes, D.S., Blair, J.B., Kovacs, K., 2008. Forest vertical structure from GLAS: an evaluation using LVIS and SRTM data. *Remote Sens. Environ.* 112, 107–117.
- Tomppo, E., Gschwantner, T., Lawrence, M., 2010. *National Forest Inventories*. Springer Netherlands.
- Wagner, W., Ullrich, A., Ducic, V., Melzer, T., Studnicka, N., 2006. Gaussian decomposition and calibration of a novel small-footprint full-waveform digitising airborne laser scanner. *ISPRS J. Photogramm.* *Remote Sens.* 60, 100–112.
- Wulder, M.A., White, J.C., Nelson, R.F., Naesset, E., Ørka, H.O., Coops, N.C., Hilker, T., Bater, C.W., Gobakken, T., 2012. Lidar sampling for large-area forest characterization: a review. *Remote Sens. Environ.* 121, 196–209.

### 3.6 Paper VI

**Title:** Roughness Spectra Derived from Multi-Scale LiDAR Point Clouds:  
A Comparison and Sensitivity Analysis

**Authors:** Milenković, M., Ressler, C., Karel, W., Mandlbürger, G. and Pfeifer, N.

**Submitted to:** ISPRS International Journal of Geo-Information

**Licence:** ©2017 Authors. This manuscript version is made available under  
the Creative Commons Attribution 4.0 (CC BY 4.0) license

Type of the Paper: Article

# Roughness Spectra Derived from Multi-Scale LiDAR Point Clouds: A Comparison and Sensitivity Analysis

Milutin Milenković <sup>1,\*</sup>, Camillo Ressel <sup>1</sup>, Wilfried Karel <sup>1</sup>, Gottfried Mandlbürger <sup>1</sup> and Norbert Pfeifer <sup>1</sup>

<sup>1</sup> Department of Geodesy and Geoinformation (GEO), Technische Universität Wien (TU Wien),  
Gußhausstraße 27-29, 1040 Vienna, Austria

\* Correspondence: milutin.milenkovic@geo.tuwien.ac.at; Tel.: +43-(1)-58801-12254

Academic Editor: name

Received: date; Accepted: date; Published: date

**Abstract:** The roughness spectrum (i.e. the power spectral density) is a derivative of digital terrain models (DTMs) that is used as a surface roughness descriptor in many geomorphological and physical models. Although light detection and ranging (LiDAR) has become one of the main data sources for DTM calculation, it is still unknown how roughness spectra are affected when calculated from different LiDAR point clouds, or when they are processed differently. In this paper, we used three different LiDAR point clouds of a 1 m x 10 m gravel plot to derive and analyse roughness spectra from the interpolated DTMs. The LiDAR point clouds were acquired using terrestrial laser scanning (TLS), and laser scanning from both an unmanned aerial vehicle (ULS) and an aeroplane (ALS). The corresponding roughness spectra are derived first as the ensemble-wise averaged periodograms, and then, the spectral differences are analysed with a dB threshold that is based on the 95 % confidence intervals of the periodograms. The aim is to determine scales (spatial wavelengths) over which the analysed spectra can be used interchangeably. The results show that one TLS scan can measure roughness spectra for wavelengths larger than 1 cm (i.e., two times its footprint size) and up to 10 m, with spectral differences less than 0.65 dB. For the same dB threshold, the ULS and TLS spectra can be used interchangeably for wavelengths larger than about 1.2 dm (i.e., five times the ULS footprint size). However, the interpolation parameters should be optimized to make the ULS spectrum more accurate at wavelengths smaller than 1 m. The plot size was, however, too small to draw particular conclusions about ALS spectra. These results show that novel ULS data has a high potential to replace TLS data for roughness spectrum calculation in many applications.

**Keywords:** laser scanning; UAV; surface interpolation; power spectral density; spectral slope; gravel roughness

## 1. Introduction

Light Detection and Ranging (LiDAR) is one of the primary measurement techniques used nowadays for derivation of digital terrain models (DTM) in environmental applications. LiDAR, also referred to as laser scanning, provides highly accurate and dense 3D point measurements (point clouds) that can be acquired at different measurement scales. For example, terrestrial laser scanning (TLS) can measure micro-scale surface features (< 1 m) such as pebbles or soil clods [1-3]. Such data typically have a coverage of a few tens of meters. A coverage of, e.g., a few km is possible when a TLS system is mounted on a moving vehicle or a river boat [4, 5]. These so-called mobile mapping systems also include a global navigation satellite system (GNSS) and/or an inertial measurement unit (IMU) for georeferencing the acquired points. Laser scanning performed from aeroplanes (ALS) constitutes another dynamic, mobile mapping system that provides even larger coverage, but also features lower resolution compared to TLS. However, such data are able to depict topographic

signatures at the landscape scale relevant for hydrology and geomorphology [5-9]. Therefore, LiDAR data are extremely useful for describing natural surfaces at several spatial scales.

One way to describe natural surfaces over different spatial scales is by using the roughness spectrum [8, 10, 11]. This is a DTM derivative that shows the distribution of the terrain variance over a certain range of spatial frequencies (wavelengths), where each frequency represents a sinusoidal component of the DTM in the spatial domain. More precisely, the roughness spectrum is the surface's power spectral density, i.e. the Fourier transform of the surface's autocorrelation function. The calculation of roughness spectra is typically based on the Fast Fourier Transform (FFT) algorithm applied on a regularly-sampled elevation profile or a gridded DTM [8, 12, 13]. Hedge and Masselink [14] summarized the major steps of this methodology for time series data, but they are also valid in case of gridded DTMs [8]. As the elevation profiles are discrete and finite, a roughness spectrum has variances only in a certain span of discrete wavelengths (a particular frequency band). The longest (DC) and the smallest (Nyquist) wavelengths of this frequency band correspond exactly to the profile length and the double of the point spacing, respectively. Thus, for a LiDAR dataset, the DC and Nyquist wavelengths are defined by its spatial coverage and sampling distance, respectively.

Roughness spectra are extensively used to characterize surface roughness in many physical and environmental models. The radar backscattering models, for example, use the roughness spectrum to better define the scattering characteristics of certain natural surfaces and to predict the amount of the backscatter energy from such surfaces [15]. Then, the roughness spectrum is used to describe the roughness length of the boundary surface and to analyse its wind velocity profile for different topographic scales [16]. Similarly, in hydraulic models, the roughness spectrum and its slope are used to characterize grain roughness and local microtopography as well as to analyse the flow velocity spectrum [17, 18]. Roughness spectra are also employed to quantify the influence of the Earth's surface processes on landscape shapes [8], or to describe the seafloor topography [19].

For most of the above applications, roughness spectra are, or can be, derived from multi-scale LiDAR point clouds. These LiDAR point clouds have first to be interpolated into gridded DTMs to apply the Fourier-based methodology and to derive the roughness spectra. It is, however, not known which frequencies of the resulting spectra are affected by the selected DTM interpolation method. Furthermore, multi-scale LiDAR datasets have different resolutions and coverages, and thus, provide spectra in different frequency bands. To combine such complementary data, it is important to know over which spatial scales the corresponding roughness spectra can be used interchangeably. Such an analysis is important to understand better how to measure surfaces with LiDAR and how to better combine these complementary LiDAR data to get roughness spectra over a larger frequency band.

In this study, we sampled a 1 m x 10 m gravel plot with three different LiDAR techniques and analysed and compared the corresponding roughness spectra. The LiDAR techniques used here comprise terrestrial laser scanning (TLS), laser scanning from both an unmanned aerial vehicle (ULS) and an aeroplane (ALS). It is noted that the ULS data were acquired with a novel RIEGL VUX-1 UAV system that was for the first time applied in a surface roughness application. Furthermore, the gravel plot was extensively sampled with TLS (2.5 hours of effective scanning with 14 high-resolution scans), whereas the ALS and ULS data were acquired in the course of a topographic survey with the aim to cover a larger river section. Therefore, the focus of the analysis was more on the TLS data. In addition, a set of high-resolution handheld images of the gravel plot was acquired and processed to have a non-LiDAR based roughness spectrum in the comparison. This data set also served as a reference for high-frequency surface components, as the ground sampling distance (GSD) of the images was ten times smaller than the TLS footprint size.

### 1.1. Objectives

In this study, roughness spectra and their confidence intervals are derived by applying the Fourier-based methodology standardized by Hedge and Masselink [14]. Previous studies were focused more on how particular Fourier-based steps such as profile windowing or detrending affect the shape of roughness spectra [10, 13]. Our analysis, in contrast, concentrates on how certain aspects

of LiDAR processing affect the shape of the resulting roughness spectrum, and then compares multiscale LiDAR spectra. More precisely, the objectives of this study are:

- To analyse the influence of basic DTM interpolation methods on TLS, ULS and ALS roughness spectra
- To analyse how the number of TLS scans affects the roughness spectrum
- To compare TLS, ULS and ALS roughness spectra

For the DTM interpolation analysis, TLS, ULS and ALS point clouds are interpolated using basic interpolation methods, and then the difference in the shape of the corresponding spectra is analysed. The aim is to determine spatial wavelengths that are not affected by the interpolation method. For the sake of simplicity, complex interpolation methods (e.g. Kriging) are not applied in this paper as they are functions of several parameters and impose stronger restrictions on the input data.

For the analysis on the number of TLS scans, different combinations of TLS scans are selected and the corresponding roughness spectra are compared with the roughness spectrum derived using all 14 TLS scans. The aim is to determine if a 1 m x 10 m gravel plot can be measured with a smaller number of TLS scans, while still providing an equally accurate roughness spectrum as opposed to using all TLS scans. An additional aim is to determine which frequency band can be covered by a single TLS scan with its roughness spectrum.

A comparison of the multiscale LiDAR spectra is done for the first time here. The aim of this analysis is to understand the differences in the TLS, ULS and ALS spectra and to determine the spatial wavelengths over which they can be used interchangeably. The spectra based on TLS and novel ULS data are separately analysed to assess to which degree the ULS spectrum can replace the TLS spectrum.

## 2. Study Site and Data

Table 1 gives an overview of datasets (and their basic characteristics) used in this study. All the data were collected on February 26, 2015 and refer to the same area, i.e. a 1 m x 10 m gravel plot. The ALS and ULS data were already available as georeferenced point clouds for this study. Their georeferencing is performed with a rigorous strip adjustment procedure that is presented in [20] and [21], in detail. The TLS data are processed here from raw point clouds to georeferenced scans. Therefore, the input data for roughness spectra calculation, and all further analysis, includes individually georeferenced ALS, ULS and TLS point clouds.

Table 1. Overview of the data used in this paper. The data characteristics refer to the gravel plot area

Technique	Sensor	Slant Range	Footprint diameter	Mean Sampling Distance	Overlapping Footprints	Processing stage
		[m]	[mm]	[mm]		
ALS	RIEGL LSM-Q1560	640 – 720	~ 160	167	No	Georef. and block adj. strips
ULS	RIEGL VUX-1 UAV	50 <sup>2</sup>	~ 25	29	No	Georef. and block-adj. strips
TLS	Z+F Imager 5010c	2.5 – 4.5	~ 5	0.7	Yes	Raw data
DIM <sup>1</sup>	Nikon D800	1.5 – 2.7	0.5 <sup>3</sup>	0.5 <sup>3</sup>	No	Raw data

<sup>1</sup> Dense Image Matching; <sup>2</sup> Flying height above ground; <sup>3</sup> Ground Sampling Distance (GSD);

Figure 1 shows basic properties of the study site. The 1 m x 10 m gravel plot is located at a point bar in the lower part of the pre-alpine Pielach river, a tributary of the Danube in Austria (N 48°12'50.70"N, E 15°22'27.50", WGS 84). The microtopography of the gravel plot (Figure 1d-e) mostly consists of unsorted fine (< 2 cm in diameter) and medium (2 to 6 cm) pebbles, while several clusters of coarse (> 6 cm) pebbles are also present. The plot also features microtopographic undulations at cm to dm scale on top of a global planar slope.

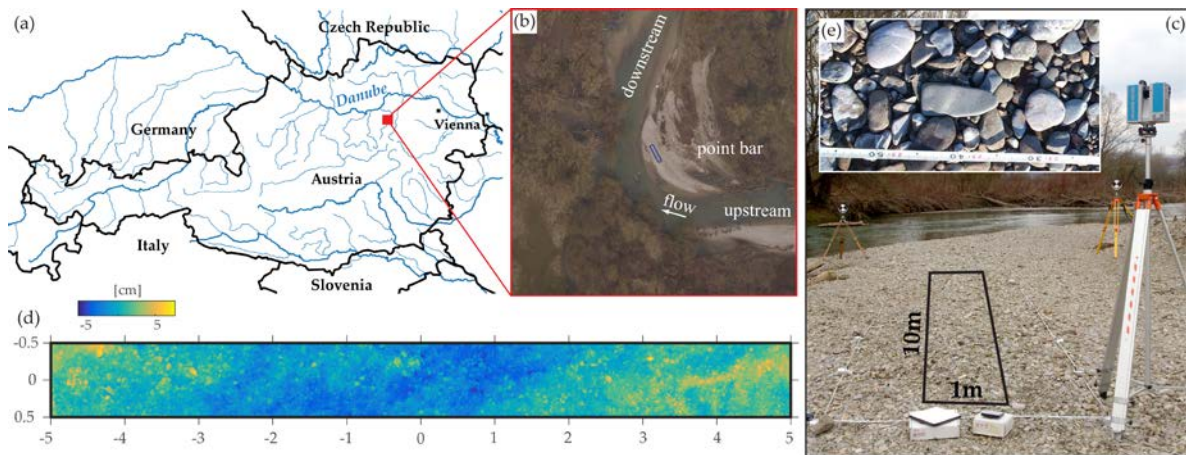


Figure 1. Study site properties: (a) Location of the study site and Pielach river; (b) A vertical photo of the gravel plot and the point bar; (c) A photo of the TLS setup and the gravel plot; (d) Microtopography of the plot visualized by the color-coded DTM of the plot ; (e) Typical pebble sizes within the plot.

### 2.1. ALS Data

The ALS data were acquired with a Riegl LMS-Q1560 dual-channel long-range laser scanning system, which acquires two scans for each strip (X-shaped scan lines on the ground, FoV:  $\pm 29^\circ$ ). The sensor additionally features GNSS/IMU to record the trajectory. The entire system was mounted on a Diamond DA42 aircraft.

The scanning parameters were set to cover the whole river reach and provide at least 10 points per  $m^2$  for a single strip, i.e. two scans. The pulse repetition rate was 400 kHz, and the flying speed was approx. 56 m/s (110 knots). The plot was covered with four strips, resulting in an average point density of 36 points per  $m^2$ . This corresponds to an average point sampling of approximately 17 cm. As the flying height was 640 m above the terrain, the footprint diameter was also approximately 16 cm (the beam divergence being 0.25 mrad). This means that the footprints of individual ALS samples were (on average) touching, or just slightly overlapping, one another.

The raw ALS data had already been preprocessed (see [20] and [21]), providing a georeferenced point cloud in the global coordinate system (ETRS89/UTM33N). The ALS preprocessing involved (a) extraction of Gaussian echoes, (b) resolving range ambiguities due to the multiple-time-around ranging of the used sensor, and (c) direct georeferencing of the extracted echoes. The preprocessing was done in the sensor manufacturer software (RiPROCESS) [21]. Additionally, a rigorous strip adjustment is done with the objective to minimize point-to-plane distances in overlapping strip areas [20]. The standard deviation of the residuals between individual ALS strips is reported to be 1 cm [21].

### 2.2. ULS Data

The ULS data were acquired with the Riegl VUX-1 UAV laser scanner mounted on the Riegl RiCOPTER, a remotely piloted octocopter. The sensor is equipped with an IMU/GNSS system to record the trajectory. The scanner itself performs online waveform processing, which provides additional attributes such as pulse shape deviation and calibrated reflectance readings for each laser echo [22].

The scanning parameters were set to cover a larger area ( $\sim 100$  ha) and provide at least one point per  $dm^2$  for a single ULS strip. The pulse repetition rate was 350 kHz, and the flying speed was approx. 8 m/s (15.5 knots). The plot was covered with ten strips (FoV:  $330^\circ$ ), resulting in an average point density of 11.8 points per  $dm^2$ . This corresponds to an average point sampling of  $\sim 2.9$  cm. As the flying height was 50 m above the terrain, the footprint diameter was  $\sim 2.5$  cm (the beam divergence being 0.5 mrad). Thus, the footprints of individual ULS samples were (on average) not overlapping one another. As in the case of the ALS data, the raw ULS data had been preprocessed before (see [20]

and [21]), providing a georeferenced point cloud in the same global coordinate system. The standard deviation of the point-to-plane residuals is reported to be below 2 cm for both the ULS strips only and the ULS and ALS strips combined [20].

### 2.3. TLS Data

The gravel plot was extensively scanned with a Z+F IMAGER® 5010c mounted on a high tripod. This scanner utilizes phase shift ranging and has a small beam divergence (0.3 mrad). The beam diameter at the exit (0.1 m range) is 3.5 mm, which allows for a high-resolution scanning of close objects (maximum range < 130 m).

The scanning parameters were set to maximize the TLS sampling of the gravel plot and still have a reasonable scanning time to acquire as many scans as possible. The aim was that the footprints of the TLS samples overlap one another already in a single TLS scan. Therefore, the angular resolution was set to  $0.036^\circ$  (10000 samples per full circle) and the scanning quality modus “high” was selected. This TLS setting leads to a scanning time of 7 min. per scan. The plot was scanned with 14 scans, seven taken from each long side of the plot. This so-called opposite scanning minimizes occlusions due to object scan shadows. The average point density was 190.3 points per  $\text{cm}^2$ , which corresponds to an average point sampling of 0.7 mm. As the scanner height above the terrain was between 2.4 m and 2.6 m, and the range not larger than 4.5 m, the TLS footprint diameter was smaller than 5 mm within the plot. This means that the TLS footprints are largely overlapping one another. For a single scan, the average sampling distance was  $\sim 2.4$  mm (i.e.  $\sim 17$  points per  $\text{cm}^2$ ), and thus, the TLS footprints are largely overlapping one another even for the single scan samples. Such a scanning maximizes the resolution of the TLS data and is also known as correlated scanning [23]. Furthermore, scanning from a high tripod ensured the incidence angle being smaller than  $52^\circ$  for 90 % of the data, which fulfils the recommendations for soil roughness scanning [3].

The raw TLS measurements were first preprocessed and then georeferenced. The pre-processing involved the following steps: (a) elimination of erroneous range measurements (so-called mixed pixels) caused by phase-based ranging [24], (b) georeferencing of the TLS scans, and (c) export of the georeferenced points inside the gravel plot. All steps were performed using the Z+F LaserControl® software [25, version 8.6]. The georeferencing of the TLS scans was done indirectly, using four ground control points (GCPs) and a “point block adjustment” method implemented in the above software. The GCPs were located outside the plot and scan positions, ensuring target visibility in all scans and a favourable network geometry for the co-registration. The coordinates of the GCPs were derived from the total station measurements and in the global coordinate system of the ALS and ULS data. After georeferencing the individual TLS scans, the standard deviation of the 3D distance residuals at the GCPs was 1.6 mm. The same statistic derived for individual TLS scans was 0.8 mm. The georeferenced TLS scans were then exported for an improved, global co-registration with a version of the Iterative Closest Point (ICP) algorithm [20]. The standard deviation of the point-to-plane distances between all scans after this global co-registration was 0.6 mm. This suggests a good co-registration as the ranging noise of the TLS scanner alone is  $\sim 0.3$  mm [26].

### 2.4. Handheld Images

A set of handheld images of the plot is also acquired to calculate an additional, non LiDAR-based, roughness spectrum. In total, 117 images were collected with the full-frame Nikon D800 camera using a 28 mm lens. The images were taken from  $\sim 1.8$  m height above the ground and with an overlap of 70-80 %, which resulted in a GSD not larger than 0.5 mm within the plot.

The images were first oriented, and then dense image matching (DIM) was applied to derive a DTM. The latter will be referred to as the DIM DTM. The image orientation and self-calibration was done using a bundle block adjustment method implemented in the Pix4D software [27]. The adjustment also included 18 3D GCPs uniformly distributed along the plot sides and whose coordinates were measured by a total station in the global coordinate system. The resulting reprojection error was 0.13 pixels, whereas the standard deviation of the height residuals at the GCPs was 0.8 mm. Based on this camera orientation, the DIM DTM was calculated using the DIM method

implemented in the SURE software [28]. We used the option for automatic interpolation of a DTM and specified its grid size to 0.5 mm, which corresponds to the GSD of our images. The latter is ten times smaller than the TLS footprint diameter, which enables DIM DTM to serve as the reference for high-frequency surface features.

### 3. Methods

#### 3.1. Derivation of Roughness Spectra

The derivation of roughness spectra follows the steps for periodogram calculation recommended by Hegge and Masselink [14]. These steps involve: detrending of surface heights, sampling of surface profiles (profiling), windowing (tapering), calculating one-sided periodograms, reducing the periodogram variance and calculating confidence intervals. As our input is a set of independently georeferenced point clouds, our processing involved additionally: (a) data co-registration and (b) interpolation of point clouds into a grid DTM. Then, DTM rows are randomly sampled to build an ensemble of gravel surface profiles to calculate corresponding roughness spectra. In the following, these processing steps are explained in detail.

##### 3.1.1. Co-registration and Detrending

The georeferenced point clouds were given in the global coordinate system. However, a fine co-registration with a version of the Iterative Closest Point (ICP) algorithm [20] was additionally applied to eliminate residual georeferencing errors before the roughness spectra comparison. The TLS dataset served as fixed reference for this fine co-registration, and ICP was used to optimize the transformation parameters of rigid body transformations (3 rotations and 3 shifts) that were subsequently applied on the remaining data sets (ULS and ALS point clouds). This processing was done using the ICP implementation in the OPALS software [29].

The point cloud detrending was done by subtracting a global planar trend from the data. Planar detrending is typically applied in practice to remove wavelengths longer than the plot length [8, 12]. The detrending is also required because of the periodicity assumption in the Fourier-based analysis, i.e. to mitigate a height jump between the start- and end-sample of a profile [14]. The planar trend was estimated here by fitting a regression plane through the TLS points within the gravel plot. More precisely, the normal of the regression plane corresponds to the eigenvector of the smallest eigenvalue of the TLS coordinates' covariance matrix. The detrending is thus performed by transforming each point cloud into a local object coordinate system (OCS) of the gravel plot. This (rigid-body) transformation aligned this eigenvector with the z-axis of the OCS, whereas the eigenvectors of the largest and the second largest eigenvalues were aligned with the x- and y-axis of the OCS, respectively.

##### 3.1.2. DTM Interpolation

For each point cloud in the OCS a DTM grid was computed using the following interpolation methods: nearest neighbour (NN), triangular irregular network (TIN), and moving planes (MP). The MP interpolation has one additional parameter compared to other methods: the number of neighbouring points. For example, the minimum required number of points for MP that allows adjustment of the plane is four, but a larger number of points can also be considered. In this study, we analysed the sensitivity of roughness spectra with respect to different interpolation methods and the number of neighbours. More details about these interpolation methods can be found in [30].

It is noted that the DTM grid size was set to 0.5 mm for all the DTMs in the study. This grid size is ten times smaller than the footprint diameter of our highest resolution LiDAR data set (the TLS point cloud). Such a small grid size has certain advantages for our roughness spectra analysis. First, it enables to analyse the behaviour of roughness spectra at frequencies around and higher than the diffraction-limit (the wavelength equal to the footprint diameter). Second, it excludes the impact of the grid size on our analysis. Furthermore, the same grid size used for all DTMs results in the same frequency axis increments, which makes the comparison of roughness spectra easier.

It is also noted that our DTM heights are free from a global planar trend, as the latter was removed during the transformation into OCS (Section 3.1.1). Furthermore, the same transformation ensured that rows and columns of the DTMs are parallel with the major and semi-major axis of the gravel plot, respectively. This means that, e.g., each DTM row is 10 m long and contains 2000 samples separated by 0.5 mm from one another. These DTM rows are used subsequently to derive roughness spectra.

### 3.1.3. Roughness Spectrum and Periodogram

The roughness spectrum was estimated as the ensemble average of hamming-windowed periodograms calculated from uniformly sampled DTM rows. The periodogram is the Fourier-based estimator of a roughness spectrum [8, 10, 12, 13, 31]. It is also the most commonly used one because it can be easily applied using, e.g., the fast Fourier transform algorithm. Here, the periodograms are calculated using the MATLAB function *periodogram* [32].

Figure 1 shows periodogram-based estimates of a roughness spectrum (derived from a TLS DTM) that are visualized as one-sided power spectral densities given in decibels (dB). Each roughness spectrum sample  $n(f_n, S_n)$  is a pair consisting of a roughness spectrum value  $S_n$  that refers to the spatial frequency  $f_n$ . There are, in total,  $N/2+1$  ( $n = 0, \dots, N/2$ ) samples of a one-sided spectrum, where  $N$  is the number of DTM row samples (where  $N$  is an even number). A spectrum sample  $n(f_n, S_n)$  corresponds to a surface harmonic  $n$  that, in the spatial domain, is a sine wave with the amplitude  $c_n$  and the spatial frequency  $f_n$ . The relation between  $S_n$  and  $c_n$  is given as:  $S_n[\text{dB}] = 2 \cdot (10 \cdot \log_{10} c_n^2) / \Delta f$ , where  $\Delta f$  is the frequency resolution. The factor 2 is used to scale for the negative frequencies, except for the DC and Nyquist frequencies ( $f_0$  and  $f_{N/2}$ , respectively) as they do not have a negative counterpart. The frequency resolution is given as:  $\Delta f = f_s / N = 1 / (N \cdot \Delta x)$ , where  $f_s = 1 / \Delta x$  is the sampling frequency and  $\Delta x$  is the sampling interval. In this paper, we analyse 10 m long DTM rows with a grid size of 0.5 mm, which means that  $\Delta x = 0.5$  mm and  $N = 2000$ . Particular frequencies  $f_n$  are a set of the following discrete frequencies:  $f_n = n / (N \cdot \Delta x)$  for  $n = 0, \dots, N/2$ , where  $n$  is the harmonic number. Each discrete frequency  $f_n$  corresponds to the wavelength  $\lambda_n = 1 / f_n$ . The frequencies  $f_n$  are typically plotted in a logarithmic scale, i.e.  $\log_{10} f_n$ , like the bottom axis in Figure 2. The top axis shows the corresponding wavelengths. Finally, it is noted that the root mean square height  $RMS h_n$  of the harmonic  $n$  is:  $RMS h_n = \sqrt{2} \cdot c_n$ . In Figure 2, the right axis shows  $RMS h_n$  values in mm that correspond to the roughness spectrum axis values in dB (the left axis).

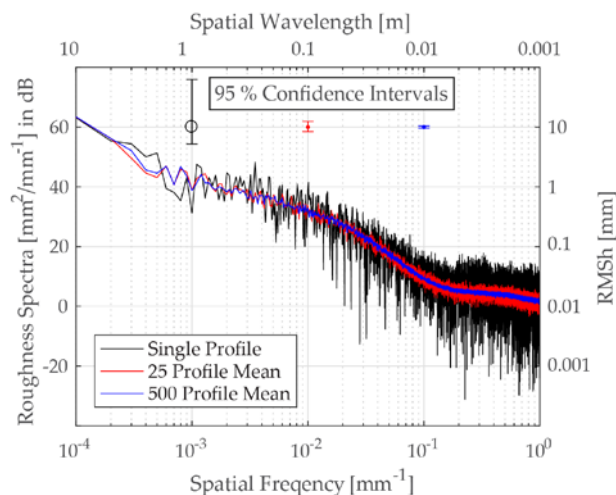


**Figure 2.** Bin-averaged Roughness Spectra from single, 25 and 500 profiles.

### 3.1.4. Windowing, Variance Reduction and Confidence Intervals

The periodogram has large variance and spectral leakage [33, p. 552]. One way to mitigate leakage is by using the hamming window [8, 14], which is also done here. This window has a very

steep roll-off at its side lobes [34], which is of advantage when analysing the slope of a spectrum at high frequencies. The periodogram variance is reduced here in the same way as in [35] by ensemble averaging. The following steps are required for computing the ensemble-wise averaged periodogram. First, a certain number ( $M$ ) of DTM rows is uniformly sampled to calculate corresponding periodograms  $n(f_n, S_{n,i})$ , where  $i = 1, \dots, M$ . Then, an ensemble-wise averaged periodogram  $n(f_n, \bar{S}_n)$  is calculated by averaging individual periodogram values  $S_{n,i}$  that refer to the same frequency  $f_n$ :  $\bar{S}_n = 1/M \sum_{i=1}^M S_{n,i}$ . There are also other approaches for variance reduction, based on binning or smoothing of the periodogram, but they reduce its resolution and are more appropriate when just a few profiles are available [14].

Figure 2 shows how ensemble averaging reduces the variance of the estimated roughness spectrum. The black roughness spectrum that has the highest variance is estimated from a single-profile periodogram. On top of this periodogram, there is its 95 % confidence interval (the black error bars) calculated as in [14, Eq.15]:

$$S_{n,i} \cdot v/\chi_{v,1-\frac{\alpha}{2}}^2 \geq S_{n,i} \geq S_{n,i} \cdot v/\chi_{v,\frac{\alpha}{2}}^2, \quad (1)$$

where  $\alpha = 0,05$  is the confidence level and  $v$  is the degree of freedom. These confidence bounds are asymmetric, which is due to the chi-square distribution and the two degrees of freedom ( $v = 2$ ):  $S_{n,i} \sim \chi_{2M}^2(v, 2v)$ . The red and blue roughness spectra are the ensemble averages based on 25 and 500 periodograms, respectively. Their confidence intervals (the red and blue error bars) are more symmetrical and much smaller than for the single periodogram case. This is because an ensemble-wise averaged spectrum has more degrees of freedom,  $\bar{S}_n \sim \chi_{2M}^2(2M, 4M)$ , compared to  $S_{n,i}$ , and consequently, converges to the Gaussian distribution. Furthermore, this shows that the variance of the ensemble-wise averaged spectrum is reduced compared to a single periodogram. In this paper, all the analyses are based on ensemble-wise averaged roughness spectra using 500 uniformly sampled periodograms.

### 3.2. Comparison of Roughness Spectra

To allow for a quantitative analysis, the comparison was based on absolute differences of spectra:  $\Delta S_n = \text{abs}(\bar{S}_{n,1} - \bar{S}_{n,2})$ . This will be referred to as the *spectral difference*. In a few cases, when more than two spectra are compared at once, the range statistics is used instead:  $\Delta S_n = \max(\bar{S}_{n,j}) - \min(\bar{S}_{n,j})$ ,  $\forall j$ . This will be referred to as the *spectral range*. Based on this  $\Delta S_n$  value (also in dB as  $\bar{S}_{n,j}$ ), it is then decided whether the spectra can be used interchangeably at the frequency  $f_n$  i.e. the wavelength  $\lambda_n$ . To put this decision on a more quantitative ground,  $\Delta S_n$  is compared with a dB threshold that was here set to the 95 % confidence level of the spectra. In other words, when  $\Delta S_n$  exceeds this dB threshold, the 95 % confidence intervals of the two spectra do not overlap any more. Therefore, it is concluded that these spectra cannot be used interchangeably at the wavelength  $\lambda_n$ . It is noted that the dB threshold is a function of only the number of profiles  $M$  (i.e., the degrees of freedom in  $\chi_{2M}^2$ ) when  $\bar{S}_n$  is analysed in the logarithmic scale (Eq.1 and [14]). For our data the dB threshold was 0.5 dB.

In total, three different comparisons are done that correspond to the three objectives set in Section 1.1. The following subsections present the spectra used in these comparisons. It is noted that, in some of the comparisons, a spectrum derived from the DIM DTM is also used. This spectrum is referred to as the DIM spectrum.

#### 3.2.1. Roughness Spectra and the DTM Interpolation Method

For each data set, three roughness spectra are derived using the NN-, TIN- and four point MP-interpolated DTMs. For the TLS data set, these three spectra are referred as: TLS NN spectrum, TLS TIN spectrum and TLS MP spectrum, respectively. The analogous naming is used for the ULS- and ALS-based spectra. For each data set, the next step is to derive the spectral range based on the corresponding NN-, TIN- and MP-spectrum. If the spectral range exceeds the dB threshold, then the corresponding spatial wavelength ( $\lambda_{th}$ ) is reported and wavelengths larger than  $\lambda_{th}$  are considered

to be insensitive on the selection of the interpolation method. The NN-, TIN- and MP-spectra are also compared with the DIM spectrum by calculating corresponding (absolute) spectral differences. It is noted that the influence of the interpolation method on the DIM spectrum is not analysed because DIM DTM was interpolated by the image matching software.

### 3.2.2. Roughness Spectra and the Number of TLS Scans

Our comparison analysed both the combination of TLS scans and the individual scans. The former includes the following scan setups: 7+7 Scan Setup, 3+3 Scan Setup, 2+2 Scan Setup and 1+1 Scan Setup, and Figure 3 shows schematically the scan positions of these setups. The 7+7 Scan Setup includes in total 14 TLS scans (seven per each long side of the plot) and its spectrum is referred to as 7+7 Scan Setup spectrum. Spectra of the remaining setups are analogously named and they refer to six, four and two TLS scans, respectively. The analysis of individual TLS scans is further distinguished in two groups: single centre scans and single corner scans. The single centre scans are placed approximately at the middle of a plot side, i.e. Scan 4 and Scan 14 in Figure 3. The single corner scans are placed at one of the corners of the plot, i.e. Scan 1, Scan 11, Scan 7 and Scan 17 in Figure 3.

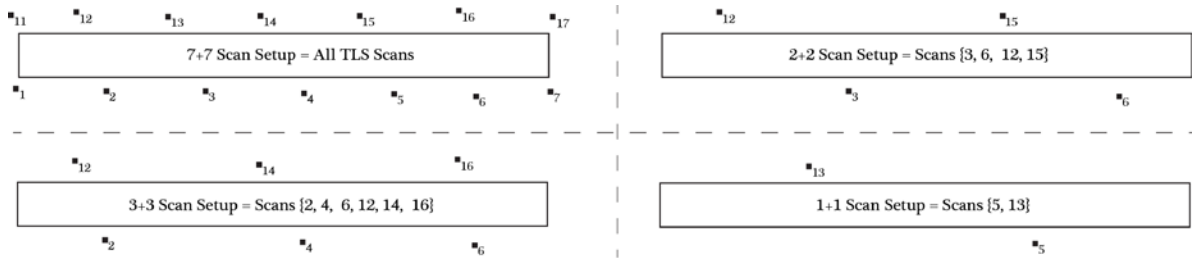


Figure 3. The analysed combinations of TLS scans, i.e. the scan setups

Each of the roughness spectra corresponding to the analysed scan setups is then compared with the 7+7 Scan Setup spectrum. The comparison was done by calculating the absolute spectral differences between these spectrum pairs. If the spectral differences are smaller than the dB threshold for all wavelengths, then the particular setup is considered to provide equally accurate roughness spectra as the 14 scan setup. In contrast, if a spectral difference exceeds the dB threshold, then the corresponding spatial wavelength ( $\lambda_{th}$ ) is reported.

### 3.2.3. Roughness Spectra and Multi-Scale LiDAR Data

The comparison of multiscale spectra is done in two steps. First, only the TLS and ULS spectra are compared as TLS has better resolution, whereas ULS has much larger coverage. The questions how two spectra fit to one another is analysed as in the previous cases, i.e. by employing the dB threshold on the absolute spectral difference and reporting  $\lambda_{th}$ . Then, the multi-scale spectra comparison is done for all the techniques. The LiDAR spectra (ALS, ULS and TLS) are plotted together with the DIM spectrum, and then it is analysed how they fit to one another. The observed differences and similarities of the spectrum shapes are interpreted (in the spatial domain) using the colour-coded DTM height maps. The LiDAR spectra used here refer to the same interpolation (the four point MP).

For the TLS and ULS spectra, their spectral slope values ( $\alpha_{TLS}$  and  $\alpha_{ULS}$ ) are additionally analysed. This parameter is the slope of the regression line fitted to a spectrum (given in the logarithmic scale) within a particular frequency band  $[1/\lambda_{n_1} \ 1/\lambda_{n_2}]$  [13]. The spectral slopes are calculated for a series of frequency bands where  $\lambda_{n_1}$  is fixed to the DC component ( $\lambda_{DC}$ ), whereas  $\lambda_{n_2}$  is constantly decreasing up to the Nyquist wavelength ( $n_2 = 1, \dots, N/2$ ). This results in a series of TLS and ULS-based spectral slopes  $\alpha_{TLS}(\lambda_{n_2})$  and  $\alpha_{ULS}(\lambda_{n_2})$ , each of them referring to a different lower wavelength  $\lambda_{n_2}$ . Finally, relative spectral differences are calculated from the corresponding ULS and TLS spectral slopes:  $\Delta\alpha(\lambda_{n_2}) = (\alpha_{ULS}(\lambda_{n_2}) - \alpha_{TLS}(\lambda_{n_2}))/\alpha_{TLS}(\lambda_{n_2})$ , where  $n_2 = 1, \dots, N/2$ . The value  $\Delta\alpha(\lambda_{n_2})$  shows how the TLS and ULS spectral slopes differ relatively from one another.

## 4. Results

### 4.1. Sensitivity on DTM Interpolation Method

Figure 4 compares the results when different interpolation methods (NN-, TIN- and four-neighbour MP) are used to interpolate TLS, ULS and ALS data. The columns from left to right in Figure 4 correspond to the three mentioned data sets, respectively. The top row shows the roughness spectra. The middle row shows spectral ranges calculated from NN-, TIN- and MP- spectrum. The bottom row shows the absolute spectral differences of the DIM spectrum to NN-, TIN- and MP-spectrum independently. For the simplicity of the figure, the DIM spectrum is plotted only once, in the figure with TLS spectra (Figure 4a).

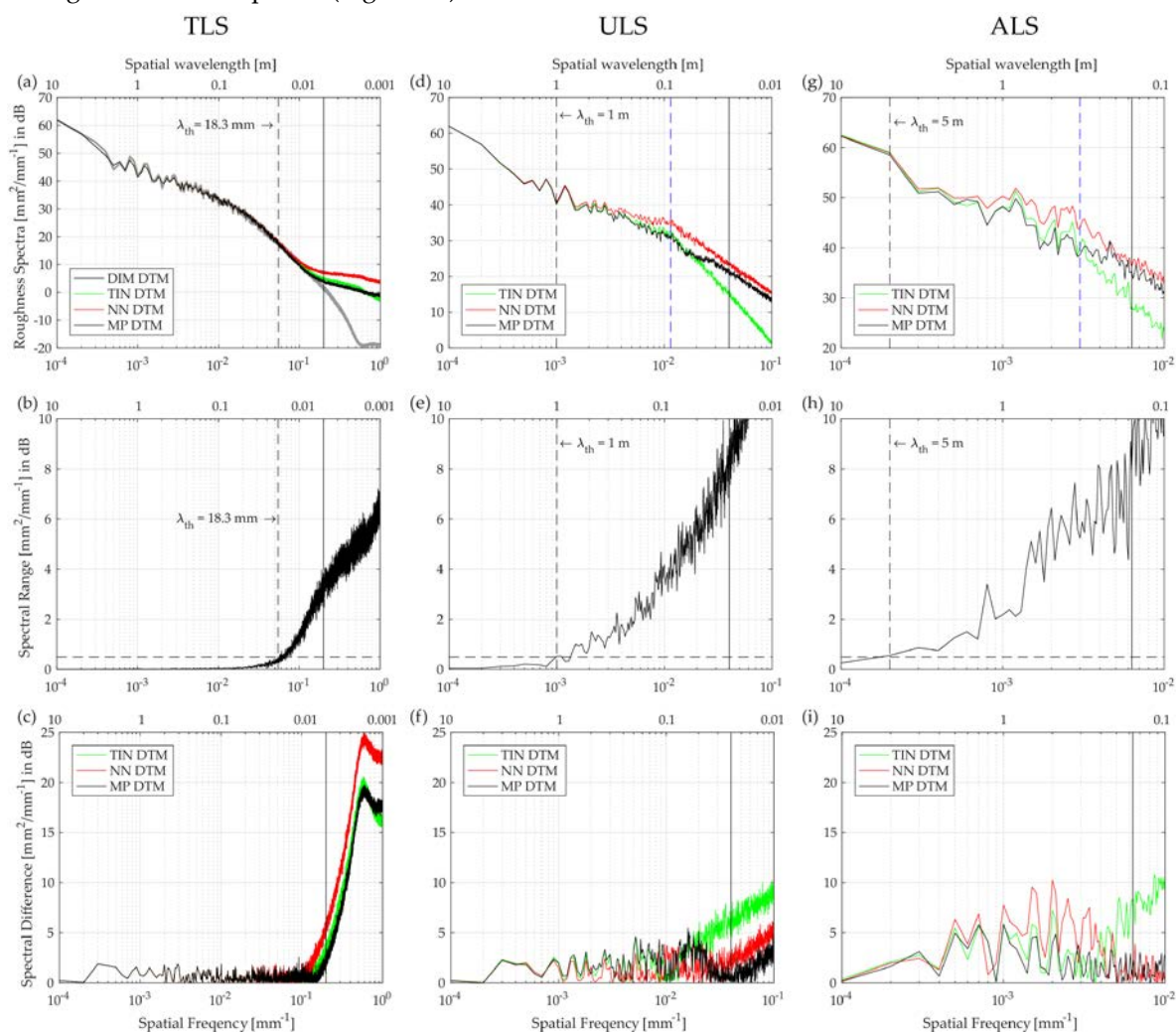


Figure 4. The influence of NN-, TIN and four points MP-interpolation on roughness spectra. The figures in columns (from left to right) refer to TLS, ULS and ALS data sets, respectively. The top-row plots show roughness spectra. The middle-row figures show the spectral ranges. The bottom-row plots show the absolute differences between the DIM spectrum and a LiDAR-based spectrum referring to each interpolation method, with the horizontal extent being adapted to the respective column. The vertical solid line shows the footprint wavelength.

Figure 4a compares the roughness spectra that refer to the TLS data. There, the NN-, TIN- and MP-spectrum visually agree with one another (and also with the DIM spectrum) for wavelengths larger than about 1 cm. As expected, the spectra depart from one another at smaller wavelengths. The analysis of the TLS spectral range (Figure 4b) shows that the dB threshold is actually exceeded at the wavelength of 18.3 mm. Therefore, for our TLS data, NN, TIN or MP interpolations do not affect the roughness spectra at wavelengths larger than 18.3 mm.

The same analyses for the ULS and ALS data (Figure 4d-e and Figure 4g-h) show that their spectral ranges exceed the dB threshold much earlier, at the wavelengths of 1 m and 5 m, respectively. This was expected as the ULS and ALS data are acquired at smaller measurement scales (coarser resolutions). For the ULS data, the NN, TIN or MP interpolations do not affect the roughness spectra at wavelengths larger than 1 m. However, for the ALS data, the selection of interpolation method is particularly important as it affects almost all wavelengths. It is only the DC component and the first harmonic that are not affected by the interpolation method. One reason why these two surface components are not affected could be that our plot length was too small for analysing the ALS data. Therefore, a longer plot should be considered to determine accurately the threshold wavelength for the ALS data.

Figure 4c shows the spectral differences of each TLS spectrum to the DIM spectrum. The spectral differences are the smallest for the MP TLS spectrum. The corresponding spectral differences of the ULS and ALS data are more complex, but generally, the differences of the MP spectra are again the smallest. This is particularly valid around the footprint wavelength (the vertical black solid lines). It is noted that these results refer to the MP interpolation when four neighbours are used. The analysis with a large number of neighbours was also done, and the results showed that the roughness spectra depart earlier (at larger wavelengths) compared to the four point MP. Thus, the four point MP interpolation was used in further analysis.

Table 2: A summary of the spectral range analysis based on the sensitivity on the basic interpolation methods (NN, TIN and MP). The dB threshold,  $\lambda_{th}$  and  $\Delta S$  are introduced in Section 3.2. The values in the  $\lambda_{\text{footprint}}$  column are spatial wavelengths that corresponds to the size of the laser footprint diameter, and in the  $\Delta S(\lambda_{\text{footprint}})$  column there are the spectral range values found at  $\lambda_{\text{footprint}}$ . The last two columns list the figures where the parameters are calculated and where they are later used.

Data	dB	$\lambda_{th}$	$\Delta S(\lambda_{th})$	$\lambda_{\text{footprint}}$	$\Delta S(\lambda_{\text{footprint}})$	Derived in	Used in
	Threshold						
	[dB]	[cm]	[dB]	[cm]	[dB]		
TLS	0.5	1.8	0.5	0.5	3.2	Figure 4b	Figure 6a; Figure 7a
ULS	0.5	100	0.5	2.5	8.5	Figure 4e	Figure 6a-c; Figure 7a
ALS	0.5	500	0.5	16	7.9	Figure 4h	Figure 7a

#### 4.2. Sensitivity on Number of TLS Scans

Figure 5 shows spectra that are derived from different combinations of TLS scans as explained in Section 3.2.2. The DIM spectrum is also plotted. The results show that the setups with multiple TLS scans and the single centre scans produce spectra that have very similar shape to both the 7+7 Scan setup spectrum and the DIM spectrum (Figure 5a-b). The spectra departure (visually) from one another at wavelengths smaller than 1 cm. However, the spectral differences exceed the dB threshold at larger wavelengths. It is only the 3+3 Scan Setup spectrum for which the threshold wavelength is 3.9 mm (Figure 5a). As this wavelength is smaller than the diffraction resolution limit of the TLS data (the vertical solid line at  $\lambda=5$  mm), it can be concluded that the 3+3 spectrum is equally accurate as the 7+7 spectrum. Figure 5a also shows that the 2+2 and 1+1 spectra are equally accurate as the 7+7 spectra for wavelengths larger than about 4 cm (the blue and green vertical dashed lines in Figure 5a, respectively). The same is true for each of the two Single Scan Centre spectra, but only for wavelengths larger than about 5 cm. However, these four spectra exceed the threshold only locally and with  $\max(\Delta S_n)$  being 0.65 dB, which is just slightly above the dB threshold. These small differences are not visible in Figure 5a-b, and thus our reported threshold wavelengths should be rather considered as a conservative estimate.

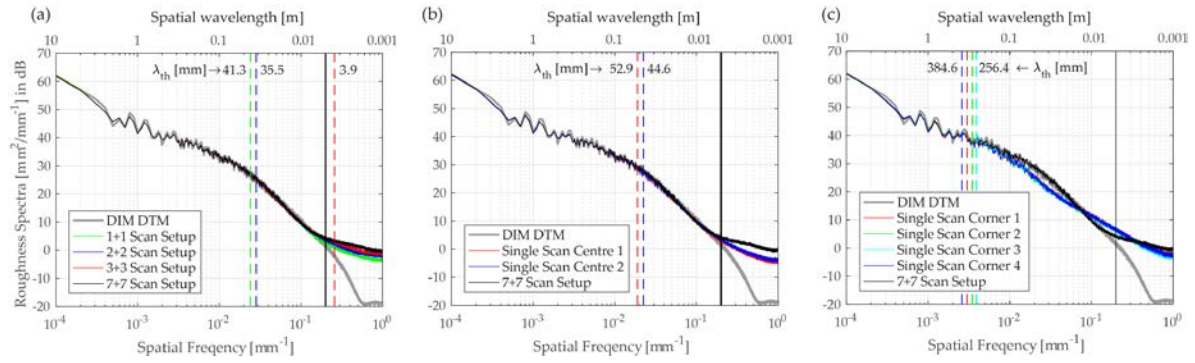


Figure 5. Influence of the number of TLS scans on roughness spectra; (a) Measurement setups when TLS scans are distributed on both sides of the plot; (b) Measurement setups with a single scan placed at the middle of one of the log plot sides; (c) Measurement setups with a single scan placed at one of the plot corners. The vertical solid line shows the footprint wavelength. For comparison, the spectra for the 7+7 Scan Setup and the DIM DTM are also shown.

The shape of the Single Scan Corner spectra (Figure 5c) notably deviate from the 7+7 spectrum compared to the Single Scan Centre spectra (Figure 5b). Their threshold wavelengths are one order of magnitude larger than the ones corresponding to the other scan setups. More precisely, for wavelengths larger than 4 dm, the spectrum derived from any single scan taken from the corner of the plot is equally accurate as the 7+7 spectrum. However, as this scan is taken from the corner of a 10 m plot, it can also be considered as a scan taken from the middle of a 20 m long plot. Therefore, based on the results presented in Figure 5b and Figure 5c, the following statements can be drawn:

- a single TLS scan can measure roughness spectra at wavelength scales of either 4 dm to 20 m or 5 cm to 10 m, with a maximum spectral difference less than 0.5 dB (the dB threshold value).
- a single TLS scan can measure roughness spectra at wavelength scales of 1 cm to 10 m (two orders of magnitude), but with a maximal difference less than 0.65 dB (the value of  $\max(\Delta S_n)$  in this frequency band, Figure 5b and Table 3)

The above statements are valid when TLS is applied from high tripods. It is expected that TLS from classical geodetic tripods is more sensitive because of larger occlusion effects. However, this is to be analysed in further studies.

It should also be noted that the spectral slope derived from the corner scans already deviates for wavelengths of a few dm and smaller. For the central scans and other setups the spectral slope is different only at sub cm wavelengths.

Table 3: A summary of the spectral range analyses based on the sensitivity of the number of TLS scans. The spectral differences ( $\Delta S$ ) are calculated relative to the 7+7 TLS spectrum (i.e. when all 14 scans are used). The dB Threshold,  $\lambda_{th}$  and  $\Delta S$  are introduced in Section 3.2. The values in the  $\Delta S(\lambda_{th})$  column are  $\Delta S$  values found at the wavelength  $\lambda_{th}$ . The values in the column are  $\lambda_{\Delta S > 0.65 \text{ dB}}$  spatial wavelengths where  $\Delta S$  exceeds 0.65 dB. The latter dB value is rounded  $\max[\Delta S(\lambda_{th})]$ , which is introduced to show that the Single Scans Centre spectra, 2+2 spectra and 1+1 spectra just slightly violate the dB threshold (0.5 dB) i.e. only around  $\lambda_{th}$  wavelengths.

Setup	Number of Scans	dB Threshold [dB]	$\lambda_{th}$ [cm]	$\Delta S(\lambda_{th})$ [dB]	$\lambda_{\Delta S > 0.65 \text{ dB}}$ [cm]	Derived in
3+3 Scan setup	6	0.5	0.4	0.5	0.3	Figure 5a
2+2 Scan Setup	4	0.5	3.6	0.57	0.5	Figure 5a
1+1 Scan Setup	2	0.5	4.1	0.62	0.8	Figure 5a
Single Scan Centre 1	1	0.5	5.3	0.61	0.6	Figure 5b
Single Scan Centre 2	1	0.5	4.5	0.58	0.5	Figure 5b

#### 4.3. Comparison of TLS and ULS Roughness Spectra

Figure 6a shows the TLS and ULS spectra. Both spectra end at the wavelength that corresponds to the TLS and ULS footprint diameter, i.e. 25 mm and 5 mm, respectively. The corresponding grey rectangles visualize the frequency band where the DTM interpolation influences the shape of the spectra (the  $\lambda_{th}$  and  $\lambda_{footprint}$  values reported in Table 2, Section 4.1). It can be seen that these rectangles (frequency bands) do not overlap, which means that the DTM interpolation does not affect the TLS spectrum in the ULS interpolation uncertainty band. Thus, the TLS spectrum can serve as the reference for the ULS spectrum on this frequency band. Figure 6b shows the absolute difference between the TLS and ULS spectra (the black line). The differences exceed the dB threshold at the wavelength of about 116 mm, which is almost five times the ULS footprint. The differences at wavelengths larger than this  $\lambda_{th}$  are almost linear as shown by their general trend (the red line representing a 20 sample running mean). The differences at wavelengths smaller than this  $\lambda_{th}$  are more complex, but still below 0.8 dB.

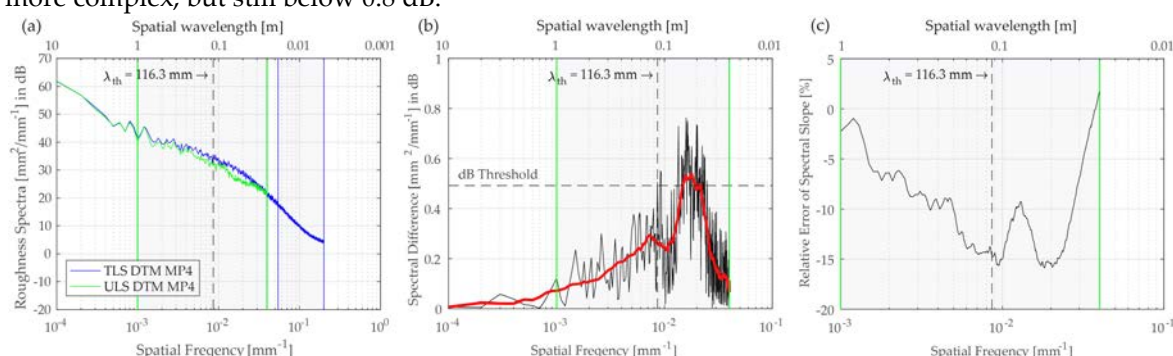


Figure 6. Comparison of TLS and ULS spectra.

Similar conclusions can be drawn from the relative differences  $\Delta\alpha$  between ULS and TLS spectral slopes (Figure 6c). Starting from a wavelength of 1 m, the slope difference constantly increases and reaches a maximum of -15 % around  $\lambda_{th}$ . However, for wavelengths smaller than  $\lambda_{th}$ , the slope differences erroneously decrease and eventually change their sign. One reason for this different behaviour of the ULS spectrum for wavelengths larger and smaller than  $\lambda_{th}$  is that the ULS data have less overlapping footprints. A deeper investigation of this behaviour, however, requires further experimentation.

#### 4.4. Multi-Scale Spectra and DTMs

Figure 7a shows all the LiDAR spectra together with the DIM spectrum. As in Figure 5a, the LiDAR spectra end at the wavelengths that corresponds to their footprint diameter (the  $\lambda_{footprint}$  values in Table 2), and the grey rectangles show the frequency bands affected by the DTM interpolation (the  $\lambda_{th}$  values in Table 2). It is only for the TLS spectrum that the frequency band is shown differently. The vertical, dashed blue line marks  $\lambda_{th}$  as reported in Table 2 (1.8 cm, the influence of interpolation method), whereas the longer wavelength of the grey rectangle (the left, vertical full blue line), refers to a wavelength where the TLS and DIM spectra difference exceeds the dB threshold. This wavelength is just slightly smaller than 1 cm, which is about two times the TLS footprint. Therefore, our DIM spectrum and MP4 TLS spectrum can be used interchangeably for wavelengths larger than 1 cm. For wavelengths smaller than 1 cm, the difference between the TLS and the DIM spectrum increases linearly.

Figure 7a also shows that the interpolation uncertainty bands of the ALS and ULS spectra overlap. This means that the ULS spectrum can serve as the reference for the ALS spectrum, but only in the non-overlapping frequency part, i.e. for wavelengths larger than 1 m. Around this wavelength, the ALS spectrum differs the most from the other spectra (Figure 7a). These modulations at the wavelengths around 1 m and larger are also visible in the spatial domain, when the color-coded DTM heights are compared (Figure 7b-e). This visualization of the DTMs shows that the global

microtopography pattern of the plot is similar for the DIM, TLS and ULS DTMs, whereas for the ALS DTM, this pattern is distorted.

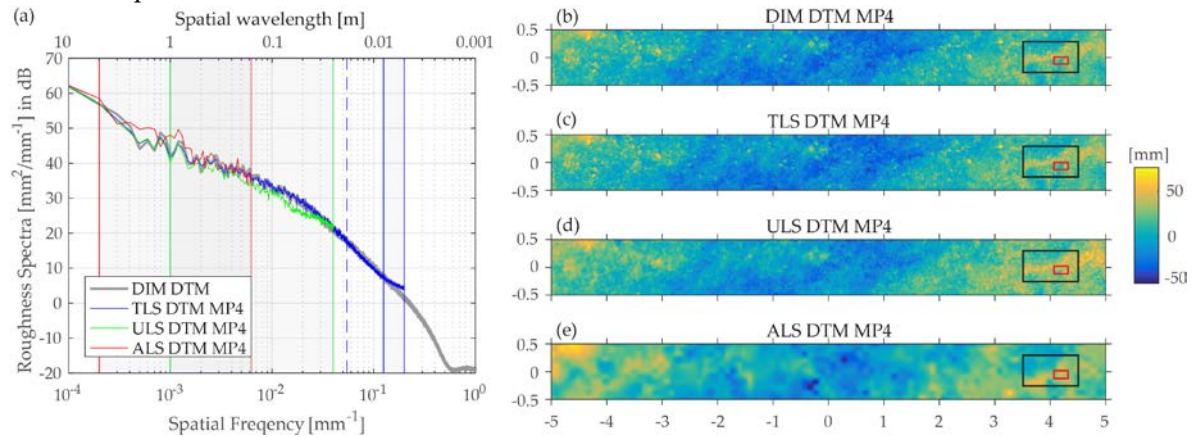


Figure 7. The spectra from the multi-scale data and the color-coded height values of the corresponding DTMs. The black and red rectangles in the DTMs mark the sub areas shown in the following figure.

The ULS spectrum differs the most from the TLS and DIM spectra at a different scale, namely at wavelengths of a few dm. Figure 8a-d renders the DTMs within the area marked by the black rectangles in Figure 7b-e to emphasize better the microtopography components of dm wavelengths. For the TLS and DIM DTMs, this microtopography pattern appears very similar at this scale. For the ULS DTM, the pattern is slightly distorted. For ALS DTM, however, the pattern is severely distorted at the scale of “few dm”, which is expected as its footprint size is of the same order of magnitude. Finally, Figure 8e-g renders the DTMs from the area marked by the red rectangles in Figure 7b-e to emphasize the differences at cm to mm wavelengths. Here, the ULS DTM shows severely deformed microtopography pattern compared to the TLS and DIM DTMs, which is again expected as the ULS footprint is larger than this scale. However, at this scale, also the differences between the TLS and DIM DEMs become visible. An example is a tiny branch (marked with the black arrow) that is still visible in the DIM DTM and in a nadir image of this area (Figure 8e and Figure 8h, respectively), whereas this element is not visible in the TLS DTM (Figure 8f). These mm-scale differences between the TLS and DIM DEMs are also reflected in the corresponding spectra which start to depart from one another at wavelengths smaller than 1 cm (Figure 7a).

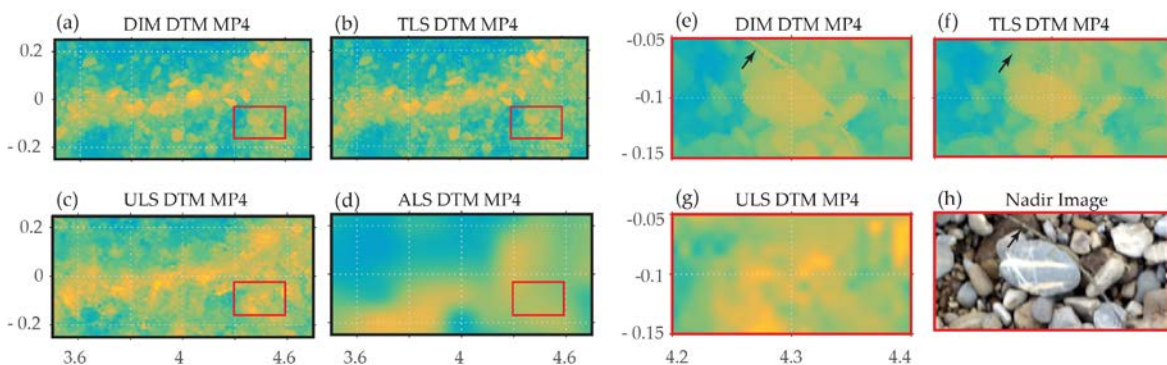


Figure 8. Color-coded height visualization of the DIM-, TLS-, ULS and ALS-DTM in the zoom-in areas marked in Figure 7.

## 5. Discussion

### 5.1.1. Spectral Analysis

Investigating the roughness spectra is a method to analyse DTMs. It gives consistent results for the TLS data in the analysis of the scan setup and quantifies the loss of information when reducing the number of scans. Also, in the extreme case of using only one scan on the edge of the plot, the loss

of quality is quantified. Likewise, the wavelength at which the spectra deviate significantly from each other due to different interpolation methods provides insight on the relevance of the choice of a certain method. The analysis of the spectra for different interpolation methods from LiDAR data at all investigated scales also allowed the conclusion that the four point moving plane interpolation, which involves smoothing, is to be preferred over NN and TIN interpolation. Finally, the analysis of the difference to a reference spectrum provides a measure that concentrates on the resolution and damping of amplitudes of a specific DTM. This is additional information compared to other methods of DTM analysis such as the DEM of Differences (DoD), or the measures of the distribution of vertical height differences (mean, standard deviation, etc.).

### 5.1.2. The dB Threshold

In this paper, the dB threshold that corresponds to the 95 % confidence interval of the ensemble-wise averaged periodogram is used to determine the wavelengths over which the spectra can be used interchangeably. For our data, this dB threshold was 0.5 dB, which is a rather strict threshold value compared to other studies. For example, in an application of roughness spectra for microwave backscatter models, a spectra difference threshold of 2 dB was acceptable [36]. Then, in a sea floor roughness application, the spectra differences were analysed using a threshold of 1 dB [19]. Therefore, the  $\lambda_{th}$  values reported in this paper should be considered as rather conservative estimates.

A dB threshold that is tailored to a particular application would exactly define requirements for the LiDAR measurements and the roughness spectrum calculation, but only for this particular application. A threshold based on the confidence interval of the roughness spectrum has the advantage of being application independent, and furthermore, it accounts for the variance of the ensemble-wise averaged spectrum.

### 5.1.3. ALS and ULS Data

Comparison of multi-scale LiDAR data is always challenging as such measurements involve many setup parameters. Our TLS data, for example, were optimal for the analysis as the plot was oversampled by a large number of scans, and by scanning in the correlated sampling mode, i.e. with highly overlapping footprints within a single scan. This then allowed for optimizing the TLS setup for the roughness spectrum calculation. On the other hand, ALS and ULS did not offer an as extensive sampling of the plot as in the TLS case. Therefore, to optimize the ALS and ULS setups for roughness spectra calculation, it would be important to acquire ALS and ULS data that have both highly overlapping footprints within the scan line and a large number of scans (strips) that cover the plot.

We have the hypothesis that an extensive sampling of the plot with ALS and ULS would certainly result in more optimistic  $\lambda_{th}$  values than the ones reported here for the ULS and ALS data. For example, in Figure 3, the spectral range value  $\Delta S_{fp}$  at the footprint wavelength is almost 8 dB for ALS and ULS data, whereas for TLS data, this value is about 3 dB. This shows that the ULS and ALS spectra are more sensitive to the interpolation method than the TLS spectra. One reason for this could be a lower footprint overlap of ULS and ALS data compared to the TLS data. It would be interesting to see, for example, if both  $\Delta S_{fp}$  and  $\lambda_{th}$  values would be smaller than the values reported in Section 4.1 when derived from ULS and ALS data with highly overlapping footprints. In addition, it would be interesting to see if the complex differences observed between the TLS and ULS spectra (Figure 6b) could become linear, like the differences observed between the TLS and DIM spectra (the grey rectangle with blue edges, Figure 7a). Highly overlapping footprints correspond to an extremely dense sampling of surface heights, and thus, roughness spectra will be less affected by the interpolation method. This means that the agreement between TLS and ULS spectra can be expected to improve even to sub dm wavelengths, e.g., when the sampling distance of ULS points is notably smaller than the ULS footprint diameter. Having further in mind that our dB threshold is rather strict compared to other publications, it can be concluded that ULS data has a high potential to replace TLS data for roughness spectrum calculation in many applications. This should be, however, shown in further experiments.

#### 5.1.4. Limitations and Suggested Further Experiments

The idea behind this work was to initiate the quality analysis of roughness spectrum calculation from LiDAR data. The outcome, indeed, provided valuable conclusions on the TLS setup and the comparison of TLS, ULS and ALS spectra (the range of their interchangeability). However, the experiment also revealed that both the experimental setup and the roughness spectra analysis can be improved in further studies.

One way to extend the analysis of roughness spectra could be, e.g., by propagating them further through geophysical models and analysing how the model predictions are sensitive to changes in the roughness spectrum. This analysis would help in defining better dB thresholds for particular applications. Then, further analysis could consider more complex interpolation methods, such as Kriging. As Section 4.3 showed, the TLS spectrum can be used as the reference in optimizing the interpolation parameters for ULS data, e.g. by minimizing the differences between the ULS- and TLS-spectrum at wavelengths smaller than 1 m. Similarly, the ULS spectrum can then be used as the reference to optimize the interpolation parameters for ALS data.

Such an analysis would also require improvements in the experimental setup and data acquisition. For example, the plot size should be much longer than 10 m for analysing the ALS spectra. A plot size of 100 m, for example, would be feasible for TLS, as it can be surveyed with 10 TLS scans (according to the conclusions from Section 4.2). ULS and ALS data should be acquired with a point spacing (both within and between the scan lines) notably smaller than their footprint diameters (the correlated scanning [23]). This means that the plot should be scanned from a large number of overlapping strips (flight lines). Such data would allow for the optimisation of ALS and ULS setups for roughness spectrum calculation as was done here for our TLS data.

## 6. Conclusions

In this paper we used TLS, ULS and ALS point clouds of a 1 m x10 m gravel plot to derive and analyse roughness spectra from interpolated DTMs. The TLS, ULS and ALS spectra are calculated as the ensemble-wise averaged periodograms. The spectral comparison is done using the dB threshold that is based on the 95 % confidence interval of the ensemble-wise averaged periodograms. The aim was to determine the scales (spatial wavelengths) over which the spectra can be used interchangeably. Furthermore, the extensive sampling of the plot with TLS allowed to optimize the TLS measurement setup for roughness spectra calculation.

The analysis showed that one TLS scan can be used to measure 10 m long plots and derive roughness spectra that are reliable for wavelengths larger than 5 cm (*ten times the TLS footprint size*). One TLS scan can also measure 20 m long plots, but then the roughness spectrum is only reliable for wavelengths larger than 4 dm. At this wavelength, the spectral differences (deformations) remain below the derived dB threshold (0.5 dB). However, one TLS scan can also measure roughness spectra over 1 cm (*two times the TLS footprint size*) to 10 m wavelengths, but with spectral differences reaching up to 0.65 dB (thus slightly violating the threshold based on the 95 % confidence interval).

The results also showed that a TLS setup with six scans (three per each longer plot side) provides equally accurate roughness spectra as any other setup that includes more than six TLS scans. Furthermore, it was shown that the TLS spectrum (based on all the scans) is not affected by basic interpolation methods (nearest neighbour, TIN or moving planes) at wavelengths larger than about 2 cm (*four times the TLS footprint size*). Finally, the comparison of TLS and DIM spectra showed that they agree well to one another for wavelengths larger than 1 cm (*two times the TLS footprint size*). These conclusions refer to a TLS scanning performed from large tripods (scan heights of about 2.5 m) and in the correlated sampling mode, i.e. overlapping footprints within a single scan.

The comparison of the ULS and TLS spectra showed that they agreed well to one another for wavelengths larger than about 1.2 dm (*about five times the ULS footprint size*). At these wavelengths, the ULS spectral slope overestimates the TLS spectral slope by about 15 %, although the spectral difference is below 0.5 dB. The results also showed that the ULS spectrum is not affected by the choice of interpolation method at wavelengths larger than about 1 m. Therefore, the optimisation of the interpolation parameters is required to get accurate ULS spectra at wavelengths smaller than 1 m.

The plot size was too small to derive more conclusions about the ALS spectrum. However, the analysis showed that only the DC component and the first harmonic (5 m wavelength) of the ALS spectrum are not affected by the interpolation methods.

The above results refer to the dB threshold that is strict compared to the dB thresholds used in other applications (e.g. 1 dB or 2 dB in sea floor roughness and microwave backscatter modelling, respectively). Thus, the above conclusions are rather conservative, and show that ULS data has high potential to replace TLS data for roughness spectra calculation in many applications. However, this has to be analysed in detail in further studies.

**Acknowledgments:** The authors would like to thank Livia Piermattei and Martin Wieser for their help in collecting the field data. The authors would also like to thank the company RIEGL, Laser Measurement Systems GmbH, for providing the ULS and ALS data for this study. In this work, a free MATLAB function *las2mat* is used to read las-formatted point clouds [37].

The research leading to these results has received funding from the European Community's Seventh Framework Programme ([FP7/2007–2013]) under the Advanced\_SAR project (grant agreement no. 606971).

**Author Contributions:** Milutin Milenković and Norbert Pfeifer conceived and designed the experiment; Milutin Milenković designed and carried out close range measurements (TLS scanning and image acquisition), processed and analysed the data, interpreted results and wrote the paper; Camillo Ressler supervised the data processing and contributed in interpreting results, reviewing and commenting the manuscript; Wilfried Karel contributed in interpreting results, reviewing and commenting the manuscript; Gottfried Mandlbürger organized the ALS and ULS measurements, contributed in interpreting results, reviewing and commenting the manuscript; Norbert Pfeifer supervised data processing and the analysis, contributed in writing the discussion section, interpreting results, reviewing and commenting the manuscript.

**Conflicts of Interest:** The authors declare no conflict of interest.

## References

1. Hodge, R., J. Brasington, and K. Richards, *In situ characterization of grain-scale fluvial morphology using Terrestrial Laser Scanning*. Earth Surface Processes and Landforms, 2009. **34**(7): p. 954–968.
2. Martinez-Agirre, A., et al., *Influence of Surface Roughness Measurement Scale on Radar Backscattering in Different Agricultural Soils*. IEEE Transactions on Geoscience and Remote Sensing, 2017. **55**(10): p. 5925–5936.
3. Milenković, M., N. Pfeifer, and P. Glira, *Applying Terrestrial Laser Scanning for Soil Surface Roughness Assessment*. Remote Sensing, 2015. **7**(2): p. 2007–2045.
4. Alho, P., et al., *Application of boat-based laser scanning for river survey*. Earth Surface Processes and Landforms, 2009. **34**(13): p. 1831–1838.
5. Brasington, J., D. Vericat, and I. Rychkov, *Modeling river bed morphology, roughness, and surface sedimentology using high resolution terrestrial laser scanning*. Water Resources Research, 2012. **48**(11): p. n/a–n/a.
6. Hohenthal, J., et al., *Laser scanning applications in fluvial studies*. Progress in Physical Geography, 2011. **35**(6): p. 782–809.
7. Korzeniowska, K., N. Pfeifer, and S. Landtwing, *Mapping gullies, dunes, lava fields, and landslides via surface roughness*. Geomorphology, 2018. **301**(Supplement C): p. 53–67.
8. Perron, J.T., J.W. Kirchner, and W.E. Dietrich, *Spectral signatures of characteristic spatial scales and nonfractal structure in landscapes*. Journal of Geophysical Research: Earth Surface, 2008. **113**(F4): p. n/a–n/a.
9. Tarolli, P., *High-resolution topography for understanding Earth surface processes: Opportunities and challenges*. Geomorphology, 2014. **216**(Supplement C): p. 295–312.
10. Shepard, M.K., et al., *The roughness of natural terrain: A planetary and remote sensing perspective*. Journal of Geophysical Research: Planets, 2001. **106**(E12): p. 32777–32795.
11. Smith, M.W., *Roughness in the Earth Sciences*. Earth-Science Reviews, 2014. **136**: p. 202–225.

12. Snapir, B., S. Hobbs, and T.W. Waine, *Roughness measurements over an agricultural soil surface with Structure from Motion*. ISPRS Journal of Photogrammetry and Remote Sensing, 2014. **96**: p. 210-223.
13. Austin, R.T., A.W. England, and G.H. Wakefield, *Special problems in the estimation of power-law spectra as applied to topographical modeling*. IEEE Transactions on Geoscience and Remote Sensing, 1994. **32**(4): p. 928-939.
14. Hegge, B.J. and G. Masselink, *Spectral Analysis Of Geomorphic Time Series: Auto-Spectrum*. Earth Surface Processes and Landforms, 1996. **21**(11): p. 1021-1040.
15. Ulaby, F.T., R.K. Moore, and A.K. Fung, *Microwave remote sensing: active and passive. Volume II. Radar remote sensing and surface scattering and emission theory*. Microwave remote sensing: active and passive. Volume II. Radar remote sensing and surface scattering and emission theory. Vol. II. 1982: Addison-Wesley, Reading, Mass; Remote Sensing Series 3.
16. Pelletier, J.D. and J.P. Field, *Predicting the roughness length of turbulent flows over landscapes with multi-scale microtopography*. Earth Surf. Dynam., 2016. **4**(2): p. 391-405.
17. Aberle, J., et al., *Statistical characterization of bed roughness due to bed forms: A field study in the Elbe River at Aken, Germany*. Water Resources Research, 2010. **46**(3): p. n/a-n/a.
18. Singh, A., F. Porté-Agel, and E. Fofoula-Georgiou, *On the influence of gravel bed dynamics on velocity power spectra*. Water Resources Research, 2010. **46**(4): p. n/a-n/a.
19. Wang, C.-C., D.-j. Tang, and T. Hefner, *Design, Calibration and Application of a Seafloor Laser Scanner*, in *Laser Scanning, Theory and Applications*, C.-C. Wang, Editor. 2011, InTech. p. 495-522.
20. Glira, P., N. Pfeifer, and G. Mandlbürger, *Rigorous Strip Adjustment of UAV-based Laserscanning Data Including Time-Dependent Correction of Trajectory Errors*. Photogrammetric Engineering and Remote Sensing, 2016. **82**(12): p. 945-954.
21. Mandlbürger, G., et al. *Complementing airborne laser bathymetry with UAV-based lidar for capturing alluvial landscapes*. 2015.
22. Pfennigbauer, M. and A. Ullrich. *Improving quality of laser scanning data acquisition through calibrated amplitude and pulse deviation measurement*. in *Laser Radar Technology and Applications XV*. 2010. Orlando, Florida, United States: Proc. SPIE.
23. Lichti, D.D. and S. Jantso, *Angular resolution of terrestrial laser scanners*. Photogrammetric Record, 2006. **21**(114): p. 141-160.
24. Langer, D., et al., *Imaging Ladar for 3-D Surveying and CAD Modeling of Real-World Environments*. The International Journal of Robotics Research, 2000. **19**(11): p. 1075-1088.
25. Z+F, *Z+F LaserControl Professional PLUS: User Manual, Version 8.6*. 2015, Zoller + Fröhlich GmbH, [www.zf-laser.com](http://www.zf-laser.com): 88239 Wangen im Allgäu, Germany.
26. Z+F. *Z+F IMAGER® 5010C, 3D Laser Scanner: Data sheet*. 2017 [cited 2017 24.10.2017]; Available from: [http://www.zf-laser.com/fileadmin/editor/Datenblaetter/Z\\_F\\_IMAGER\\_5010C\\_Datasheet\\_E.pdf](http://www.zf-laser.com/fileadmin/editor/Datenblaetter/Z_F_IMAGER_5010C_Datasheet_E.pdf).
27. Pix4Dv2.0, *Pix4Dmapper 2.0 - Software Manual*. 2016, [www.pix4d.com](http://www.pix4d.com): 1015 Lausanne, Switzerland.
28. Rothermel, M., et al. *Sure: Photogrammetric surface reconstruction from imagery*. in *LC3D Workshop, December 2012*. 2012. Berlin.
29. Pfeifer, N., et al., *OPALS – A framework for Airborne Laser Scanning data analysis*. Computers, Environment and Urban Systems, 2014. **45**: p. 125-136.
30. Lancaster, P. and K. Šalkauskas, *Curve and surface fitting : an introduction*. 1986, London [u.a.]: London [u.a.] : Acad. Press.
31. Dierking, W., *Quantitative roughness characterization of geological surfaces and implications for radar signature analysis*. Ieee Transactions on Geoscience and Remote Sensing, 1999. **37**(5): p. 2397-2412.

32. MATLAB, *Signal Processing Toolbox: Release Notes (R2016b)*. 2016, The MathWorks.
33. Press, W.H., et al., *Numerical recipes in C: the art of scientific computing*. 2nd ed. 1992, New York, NY, USA: Cambridge University Press. 994.
34. Harris, F.J., *On the use of windows for harmonic analysis with the discrete Fourier transform*. Proceedings of the IEEE, 1978. **66**(1): p. 51-83.
35. Brown, S.R. and C.H. Scholz, *Broad bandwidth study of the topography of natural rock surfaces*. Journal of Geophysical Research: Solid Earth, 1985. **90**(B14): p. 12575-12582.
36. Yisok, O. and K. Young Chul, *Condition for precise measurement of soil surface roughness*. IEEE Transactions on Geoscience and Remote Sensing, 1998. **36**(2): p. 691-695.
37. Litkey, P. and E. Puttonen, *Matlas tools Toolbox: A mex Gateway for Utilizing lastools Read and Write Functions in Matlab*. 2014, Finnish Geodetic Institute: FI-02430 Masala, Finland.



© 2017 by the authors. Submitted for possible open access publication under the terms and conditions of the Creative Commons Attribution (CC BY) license (<http://creativecommons.org/licenses/by/4.0/>).

## 4 Discussion

Most of the particular aspects are already discussed within the studies (papers) presented in the previous section. Therefore, the focus here is on a more general discussion. First, each of the particular parametrisation (surface roughness, 3D shoot model and the canopy transmittance) is separately discussed with respect to the following aspects: current open questions and possible solutions, possibilities for upscaling and their further applications. The last subsection here discusses the three different description approaches exercised in this work (geometric-stochastic, geometric-deterministic and geometric-radiometric descriptions) and presents certain observations drawn from the studies.

### 4.1 Surface Roughness

#### 4.1.1 Standardization of Roughness Parametrisation

In this work, different measurement techniques are applied and analysed for roughness assessment. Therefore, one practical question is how to standardize roughness results that are derived from different measurement techniques. Shepard et al. (2001) recognized this problem very early and suggested to standardize (a) the data processing methodology (i.e. certain processing steps such as detrending, filtering and intervening) and (b) a list of the important parameters to report (e.g. RMS<sub>h</sub>, Hurst exponent, RMS deviation, etc.). The standardization is then exercised in the same study on traditional roughness measurements such as mechanical profilers, helicopter-borne stereophotography, differential GPS and profiling with a levelling instrument and a measurement tape). Jester and Klik (2005) compared roller chain, pin meter, portable laser scanner and close-range stereophotography for soil roughness assessment. Their analysis showed that each measurement technique has its field of application. Furthermore, they observed that some measurement techniques, such as stereophotogrammetry, require expert knowledge in order to avoid measurement errors in the resulting DSM. The roughness standardisation is also a subject in more recent studies. Smith (2014) suggested the standardization of the roughness definition, terminology and the measurement scale in the characterization of roughness in Earth science. Martinez-Agirre et al. (2016) analysed cross-correlation of 21 roughness parameter derived for different soil roughness types, and suggested just two of them (the limiting elevation difference and the mean upslope depression index) to be used for differencing among the soil roughness types.

The results of this dissertation directly contribute to the roughness standardization topic. In Paper II, Paper III and Paper VI, it was shown that each measurement technique has their roughness spectra accurate only in a particular frequency band and that some of these bands are overlapping one another. When parameters such as spectral slope or RMS<sub>h</sub> are derived in the overlapping frequency band, then their values are also independent of the measurement technique used. However, one open question is *how to compare roughness parameters derived from the non-overlapping frequency band*. Another related question is how to quantify the differences (modulations) of roughness spectra in the non-overlapping band?

One method for this problem can be to estimate the transfer function (the frequency response and filter kernel functions) between two spectra. The frequency response  $H(j2\pi f)$  is a complex

function that defines how the magnitudes and phases of a so-called input spectrum (X) need to be modulated to produce the magnitudes and phases of an output spectrum (Y), in a linear shift-invariant system. The magnitude modulation, i.e. gain  $G(f)$ , is the ratio of individual magnitudes of the two spectra, as a function of the frequency  $f$  (Ingle and Proakis 1997, p53-60):

$$G^2(f) = \frac{S_{yy}(f)}{S_{xx}(f)}, \quad (2)$$

where  $S_{yy}(f)$  and  $S_{xx}(f)$  are the power spectral densities (squared magnitudes) of the output and input spectra, respectively. The inverse Fourier transform of the frequency response  $H(j2\pi f)$  gives the corresponding filter kernel in the spatial domain. The output signal can then be calculated as the convolution of the input signal with the kernel function. In optical imaging, for example, the filter kernel corresponds to the point spread function and its Fourier transform gives the optical transfer function (Fiete 2010, p62).

Figure 4 shows how a filter kernel and its gain function looks like when estimated using the ensemble averaged spectra of a TLS DEM and a DIM DEM. The TLS DEM has lower resolution compared to the DIM DEM as its magnitudes are modulated at wavelengths smaller than about 1 cm (Figure 4c). Furthermore, this modulation is linear up to 5 mm wavelength, which was the diameter of the laser footprint. Figure 4b shows the empirical gain function (blue line) derived for the two spectra, and Figure 4a shows the corresponding empirical filter kernel (the blue dots) derived as the inverse Fourier transform of the frequency response function. Finally, the empirical filter kernel is approximated by a Gaussian function (the red lines in Figure 4a-b) with a standard deviation of 8.7 samples (4.4 mm), whereas the amplitude was 0.07 (the area below the Gaussian is 1).

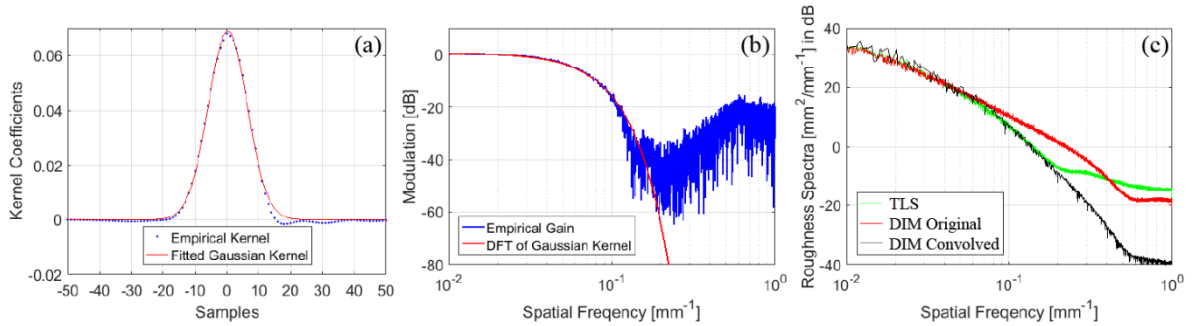


Figure 4: Estimation of the filter kernel: (a) the empirical filter kernel and its Gaussian approximation, (b) empirical gain function (the magnitude modulation) and its Gaussian approximation and (c) The original TLS and DIM spectra and the spectra from the DIM DEM convolved with the Gaussian kernel.

The above example shows that linear spectral differences can be quantified by a Gaussian kernel in the spatial domain. Therefore, the high-resolution DIM DEM can be convolved with such a kernel to get a smoothed DEM from which a TLS spectrum can be simulated. As shown in Figure 4c, this simulated TLS spectrum (the black line) approximates well the original TLS spectrum (the green line) in the frequency band of linear spectral differences (5 mm – 1 cm wavelengths). Therefore, the filter kernel gives a theoretical framework for standardizing the roughness parameters derived from a roughness spectrum. This concept should be explored and proofed in further roughness spectra studies.

#### 4.1.2 Surface Roughness Reference

Introducing an absolute reference for roughness measurements and derived parameters is a challenging task. In studies where old measurements techniques are replaced with new ones this

is not the problem, as the old technique can serve as a relative reference to the new one. This relative comparison is important for transferability of old results. For example, Mattia et al. (2003) analysed the differences in roughness indices derived from a mechanical and laser profilometers, and Alex Martinez-Agirre et al. (2018) analysed the differences between laser profilometers and point clouds derived from TLS and DIM of close-range images.

In this dissertation, only new measurement technologies are analysed, and the relative reference is always derived by using a dataset with the highest spatial resolution. For example, in Paper II, the triangulating laser scanner is used as the relative reference for TLS. This triangulating scanner has a GSD of about 0.7 mm, which is about five times smaller than the TLS footprint diameter in this study (4 mm). Then, in Paper VI, the DIM DEM was used as the relative reference for TLS. The DIM DEM was derived using handheld images with a GSD of 0.5 mm, which was ten times smaller than the TLS footprint diameter in this study (5 mm). Within the same study and for optimizing the number of TLS scans, a point cloud of 14 merged TLS scans was used as the reference for TLS setups using a smaller number of scans. Paper VI also showed that TLS can serve as the reference for ULS- or ALS-spectrum, and that ULS-spectrum can serve as the reference for ALS spectrum. This shows that the selection of relative reference depends also on the question analysed.

The results of this dissertation also show that there is no single measurement technique that can serve as the relative reference for both low- and high-frequency surface components. For *high-frequency surface components* (wavelengths  $< \sim 1$  m), DIM of close-range images can be used as the relative reference for laser scanning data. However, it is strongly recommended that the GSD of the images is notably smaller than the laser footprint. As a rule of thumb, it can be recommended that the GSD is one order of magnitude smaller than the laser footprint. However, the question how much exactly the GSD should be smaller than the footprint (or one footprint from another, or one pixel from-another) is important and should be analysed in further studies.

For *low-frequency surface components* (wavelengths  $> \sim 1$  m), it is, however, still questionable whether DIM of close-range images can serve as the reference. The reason is that DEMs based on images may contain systematic residuals due to an imperfect functional model set in the bundle block adjustment (BBA). These systematic errors are also known as block bending, or dome effects (Eltner and Schneider 2015; Heng et al. 2010; James and Robson 2014). Eltner et al. (2015) reported a large dome effect when BBA neither estimates radial lens distortions, nor comprises ground control points, which is for example the case for the VisualSFM software. Kaiser et al. (2014) and Eltner and Schneider (2015) used undistorted images to mitigate the dome effect, relying on a camera calibration done beforehand. James and Robson (2014) showed that convergent images can improve the estimation of image distortion parameters and reduce the dome effect. Paper III shows that systematic errors can occur due to weakly tied sub-blocks of BBA. This paper also showed that these systematic errors introduce notable deformations in the shape of the roughness spectrum at low frequencies (at wavelengths corresponding to the image footprint side or larger). Therefore, DIM of close-range images can serve as the reference, but only when the results of BBA are free from systematic residuals. Another reference technique for low-frequency surface components can be TLS. Paper VI showed that one TLS scan can measure accurate roughness spectra for wavelengths between 5 cm and 10 m. This would be enough to serve as the reference for both ALS and ULS data.

### 4.1.3 Roughness Spectra as Quality Measure of a DEM

It is already discussed in the Section 5.1.1 of Paper VI that spectral analysis is also a suitable method to analyse the quality of DEMs/DTMs/DSMs. It is shown that the roughness spectra can quantify the quality loss when using one or more TLS scans, or when using different interpolation methods. The quality loss is reflected as the magnitude modulation, which can also be quantified with the gain (see Eq.(2) and Figure 4) as discussed in in Section 4.1.1. In Paper II (and in Paper III and Paper VI indirectly), it was shown that the magnitude modulation is directly related with the DEM/DTM/DSM resolution and with angular resolution of the laser scanning data as defined in Lichti and Jamtsho (2006). Paper II showed that the amount of noise (coming from random measurement errors) present in a DEM is reflected well by the deformations of the spectrum shape at high frequencies. Finally, Paper III showed that systematic errors in a DEM cause the deformations of the roughness spectrum at low frequencies. Therefore, the spectral analysis provides additional information to classical quality assessment methods such as histogram analysis of the residuals and the DEM of differences (DoD).

## 4.2 3D Shoot Model

Paper I presented the methodology and the 3D shoot model derived from micro-scale triangulating laser scanning data. This is the first (to the author's best knowledge) 3D shoot model at individual needle level on the basis of laser scanning data. However, to understand the canopy scattering problem, complete 3D tree architectures (stem-branch-foliage models) are also required (Côté et al. 2009; Disney et al. 2006). Therefore, one of the open questions here is how to upscale the 3D shoot model and derive a realistic 3D model of the whole tree or even a tree patch. One way for upscaling the 3D shoot model is to clone the 3D branch model on the basis of tree information derived from TLS, ULS and ALS. Such an upscaling approach will be shortly discussed here.

An upscaling of the 3D shoot model by its cloning would require the following input: a point cloud of a tree or a 3D stem-branch model, positions and orientations for cloning the 3D shoot model. A high-resolution TLS point cloud can be used for a stem-branch modelling, but such data underrepresent the crown top due to the occlusions associated with scanning a tree from the ground (Eysn et al. 2013; Raumonon et al. 2013; Wang et al. 2016). Novel ULS do not have this problem as the scanning is performed from the air (above the canopy), while the resulting point clouds depict similar within and below canopy details as TLS point clouds (Wang et al. 2016; Wieser et al. 2017). Foliage points classified from TLS or ULS data would be an ideal starting point for deriving the position and orientation for the cloning of the 3D shoot model. This classification can be done, e.g., using the machine learning methodology presented in Wang et al. (2017). Another possibility would be to classify foliage points using a 3D stem-branch model, e.g., derived by the methodology suggested by Raumonon et al. (2013) or Eysn et al. (2013).

Figure 5 shows major upscaling steps done for the needs of the 3DVegLab project (Felix Morsdorf et al. 2015). The aim was to derive a realistic 3D tree model up to the needle level that is based entirely on laser scanning data. Figure 5a shows the input 3D cylinder model of the stems and branches that is derived by Lothar Eysn using the methodology explained in Eysn et al. (2013). Figure 5b-c show the steps performed by the author of this dissertation to derive the

cloning positions and orientations for the 3D shoot model from Paper I. The green points in Figure 5b are the needle points classified by analysing the distance to the input 3D stem-branch model. Figure 5c shows the alpha hull derived from the needle points to definite the tree crown. The green points in Figure 5d shows the cloning locations determined from local TLS point density. Figure 5e shows the shoot orientation visualized by the blue arrows that was derived for each cloning position. The orientation was defined using the nearest point at the 3D stem-branch model to the cloning position and implying certain predefined orientation rules of the shoot plane.

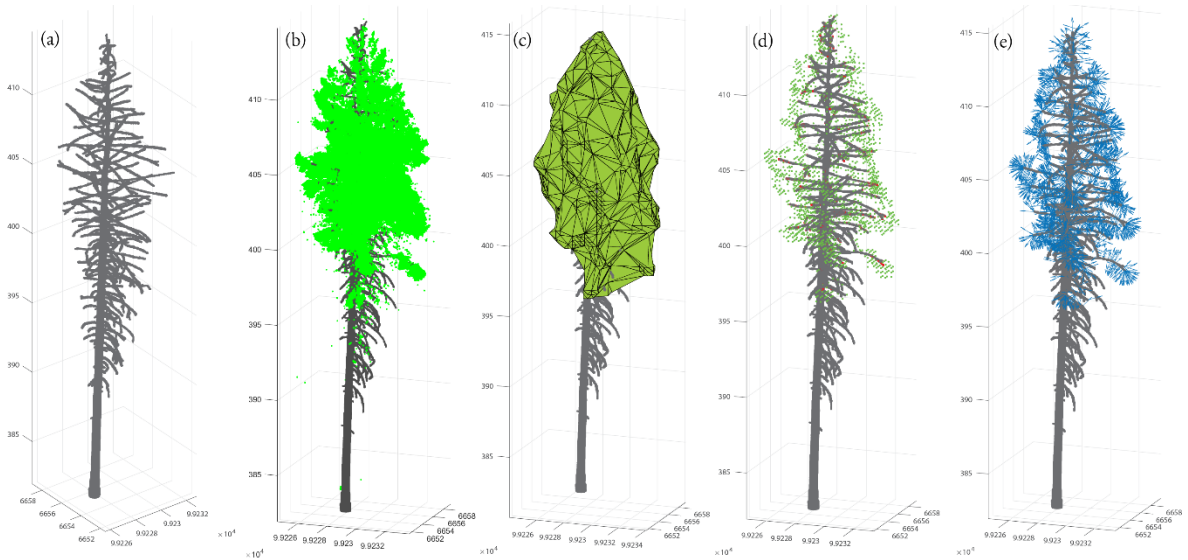


**Figure 5: Major processing steps for upscaling the 3D shoot model. (a) 3D stem-branch model derived by Lothar Eysn (Eysn et al. 2013), (b) classified needle points, (c) alpha hull derived from the needle points, (d) cloning positions and (e) cloning orientation.**

Cloning positions and orientations (Figure 5d-e) are then provided for further modelling of the 3D forest scene. This modelling and visualisations of individual trees and the final scene is done by another 3D VegLab project partner (the Remote Sensing Laboratories, University of Zürich). More details about these steps can be found in Reik Leiterer et al. (2012) and Felix Morsdorf et al. (2015). Figure 6 shows the main elements of the upscaling approach done within the 3DVegLab project.

Finally, it is noted that Paper I also presented a method for a broad leaf modelling with micro-scale laser scanning data. However, this output was not explored within the 3DVegLab project. In contrast to the needle modelling, there are few studies on single broad leaf modelling reported in the meanwhile (Tang et al. 2017; Wang et al. 2013)



Figure 6: Generation of the 3D forest scene within the 3DVegLab project (Felix Morsdorf et al. 2015; Reik Leiterer et al. 2012). (a) 3D stem-branch model (credits: Lothar Eysn), (b) 3D shoot model (Paper I); (c) and (d) visualisations of the single tree 3D model and 3D model of the forest scene, respectively. Figures (c) and (d) are prepared by the Remote Sensing Laboratories, University of Zürich (Felix Morsdorf et al. 2015; Reik Leiterer et al. 2012, [www.geo.uzh.ch/microsite/3dveglab/](http://www.geo.uzh.ch/microsite/3dveglab/)).

## 4.3 Canopy Transmittance

### 4.3.1 Leaf-Off vs. Leaf-On ALS Data

It is already discussed in Section 6.2 of Paper IV that the canopy transmittance method does not require assumptions on vegetation-ground scattering characteristics as it only relies on the energy of ground echoes. The observed ground echo energies are normalized by the energy of single ground echoes found in their vicinity, which makes that the calibration constant cancels out. This means that the method also does not require calibration of the echo energies. However, the method relies on the single ground echoes, as they are necessary for the normalization of the observed ground echo energies. This discussion focuses more on this issue by analysing a leaf-on ALS dataset, where the number of single ground echoes is limiting due to closed canopy, i.e. less canopy gaps compared to leaf-off data. In Paper IV, a leaf-off data set was analysed.

Figure 7 illustrates possible cases with respect to the number of single ground echoes (green asterisks) when applying the transmittance method. In Case 1 and Case 2, there are single ground echoes in a cell (the aggregating unit), and thus,  $T_c$  can be readily calculated. In Case 2,  $T_c$  is 1 as there are only the single ground echoes in a cell. In Case 3, the observed ground energy is 0, and thus,  $T_c$  is also 0. However, the most interesting case is Case 4 where there is no single ground echo within the cell, but there are other ground echoes to be normalized. If the calculation is strictly referred to cell, then on Case 4 the  $T_c$  method cannot be applied. However, if the cell size is larger, some neighbouring single ground echoes may fall within the larger cell. Therefore, the

critical parameter to analyse the applicability of the  $T_c$  method is distance from a ground echo to its nearest neighbouring single ground echo  $d_{nn}$  (Figure 7, Case 4).

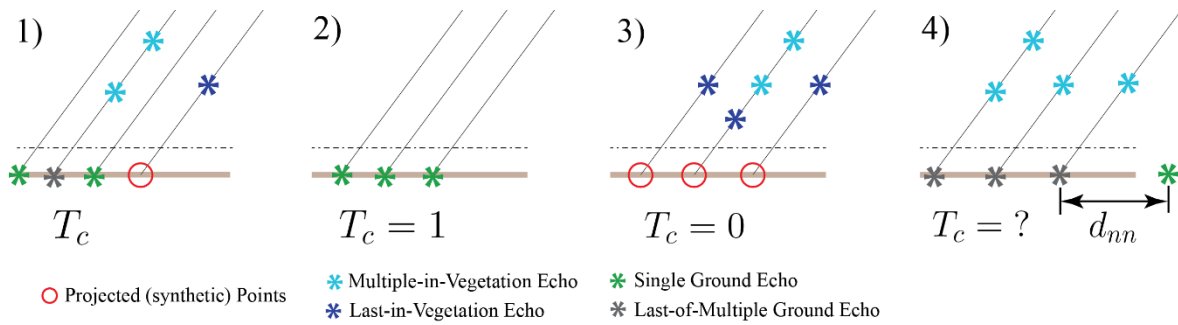


Figure 7: Different cases when applying the canopy transmittance method.

The test area used in Paper IV is also used here to analyse the relation between  $T_c$  and  $d_{nn}$  for the leaf-on and leaf-off LiDAR data. Therefore, the leaf-off ALS strip used here is the same ALS strip used in Paper IV. For the same area, a leaf-on ALS strip is also available, but with slightly different flight direction compared to the leaf-off ALS strip. This ALS strip was collected with the RIEGL LMS-Q 680i full-waveform LiDAR instrument. Therefore, these leaf-on data are associated with a larger footprint size and different wavelength compared to the leaf-off data (0.3 m vs. 0.15 m and 1550 nm vs. 1064 nm, respectively). Mean point density was similar for both datasets (6 and 6.9 last echoes per  $m^2$ ). It is noted that the data acquisition and preprocessing of this leaf-on ALS strip was done by Gottfried Mandlbürger within a long-term project of studying the morphodynamics of the Pielach river (Mandlbürger et al. 2015a; Mandlbürger et al. 2015b).

Figure 8a-b shows the scatterplots of  $d_{nn}$  and  $T_c$  for a leaf-on ALS strip and the leaf-off ALS strip. The scatterplots refer to the overlapping area between the two strips (the orange polygons in Figure 8c-d). Both scatterplots shows larger  $d_{nn}$  distance for smaller  $T_c$  values ( $T_c < 0.2$ ), which is expected as the latter indicates at dense vegetation. However, the scatterplot for the leaf-on data (Figure 8a) shows more points at  $d_{nn}$  distances larger than 5 m (points above the horizontal dashed line in Figure 8a-b). This suggests that the cell size should be larger than 5 m in order to avoid Case 4 in Figure 7. Now, the question is where such cases occur spatially. Figure 8c-d shows that, for leaf-on data (red points),  $d_{nn}$  larger than 5 m occurs mostly around Plot 3-5. The former two plots contain extremely dense coniferous forest and for them the quantile 99 % of  $d_{nn}$  is 8.3 m. Plot 3 contains dense deciduous vegetation and the same  $d_{nn}$  statistics for this polygon is 5.6 m. Another notable cluster of red points is marked with the black arrows in Figure 8c. These points appear at slopes where the terrain exposition is oriented away from the LiDAR line of sight. Thus, topography causes unfavourable scanning geometry, which then leads to no single ground echoes found in the vicinity.

The above analysis shows that the  $T_c$  method works for leaf-on data, but with certain limitations. The limitations can occur when there are no single ground returns near the last-of-multiple ground returns. This occurs when scanning with a larger footprint ( $> 0.2$  m) over extremely dense coniferous forest and extremely dense deciduous forest under leaf-on conditions (in both cases with  $T_c < 0.2$ ). In addition, no single ground echoes may occur when the slope is oriented away from the LiDAR line of sight. These particular issues, however, affect only the spatial resolution of  $T_c$  as they can be overcome by using a larger cell size, or search radius. Another possibility would be to work on segments and not on cells.

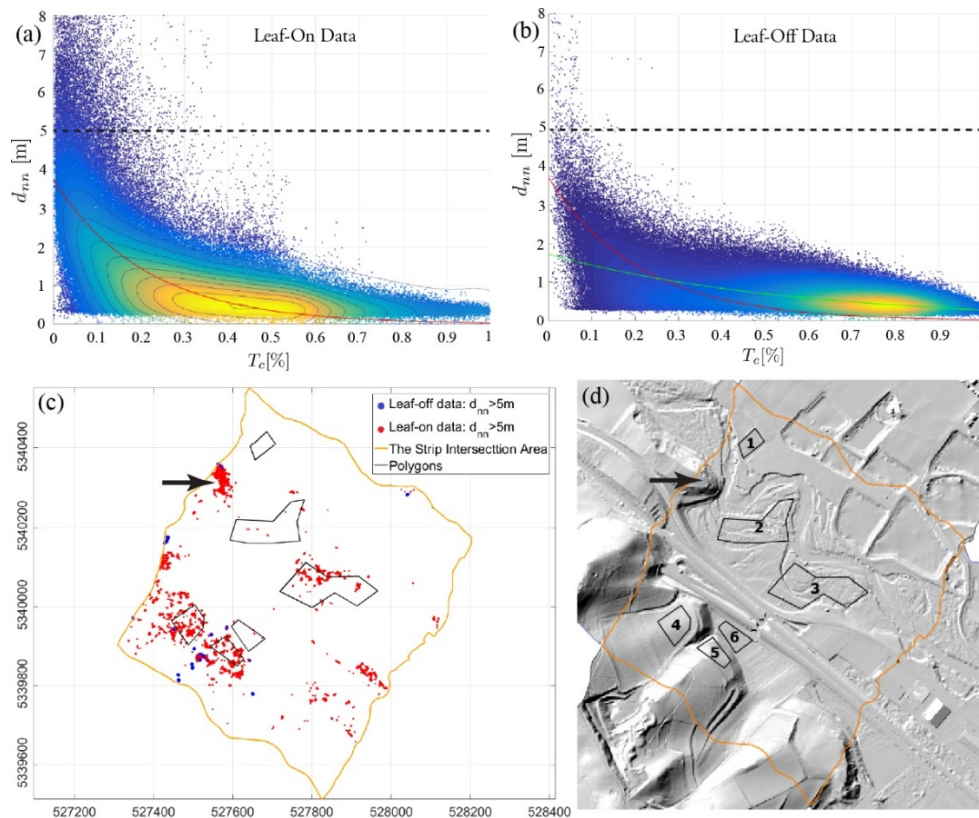


Figure 8: Analysis of distance to the nearest neighbouring single ground echo ( $d_{nn}$ ) for a leaf-on and the leaf-off ALS data over the test area of Paper IV.

### 4.3.2 Upscaling and Comparing Canopy Transmittance

Canopy transmittance is related to the vegetation-structural and biophysical parameters such as LAI and gap fraction. However, canopy transmittance is also well-defined physical parameter that quantifies the amount of (laser) radiation attenuated when passing through a vegetation layer. Therefore, canopy transmittance is also important for understanding space-borne LiDAR signals. The LAI will be, for example, Level-2&3 product of the upcoming space-borne GEDI (Global Ecosystems Dynamics Investigation LiDAR) mission. The GEDI instrument will be mounted on International Space Station and provide nearly global sampling with a waveform LiDAR sensor that operates at 1064 nm wavelength and has a footprint diameter of 22 m (Marselis et al. 2016). Therefore, an upscaling of the canopy transmittance at the GEDI footprint size will help separating vegetation and ground portions of GEDI waveforms recorded over vegetated area. The waveform stacking method presented in Paper VI can be used to extend the canopy transmittance method for deriving  $T_c$  values at the GEDI footprint scale. For such a global application, it would also be interesting to test the performance of the  $T_c$  method in dense tropical forest. Furthermore, it would be interesting to compare the  $T_c$  method that is based only on ground echoes with the gap fraction method suggested by Armston et al. (2013) where data-derived vegetation-ground reflectance ratio is used.

There are also other possibilities to extend this work on canopy transmittance. Recent studies on UAV-borne tomoradar showed that this technique can also be used for deriving canopy transmittance and vegetation-structural parameters (Piermattei et al. 2017). In such studies, the LiDAR-based canopy transmittance from Paper IV can serve as the optical limit for the radar based canopy transmittance. Also, a number of studies is recently focusing on exploring

multispectral LIDAR data (mostly green and infrared channels) for land cover or tree species classification (Matikainen et al. 2017; Yu et al. 2017). Therefore, it would be interesting to analyse and compare the canopy transmittance derived from green and infrared channels, especially knowing that the former is associated with a larger beam divergence angle.

## 4.4 Surface Observations from Laser Scanning

*... Selection of the Surface Description Approach:* In this work, geometric-stochastic, geometric-deterministic and geometric-radiometric descriptions of natural surfaces are exercised. The selection of one particular description depends on many factors, but primarily depends on the fact how the natural surface is treated in particular environmental or physical models (e.g. of hydraulic flows, erosion rates, landscape evolution or electromagnetic scattering). However, many of these models are tailored for outdated geometric and radiometric measurements available at the time when the model is developed. There is, however, an impression that contemporary measurements offer even more information than the current environmental and physical models can handle. For example, it is a question if current radiative transfer models can handle a 3D model of a forest patch containing the needle level objects. Another question is whether current scattering or hydraulic models can be extended to include information on individual soil clods and pebble clusters that can be readily derived from, e.g., TLS or ULS data. Therefore, it would also be interesting to revisit current definitions of natural surfaces in environmental and physical models from the perspective of the contemporary measurements.

*... Laser Scanning Data and Spatial and Frequency Surface Information:* One interesting observation is how the requirements on laser scanning data can be totally different when a geometric-stochastic description is analysed in spatial or frequency domain. This is nicely illustrated in Paper VI, where it was shown that a roughness spectrum derived from one TLS scan is equally accurate as the spectrum derived from 14 TLS scans. However, a DTM interpolated from single TLS scan over a 1 m x 10 m plot would be suboptimal compared to a DTM interpolated from 14 TLS scans. This is because the occlusion effects<sup>1</sup> are much larger for a single- than for 14-TLS scans, which would result in different interpolation errors in the single-scan DTM. In contrast, the roughness spectrum is perfectly appropriate, as statistics derived from ensemble averaging based on 500 profiles is simply not sensitive on these interpolation artefacts. This is another argument why it is important to reconsider the surface descriptions in existing environmental and physical models so that the maximum of the contemporary measurements is explored.

Paper II, in contrast, shows that there are methods that provide good performance in both spatial and frequency domain. There, the DTM interpolation parameter is optimized by following the behaviour of the spectral slope at high frequencies. The result is a DTM that has stochastically unique property, i.e. maximizes fractal dimension (minimizes spectral slope) at high-frequency surface components. However, this DTM also has good performance in the spatial domain as its shaded heights (a visualisation based on surface first derivative) neither show the presence of the measurement noise or the oversmoothing effects ( Figure 5a-c in Paper II).

<sup>1</sup>The TLS occlusion effects are discussed and illustrated by the Figure 3c, Figure 4b-c and Figure 8 of Paper II

... *Smallest Surface Details*: Apart from the canopy transmittance, surface roughness analysis and 3D shoot modelling tackle one very interesting photogrammetric question is – what is the smallest object that can be modelled/reconstructed/described by laser scanning or digital images? In many applications, the objects of interest are notably larger than the measurement noise or resolution (instantaneous field of view of the instrument). Therefore, investigating the modulations/deformations of objects at the scale similar to data resolution is irrelevant in such applications. However, in roughness analysis, these objects have to be characterized. Therefore, for roughness studies, it will always be important to understand high-frequency modulations associated to particular measurement technique. Furthermore, it would be interesting to analyse what is the smallest frequency that can be reconstructed and what is its relation to the laser footprint size or the image's GSD. For example, TLS resolution is diffraction limited and depends on the laser beam diameter at the exit designed by the sensor manufacturer. In contrast, with digital images (multi-view stereo techniques) one can approach to the object much closer. However, the question would be what is the smallest GSD that would still provide enough texture for image matching. Then, it is also important to know the maximum area that can be measured at such high resolution. For roughness studies, these measurements should minimize the systematic errors of the block and the number of ground control measurements.

The above aspects are challenging and require further measurement experiments as well as profound photogrammetric knowledge. Ideally, independent experimentation performed by different groups in a form of a benchmark would give a perfect base to arrive at the best solution. The aim of such a benchmark would be on the reconstruction of the smallest detail with minimal systematic errors for the given measurement technique.

## 5 Conclusions

In this research high-resolution laser scanning data (including both geometric and radiometric observations) are used to describe different natural surfaces, such as soil, gravel, and vegetation by using geometric-stochastic, geometric-deterministic, and geometric-radiometric approaches. The research contributed by introducing new and improved methods of modelling high-resolution laser scanning data for land-surface parametrisations such as surface roughness, 3D vegetation models, and canopy transmittance. These parametrisations serve as the description of natural surfaces in many environmental and physical models, such as water flows, soil erosions, landscape evolution, radiative transfer, and surface scattering models.

*Surface Roughness* of soil and gravel surface is analysed here mainly with roughness spectra derived from TLS, ULS, and ALS data, but also from UAV and handheld images. A new method is suggested for interpolating a DTM with a unique stochastic property by using laser scanning point clouds. Such a DTM has favourable characteristics for roughness analysis, as it filters out the measurement noise and avoids the oversmoothing of the high-frequency surface components. Furthermore, a methodology for roughness spectrum calculation and analysis is suggested for comparison of roughness spectra derived from different photogrammetric point clouds. Analysis of different measurement setups and laser scanning data showed that one TLS scan can measure a roughness spectrum at wavelengths from one centimetre to a few tens of metres. However, when particular roughness parameters are estimated, such as RMS<sub>h</sub>, correlation length, and spectral slope in a high-frequency band, then the incidence angle of laser beams should be below 50° to avoid scanning artefacts due to an oblique scanning geometry. Novel ULS can readily provide accurate roughness spectra at wavelengths larger than one metre. Smaller wavelengths of up to a few centimetres would also be possible to depict with the ULS, but that would require further experiments and method optimisation. Finally, DIM of handheld images showed a considerable potential to serve as the reference and provide accurate spectra at millimetre wavelengths. The UAV images showed that they could be a flexible alternative for laser scanning in roughness measurements. However, further investigation will be required to optimise this measurement method.

*A 3D Shoot Model* with individual needle details is derived for the first time in this work from a micro-scale triangulating laser scanner. The suggested method is semiautomatic and involves a manual digitization of an end shoot and its cloning on the basis of a skeleton derived from an automatic classification of needle and wooden branch parts of the analysed shoot. The method can be applied for deriving a database of 3D shoot models for different species. This information can be used later to generate realistic 3D tree models, as was done within the 3DVegLab project. One way to do so is by using TLS or ULS point clouds of a tree to determine the cloning positions and the orientations for the 3D shoot model. Such data are relevant for building a 3D scene of a forest patch, which, in turn, can be used for simulating and analysing EO data with radiative transfer models.

*Canopy Transmittance* is a physical and vegetation-structural parameter that is analysed here as a geometric-radiometric description of the vegetation surface. An improved method is suggested for deriving canopy transmittance from small-footprint ALS waveform data. The method considers only the energy of ground echoes that is normalized by the energy of single ground echoes. The method does not require calibration of the observed energies, because the

calibration constant is cancelled out in the normalization step. Furthermore, the method does not require the vegetation-ground reflectance correction or an assumption for the vegetation extinction coefficient. An analysis of the leaf-on and leaf-off data showed that the canopy transmittance method could be readily applied for both data sets, but with certain parameter adoptions for extremely dense vegetation. In addition to the canopy transmittance method, another method is suggested for stacking the ALS waveforms to the space-borne LiDAR footprint level. This method can be used for an upscaling of the canopy transmittance method, which is relevant for interpretation and global biomass prediction with incoming space-borne LiDAR data.

The information and novel methods about surface roughness, 3D vegetation models, and canopy transmittance presented in this dissertation provide a basis for a better understanding and description of natural surfaces. Further work should be focused more on their upscaling and implementation in new environmental and physical models.

# Bibliography

- Alex Martinez-Agirre, Jesús Álvarez-Mozos, Milutin Milenković, Norbert Pfeifer, Rafael Giménez, Melón, J.M.V., & Miranda, Á.R. (2018). Surface roughness measurements techniques and parameters evaluation in agricultural soils. (*Submitted to Earth Surface Processes and Landforms*)
- Álvarez-Mozos, J., Verhoest, E.N., Larrañaga, A., Casali, J., & González-Audicana, M. (2009). Influence of Surface Roughness Spatial Variability and Temporal Dynamics on the Retrieval of Soil Moisture from SAR Observations. *Sensors*, 9
- Armston, J., Disney, M., Lewis, P., Scarth, P., Phinn, S., Lucas, R., Bunting, P., & Goodwin, N. (2013). Direct retrieval of canopy gap probability using airborne waveform lidar. *Remote Sensing of Environment*, 134, 24-38
- Axelsson, P. (1999). Processing of laser scanner data—algorithms and applications. *ISPRS Journal of Photogrammetry and Remote Sensing*, 54, 138-147
- Baltsavias, E.P. (1999). Airborne laser scanning: basic relations and formulas. *ISPRS Journal of Photogrammetry and Remote Sensing*, 54, 199-214
- Beraldin, J.-A., Blais, F., & Lohr, U. (2010). Laser Scanning Technology. In G. Vosselman, & H.G. Maas (Eds.), *Airborne and Terrestrial Laser Scanning* (pp. 1-42). Scotland, UK: Whittles Publishing
- Besl, P.J., & McKay, N.D. (1992). A method for registration of 3-D shapes. *IEEE Transactions on Pattern Analysis and Machine Intelligence*, 14, 239-256
- Bréda, N.J.J. (2003). Ground - based measurements of leaf area index: a review of methods, instruments and current controversies. *Journal of Experimental Botany*, 54, 2403-2417
- Bretar, F. (2008). Feature Extraction from LiDAR Data in Urban Areas. *Topographic Laser Ranging and Scanning* (pp. 403-420): CRC Press
- Briese, C. (2010). Extraction of Digital Terrain Models. In G. Vosselman, & H.-G. Maas (Eds.), *Airborne and Terrestrial Laser Scanning* (pp. 135-167). Scotland, UK: CRC Press, Taylor & Francis Group
- Bucksch, A., & Lindenbergh, R. (2008). CAMPINO — A skeletonization method for point cloud processing. *ISPRS Journal of Photogrammetry and Remote Sensing*, 63, 115-127
- Chan, T.O., Lichti, D.D., & Belton, D. (2015). A rigorous cylinder-based self-calibration approach for terrestrial laser scanners. *ISPRS Journal of Photogrammetry and Remote Sensing*, 99, 84-99
- Côté, J.-F., Widlowski, J.-L., Fournier, R.A., & Verstraete, M.M. (2009). The structural and radiative consistency of three-dimensional tree reconstructions from terrestrial lidar. *Remote Sensing of Environment*, 113, 1067-1081
- Disney, M., Lewis, P., & Saich, P. (2006). 3D modelling of forest canopy structure for remote sensing simulations in the optical and microwave domains. *Remote Sensing of Environment*, 100, 114-132

- Disney, M.I., Kalogirou, V., Lewis, P., Prieto-Blanco, A., Hancock, S., & Pfeifer, M. (2010). Simulating the impact of discrete-return lidar system and survey characteristics over young conifer and broadleaf forests. *Remote Sensing of Environment*, 114, 1546-1560
- Doneus, M., Briese, C., Fera, M., & Janner, M. (2008). Archaeological prospection of forested areas using full-waveform airborne laser scanning. *Journal of Archaeological Science*, 35, 882-893
- Dorning, P., Nothegger, C., Pfeifer, N., & Molnár, G. (2008). On-the-job detection and correction of systematic cyclic distance measurement errors of terrestrial laser scanners. *Journal of Applied Geodesy*, 2
- El-Sheimy, N. (2008). Georeferencing Component of LiDAR Systems. *Topographic Laser Ranging and Scanning* (pp. 195-214): CRC Press
- Eltner, A., Baumgart, P., Maas, H.-G., & Faust, D. (2015). Multi-temporal UAV data for automatic measurement of rill and interrill erosion on loess soil. *Earth Surface Processes and Landforms*, 40, 741--755
- Eltner, A., & Schneider, D. (2015). Analysis of Different Methods for 3D Reconstruction of Natural Surfaces from Parallel-Axes UAV Images. *The Photogrammetric Record*, 30, 279--299
- Eysn, L., Pfeifer, N., Ressel, C., Hollaus, M., Graf, A., & Morsdorf, F. (2013). A Practical Approach for Extracting Tree Models in Forest Environments Based on Equirectangular Projections of Terrestrial Laser Scans. *Remote Sensing*, 5
- Felix Morsdorf, Reik Leiterer, Markus Hollaus, Fabian Schneider, Daniel Kükenbrink, Jason Brazile, Nicolas Lauret, Jean-Phillipe Gastellu-Etchegorry, Tristan Gregoire, Tianggang Yin, Mathias Disney, Philip Lewis, Milutin Milenković, Lothar Eysn, Werner Mücke, Norbert Pfeifer, & Schaeppman, M. (2015). 3D Vegetation Lab - Final Report. In (pp. 1-30). Remote Sensing Laboratories, Department of Geography, University of Zürich
- Fieber, K.D., Davenport, I.J., Tanase, M.A., Ferryman, J.M., Gurney, R.J., Becerra, V.M., Walker, J.P., & Hacker, J.M. (2015). Validation of Canopy Height Profile methodology for small-footprint full-waveform airborne LiDAR data in a discontinuous canopy environment. *ISPRS Journal of Photogrammetry and Remote Sensing*, 104, 144-157
- Fiete, D.R. (2010). *Modeling the Imaging Chain of Digital Cameras*. Bellingham, Washington USA: Society of Photo-Optical Instrumentation Engineers (SPIE)
- Glira, P., Pfeifer, N., & Mandlbauer, G. (2016). Rigorous Strip Adjustment of UAV-based Laserscanning Data Including Time-Dependent Correction of Trajectory Errors. *Photogrammetric Engineering and Remote Sensing*, 82, 945-954
- Harding, D. (2008). Pulsed Laser Altimeter Ranging Techniques and Implications for Terrain Mapping. *Topographic Laser Ranging and Scanning* (pp. 173-194): CRC Press
- Heipke, C. (2017). Photogrammetrie und Fernerkundung – eine Einführung. In C. Heipke (Ed.), *Photogrammetrie und Fernerkundung: Handbuch der Geodäsie, herausgegeben von Willi Freeden und Reiner Rummel* (pp. 1-27). Berlin, Heidelberg: Springer Berlin Heidelberg
- Heng, B.C.P., Chandler, J.H., & Armstrong, A. (2010). Applying close range digital photogrammetry in soil erosion studies. *The Photogrammetric Record*, 25, 240-265

- Heritage, G.L., & Large, A.R.G. (2009). *Laser Scanning for the Environmental Sciences*. West Sussex, UK: Wiley-Blackwell
- Höfle, B., & Pfeifer, N. (2007). Correction of laser scanning intensity data: Data and model-driven approaches. *ISPRS Journal of Photogrammetry and Remote Sensing*, 62, 415-433
- Hollaus, M., Aubrecht, C., Höfle, B., Steinnocher, K., & Wagner, W. (2011). Roughness Mapping on Various Vertical Scales Based on Full-Waveform Airborne Laser Scanning Data. *Remote Sensing*, 3
- Hopkinson, C., & Chasmer, L. (2009). Testing LiDAR models of fractional cover across multiple forest ecozones. *Remote Sensing of Environment*, 113, 275-288
- Huising, E.J., & Gomes Pereira, L.M. (1998). Errors and accuracy estimates of laser data acquired by various laser scanning systems for topographic applications. *ISPRS Journal of Photogrammetry and Remote Sensing*, 53, 245-261
- Hyypä, J., Hyypä, H., Yu, X., Kaartinen, H., Kukko, A., & Holopainen, M. (2008). Forest Inventory Using Small-Footprint Airborne LiDAR. *Topographic Laser Ranging and Scanning* (pp. 335-370): CRC Press
- Ingle, V.K., & Proakis, J.G. (1997). *Digital Signal Processing Using MATLAB*. PWS Publishing Company
- James, M.R., & Robson, S. (2014). Mitigating systematic error in topographic models derived from UAV and ground-based image networks. *Earth Surface Processes and Landforms*, 39, 1413--1420
- Jean-Philippe Gastellu-Etchegorry, Eloi Grau, & Lauret, N. (2012). DART : a 3D model for remote sensing images and radiative budget of earth surfaces. In C. Alexandru (Ed.), *Modeling and Simulation in Engineering*. InTech
- Jester, W., & Klik, A. (2005). Soil surface roughness measurement—methods, applicability, and surface representation. *CATENA*, 64, 174-192
- Jutzi, B., Meyer, F.J., & Hinz, S. (2017). Aktive Fernerkundungssensorik – Technologische Grundlagen und Abbildungsgeometrie. In C. Heipke (Ed.), *Photogrammetrie und Fernerkundung: Handbuch der Geodäsie, herausgegeben von Willi Freuden und Reiner Rummel* (pp. 65-103). Berlin, Heidelberg: Springer Berlin Heidelberg
- Jutzi, B., & Stilla, U. (2006). Range determination with waveform recording laser systems using a Wiener Filter. *ISPRS Journal of Photogrammetry and Remote Sensing*, 61, 95-107
- Kaasalainen, S., Ahokas, E., Hyypä, J., & Suomalainen, J. (2005). Study of surface brightness from backscattered laser intensity: calibration of laser data. *IEEE Geoscience and Remote Sensing Letters*, 2, 255-259
- Kaiser, A., Neugirg, F., Rock, G., Müller, C., Haas, F., Ries, J., & Schmidt, J. (2014). Small-Scale Surface Reconstruction and Volume Calculation of Soil Erosion in Complex Moroccan Gully Morphology Using Structure from Motion. *Remote Sensing*, 6
- Kilian, J., Haala, N., & Englich, M. (1996). Capture and Evaluation of Airborne Laser Scanner Data. In K. Kraus, & P. Waldhäusl (Eds.), *XVIIIth ISPRS Congress* (pp. 383-388). Vienna, Austria: ISPRS Archives

- Krabill, W.B.C., J. G.; Link, L.E.; Swift, R. N.; Butler, M. L. (1984). Airborne Laser Topographic Mapping Results (Joint NASA/US Army Corps of Engineers experiments indicate the feasibility of meeting stream valley cross-sectional mapping requirements under winter foliage conditions). *Photogrammetric Engineering and Remote Sensing*, 50, 685-694
- Kraus, K. (2000). *Topographische Informationssysteme (Photogrammetrie, Band 3)*. Köln, Deutschland: Dümmler
- Kraus, K. (2007). *Photogrammetry: Geometry from Images and Laser Scans*. (2 ed.). Berlin New York: Walter de Gruyter
- Kraus, K., & Pfeifer, N. (1998). Determination of terrain models in wooded areas with airborne laser scanner data. *ISPRS Journal of Photogrammetry and Remote Sensing*, 53, 193-203
- Lefsky, M.A., Cohen, W.B., Acker, S.A., Parker, G.G., Spies, T.A., & Harding, D. (1999). Lidar Remote Sensing of the Canopy Structure and Biophysical Properties of Douglas-Fir Western Hemlock Forests. *Remote Sensing of Environment*, 70, 339-361
- Lichti, D., & Skaloud, J. (2010). Registration and Calibration. In G. Vosselman, & H.-G. Maas (Eds.), *Airborne and Terrestrial Laser Scanning* (pp. 83-133). Scotland, UK: CRC Press, Taylor & Francis Group
- Lichti, D.D. (2010). A Review Of Geometric Models And Self-Calibration Methods For Terrestrial Laser Scanners. *Boletim de Ciências Geodésicas*, 16
- Lichti, D.D., & Jamtsho, S. (2006). Angular resolution of terrestrial laser scanners. *Photogrammetric Record*, 21, 141-160
- Lindberg, E., Olofsson, K., Holmgren, J., & Olsson, H. (2012). Estimation of 3D vegetation structure from waveform and discrete return airborne laser scanning data. *Remote Sensing of Environment*, 118, 151-161
- Lindenbergh, R. (2010). Engineering Applications. In G. Vosselman, & H.-G. Maas (Eds.), *Airborne and Terrestrial Laser Scanning* (pp. 237-269). Scotland, UK: CRC Press, Taylor & Francis Group
- Maas, H.-G. (2000). Least-Squares Matching With Airborne Laserscanning Data In A Tin Structure. In T. Schenk, & G. Vosselman (Eds.), *XIXth ISPRS Congress* (pp. 548-555 ). Amsterdam, The Netherlands: ISPRS Archives
- Maas, H.-G. (2010). Forestry Applications. In G. Vosselman, & H.-G. Maas (Eds.), *Airborne and Terrestrial Laser Scanning* (pp. 213-235). Scotland, UK: CRC Press, Taylor & Francis Group
- Maas, H.-G., & Vosselman, G. (1999). Two algorithms for extracting building models from raw laser altimetry data. *ISPRS Journal of Photogrammetry and Remote Sensing*, 54, 153-163
- Mallet, C., & Bretar, F. (2009). Full-waveform topographic lidar: State-of-the-art. *ISPRS Journal of Photogrammetry and Remote Sensing*, 64, 1-16
- Maltamo, M., Næsset, E., & Vauhkonen, J. (2014). *Forestry Applications of Airborne Laser Scanning: Concepts and Case Studies*. Springer

- Mandlbürger, G., Hauer, C., Wieser, M., & Pfeifer, N. (2015a). Topo-Bathymetric LiDAR for Monitoring River Morphodynamics and Instream Habitats—A Case Study at the Pielach River. *Remote Sensing*, 7
- Mandlbürger, G., Pfennigbauer, M., Riegl, U., Haring, A., Wieser, M., Glira, P., & Winiwarter, L. (2015b). Complementing airborne laser bathymetry with UAV-based lidar for capturing alluvial landscapes. In (pp. 96370A-96370A-96314)
- Manning, R. (1891). On the flow of water in open channels and pipes. *Transactions of the Institution of Civil Engineers of Ireland*, XX, 161-207
- Marselis, S., Armston, J., & Dubayah, R. (2016). Summary of the Second GEDI Science Team Meeting. In, *The Earth Observer* (pp. 30-36). Greenbelt, Maryland 20771, US: NASA Goddard Space Flight Center, Earth Observing System Project Science Office
- Martinez-Agirre, A., Álvarez-Mozos, J., & Giménez, R. (2016). Evaluation of surface roughness parameters in agricultural soils with different tillage conditions using a laser profile meter. *Soil and Tillage Research*, 161, 19-30
- Matikainen, L., Karila, K., Hyypä, J., Litkey, P., Puttonen, E., & Ahokas, E. (2017). Object-based analysis of multispectral airborne laser scanner data for land cover classification and map updating. *ISPRS Journal of Photogrammetry and Remote Sensing*, 128, 298-313
- Mattia, F., Davidson, M.W.J., Toan, T.L., Haese, C.M.F.D., Verhoest, N.E.C., Gatti, A.M., & Borgeaud, M. (2003). A comparison between soil roughness statistics used in surface scattering models derived from mechanical and laser profilers. *Ieee Transactions on Geoscience and Remote Sensing*, 41, 1659-1671
- Morsdorf, F., Kötz, B., Meier, E., Itten, K.I., & Allgöwer, B. (2006). Estimation of LAI and fractional cover from small footprint airborne laser scanning data based on gap fraction. *Remote Sensing of Environment*, 104, 50-61
- Musselman, K.N., Margulis, S.A., & Molotch, N.P. (2013). Estimation of solar direct beam transmittance of conifer canopies from airborne LiDAR. *Remote Sensing of Environment*, 136, 402-415
- Nelson, R., Krabill, W., & MacLean, G. (1984). Determining forest canopy characteristics using airborne laser data. *Remote Sensing of Environment*, 15, 201-212
- Nilsson, M. (1996). Estimation of tree heights and stand volume using an airborne lidar system. *Remote Sensing of Environment*, 56, 1-7
- Ogilvy, J.A. (1987). Wave scattering from rough surfaces. *Reports on Progress in Physics*, 50, 1553
- Perez-Gutierrez, C., Martínez-Fernández, J., Sanchez, N., & Alvarez-Mozos, J. (2007). *Modeling of soil roughness using terrestrial laser scanner for soil moisture retrieval.*
- Petrie, G., & Toth, C. (2008). Introduction to Laser Ranging, Profiling, and Scanning. *Topographic Laser Ranging and Scanning* (pp. 1-28): CRC Press
- Pfeifer, N., & Mandlbürger, G. (2008). LiDAR Data Filtering and DTM Generation. *Topographic Laser Ranging and Scanning* (pp. 307-334): CRC Press

- Pfeifer, N., Mandlbürger, G., & Glira, P. (2017). Laserscanning. In C. Heipke (Ed.), *Photogrammetrie und Fernerkundung: Handbuch der Geodäsie, herausgegeben von Willi Freuden und Reiner Rummel* (pp. 431-481). Berlin, Heidelberg: Springer Berlin Heidelberg
- Pfeifer, N., & Winterhalder, D. (2004). Modelling of tree cross sections from terrestrial laser scanning data with free-form curves. In M. Thies, B. Koch, H. Spiecker, & H. Weinacker (Eds.), *Laser-scanners for Forest and Landscape Assessment* (pp. 76-81): ISPRS-International Archives of Photogrammetry, Remote Sensing and Spatial Information Sciences
- Piermattei, L., Hollaus, M., Milenković, M., Pfeifer, N., Quast, R., Chen, Y., Hakala, T., Karjalainen, M., Hyyppä, J., & Wagner, W. (2017). An Analysis of Ku-Band Profiling Radar Observations of Boreal Forest. *Remote Sensing*, 9
- Raunonen, P., Kaasalainen, M., Åkerblom, M., Kaasalainen, S., Kaartinen, H., Vastaranta, M., Holopainen, M., Disney, M., & Lewis, P. (2013). Fast Automatic Precision Tree Models from Terrestrial Laser Scanner Data. *Remote Sensing*, 5
- Reik Leiterer, Markus Hollaus, Fabian Schneider, Felix Morsdorf, Milutin Milenkovic, Lothar Eysn, Werner Mücke, Norbert Pfeifer, & Schaepman, M. (2012). 3D Vegetation Lab (3DVegLab) – In-Situ Dataset Document. In. Remote Sensing Laboratories, Department of Geography, University of Zurich
- Roncat, A., Bergauer, G., & Pfeifer, N. (2011). B-spline deconvolution for differential target cross-section determination in full-waveform laser scanning data. *ISPRS Journal of Photogrammetry and Remote Sensing*, 66, 418-428
- Roncat, A., Morsdorf, F., Briese, C., Wagner, W., & Pfeifer, N. (2014). Laser Pulse Interaction with Forest Canopy: Geometric and Radiometric Issues. In M. Maltamo, E. Næsset, & J. Vauhkonen (Eds.), *Forestry Applications of Airborne Laser Scanning: Concepts and Case Studies* (pp. 19-41): Springer
- Schenk, T. (2001). Modeling and Analyzing Systematic Errors in Airborne Laser Scanners. In, *Technical Notes in Photogrammetry No 19* (p. 46). Columbus, OH, USA: The Ohio State University, Department of Civil and Environmental Engineering and Geodetic Science
- Shan, J., & Sampath, A. (2008). Building Extraction from LiDAR Point Clouds Based on Clustering Techniques. *Topographic Laser Ranging and Scanning* (pp. 421-444): CRC Press
- Shepard, M.K., Campbell, B.A., Bulmer, M.H., Farr, T.G., Gaddis, L.R., & Plaut, J.J. (2001). The roughness of natural terrain: A planetary and remote sensing perspective. *Journal of Geophysical Research: Planets*, 106, 32777--32795
- Skaloud, J., & Lichti, D. (2006). Rigorous approach to bore-sight self-calibration in airborne laser scanning. *ISPRS Journal of Photogrammetry and Remote Sensing*, 61, 47-59
- Smith, M.W. (2014). Roughness in the Earth Sciences. *Earth-Science Reviews*, 136, 202-225
- Smolander, S., & Stenberg, P. (2003). A method to account for shoot scale clumping in coniferous canopy reflectance models. *Remote Sensing of Environment*, 88, 363-373
- Sohn, G., Huang, X., & Tao, V. (2008). A Data-Driven Method for Modeling 3D Building Objects Using a Binary Space Partitioning Tree. *Topographic Laser Ranging and Scanning* (pp. 479-510): CRC Press

- Solberg, S., Brunner, A., Hanssen, K.H., Lange, H., Næsset, E., Rautiainen, M., & Stenberg, P. (2009). Mapping LAI in a Norway spruce forest using airborne laser scanning. *Remote Sensing of Environment*, 113, 2317-2327
- Stilla, U., & Jutzi, B. (2008). Waveform Analysis for Small-Footprint Pulsed Laser Systems. *Topographic Laser Ranging and Scanning* (pp. 215-234): CRC Press
- Tang, J., Wang, Y., Zhao, Y., Hao, W., Ning, X., Lv, K., Shi, Z., & Zhao, M. (2017). A Modeling Method Of Fluttering Leaves Based On Point Cloud. *Int. Arch. Photogramm. Remote Sens. Spatial Inf. Sci.*, XLII-2/W7, 1373-1379
- Thies, M., Pfeifer, N., Winterhalder, D., & Gorte, B.G.H. (2004). Three-dimensional reconstruction of stems for assessment of taper, sweep and lean based on laser scanning of standing trees. *Scandinavian Journal of Forest Research*, 19, 571-581
- Tsang, L., Kong, J.A., & Ding, K.-H. (2000). Characteristics of Discrete Scatterers and Rough Surfaces. *Scattering of Electromagnetic Waves: Theories and Applications* (pp. 167-197): John Wiley & Sons, Inc.
- Ulaby, F.T., Moore, R.K., & Fung, A.K. (1982). *Microwave remote sensing: active and passive. Volume II. Radar remote sensing and surface scattering and emission theory.*: Addison-Wesley, Reading, Mass; Remote Sensing Series 3
- Vidal Vázquez, E., Miranda, J.G.V., & Paz-Ferreiro, J. (2010). A multifractal approach to characterize cumulative rainfall and tillage effects on soil surface micro-topography and to predict depression storage. *Biogeosciences*, 7, 2989-3004
- Wagner, W. (2010). Radiometric calibration of small-footprint full-waveform airborne laser scanner measurements: Basic physical concepts. *ISPRS Journal of Photogrammetry and Remote Sensing*, 65, 505-513
- Wagner, W., Ullrich, A., Ducic, V., Melzer, T., & Studnicka, N. (2006). Gaussian decomposition and calibration of a novel small-footprint full-waveform digitising airborne laser scanner. *ISPRS Journal of Photogrammetry and Remote Sensing*, 60, 100-112
- Wang, D., Hollaus, M., & Pfeifer, N. (2017). Feasibility Of Machine Learning Methods For Separating Wood And Leaf Points From Terrestrial Laser Scanning Data. *ISPRS Ann. Photogramm. Remote Sens. Spatial Inf. Sci.*, IV-2/W4, 157-164
- Wang, D., Hollaus, M., Puttonen, E., & Pfeifer, N. (2016). Automatic and Self-Adaptive Stem Reconstruction in Landslide-Affected Forests. *Remote Sensing*, 8
- Wang, Y., Hao, W., Wang, G., Ning, X., Tang, J., Shi, Z., Wang, N., & Zhao, M. (2013). A method of realistic leaves modeling based on point cloud. In, *Proceedings of the 12th ACM SIGGRAPH International Conference on Virtual-Reality Continuum and Its Applications in Industry* (pp. 123-130). Hong Kong, Hong Kong: ACM
- Wehr, A. (2008). LiDAR Systems and Calibration. *Topographic Laser Ranging and Scanning* (pp. 129-172): CRC Press
- Wieser, M., Mandlbürger, G., Hollaus, M., Otepka, J., Glira, P., & Pfeifer, N. (2017). A Case Study of UAS Borne Laser Scanning for Measurement of Tree Stem Diameter. *Remote Sensing*, 9

Woodhouse, I.H. (2005). *Introduction to Microwave Remote Sensing*. Boca Ranton, USA: Taylor & Francis Group/CRC Press

Yu, X., Hyypä, J., Litkey, P., Kaartinen, H., Vastaranta, M., & Holopainen, M. (2017). Single-Sensor Solution to Tree Species Classification Using Multispectral Airborne Laser Scanning. *Remote Sensing*, 9

Zhang, K., Yan, J., & Chen, S.-C. (2008). A Framework for Automated Construction of Building Models from Airborne LiDAR Measurements. *Topographic Laser Ranging and Scanning* (pp. 511-534): CRC Press